

Alma Mater Studiorum - Università di Bologna

DOTTORATO DI RICERCA IN  
MECCANICA E SCIENZE AVANZATE DELL'INGEGNERIA

Ciclo 33

**Settore Concorsuale:** 09/C2 - FISICA TECNICA E INGEGNERIA NUCLEARE

**Settore Scientifico Disciplinare:** ING-IND/11 - FISICA TECNICA AMBIENTALE

STANDARDIZATION OF PROCEDURES AND CALCULATION MODELS FOR THE  
NUMERICAL SIMULATION OF ACOUSTICS IN ENCLOSED SPACES

**Presentata da:** Giulia Fratoni

**Coordinatore Dottorato**

Marco Carricato

**Supervisore**

Massimo Garai

**Co-supervisor**

Gian Luca Morini

Dario D'Orazio

**Esame finale anno 2021**



*Qui,  
sul bordo di quello che sappiamo,  
a contatto con l'oceano  
di quanto non sappiamo,  
brillano il mistero del mondo,  
la bellezza del mondo,  
e ci lasciano senza fiato.*

CARLO ROVELLI  
Sette brevi lezioni di fisica



# Sommario

In acustica, poter prevedere e progettare le caratteristiche di un campo sonoro all'interno di un ambiente confinato ha sempre rappresentato una potenzialità altamente utile e attraente. I campi sonori riprodotti digitalmente non solo offrono la possibilità di restituire l'impressione percettiva della reale acustica dell'ambiente ma anche di riprodurre accuratamente numerose caratteristiche acustiche oggettivamente misurabili. In questo scenario, le simulazioni virtuali giocano un ruolo fondamentale in un ampio numero di applicazioni pratiche e scientifiche. Il ventaglio di campi applicativi che richiedono un alto livello di accuratezza può estendersi dalle simulazioni in tempo reale dei video game alla progettazione di grandi spazi d'ascolto, o ancora da approcci archeoacustici volti a ricerche storiche a simulazioni di interventi di miglioramento del comfort acustico in ambienti ordinari.

Nel simulare l'acustica di un ambiente confinato la domanda basilare è: come è possibile riprodurre il campo sonoro in un ambiente tridimensionale virtuale? Nel rispondere a questa domanda tipicamente viene coinvolta la computazione della risposta all'impulso della sala, che può essere vista come un tratto peculiare della stessa, contenente numerose informazioni sulla sua caratterizzazione acustica. Tenendo in considerazione la natura fisica del suono, il range di frequenze interessate dal sistema uditivo umano e le dimensioni degli ambienti destinati ad attività antropiche, si sono sviluppati nel tempo due principali approcci per simulare la risposta all'impulso dell'ambiente e modellare la propagazione sonora nel tempo e nello spazio: i metodi ondulatori e i metodi di acustica geometrica.

Nell'approccio ondulatorio, la riproduzione del campo sonoro all'interno di un ambiente avviene partendo dalla risoluzione dell'equazione delle onde completata con opportune condizioni iniziali e a contorno e, tipicamente, tramite una scomposizione del dominio del sistema. Tale macrocategoria di metodi offre risultati fisicamente validi in tutto il range di frequenza ma, per via dell'elevato costo computazionale dovuto alla discretizzazione del dominio spaziale, e a volte anche temporale, è di fatto limitata all'analisi delle basse frequenze e alle sale di dimensioni ridotte. L'approccio geometrico,

ereditando i principi teorici dall'ottica, si basa sull'approssimazione secondo cui l'energia sonora si propaga lungo le traiettorie perpendicolari ai fronti d'onda. Questo secondo gruppo di tecniche fornisce una maggiore accuratezza nell'analisi delle frequenze medio-alte e nello studio di sale di grandi dimensioni, dove l'approssimazione dell'utilizzo dei "raggi" è più affidabile e verosimile. Dal secolo scorso, in cui entrambi gli approcci hanno avuto origine, sono stati compiuti significativi passi avanti per migliorare il rispettivo rendimento e per compensare i limiti reciproci. Tuttavia, la distinzione fondamentale alla base dei due gruppi di tecniche di simulazione rimane definita, in quanto insita nella differenza di approccio alla fisica del problema in questione. Data la complementarità dei due approcci di simulazione numerica, la comunità scientifica si trova tendenzialmente d'accordo nella potenzialità dell'utilizzo di algoritmi ibridi che combinino i benefici e minimizzino i limiti di ciascun metodo, offrendo la possibilità di riprodurre in maniera accurata il comportamento dell'energia sonora in un ampio spettro di frequenza. Per quanto a conoscenza dell'autrice, fino ad ora le applicazioni di tecniche ibride di simulazione sono state svolte perlopiù in spazi di piccole e medie dimensioni.

Il presente lavoro si pone come indagine sulla fattibilità e l'accuratezza di un modello ibrido ondulatorio-geometrico applicato ad ambienti di grandi dimensioni. Il modello utilizzato è stato sviluppato dal team di ricerca *Acoustics and Audio Group* dell'Università di Edimburgo e il lavoro della presente tesi può essere considerato come una parte della fase di beta testing del codice in ambito applicativo. Tale modello combina nel dominio delle frequenze un approccio ondulatorio, *finite-difference time-domain* (FDTD), con un approccio geometrico tradizionale di *ray tracing*, ossia di acustica geometrica (GA). Durante l'indagine l'attenzione viene posta sulle recenti opportunità fornite al modello ondulatorio dalla crescente potenza di calcolo ottenuta dalle attuali tecnologie e dalla maggiore efficienza degli algoritmi adottati nel modello. Preso atto della possibilità di un punto di svolta nel campo di applicazione dei modelli FDTD nell'acustica dei grandi spazi, la presente tesi espone il metodo con cui sono state testate e valutate queste nuove potenzialità, unendo alle valutazioni sulla performance un'attenta analisi dei criteri di scelta dei fattori più significativi nel processo di simulazione.

Quattro diverse sale di ampie volumetrie, che solitamente sarebbero gestite unicamente tramite acustica geometrica, sono state selezionate per lo studio, ciascuna per motivazioni specifiche diverse: un teatro tradizionale all'italiana, un teatro moderno, una sala ellittica polivalente e un'aula universitaria. Ogni ambiente preso in considerazione è stato caratterizzato acusticamente tramite misurazioni acustiche svolte *in situ* con il fine di ottenere parametri oggettivi riguardanti le caratteristiche acustiche di ciascun campo sonoro. Una volta

calibrati tutti i modelli numerici, l'affidabilità del metodo di simulazione utilizzato è stata valutata tramite specifiche analisi - opportunamente scelte a seconda della tipologia di ambiente - sulle risposte all'impulso simulate. Dei teatri sono state principalmente indagate le caratteristiche acustiche legate al decadimento non lineare di energia sonora, fenomeno strettamente collegato alle diversità di condizioni acustiche caratterizzanti ciascuna area di ascoltatori considerata. La sala ellittica polivalente ha offerto la possibilità di indagare i fenomeni di *flutter echoes* e di focalizzazione dell'energia sonora dovuti alla peculiare forma dell'architettura. Il caso studio dell'aula universitaria ha inoltre reso possibile un'analisi delle matrici di trasferimento del segnale del parlato e una resa appropriata delle caratteristiche d'impedenza acustica di pannelli microforati inseriti al suo interno. Il modello ondulatorio impiegato in ciascuno di questi casi è quindi stato utilizzato come strumento di ricerca all'interno di ambienti con peculiarità acustiche differenti.

Tutte le fasi della simulazione e il metodo con cui sono state validati i modelli sono riportati e descritti nel dettaglio: la modellazione 3D, i dati di input, le impostazioni di calcolo, il tempo di simulazione necessario e gli indicatori acustici interessati di volta in volta nei casi studio valutati. Parallelamente, un confronto con le corrispondenti fasi della tradizionale prassi di algoritmi di acustica geometrica è sistematicamente proposto, garantendo il mantenimento di un punto di riferimento, di paragone e di contatto con la procedura standard solitamente adottata negli spazi di medie e grandi dimensioni. La tesi permette di definire un paragone complessivo e neutrale tra ciò che è lo stato dell'arte della simulazione acustica dei grandi spazi e le nuove frontiere, rese accessibili dai recenti successi della ricerca nel settore dei metodi ondulatori, tramite il sistematico studio di fattibilità di un modello appartenente a quest'ultima categoria.

Il lavoro fornisce inoltre una cospicua quantità di dati relativi alle condizioni a contorno adottate come dati di input in ciascuna simulazione, creando un prezioso database in cui sono state evidenziate le principali differenze con la natura dei dati solitamente utilizzati in acustica geometrica. Lo studio, dunque, delinea considerazioni pratiche e teoriche sull'efficienza del metodo di simulazione ibrida adottato, arricchendo la letteratura scientifica esistente di ulteriori dati e casi studio per un benchmark sempre più corposo di acustica computazionale.



# Abstract

In acoustics, the possibility to predict and synthesize sound fields in enclosed spaces has always represented an important and attractive opportunity. Digitally computed acoustic environments are able not only to provide a perceptual impression of the actual sound field in the enclosures assessed but also to accurately model several objective measurable acoustic characteristics. In this scenario, computer simulations play a fundamental role in a large number of practical and scientific applications. The demands of situations with a high level of accuracy required may widely vary: from real-time simulation in virtual reality and video games settings to the prediction of large performance spaces, from archaeoacoustic approaches in historical research to computer-aided design of treatments for better acoustic comfort in ordinary rooms.

In room acoustics simulation the general question is: how to derive sound from a three-dimensional virtual room? The answer typically involves the computation of the room impulse response, which may be seen as a specific trait including all the peculiar characteristics of the enclosed space under study. Taking into account the physical nature of the sound, the frequency range concerned by our hearing system, and the common size of environments designed for human activities, the numerical calculation methods offer two distinct approaches to simulate the impulse response and to model the sound propagation in space and time: the wave-based and the ray-based techniques.

To synthesize the sound field within an enclosed space, the wave-based approach directly deals with the resolution of the problem expressed by the wave equation and is properly completed with initial and boundary conditions. This typically occurs by employing a discretization of the problem domain. The outcomes of this category of techniques remain valid in the whole frequency range but the applications are usually limited to low frequencies analysis and small rooms because of the high computational requirements caused by the spatial - and in some cases spatiotemporal - domain discretizations. The ray-based approach finds its roots in the assumption that sound propagates through the trajectories - the *rays* - defined by the local directions

of propagation, pointwise normal to the wavefronts. It is commonly defined as Geometrical Acoustics (GA) because of the similarity to the geometrical basics adopted by the optics theory. This second group of techniques is generally more suited to medium-high frequencies analysis and large-scale rooms, where the approximation with rays is more reliable and accurate.

From the last century - when both the approaches originated - huge steps have been made to enhance the performances and to compensate for the respective weaknesses of these two kinds of modeling techniques. Nevertheless, the essential distinction between them remains clearly defined, as it is embedded in the way the issue is physically managed. As the advantages and disadvantages of the two macro-categories of methods can be considered complementary, scholars generally agree with the use of hybrid models, that are expected to provide accurate broadband results combining the benefits and minimizing the drawbacks of each method. To the best of the author's knowledge, up to this moment, the application of hybrid techniques has been mostly limited to small and mid-sized rooms.

The present work is an exploration of the feasibility and the accuracy of a hybrid model when applied to large-scale environments. The model selected has been developed by the *Acoustics and Audio Group* research team of the University of Edinburgh (UK) and the present thesis may be considered as a part of the beta testing phase of the code when applied to large scale case studies. In the frequency domain the model combines a wave-based method, a *finite-difference time-domain* (FDTD) code, with a traditional GA approach, the *ray tracing* method. During the investigation, the attention is focused on the possibilities recently achieved in the wave-based part of the model thanks to the increasing computational power and to new efficient algorithms adopted. In fact, the increased computational performance of modern devices and the recent state-of-the-art research concerning optimized calculation schemes represent a great breakthrough in room acoustic FDTD simulations. The present thesis concerns the method employed to test and assess these new potentials through various application contexts. Moreover, a thorough analysis of the most significant factors affecting the simulation process is carried out with specific assessments on the outcomes.

A sample of four large environments, that commonly would be handled with GA techniques, is employed in this study, each one of them for specific peculiar reasons: a traditional opera house, a modern theatre, a multipurpose elliptical hall, and a historical university lecture hall. The sound field of the halls has been characterized with acoustic measurements performed *in situ* to collect the objective criteria describing the peculiar acoustic features in each environment. Once having calibrated the 3D virtual models, the reliability of the simulation method has been assessed through specific investigations

performed on the simulated impulse responses. In the first two cases, i.e. the opera houses, the multi-slope analysis on the energy decays has been employed to detect the acoustic coupling effects characterizing in distinct ways each audience area. The elliptical concert hall gave the author the possibility to investigate the presence of flutter echoes and focusing effects due to the peculiar shape of the architecture. In the university lecture hall, the chance to explore the rendering of time-dependent phenomena - as the modulation transfer functions of the speech signal - by means of time-domain methods was exploited. Moreover, the same hall was used to study the proper simulation of complex impedances of specific acoustic treatment made up of micro-perforated panels. Therefore, the wave-based simulation method was employed in each of those case studies as a research tool assessing specific acoustic aspects in different acoustic contexts.

All the simulation process steps and the method adopted to validate the models are reported and described in detail: the 3D modeling phase, the input data, the setting of proper calculation parameters, the time cost, and the acoustic metrics considered time by time in the halls assessed. In parallel, a systematic comparison with the corresponding steps of the geometrical acoustics process is provided to keep a reference point during the process and to outline a comparison with the usual acoustic simulation procedure. The thesis allows defining an objective benchmark between the state-of-art of acoustic simulation in medium and large scale environments and the new advances allowed by recent research in wave-based methods.

Finally, the present thesis provides a considerable amount of data concerning the material properties employed as input boundary conditions in each simulation, creating an important database in which the main differences with the common energy parameters adopted in geometrical acoustics are highlighted. The work outlines theoretical and practical remarks on the effectiveness of the hybrid simulation method adopted, enhancing the existing scientific literature with further data and case studies for an increasingly thorough benchmark of computational acoustics techniques.



# Contents

<b>Sommario</b>	<b>1</b>
<b>Abstract</b>	<b>5</b>
<b>1 Introduction</b>	<b>13</b>
1.1 Introductory concepts . . . . .	13
1.2 Thesis objectives . . . . .	15
1.3 Overview of the thesis . . . . .	16
1.4 Main contributions . . . . .	18
<b>2 Room acoustics simulation</b>	<b>21</b>
2.1 Theoretical fundamentals . . . . .	22
2.1.1 The wave equation . . . . .	26
2.1.2 Material properties . . . . .	27
2.2 Wave-based simulation methods . . . . .	32
2.2.1 Finite element . . . . .	34
2.2.2 Boundary element . . . . .	38
2.2.3 Finite-difference time-domain . . . . .	40
2.3 Ray-based methods . . . . .	46
2.3.1 Image Source Method . . . . .	48
2.3.2 Stochastic ray-tracing . . . . .	50
2.3.3 The inclusion of diffraction in GA++ techniques . . . . .	53
<b>3 Method</b>	<b>57</b>
3.1 Combined FDTD/GA simulations . . . . .	57
3.1.1 Air absorption . . . . .	61
3.1.2 Computational cost . . . . .	62
3.2 Approach to the simulation setup . . . . .	63
3.3 Simulation studies on specific aspects . . . . .	65
3.4 Practical procedure . . . . .	72
3.5 GA++ simulations setup . . . . .	77

<b>4</b>	<b>Systems of coupled rooms</b>	<b>81</b>
4.1	A traditional historical opera house . . . . .	82
4.1.1	Acoustic measurements . . . . .	84
4.1.2	FDTD calibration . . . . .	89
4.1.3	Acoustic coupling . . . . .	96
4.2	A modern opera house . . . . .	101
4.2.1	Acoustic measurements . . . . .	104
4.2.2	FDTD calibration . . . . .	109
4.2.3	Sound reflectors . . . . .	115
<b>5</b>	<b>Elliptic performance space</b>	<b>121</b>
5.1	An elliptic multipurpose hall . . . . .	122
5.1.1	Acoustic measurements . . . . .	123
5.1.2	FDTD calibration . . . . .	128
5.1.3	Flutter echoes . . . . .	132
5.1.4	Focusing effects . . . . .	134
<b>6</b>	<b>Space for verbal communication</b>	<b>137</b>
6.1	An university lecture hall . . . . .	138
6.1.1	Acoustic measurements . . . . .	138
6.1.2	FDTD calibration . . . . .	142
6.1.3	Micro-perforated acoustic treatment . . . . .	146
<b>7</b>	<b>Discussions</b>	<b>153</b>
7.1	3D modeling . . . . .	154
7.2	Input data . . . . .	157
7.3	Multi-decay analysis . . . . .	159
7.4	Frequency response . . . . .	164
<b>8</b>	<b>Conclusions</b>	<b>169</b>
8.1	Summary . . . . .	169
8.2	Outlook and future work . . . . .	172
<b>A</b>	<b>Boundary conditions</b>	<b>175</b>
A.1	LRC coefficients . . . . .	175
A.2	Energy parameters . . . . .	180
<b>B</b>	<b>Repository</b>	<b>183</b>
B.1	Aim and description . . . . .	183
	<b>Symbols</b>	<b>185</b>

<b>Abbreviations</b>	<b>187</b>
<b>Bibliography</b>	<b>187</b>
<b>List of figures</b>	<b>211</b>
<b>List of tables</b>	<b>214</b>



# Chapter 1

## Introduction

### 1.1 Introductory concepts

The acoustic community has always been interested in the chance to predict the sound field within enclosed environments. Indeed, the opportunity to handle the acoustic design even in a preliminary phase of the whole design process of any room is of essential importance. Generally, there are two main ways to predict the acoustics of spaces: analytical formulas and computer aided simulations [1]. This distinction should not be intended as a reason for a unique choice between the chances but, instead, as a range of possibilities aimed to pursue the same objective. In research practice it is quite common to employ both the analytical models and the numerical simulations, even just for obtaining a double set of results supporting each other. Indeed, both analytical models and simulation approaches have their own assumptions and approximations. The awareness of those latter is extremely important to understand and assess the relative outcomes.

In room acoustics simulation, the impulse response of the room definitely plays a key role. The current technological advances and the considerable range of existing simulation methods aim to synthesize the impulse response with as much fidelity as possible between simulation and reality. The methods to model the sound propagation offer two distinct approaches: the first one focused on the wave nature of the sound, the second one built on ray optics rules [2, 3]. The wave-based approach directly deals with the resolution of the wave equation generally by employing spatial and time discretization [4, 5]. The outcomes of this category remain physically and theoretically valid in all the frequency bands assessed, at the expense of high computational cost and a certain degree of numerical dispersion. For this reason, in room acoustics simulations the wave-based approach is generally employed

on low frequency analysis and in small-sized enclosed spaces [6]. The ray-based approach, commonly defined as Geometrical Acoustics (GA), finds its roots in computer graphics principles, i.e. the assumption that sound propagates through *rays* [7, 8]. In acoustics, the so-called rays are not conceived to replace the waves. The rays represent the trajectories created by the directions of the sound energy propagation, which is normal to the wavefronts [9]. The approximation of considering the sound propagating through rays is valid assuming specific hypotheses [10].

Since classical GA techniques neither directly handle wave phenomena nor carry phase information, they are more suitable for medium-high frequencies analysis - because the ray approximation is much reliable whether the wavelength is enough smaller than the wavefront - and in large-scale spaces, where low Schroeder frequencies entail statistical description of the sound field in most of the octave bands concerned [11, 12].

Recently, significant efforts have been made from the two macro-categories of methods to push the boundaries improving their performance and compensate their respective weaknesses. On one hand, phased GA simulation models have been proposed [13, 14], involving the introduction of the phase information, which is fundamental for the analysis of wave interference at low frequencies [15]. Furthermore, it has been several years that the intention of representing the wave phenomena results, for instance, in the use of the so-called *scattering coefficient*. The computation of scattering effects, even though approximated at a certain level, requires the definition of GA++ techniques [16]. On the other hand, thanks to the latest advances in GPU technology, it is possible to extend the application of wave-based methods to larger environments and higher frequencies maintaining reasonable dispersion errors and computational costs [6, 17]. In particular, among the wave-based models the finite-difference time-domain algorithms are the most suited to describe transient phenomena. Moreover, FDTD models proved to have the most straightforward computation to parallelize and to be distributed to independent processors [18, 19]. While for decades the wave-based application field has been constrained by the inherent computational cost, which increases with the implementation at higher frequencies and with the volume of the 3D geometry, nowadays the technological successes in parallel computing tasks combined with new efficient calculation schemes opened new opportunities in applications on large-scale rooms. Moreover, the recent implementation of frequency-dependent wall impedances in non-trivial geometries has allowed to enhance the accuracy of input data at the boundaries [19].

Notwithstanding these considerable enhancements in wave and geometrical techniques, a hybrid simulation approach is expected to return the best

accuracy and efficiency, according to the state-of-the-art research [20, 21]. From this perspective, it is extremely useful to compare the advantages and the disadvantages of the two simulation methods' macro-categories. The specific knowledge of the strengths and the weaknesses of the approaches helps to define the inherent accuracy of the results, allowing to properly combine the best qualities of each approach.

## 1.2 Thesis objectives

The present thesis is intended to thoroughly investigate the feasibility of a recent hybrid model developed by the *Acoustics and Audio Group* of the University of Edinburgh (UK) when applied to broadband frequency analysis in large non-trivial enclosed spaces. The model chosen combines a finite-difference time-domain (FDTD) method, comprehensive of the implementation of finite-volume time-domain (FVTD) at the boundaries, and a classical ray-tracing for high frequencies. The technological and research advances allow to considerably push the boundary of the wave-based part of the model and thus, the threshold frequency between it and the ray-tracing algorithm will be chosen as high as possible. For this reason, in the present thesis most of the attention will be focused specifically on the wave-based part of the model.

In the present work, the hybrid model aforementioned is applied to specific case studies, which have been selected by the author as suited to the purpose. The set of reference environments, which differ in size, shape, use, and surfaces typology, is used as test sample in the present study. Since the rooms selected are of medium and large scale, it should be noted that the performance of the wave-based part of the model will be pushed exactly in the field generally covered by the ray-based methods. The basic principles of FDTD models, the required input data, the procedures followed, and the accuracy of simulated results are described and discussed in detail.

The results of the acoustic measurements carried out in the rooms investigated represent the overall reference point during the calibration process and the analysis of the simulation outcomes. In parallel, all the necessary steps of the workflow are systematically compared with the corresponding state-of-the art procedure that implies ray-based algorithms.

The objective of the work is the neutral exploration on the possibilities of the FDTD model chosen in comparison with the usual geometrical approach, pointing out feasible applications, benefits and limitations. The performances of the approach is evaluated according to specific analysis that vary depending on the peculiar acoustic features of the spaces assessed. At the best of

the author's knowledge there are a few examples of broadband wave-based simulations in medium and large spaces. The aim of this thesis is to analyse the consequences of the cutting-edge advances, both in computational power and in recent research based implementations, when applied to a peculiar set of case studies. The author remains confident that the outline of an accurate benchmark procedure in room acoustic simulations will be useful to acquire awareness about the current possibilities at the time of writing and the way they could influence the acoustic simulations in enclosed environments.

### 1.3 Overview of the thesis

The present thesis is divided into eight chapters, presented hereafter.

#### **Chapter 1**

Chapter 1 provides an overview of the whole thesis. It includes the introductory remarks, the objective of the work, the division in chapters, the main contributions and the related publications. The subdivision in chapters helps the reader to follow the approach to the problem and each phase of the workflow.

#### **Chapter 2**

Chapter 2 contains an overview on the background theory, along with the most relevant literature concerning the wave-based and the ray-based approaches to the room acoustic simulation. An overall outline of wave-based methods is presented, including finite and boundary element methods. In particular, the general features of FDTD methods are described as thoroughly as it is necessary for the objective of this work. A brief summary of the main ray-based models is reported to provided a parallel with the aforementioned wave-based methods. It should be reminded that the ray-based approach is the one that is usually employed in medium and large-scale room environments, as those ones under study. Furthermore, an insight of material properties is provided in terms of necessary input data required for each simulation model.

#### **Chapter 3**

In Chapter 3 the hybrid wave/ray-based method employed in this thesis is described, focusing on the FDTD part of the model. The author's aim is to describe the general features of the algorithm functioning as long as they

help the reader to obtain useful recommendations for the best use of it. Most of the attention should be paid to the necessary considerations for efficient calculation setups and the most straightforward way to maintain a comparison term with the ray-based usual procedure. Moreover, the specific reasons that justify the choice of the rooms assessed as test sample are thoroughly explained to the reader. Finally, the method followed by the author during the workflow is presented in detail, highlighting the choices and the relative consequences in any step of the simulation process.

## **Chapter 4**

In Chapter 4 two large opera houses are considered: the first with a traditional shape and the second with a modern shape. These performance spaces have been selected as case studies not only for their huge volume - which represents a considerable challenge for a wave-based method - but also for their articulated geometrical shape. The presence of coupled volumes significantly affects in different ways the acoustic conditions at the listeners in the various audience areas. The opera houses give the opportunity to explore the feasibility of the wave-based model in the systematic simulation of the specific acoustic condition referred to several combinations of source-receiver pair. A further motivation is the intention to simulate all the wave phenomena occurring in these composite architectures with an algorithm that naturally computes the edge diffraction. The modern opera house also allows the assessment of the scattering effects - closely related to the wave nature of the sound - due to an array of sound reflectors in the stage house.

## **Chapter 5**

In Chapter 5 an elliptical-domed concert hall is evaluated. This time the challenge for the wave-based model is rendering the peculiar acoustics of a multipurpose hall with curved walls and a double dome as ceiling. The typical effects caused by curved surfaces, such as the sound concentration in some points of the hall, are investigated. The concert hall differs from the first two case studies not only in the shape but also in its moderate size, allowing full wave-based simulations up to the frequencies of interest (4 kHz octave band included).

## **Chapter 6**

In Chapter 6 an university lecture hall is investigated. The reason behind the choice of the hall is connected with the oral communication. The fact that the model employed is a time domain algorithm fits well with the

strong dependence of speech modulations from the time. As the case study in Chapter 5, also in this case the mid size of the hall allows a full FDTD simulation in the octave bands concerned by the speech intelligibility (8 kHz octave band included). Moreover, the availability of experimental data of a microperforated sample by impedance tube gives the chance to simulate an acoustic treatment in the hall directly using the complex acoustic impedances as boundary conditions. This allows to avoid the typical uncertainties connected with the backward process from the widely available material properties databases in terms of random incidence absorption coefficient to the complex acoustic impedance data.

## Chapter 7

Chapter 7 is focused on the discussion about the consequences of methodological approach explained in Chapter 3 and the results of the work described in Chapters 4, 5, and 6. The calibration of the same models through GA++ techniques allows to establish connections between the standard ray-based simulation and the hybrid FDTD/GA approach. Insights are provided in terms of remarks on the different choices adopted in 3D modeling step, the analysis of discrepancies in input data required for the two simulation approaches, the energy decay curves and the energy contribution as a function of the frequency.

## Chapter 8 and Appendices

Chapter 8 contains the concluding remarks and some insights into possible future developments. The first part of Appendix A provides the equivalent LRC components of the circuits used for the boundary impedances. The second part of Appendix A provides the energy parameters derived from the acoustic impedances of FDTD simulation compared with the energy parameters used in GA++ process. In Appendix B the freely available online repository containing all the materials involved in the calibration of the models is described. The list of symbol, acronyms and abbreviation used in the manuscript is provided at the end of the thesis, along with the lists of tables and figures.

## 1.4 Main contributions

The main contributions of this thesis are:

- 
- The proposal of a rigorous method to optimize the acoustic simulation process in medium and large rooms using hybrid FDTD/GA methods. This goal is pursued by analysing the accuracy of the outcomes, the computational time cost, the proper choice of the threshold frequency, and the typology of available input data. Each assessment is developed considering the specific traits of the acoustic features of the different environments under study (Chapters 3, 4, 5, 6).
  - A group of theoretical and practical recommendations and suggested methodologies that can help in the choice of the threshold frequency in hybrid methods (Chapter 3).
  - A thorough investigation on the feasibility, the time cost, the accuracy and the required procedure for pushing the boundary of the FDTD model chosen in non-trivial large performance spaces (Chapter 4).
  - The evaluation of the physically correct computation of wave phenomena, as those ones related to edge diffraction from sound reflectors installed in a stage house (Chapter 4).
  - The detection of flutter echoes and sound concentration (focusing effects) caused by curved performance spaces in a 3D model calibrated with FDTD techniques (Chapter 5).
  - The full spectrum FDTD simulation of experimental material properties of sustainable materials when applied to a lecture room context, in which the verbal communication is fundamental (Chapter 6).
  - A comprehensive analysis and comparison between the uncommon application of the wave-based method to large-sized enclosures and the standard state-of-art ray-based simulations on the same rooms, in order to provide a neutral benchmark of the current advances in both the fields (Chapter 7).
  - An exhaustive dataset of input data for boundary conditions both for wave-based and ray-based algorithms (Appendix A).
  - A freely available repository containing all the necessary data for allowing any other research to perform the same simulations (Appendix B).



# Chapter 2

## Room acoustics simulation

In room acoustics virtual sound fields are expected to render the natural propagation of sound waves throughout the spaces, considering the geometrical and material properties of the room. The main distinction among the methods used to model the sound propagation is generally determined depending on whether the wave nature of the sound is directly handled or not. This chapter summarizes the background theory and the scientific literature concerning the two macro-categories of approaches in numerical simulations: the wave-based and the ray-based methods (see Fig. 2.1). A third category of methods, i.e. the diffuse field equation models [22, 23, 24], are beyond the objective of the present thesis. A brief summary of the theoretical fundamentals underlying the wave equation problem is here presented.

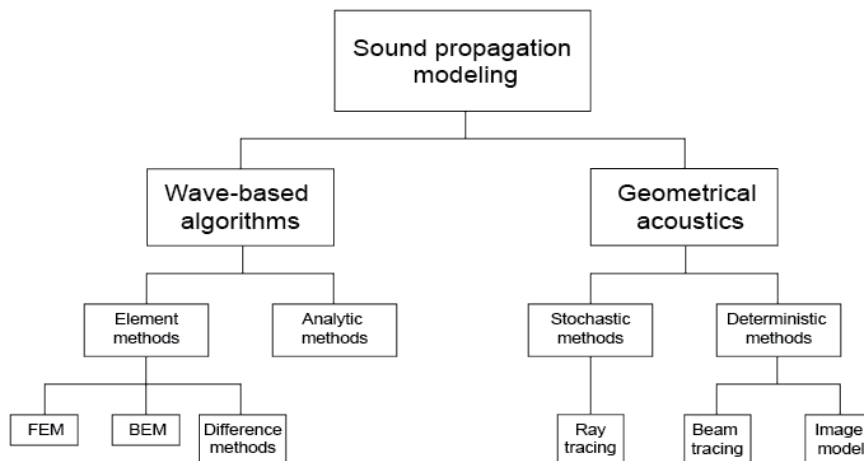


Figure 2.1: Sound propagation modeling: the two macro-categories to simulate the sound field behaviour are the wave-based algorithms and the geometrical acoustics [25]. The diffuse field equation models are beyond the objective of the present thesis.

## 2.1 Theoretical fundamentals

Acoustic waves are a specific typology of pressure fluctuations that can occur in a transmission medium. Room acoustics deals with acoustic waves propagating through a compressible fluid, the air. Hence, the attention will be mostly focused on the only waves that can exist in fluids: the *longitudinal waves* [9]. The energy propagation in air occurs by means of compression and expansion of the fluid, as shown in Figure 2.2.

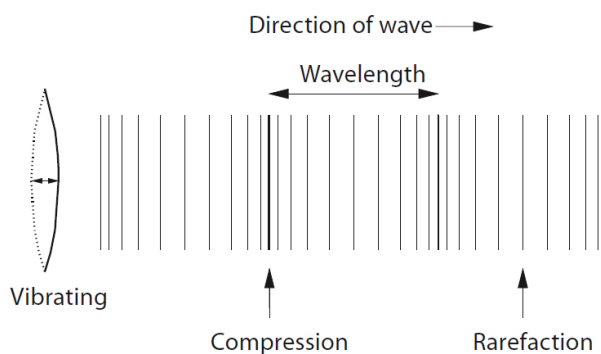


Figure 2.2: Compression and rarefaction of the air caused by acoustic waves. Credits picture: Barron, M. (2009) [26].

The pressure variations that occur when the fluid is compressed or expanded are the responsible forces for the propagation of acoustic waves [10]. The single particles of the fluid move back and forth following the directions of the forces, leading to adjacent regions of compression and expansion. The term *particle*, or *fluid element*, is referred to an infinitesimal volume of the fluid, large enough to allow to consider the whole medium as a continuum and at the same time small enough to be characterised by uniform acoustic variables. Even without the acoustic waves, molecules in a fluid are not fixed in their positions, but they randomly move. Nevertheless, a small volume of a fluid can be assumed as a constant unit considering the replacement of molecules getting out of the volume with other molecules - on average the same number - entering its confines (see Fig. 2.3).

Therefore, it is possible to speak of particle displacement,  $\xi$ :

$$\xi = \xi_x \hat{x} + \xi_y \hat{y} + \xi_z \hat{z} \quad (2.1)$$

and particle velocity,  $\mathbf{v}$ :

$$\mathbf{v} = \frac{d\xi}{dt} = v_x \hat{x} + v_y \hat{y} + v_z \hat{z}, \quad (2.2)$$

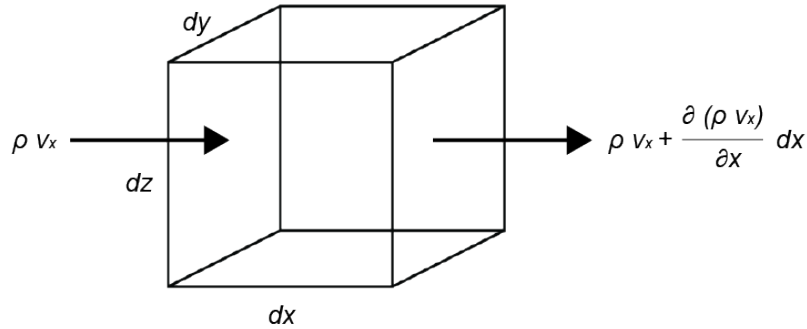


Figure 2.3: A fixed volume of the fluid showing the rate of mass flow going into and out the volume in the  $x$  direction.

where the term *displacement* is referred to a variation from the equilibrium position,  $\mathbf{r}$ :

$$\mathbf{r} = x\hat{x} + y\hat{y} + z\hat{z} \quad (2.3)$$

where  $x, y, z$  are the directions and  $\hat{x}, \hat{y}, \hat{z}$  are the corresponding unit vectors.

It should be noticed that even though acoustic waves cause compression and rarefaction, the macroscopic properties of the fluid remain unchanged.

### The speed of sound

As the acoustic waves travel with a speed that depends on the medium they are passing through, it is important to recall the typical assumptions made in case the medium is the air, i.e. in room acoustics field.

- The air is a homogeneous, quiescent and vortex free medium.
- The air is an inviscid and lossless fluid, and thus, lacking of dissipative effects due to viscosity ( $\mu_0 = 0$ ).
- Relationships in the medium are subject to linear differential equations. Therefore, it is possible to formulate the sound pressure and density variations caused by acoustic waves as follows:

$$p_{tot} = p + p_0, \quad \rho_{tot} = \rho + \rho_0 \quad (2.4)$$

where  $p$  is the sound pressure variation,  $p_0$  is the atmospheric pressure,  $\rho$  is the density variation,  $\rho_0$  is the atmospheric density.

- Pressure and density perturbations are small compared to the mean values of the atmospheric pressure and density [27]:

$$p \ll p_0, \quad \rho \ll \rho_0. \quad (2.5)$$

- State changes are adiabatic ( $pV^\gamma = \text{constant}$  with  $p$  the sound pressure in Pa,  $V$  as the volume in  $\text{m}^3$  and  $\gamma$  the adiabatic index), meaning that there is no heat interchange between areas of low pressure and areas of high pressure due to the rapid movement of the particles.

Assuming the sound propagation as an adiabatic process the speed of sound,  $c$ , can be expressed through the expression:

$$c = \sqrt{\left(\frac{\partial p}{\partial \rho}\right)_\gamma} = \sqrt{\frac{\gamma p_0}{\rho_0}} = \sqrt{\gamma RT} \quad \text{m/s} \quad (2.6)$$

where

- $\gamma$  is the ratio between the isobaric specific heat  $c_p$  and the isochoric specific heat  $c_v$ ,
- $p_0$  is the atmospheric pressure, in Pa,
- $\rho_0$  is the atmospheric density, in  $\text{kg}/\text{m}^3$ .

Assuming the ideal conditions aforementioned, the velocity of propagation, i.e. the speed of sound in the air, could be assumed as [9]:

$$c \approx 331.4 + 0.6T \quad \text{m/s} \quad (2.7)$$

where  $T$  is the temperature of the air expressed in Celsius degrees. Equation 2.7 implies that the theoretical value of the sound speed at  $0^\circ$  at 1 atm is 331.4 m/s, that is a value confirmed and consolidated by experimental results.

Moreover, the density of the air, the instantaneous  $\rho$  value, may be assumed as a constant,  $\rho_0$ , because its variations due to the small amplitude of the acoustic waves are small compared to the mean density value. The aforementioned assumptions are of fundamental importance for the following description of the wave equation for sounds propagating through the air. Experimental results confirmed the reliability of these hypotheses granting that wave phenomena are properly described with those assumptions.

### The continuity equation

Fundamentals of linear acoustics are based on continuum mechanics principles. Therefore, considering a small rectangular volume  $dV = dx dy dz$  fixed in the space (see Fig. 2.3) with a fluid traveling through it, the rate with which mass flows into the volume must be equal to the rate with which mass

increases in the volume. The mass flow entering the volume in the  $x$  direction is:

$$\left[ \rho v_x - \left[ (\rho v_x + \frac{\partial(\rho v_x)}{\partial x} dx) \right] \right] dydz = -\frac{\partial(\rho v_x)}{\partial x} dV \quad (2.8)$$

and the same equation may be expressed for the flow entering in the  $y$  and  $z$  direction. Globally, the combination of these three contributions may be expressed as:

$$-\left( \frac{\partial(\rho v_x)}{\partial x} + \frac{\partial(\rho v_y)}{\partial y} + \frac{\partial(\rho v_z)}{\partial z} \right) dV = -\nabla \cdot (\rho \mathbf{v}) dV. \quad (2.9)$$

The net incoming flux must be equal to the rate the mass increase  $(\partial\rho/\partial t) dV$ :

$$\frac{\partial\rho}{\partial t} = -\nabla \cdot (\rho \mathbf{v}). \quad (2.10)$$

The equation 2.10 is the continuity equation, also known as the *conservation mass law*. It describes the relation between the particle velocity,  $\mathbf{v}$ , due to the compression and expansion of the fluid with the instantaneous density,  $\rho$ . Basically it states that the change in time of the mass contained in the volume considered is equal to the mass that passes through the volume [10]. Assuming  $\rho \approx \rho_0$ , equation 2.10 becomes:

$$\frac{\partial\rho}{\partial t} = -\rho_0 \nabla \cdot \mathbf{v} \quad (2.11)$$

and Equation 2.11 will be assumed as valid from now onwards in the manuscript.

### The Euler's equation

The second fundamental law is the linear Euler's equation, also known as conservation of momentum [10]:

$$\rho_0 \frac{\partial \mathbf{v}}{\partial t} = -\nabla p \quad (2.12)$$

where

- $\rho_0$  is the static value of the air density, in  $\text{kg}/\text{m}^3$ ,
- $\mathbf{v}(\mathbf{x}, t)$  is the vector field particle velocity, in  $\text{m}/\text{s}$ ,
- $t$  is the time, in seconds,
- $p(\mathbf{x}, t)$  is the sound pressure, i.e. the deviation from the ambient pressure  $p_0$ , in Pa.

Equation 2.12 expresses the *momentum conservation law* in case of acoustic waves of small amplitude.

Since the vector particle velocity  $\mathbf{v}(\mathbf{x}, t)$  is irrotational ( $\nabla \times \mathbf{v} = 0$ ), it may be expressed as the gradient of the scalar function  $u(\mathbf{x}, t)$ , the so-called velocity potential:

$$\mathbf{v} = -\nabla u. \quad (2.13)$$

This is a consequence of the inviscid fluid assumption: with this hypothesis the acoustic excitation does not provoke rotational flows. A real fluid is not vortex free everywhere in the space but the rotational effects - most evident near the boundaries - are in most of the cases enough small to be neglected. Combining Eq. 2.13 with the linear Euler's equation described in Eq. 2.12, the relation between  $u(\mathbf{x}, t)$  and  $p(\mathbf{x}, t)$  may be derived:

$$p = -\rho \frac{\partial u}{\partial t}. \quad (2.14)$$

### 2.1.1 The wave equation

Typically, the whole problem of the behaviour of the sound pressure is handled through a single partial differential equation, the so-called *wave equation*. Combining the time derivative of Equation 2.11 with the divergence of Eq. 2.12, it is possible to eliminate the vector field particle velocity related terms, by subtracting the second equation from the first one. These steps allow to obtain a second order differential equation, expressed according to the linear formulation:

$$\frac{\partial^2 p}{\partial t^2} = c^2 \nabla^2 p \quad (2.15)$$

where  $c$  is the speed of sound in the air, in m/s, and  $\nabla^2$  is the three-dimensional Laplacian operator, also expressed as  $\Delta$ . Again, assuming the absence of significant air flows, high sound pressures or any nonlinearities, the Eq. 2.15 is the *linear, lossless wave equation* describing the propagation of sound waves in fluids with phase speed  $c$ . Therefore, it is of fundamental importance for most phenomena concerning the room acoustics.

As a function of the scalar field velocity potential,  $u(\mathbf{x}, t)$ , the wave equation may be also expressed as [9]:

$$\frac{\partial^2 u}{\partial t^2} = c^2 \nabla^2 u. \quad (2.16)$$

It should be noticed that Eq. 2.15 is the wave equation in its time dependent form. Generally, assuming that the sound pressure is a time-harmonic signal of the type

$$p(\mathbf{x}, t) = P(\mathbf{x})e^{-i\omega t} \quad (2.17)$$

where  $P(\mathbf{x})$  is the pressure amplitude and  $\omega$  is the angular frequency of oscillation, in rad/s, it is possible to express the wave equation in its time independent form. Equation 2.17 represents a plane wave solution and it can be also expressed as:

$$p(\mathbf{x}) = P(\mathbf{x})e^{-i\beta x} \quad (2.18)$$

where  $\beta x$  is the scalar product of the point  $\mathbf{x}$  in cartesian coordinates and the propagation vector  $\beta$ . The plane wave solution describes a harmonic sound wave that does not vary in the space on each plane normal to the propagation vector  $\beta$  [28]. In fact, combining Eq. 2.17 with Eq. 2.15 the *Helmholtz equation* for a time-harmonic signal is defined:

$$\nabla^2 p = -\beta^2 p \quad (2.19)$$

where  $\beta$  is the spatial wavenumber, that is defined as:

$$\beta = \frac{\omega}{c} = \frac{2\pi f}{c} = \frac{2\pi}{\lambda} \quad \text{rad/m} \quad (2.20)$$

being  $\omega$  the angular frequency, in rad/s,  $f$  the frequency, in Hz,  $\lambda$  the wavelength, in m.

The Helmholtz equation alone does not specify a physical solution, but further conditions are required. In order to solve this equation, information about the regions over which they are defined, material properties, boundary conditions, and initial conditions that describe the physical problem are required. The initial conditions and the boundary conditions are of fundamental importance to define correctly the problem. At this point an overview of the analytical definition of the material properties and boundary conditions seems necessary, therefore a brief summary of the relative theory is provided hereafter.

### 2.1.2 Material properties

When a sound wave hits a uniform and infinite surface, part of the sound energy is reflected with different phase and amplitude. The variation of phase and amplitude occurring during the reflection of the wave is expressed by the complex reflection factor:

$$R = |R|e^{i\chi} \quad (2.21)$$

where  $|R|$  is the magnitude and  $\chi$  yields information about the phase of the reflected sound wave. The magnitude and the phase depend on the incident angle,  $\theta$ , and the frequency. The reflection factor  $R$  completely describes the properties of a surface for all the incident angles and for all the frequencies

considered. As the intensity of a plane wave is proportional to the square of the pressure amplitude ( $I = p^2/\rho_0 c$ ), the fraction of intensity of the reflected wave is reduced proportionally to a quantity equal to  $|R|^2$  with respect to the total energy of the incident sound wave. Therefore, for plane waves incident on infinite surfaces, the quantity  $1 - |R|^2$  indicates the fraction of intensity lost during the reflection, which is defined as the absorption coefficient  $\alpha$ :

$$\alpha = 1 - |R|^2. \quad (2.22)$$

Taking into account  $R$ ,  $\alpha$ ,  $\chi$ , three limit cases can be described as follows:

- $R = 0, \alpha = 1 \Rightarrow$  the wall with zero reflectivity is able to absorb the whole intensity of the incident sound wave;
- $R = 1, \alpha = 0, \chi = 0 \Rightarrow$  the wall is called “hard” or “rigid”;
- $R = 1, \alpha = 0, \chi = \pi \Rightarrow$  the wall is called “soft” (rarely encountered in room acoustics).

It should be noted that, since  $\alpha$  is defined as  $1 - |R|^2$  (Eq. 2.22), information about the phase is omitted in the absorption coefficient. Absorption coefficients are energy parameters and they usually represent the input data in ray-based methods. The material characteristics of a surface can be also described with another quantity, the so-called surface impedance  $Z_a$  that is the complex ratio between the acoustic pressure  $p$  on the surface to the acoustic volume flow  $U$ :

$$Z_a = \frac{p}{U} = \frac{p}{uS} \quad \left( \frac{\text{kg}}{\text{m}^4\text{s}} \right) \quad (2.23)$$

where  $u$  is the particle velocity potential and  $S$  is the area of the surface. As the reflection factor, the surface impedance is a complex number and its value strongly depends on the frequency and the angle of the incident sound. At any frequency, the acoustic impedance quantifies how much sound pressure is generated by a given acoustic volume flow. It can also be expressed as:

$$Z_a = \text{Re}(Z_a) + i\text{Im}(Z_a) \quad (2.24)$$

being  $\text{Re}(Z_a)$  the real part of the acoustic impedance, the *acoustic resistance*, and  $\text{Im}(Z_a)$  the imaginary part of the acoustic impedance, the *acoustic reactance*.

Generally, in room acoustics it is more important to focus the attention on the *specific acoustic impedance*, that is the ratio between the sound pressure  $p$  on a wall and the velocity component normal to the surface:

$$Z_s = \frac{p}{v_n} \quad (\text{rayl}) \quad (2.25)$$

where the rayl=kg/m<sup>2</sup>s.

In the particular case of forward plane waves, the acoustic impedance can be written as *characteristic acoustic impedance*:

$$Z_c = \rho c \quad (\text{rayl}) \quad (2.26)$$

being  $\rho$  the density of the medium.

With respect to the characteristic acoustic impedance of the air ( $Z_0 = \rho_0 c_0 \approx 415$  at 20° C), it is possible to derive the *normalized specific acoustic impedance*:

$$\zeta = \frac{Z_s}{\rho_0 c_0}. \quad (2.27)$$

Being  $\zeta$  a complex number, the relation between the coordinates  $\text{Re}(\zeta)$  and  $\text{Imm}(\zeta)$  with the absorption coefficient is shown in Figure 2.4. The same figure shows how the maximum  $\alpha$  value allowed is 0.951 corresponding to  $\zeta = 1.567$  according to consolidated literature [9]. The inverse of the specific acoustic impedance is the *specific wall admittance*  $\gamma$ :

$$\gamma = \frac{1}{\zeta} = \frac{\rho_0 c_0}{Z_s}. \quad (2.28)$$

The general relations between the reflection factor  $R$ ,  $Z_s$  and  $\zeta$  are expressed as follows:

$$R(\theta) = \frac{Z_s \cos \theta - Z_0}{Z_s \cos \theta + Z_0} = \frac{\zeta \cos \theta - 1}{\zeta \cos \theta + 1} \quad (2.29)$$

where  $\theta$  is the oblique angle of incidence. In the simple case of perpendicular sound incidence ( $\theta = 0$ ) the Equation 2.29 becomes:

$$R(\theta) = \frac{Z_s - Z_0}{Z_s + Z_0} = \frac{\zeta - 1}{\zeta + 1} \quad (2.30)$$

while the three simple cases aforementioned may be rewritten as [9]:

- $R = 0, \alpha = 1 \Rightarrow Z_s = Z_0$  the impedance of a totally absorbent surface is equal to the impedance of the medium;
- $R = 1, \alpha = 0, \chi = 0 \Rightarrow Z_s \rightarrow \infty$  the rigid wall has an impedance that tends to infinity;
- $R = 1, \alpha = 0, \chi = \pi \Rightarrow Z_s \rightarrow 0$  the soft wall has an impedance that vanishes.

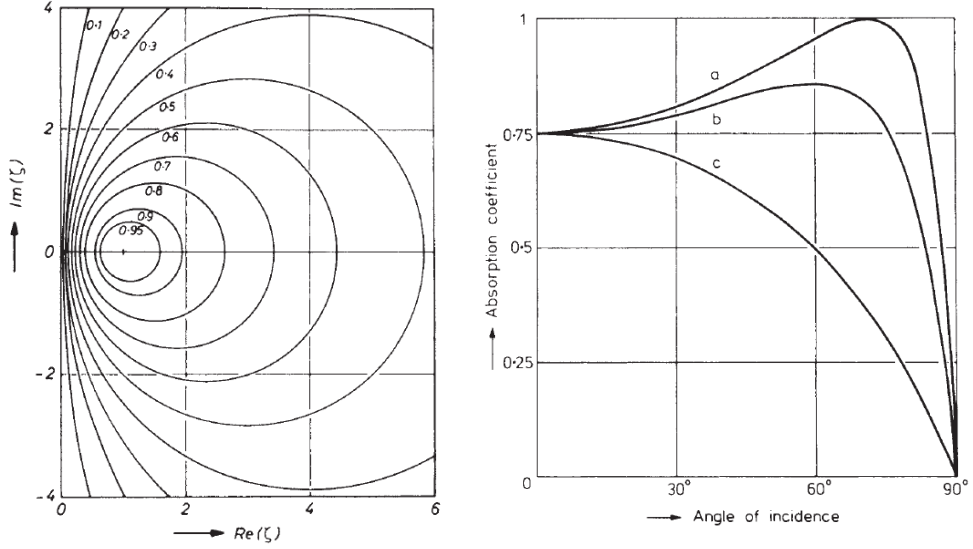


Figure 2.4: Absorption coefficient depending on the specific acoustic impedance  $\zeta$  and the angle of incidence  $\theta$  [9]. The curve a, b, c are referred to three different  $\zeta$  values [9].

Combining Equation 2.22 with Equation 2.30 it is possible to express the sound absorption coefficient as a function of  $\zeta$  and  $\theta$ :

$$\alpha_{\theta}(\zeta) = \frac{4\text{Re}(\zeta) \cos \theta}{|\zeta|^2 \cos^2 \theta + 2\text{Re}(\zeta) \cos \theta + 1}. \quad (2.31)$$

Also the relation between  $\alpha$  value and the incidence angle  $\theta$  is provided in Figure 2.4. This figure may be considered as the relation between the boundary conditions required by wave-based methods and the energy parameters employed in ray-based methods.

The random incidence absorption coefficient  $\alpha_{rand}$  can be derived with the Paris formula, that states:

$$\alpha_{rand} = \int_0^{\frac{\pi}{2}} \alpha_{\theta}(\theta_i) \sin(2\theta_i) d\theta = 2 \int_0^{\frac{\pi}{2}} \alpha_{\theta}(\theta_i) \cos(\theta) \sin(\theta) d\theta. \quad (2.32)$$

Kuttruff explicated the calculation providing the direct expression for  $\alpha_{rand}$  (see Fig. 2.4):

$$\alpha_{rand} = \frac{8}{|\zeta|^2} \cos \mu \left[ |\zeta| + \frac{\cos 2\mu}{\sin \mu} \tan^{-1} \left( \frac{|\zeta| \sin \mu}{1 + |\zeta| \cos \mu} \right) - \cos \mu \ln(1 + 2|\zeta| \cos \mu + |\zeta|^2) \right] \quad (2.33)$$

where  $\mu$  is the phase angle of the wall impedance:

$$\mu = \arg(Z_s) = \arctan \left( \frac{\text{Im}(Z_s)}{\text{Re}(Z_s)} \right). \quad (2.34)$$

In the Paris formula (Eq. 2.32) the random incidence absorption coefficient is referred to the idealized case of diffuse sound incidence on an infinite surface. Actually, edge effects and consequences of the finite size of any material led further scholars as Thomasson, Rindel, Davy, Brunksog to propose adjustment to that law [29, 30, 31, 32].

Considering the nature of the common materials, in general it is convenient to make the assumptions that  $\zeta$  is a real number. Being the imaginary part of the specific normalised acoustic impedance enough smaller to be neglected ( $\text{Imm}(\zeta) \rightarrow 0$ ), consequently also the phase angle of the surface impedance tends to zero ( $\mu \rightarrow 0$ ). This assumption corresponds to neglect the mass and the stiffness of the wall and this is true in case of moderate absorbing surfaces, as a painted concrete wall [33].

With this assumption, the relationship between the random-absorption coefficient  $\alpha_{rand}$  and the specific normalised acoustic impedance  $\zeta$ , expressed in equation 2.33, becomes [10]:

$$\alpha_{rand} = \frac{8}{\zeta} \left[ 1 + \frac{1}{1 + \zeta} - \frac{2}{\zeta} \ln(1 + \zeta) \right]. \quad (2.35)$$

## Boundary conditions

The form of Eq. 2.19 suggests that the Helmholtz problem is an eigen problem where  $\beta$  is the eigenvalue and  $p$  the eigenfunction. In fact, it can be shown that the Helmholtz equation yields non-zero solutions only for specific discrete values of  $\beta$ , the eigenvalues [9].

The boundary conditions are generally described as follows:

$$v_n(\mathbf{x}) - v_s(\mathbf{x}) = \gamma(\mathbf{x})p(\mathbf{x}) \quad x \in \Gamma \subset \mathbb{R}^{d-1} \quad (2.36)$$

where  $v_n(\mathbf{x})$  is the normal fluid particle velocity, which is related to the pressure by the Euler's equation (Eq. 2.12), and  $v_s(\mathbf{x})$  is the normal structural particle velocity. At the same time, according to the Euler's equation (Eq. 2.12), the normal component of the velocity to any boundary of the room is:

$$v_n = -\frac{1}{i\omega\rho_0}(\nabla p)_n = \frac{1}{i\omega\rho_0}\frac{\partial p}{\partial n} \quad (2.37)$$

where  $\partial/\partial n$  means the partial differential operator in the direction normal to the boundary. Replacing  $v_n$  with  $p/Z_s$ , it is possible to derive the following expression:

$$Z_s \frac{\partial p}{\partial n} + i\omega\rho_0 p = 0 \quad (2.38)$$

and using the normalized specific impedance  $\zeta$ :

$$\zeta \frac{\partial p}{\partial n} + i\beta p = 0. \quad (2.39)$$

Equation 2.39 shows that the the wave equation yields non-zero solutions fulfilling the boundary condition only for particular discrete values of  $\beta$ , the eigenvalues.

There are only a few trivial room shapes that along with simple boundary conditions allows the exact analytical evaluation of the eigenfunctions. Generally, the determination of the eigenvalues and eigenfunctions is quite difficult and requires the application of numerical methods.

## 2.2 Wave-based simulation methods

The Helmholtz equation (Eq. 2.19) is the starting point of the numerical analysis of acoustic problems. It can be seen as the equivalent of the wave equation (Eq. 2.15) formulated in the frequency domain, provided that the pressure signal, solution of the problem, is harmonic in time. It should be noted that this approach can be employed when the system under study is linear and time-invariant (LTI). In LTI systems the reaction to signals can be described by the impulse response (time domain) or the stationary transfer function (frequency domain). This hypothesis is typically assumed valid in room acoustics [25].

Given the almost total impossibility of finding the exact analytical solution of the wave equation, except for the simplest cases as rectangular rooms, a common feature of all the wave-based simulation methods is the replacement of continuous domains with meshes (discrete grids). The sound pressure in the Helmholtz equation represents the continuous variable of the problem. In a discrete model, this continuous variable is approximated by a finite number of discrete parameters. According to this mathematical description of the model, the pressure amplitude (or the velocity potential) can be calculated in the discretized parts of the initial domain. It is important to remark that in general the approximated solution does not correspond to the analytical correct one [34].

The wave-based methods have a wide amount of applications in various acoustic engineering fields: modal behaviour, sound barriers, vibration analysis, loudspeaker optimization, and so on. In the specific field of acoustic simulation of enclosures, it is more likely to encounter one of these methods only for low frequency and small rooms analysis. In fact, in broadband large-scale room simulation they still prove to be significantly constrained. The

intrinsic disadvantage of wave-based algorithms consists of the high computational and memory requirement, that typically increases with the frequency and the number of the elements in the mesh and thus, with the volume of the room investigated. Moreover, the need of frequency dependent complex acoustic impedances - to be assigned as boundary conditions - entails a series of practical problems, also caused by the poor availability of impedance values databases of common materials [35, 36].

There are various methods for the numerical solution of Helmholtz problems. The three most used wave-based modeling methods in room acoustics are: the Finite Element Method (FEM), the Boundary Element Method (BEM) and the Finite-Difference Method (FDM) [2]. The main characteristics and differences of these three techniques may be visualized in Figure 2.5 in a two-dimensional representation.



Figure 2.5: Main differences between the currently used wave-based modeling methods: Finite Element Method (FEM), Boundary Element Method (BEM), and Finite-Difference Method (FDM) [2].

According to FEM principles, the domain of the problem is handled as a mesh of smaller volumes; in BEM only the boundary domain is divided into smaller surfaces; in FDM a grid of nodes is created. As a consequence of the discretization shown in Figure 2.5, all these wave-based methods are characterised by high computational costs.

Since FDM methods work with regularly spaced grids, they proved to be the most straightforward to be parallelized with GPUs [18] for the purpose of the present thesis. This efficiency is considerable when the next time step is solved only basing with the previous time steps avoiding the need to compute all the nodes at the same time. Given all these considerations, in medium-large composite room environments as the objects of the study, a Finite-Difference Time-Domain (FDTD) model was chosen (see details in Chapter 3). Nevertheless, for the sake of completeness, in the following

sections FEM and BEM are briefly described, along with their advantages and their limits in room acoustic simulations.

### 2.2.1 Finite element

The Finite Element Method (FEM) is a peculiar category of numerical methods for solving partial differential equations (PDEs) as the Helmholtz equation. This method is a powerful tool for the numerical solution of those PDEs with given boundary conditions and it is widely used in numerous fields of engineering sciences [28]. Their typical application fields are referred to engineering issues such as structure-borne vibration analysis, heat transfer, and fluid mechanics [37]. In frequency domain methods as FEM a linear eigenvalue problem is the natural solution. Generally, modes and resonant frequencies are detected by means of this method and thus, the response under excitation may be determined using modal basis [38].

The present section gives a short overview of the principles and the fundamental equations of finite element methods applied to room acoustics. The name of this macro-group of methods is due to the subdivision of the domain into smaller parts, the so called finite elements [39]. This is allowed by the spatial discretization of the space domain through a mesh. The domain of the solution becomes a finite number of volumetric subspaces in which the test functions will be computed. The domain of the problem can be interior or exterior, corresponding to an inner or outer region of a closed boundary (see Figure 2.6).

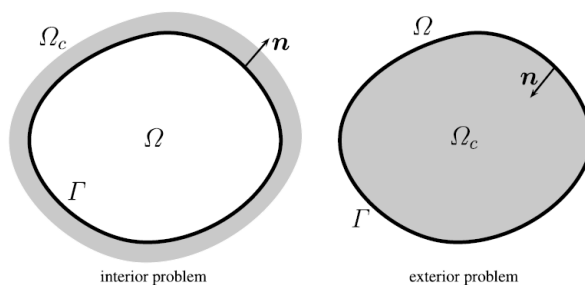


Figure 2.6: 2D visualization of interior and exterior problem referred to a closed boundary.  $\Omega$  is the domain,  $\Omega_c$  is complementary region,  $\Gamma$  is the boundary and  $\mathbf{n}$  is the outward normal vector [40].

Considering the interior problem, i.e. the left part of Figure 2.6, the wave propagation through the air may be described by the Helmholtz equation (Eq. 2.19) with certain impedance boundary conditions (Eq. 2.38) on the boundaries  $\Gamma$ .

A weak formulation of the problem is based on the following starting point [40]:

$$\int_{\Omega} \chi(\mathbf{x}) \left( \nabla^2 p(\mathbf{x}) + \beta^2 p(\mathbf{x}) \right) d\Omega(\mathbf{x}) = 0 \quad (2.40)$$

where  $\nabla^2 p(\mathbf{x}) + \beta^2 p(\mathbf{x})$  comes from the Helmholtz equation,  $\Omega$  is the domain, and  $\chi(\mathbf{x})$  is a weighting factor introduced to test whether the Eq. 2.40 is fulfilled or not. Then, integrating by parts Eq. 2.40 and defining  $a = i\omega\rho_0$ , the following expression is derived:

$$\int_{\Gamma} \chi(\mathbf{x}) a v_f(\mathbf{x}) d\Gamma(\mathbf{x}) - \int_{\Omega} \left( \nabla \chi(\mathbf{x}) \cdot \nabla p(\mathbf{x}) - \beta^2 \chi(\mathbf{x}) p(\mathbf{x}) \right) d\Omega(\mathbf{x}) = 0 \quad (2.41)$$

that is the starting point for conventional finite element discretizations [40]. The domain integral can be transformed into an integral-free term by using fundamental solutions  $G(\mathbf{x}, \mathbf{y})$ , the so-called Green functions, that fulfill the following formulation:

$$\nabla^2 G(\mathbf{x}, \mathbf{y}) + \beta^2 G(\mathbf{x}, \mathbf{y}) = -\delta(\mathbf{x}, \mathbf{y}) \quad (2.42)$$

where  $\delta(\mathbf{x}, \mathbf{y})$  is the Dirac function at the origin of the point source  $\mathbf{y}$ . From a physical point of view,  $G(\mathbf{x}, \mathbf{y})$  may be considered as the sound pressure distribution according to a point source in  $\mathbf{y}$ . Reminding the harmonic time-dependence of  $e^{i\omega t}$ , it represents an outgoing wave. In 3D domains,  $G$  is written as:

$$G(\mathbf{x}, \mathbf{y}) = \frac{1}{4\pi} \frac{e^{i\beta r(\mathbf{x}, \mathbf{y})}}{r(\mathbf{x}, \mathbf{y})} \quad \mathbf{x}, \mathbf{y} \in \mathbb{R}^3 \quad (2.43)$$

where  $r$  is the Euclidean distance between field point  $\mathbf{x}$  and source point  $\mathbf{y}$  as  $r(\mathbf{x}, \mathbf{y}) = |\mathbf{x} - \mathbf{y}|$ . Applying the property of the fundamental solution and the delta function, calculations provides the following formulation:

$$c(\mathbf{y}) p(\mathbf{y}) + \int_{\Gamma} \frac{\partial G(\mathbf{x}, \mathbf{y})}{\partial n(\mathbf{x})} p(\mathbf{x}) d\Gamma(\mathbf{x}) - \int_{\Gamma} G(\mathbf{x}, \mathbf{y}) a v_f(\mathbf{x}) d\Gamma(\mathbf{x}) = 0 \quad (2.44)$$

where  $c(\mathbf{y})$  is a function that varies with the source position  $\mathbf{y}$ :

- for internal points ( $y \in \Omega$ )  $c(\mathbf{y}) = 1$ ,
- for points closer to the boundary  $0 < c(\mathbf{y}) < 1$ ,
- for external points, i.e.  $\mathbf{y}$  neither belonging to  $\Omega$  nor to  $\Gamma$ ,  $c(\mathbf{y}) = 0$ .

For  $\mathbf{y} \in \Gamma$ , the Eq. 2.44 is also known as the Kirchhoff–Helmholtz boundary integral equation.

Now, combining the general form of boundary conditions (Eq. 2.38) with the weak formulation (Eq. 2.40) and the Kirchhoff–Helmholtz boundary integral equation (Eq. 2.44), these calculations lead to:

$$\begin{aligned} \int_{\Omega} \left( \nabla \chi(\mathbf{x}) \cdot \nabla p(\mathbf{x}) - \beta^2 \chi(\mathbf{x}) p(\mathbf{x}) \right) d\Omega(\mathbf{x}) - i\omega\rho_0 \int_{\Gamma} \chi(\mathbf{x}) \frac{p(\mathbf{x})}{Z_s(\mathbf{x})} d\Gamma(\mathbf{x}) = \\ = i\omega\rho_0 \int_{\Gamma} \chi(\mathbf{x}) v_s(\mathbf{x}) d\Gamma(\mathbf{x}), \end{aligned} \quad (2.45)$$

that is the basis for the Galerkin discretization using finite elements [40]. Before discretizing the domain, the pressure  $p(\mathbf{x})$  should be approximated by:

$$p(\mathbf{x}) = \sum_{i=1}^N \phi_i(\mathbf{x}) p_i = \phi^T(\mathbf{x}) \mathbf{p} \quad (2.46)$$

where  $p_i$  is the discrete sound pressure at point  $x_i$  and  $\phi_i$  is the  $i$ -th basis function for the approximation. Similarly, the particle velocity of the structure and the boundary admittance can be discretized as follows:

$$v_s(\mathbf{x}) = \sum_{i=j}^{\tilde{N}} \bar{\phi}_j(\mathbf{x}) p_j = \bar{\phi}^T(\mathbf{x}) \mathbf{v}_s \quad (2.47)$$

$$\gamma(\mathbf{x}) = \sum_{i=k}^{\tilde{N}} \tilde{\phi}_k(\mathbf{x}) p_k = \tilde{\phi}^T(\mathbf{x}) \gamma \quad (2.48)$$

Finite element discretization are referred to a Galerkin discretization of the weak formulation as shown in Eq. 2.45, where Galerkin discretization means that the basis functions  $\phi_i$  used in Eq. 2.46 are replaced by the test function  $\chi$ . At this point it seems helpful to use matrices to obtain the simpler final expression [41, 42]:

$$(\mathbf{K} - i\beta\mathbf{C} - \beta^2\mathbf{M})\mathbf{p} = i\rho_0\Theta v_n = \mathbf{f} \quad (2.49)$$

where

- $K$  is the stiffness matrix, with  $k_{ij}$  elements:

$$k_{ij} = \int_{\Omega} \nabla \phi_i(\mathbf{x}) \cdot \nabla \phi_j(\mathbf{x}) d\Omega(\mathbf{x}) \quad (2.50)$$

- $C$  is the damping matrix, with  $c_{lj}$  elements:

$$\begin{aligned} c_{lj} &= \rho_0 c \int_{\Gamma} \phi_l(\mathbf{x}) [\tilde{\phi}^T(\mathbf{x}) \gamma] \bar{\phi}_j(\mathbf{x}) d\Gamma(\mathbf{x}) = \\ &= \int_{\Gamma} \phi_l(\mathbf{x}) [\tilde{\phi}^T(\mathbf{x}) \tilde{\gamma}] \bar{\phi}_j(\mathbf{x}) d\Gamma(\mathbf{x}) \end{aligned} \quad (2.51)$$

where  $\tilde{\gamma} = \rho_0 c \gamma$ ,

- $M$  is the mass matrix, with  $m_{lj}$  elements:

$$m_{lj} = \int_{\Omega} \phi_l(\mathbf{x}) \phi_j(\mathbf{x}) d\Omega(\mathbf{x}) \quad (2.52)$$

,

- $\Theta$  is the boundary mass matrix, with entries  $\theta_{lj}$ :

$$\theta_{lj} = \int_{\Gamma} \bar{\phi}_l(\mathbf{x}) \phi_j(\mathbf{x}) d\Gamma(\mathbf{x}), \quad (2.53)$$

- $f$  is the vector that includes the excitation of the system.

To summarize the whole process, basing on the Eq. 2.40 as starting point for FEM analysis, typically three main steps are involved.

1. It is possible to reduce the highest derivation order in Eq. 2.40 to a first order equation by using Green's first identity and thus eliminating the normal pressure derivatives in the boundary integrals.
2. The second step is defined as the *meshing* phase, i.e. the subdivision of the integration domain (the volume and the boundary surfaces) into finite elements. This process transforms Eq. 2.40 into a sum of integrals over all finite elements.
3. The third step involves the resolution of the linear equations introduced to obtain pointwise approximations of the solution function. In order to limit the solution space of the pressure and weighting functions in each element, the classical FEM implies an elementwise polynomial approximations (also called *test functions*).

## 2.2.2 Boundary element

The Boundary Element Method (BEM) is another consolidated group of numerical and computational methods that can be encountered in engineering and physical sciences. Similarly to FEM, the typical aim of BEM is the knowledge of a certain variable of interest or physical property, which is governed by PDEs, as the Helmholtz problem. Also in this case, the process over test functions is performed over a discretized system. The difference with FEM is that in a boundary based scheme the discrete points are on the boundary only, meaning that only the boundary of the space assessed - and not the whole geometrical volume of the enclosed space - is discretized into surface elements. The output of the BEM, however, includes the sound pressure distribution not only on the surface of the object under study but also on other points in the field.

Indeed, the number of elements in the BEM is expected to be much lower than the number of elements in the corresponding finite element method, keeping constant the size of the element and the required accuracy. As there will be fewer nodes in BEM, compared to FEM, there is often a potential for significant efficiency savings [38].

The direct BEM involves the application of Green's theorems while the indirect BEM implies the application of layer potentials [40]. The problem is usually formulated in the Fourier domain and solved as a function of the frequency and the space. Generally, the steady state or the harmonic solution are taken into account to consider the independence of the sources from time variations. Otherwise a further associated differential equation for the temporal solution should be considered. After that, the solution must be converted back to the time domain by Fast Fourier Transform (FFT).

Using the matrices notation, it is possible to write:

$$(\mathbf{H} - \mathbf{D})\mathbf{p} = \mathbf{G}\mathbf{v}_n = \mathbf{f} \quad (2.54)$$

where

-  $H$  is the matrix with  $h_{lj}$  elements:

$$h_{lj} = c(z_l)\delta_{lj} + \int_{\Gamma} \frac{\partial G(\mathbf{x}, z_l)}{\partial n(\mathbf{x})} \phi_j(\mathbf{x}) d\Gamma(\mathbf{x}), \quad (2.55)$$

-  $D$  is the boundary matrix with  $d_{lj}$  elements:

$$\begin{aligned} d_{lj} &= i\omega\rho_0 \int_{\Gamma} G(\mathbf{x}, z_l) [\tilde{\phi}^T(\mathbf{x})\gamma] \phi_j(\mathbf{x}) d\Gamma(\mathbf{x}) = \\ &= i\beta \int_{\Gamma} G(\mathbf{x}, z_l) [\tilde{\phi}^T(\mathbf{x})\tilde{\gamma}] \phi_j(\mathbf{x}) d\Gamma(\mathbf{x}), \end{aligned} \quad (2.56)$$

-  $G$  is the system matrix with  $g_{lj}$  elements:

$$g_{lj} = i\omega\rho_0 \int_{\Gamma} G(\mathbf{x}, z_l)\phi_j(\mathbf{x})d\Gamma(\mathbf{x}), \quad (2.57)$$

-  $f$  is the vector that includes the excitation of the system.

As occurs in FEM, the boundary element method typically implies three steps: the reformulation of the direct solution of the PDEs as integral equations, the discretization of the boundary only in a finite number of smaller surfaces, the solution at the domain points computed by means of integration over the known boundary data.

Concerning the domain discretization in FEM and BEM, it is important to highlight that in element-based acoustic computations the size of each element is related to the maximum frequency - and thus the minimum wavelength - handled [43]. Generally, the element size derives from a minimum number of elements per wavelength. Usually recalled as “six elements per wavelength” rule of thumb, the element size is described by the following expression:

$$\beta h < 1 \quad (2.58)$$

where  $\beta$  is the wavenumber and  $h$  is the element size [43]. Since  $\beta = 2\pi/\lambda$ , it means that at least six ( $\sim 6.28$ ) elements are required for each wavelength. It has been demonstrated that the lower is the wavenumber the higher is the reliability of Equation 2.58. Even though this expression should be modified for higher number of wavenumber, it has been also demonstrated that  $\beta^2 h < 1$  is a too severe requirement [43].

In room acoustics the use of FEM and BEM is usually limited to small rooms and low frequencies analysis because of the computational cost, which increases with the size of the room and the frequency computed [44]. The most common application fields are the prediction of the part of the room transfer function (RTF) dominated by the modal behaviour, i.e. at low frequencies [45], and the prediction of sound fields in geometries with moderate complexity affected by near field, as the small rooms. Within these areas, it has been demonstrated that FEM and BEM are highly accurate and reliable methods.

The constraints intrinsic to these methods are still significant when it comes to tackling huge environments and broadband analysis in frequency. Nowadays, the scientific research is still focused on the feasibility of increasing the volume to be computed together with the modelling of higher frequencies problems, maintaining reasonable processing time [38].

### 2.2.3 Finite-difference time-domain

The finite-difference time-domain (FDTD) methods are among the oldest methods to solve partial differential equations (PDEs). Their algorithms have been studied by scholars and researchers for almost a century [46]. The terminology *finite difference time domain* dates back to the 1920s when the application of the method was limited by the technology of that period [47]. The 1940s and 1950s saw a significant boost in the development and the application of FDTD to fluid dynamics, thanks to the appearance of electronic computers [48, 49]. Successively, these methods were widely employed in the electromagnetic field, becoming increasingly popular in the 1980s [50, 51]. Indeed, a vast literature is connected with this method because of its wide range of applications. Botteldooren was one of the first scholars to apply FDTD methods to room acoustics field [4]. With *finite difference* it is meant the spatial or time approximation of a set of partial differential equations. When a time-dependent system is assessed, the term *finite difference time domain* is usually used. The numerical solution is calculated as a temporal recursion over a space grid. A qualitative description of the method is shown in Figure 2.7. On the left of the figure there is a time-dependent continuous system, which is defined by a group of partial differential equations (PDEs) together with boundary conditions and excitation typology. On the right there is the time-space discretization, i.e. a recursion updated every time step. In other words the spatial domain of the problem is discretized in a set of points, where the solution of the PDE is calculated. In the same way time is discretized in a finite set of time instants, where the solution of the PDE is calculated. In a few words, the finite difference time domain method approximates the spatial and the temporal derivatives of the differential equations [34].

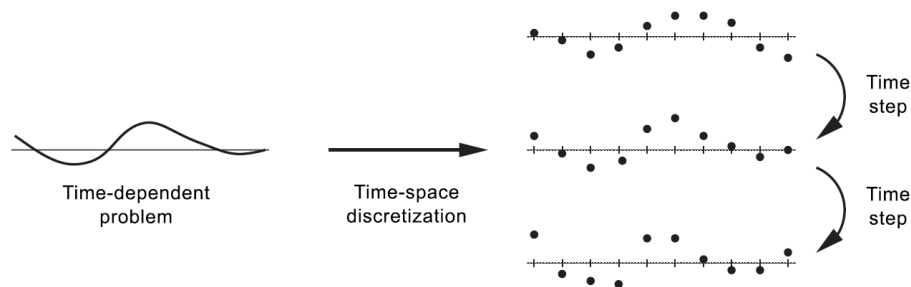


Figure 2.7: Finite difference simulation. The real phenomenon (on the left) is discretized in space with a certain number of dots, and in time, with a given time step (on the right). Credits picture: Bilbao, S. D. (2009) [34].

The time step,  $k$ , corresponds to the inverse of the sample rate,  $F_s$ :

$$k = \frac{1}{F_s}. \quad (2.59)$$

In a finite difference time domain scheme, the continuous functions of time are approximated by time series. For instance, the function  $u(t)$  can be described as  $u(t_n)$  with  $t_n = nk$  and approximated by time series  $u_d^n$  where “d” means “discrete” and  $n$  is an integer number. Considering the function  $u(t)$  as a solution of a set of PDEs, it is important to state that the approximating series  $u_d^n$  is not a sampled solution:

$$u_d^n \neq u(t_n) \quad (2.60)$$

meaning that  $u_d^n$  is not simply the sampled version of the true solution [34].

The solution of the wave equation 2.16  $u(\mathbf{x}, t)$  is approximated by a grid function  $u_{l,m,p}^n$  where

$$x = lh \quad y = mh, \quad z = ph \quad (2.61)$$

and

$$t = nk \quad (2.62)$$

where

- $l, m, n, p$  are integer numbers,
- $k$  is the time step, in seconds,
- $h$  is the grid spacing, in meters, i.e. the distance between two adjacent nodes in the regular grid (see Fig. 2.8).

A wide amount of explicit FDTD methods employ the same general scheme:

$$\delta_t^2 u_{l,m,p}^n = \lambda^2 [(\delta_x^2 + \delta_y^2 + \delta_z^2) + a(\delta_x^2 \delta_y^2 + \delta_x^2 \delta_z^2 + \delta_y^2 \delta_z^2) + b(\delta_x^2 \delta_y^2 \delta_z^2)] u_{l,m,p}^n \quad (2.63)$$

where  $a$  and  $b$  are the specific coefficients of a general family of compact explicit schemes [53, 5]. Over the same regular Cartesian grid, several schemes - Cartesian or not - may be built. For instance, the simple case of the standard 7-point scheme implies  $a = b = 0$  and it is here provided as an example. The operators for the second derivatives in the wave equation may be expressed as:

$$\delta_t^2 u_{l,m,p}^n \equiv \frac{1}{k^2} (u_{l,m,p}^{n+1} - 2u_{l,m,p}^n + u_{l,m,p}^{n-1}) \cong \frac{\partial^2}{\partial t^2} u \quad (2.64)$$

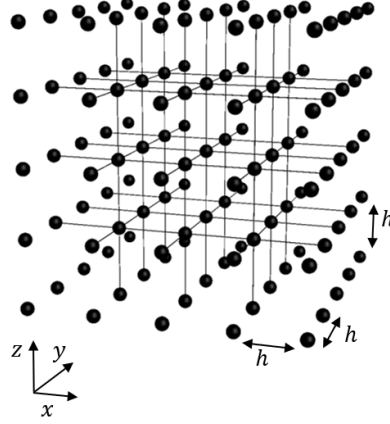


Figure 2.8: Visualization of the Cartesian grid. Credits picture: B. Hamilton (2016) [52].

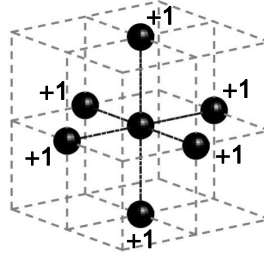


Figure 2.9: Visualization of adjacent points in the Cartesian grid, considering the central point as reference. Credits picture: B. Hamilton (2016) [52].

$$\delta_x^2 u_{l,m,p}^n \equiv \frac{1}{h^2} (u_{l+1,m,p}^n - 2u_{l,m,p}^n + u_{l-1,m,p}^n) \cong \frac{\partial^2 u}{\partial^2 x} \quad (2.65)$$

$$\delta_y^2 u_{l,m,p}^n \equiv \frac{1}{h^2} (u_{l,m+1,p}^n - 2u_{l,m,p}^n + u_{l,m-1,p}^n) \cong \frac{\partial^2 u}{\partial^2 y} \quad (2.66)$$

$$\delta_z^2 u_{l,m,p}^n \equiv \frac{1}{h^2} (u_{l,m,p+1}^n - 2u_{l,m,p}^n + u_{l,m,p-1}^n) \cong \frac{\partial^2 u}{\partial^2 z} \quad (2.67)$$

where “+1” and “-1” refer to the adjacent nodes from a spatial and time point of view (see Fig. 2.9).

Combining the Equations 2.64, 2.65, 2.66, and 2.67 with the explicit form of equation 2.16, which is expressed as follows:

$$\frac{\partial^2 u}{\partial t^2} = c^2 \left( \frac{\partial^2 u}{\partial^2 x} + \frac{\partial^2 u}{\partial^2 y} + \frac{\partial^2 u}{\partial^2 z} \right) \quad (2.68)$$

it is possible to obtain

$$u_{l,m,p}^{n+1} - 2u_{l,m,p}^n + u_{l,m,p}^{n-1} = \frac{c^2 k^2}{h^2} (u_{l+1,m,p}^n + u_{l-1,m,p}^n + u_{l,m+1,p}^n + u_{l,m-1,p}^n + u_{l,m,p+1}^n + u_{l,m,p-1}^n - 6u_{l,m,p}^n). \quad (2.69)$$

Let  $S$  be

$$S = u_{l+1,m,p}^n + u_{l-1,m,p}^n + u_{l,m+1,p}^n + u_{l,m-1,p}^n + u_{l,m,p+1}^n + u_{l,m,p-1}^n \quad (2.70)$$

and let  $\lambda$  be

$$\lambda = \frac{ck}{h}, \quad (2.71)$$

the Eq. 2.69 can be written as the *nearest neighbour scheme* (see figure 2.9):

$$u_{l,m,p}^{n+1} - 2u_{l,m,p}^n + u_{l,m,p}^{n-1} = \lambda^2 (S - 6u_{l,m,p}^n), \quad (2.72)$$

which is most commonly expressed as:

$$u_{l,m,p}^{n+1} = (2 - 6\lambda^2)u_{l,m,p}^n + \lambda^2 S - u_{l,m,p}^{n-1}. \quad (2.73)$$

The quantity  $\lambda = \frac{ck}{h}$  is defined as the *Courant number* and it should be noticed that it increases with the time step  $k$  and it decreases with the increasing of the grid spacing  $h$ .

The most crucial points that play a key role in a FDTD scheme are the numerical stability, the initial and boundary conditions, dispersion error and the computational cost.

### Numerical stability

A scheme is defined *stable* if the solutions of the system do not grow exponentially, as demonstrated by von Neumann and Fourier analyses [46].

It is possible to define the stability conditions considering a test solution for the simplest 3D problem:

$$u_{m,l,p}^n = z^n e^{ih(l\beta_x + m\beta_y + p\beta_z)} \quad (2.74)$$

where  $z = e^{jwk}$ ,  $h$  is the grid spacing, and  $\beta_x$ ,  $\beta_y$ ,  $\beta_z$  are the components of the wave vector  $\beta$  in  $\mathbb{R}^3$ , i.e. a multidimensional spatial frequency with magnitude  $|\beta|$ .

Given a  $z$ -plane with  $\text{Re}(z)$  on x-axis and the  $\text{Imm}(z)$  part on y-axis,  $z$  values should be within the unit circle to be stable (see Fig. 2.10).

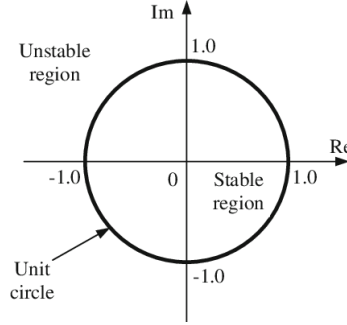


Figure 2.10: The stable and unstable regions in the  $z$ -plane.

The goal is to find the range of values of the Courant number,  $\lambda$ , that allows the stability of the scheme. Combining Eq. 2.74 with Eq. 2.69 the equation obtained is:

$$z - 2 + 4\lambda^2(\sin^2(\beta_x h/2) + \sin^2(\beta_y h/2) + \sin^2(\beta_z h/2)) + z^{-1} = 0. \quad (2.75)$$

The solutions in  $z$  should be within the unit circle (see Fig. 2.10) to be stable, leading to the following condition:

$$0 \leq \lambda^2(\sin^2(\beta_x h/2) + \sin^2(\beta_y h/2) + \sin^2(\beta_z h/2)) \leq 1. \quad (2.76)$$

Since the  $\sin^2$  values always fall in the range between 0 and 1, the stability condition depends only on the Courant number  $\lambda$ , becoming:

$$\lambda \leq \frac{1}{\sqrt{3}} \quad (2.77)$$

that is the so-called Courant-Friedrichs-Lewy (CLF) condition in a 3D case [47]. In a more generalized form the CLF condition may be defined as  $\lambda \leq \frac{1}{\sqrt{D}}$  where  $D$  is the dimension of the domain of the problem. Since this condition may be seen also as  $\frac{ck}{h} \leq \frac{1}{\sqrt{3}}$  the consequent minimum value of grid spacing, for a certain sample rate, is  $h \geq \sqrt{3}ck$ . It should be noticed that when the grid spacing  $h$  is reduced, the upper limit for the time step  $k$  decreases. When  $\lambda = 1/\sqrt{3}$ , the 7-point simple scheme is at the Courant limit and it is expressed as:

$$u_{l,m,p}^{n+1} = \frac{1}{3}S - u_{l,m,p}^{n-1}. \quad (2.78)$$

### Initial conditions

The initial conditions specify the values of  $u$  and  $\partial_t u$  at the initial instant, i.e. when  $t = 0$ , as follows:

$$u(\mathbf{x}, 0) = u_0(\mathbf{x}) \quad (2.79)$$

$$\partial_t u(\mathbf{x}, 0) = v_0(\mathbf{x}). \quad (2.80)$$

Typically, assuming  $v_0(\mathbf{x}) = 0$ , the first initial condition defines the system excitation, that can be represented by a normalised Gaussian centered in a point  $x_0$ :

$$u_0(\mathbf{x}) = \frac{1}{(\sigma\sqrt{2\pi})^3} \exp\left(-\frac{\|x - x_0\|^2}{2\sigma^2}\right) \quad (2.81)$$

where  $\sigma$  is the standard deviation of the Gaussian curve. In the limit of  $\sigma \rightarrow 0$ , the normalised Gaussian may be used as a simple approximation of the Dirac delta function  $\delta(x - x_0)$ , or Kronecker delta in its discrete form [54].

### Boundary conditions

The three simplest boundary conditions compatible with the stability of the system are:

$$u(\mathbf{x}, t) = 0 \quad (R = -1, \text{Dirichlet}) \quad (2.82)$$

$$\hat{\mathbf{n}} \cdot \nabla u = \frac{\partial u}{\partial n}(\mathbf{x}, t) = 0 \quad (R = 1, \text{Neumann}) \quad (2.83)$$

$$\hat{\mathbf{n}} \cdot \nabla u + \frac{\gamma}{c} \frac{\partial u}{\partial t} = 0 \quad (2.84)$$

where

- $\mathbf{n}$  is the normal vector to the boundary,
- $\frac{\partial}{\partial n}$  is the spatial derivative along  $\mathbf{n}$  direction,
- $\gamma$  is the specific surface admittance of the boundary surface,
- $R$  is the reflection factor.

The Eq. 2.82 models lossless “soft” walls, rarely encountered in room acoustics. The Eq. 2.83 models lossless “rigid” walls, that represent a reference point in acoustic simulations. The Eq. 2.84 models the loss of energy by frequency independent  $\gamma$  values [9]. Moreover, efficient methods to compute frequency-dependent admittances have been optimized by recent works as well [17, 19, 52].

## Dispersion error

The numerical dispersion is an inherent issue in methods that employ approximated schemes. The dispersion relation is:

$$\omega = \pm c_\phi |\beta|. \quad (2.85)$$

where  $c_\phi$  is called *phase speed* and it represents the speed at which waves of a given wave number propagate in the finite difference scheme [55]. The phase speed should be constant for all the wavenumbers but in FDTD schemes it is not always granted [46]. The dispersion is the resulting effect and certainly the goal is to minimise this quantity [56]. A possible scenario of phase speed variation includes errors at high frequencies leading to waves travelling slower than the expected speed [57].

In FDTD, the greater the grid spacing  $h$ , the higher the numerical dispersion. Consequently, the range of values for the grid spacing  $h$  should be upper limited by the numerical dispersion issue and lower limited by the stability issue [19].

## 2.3 Ray-based methods

Up to this moment, the propagation of sound has been assumed as the wave propagation in a homogeneous medium at constant speed. Nevertheless, since the 1960s the second category of numerical methods is based on the following assumptions: sound propagates through the local directions of propagation, pointwise normal to the wave fronts [10, 9]. These trajecto-

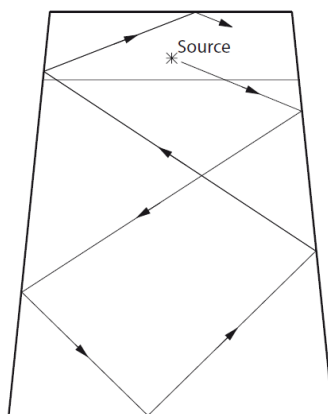


Figure 2.11: Approximation of sound waves to rays: paths between successive reflections. Credit picture: Vorlander, M. (2018) [1].

ries - the rays - should not be considered as a replacement of waves, but only a reasonable approximation under certain assumptions [58]. Ray-based methods are employed in a wide variety of scientific fields, among which the most popular one is the optics [59]. In geometrical acoustics, sound waves emitted by any sound source are handled as they are travelling with a constant speed through straight lines, the rays, as shown in Figure 2.11 [60, 61]. The surrounding condition is the assumption of the homogeneous medium at rest [16]. The assumption that the sound wave propagates with straight lines involves the idea that the curvature radius of the wavefront is enough larger than its wavelength [62]. The approximation is as much reliable as the environment has dimensions far larger than the wavelength of the wave considered [63, 64]. In room acoustics, this condition is not so unrealistic as one might think: at the mid frequency of 1000 Hz, corresponding to 34 cm of wavelength, the size of the walls, the height of the ceiling, and the paths covered by the sound waves, are generally larger than the wavelength by at least one or two orders of magnitude [9].

The ray-based methods - also popular with the name Geometrical Acoustics (GA) - have been largely employed to compute virtual sounds with great success since the 1960s, when the first scientific papers concerning ray tracing technique were published, becoming one of the reference points for the sound field models in enclosed spaces [12, 65]. In GA models both sound sources and receivers are generally considered enough small compared to the wavelength.

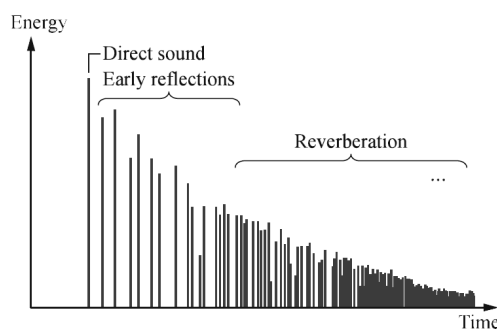


Figure 2.12: Typical energy room impulse response.

A wide amount of methods are usually indicated with the term GA: they are employed in computing sound waves and their propagation both in indoor and outdoor scenarios. The main computer task is to find the intersection of a vector (the ray) with a certain plane (the polygon, the wall of the virtual room) [1]. While FEM and BEM usually work in frequency domain (time independent) and then convert the solution in time domain with inverse

Fourier Transform, GA methods compute the impulse response in a certain position directly in the time domain, as can be seen in Figure 2.12. The ray-based methods are able to recreate a detailed impulse response of the virtual environment by calculating the paths of the rays [1]. The several methods developed over the time differ in the way they compute the pathways. The two most famous and used methods are the image source method (ISM) and the stochastic ray tracing (SRT). As they are complementary in their advantages and disadvantages, the current commercial softwares combines the two methods creating what are defined “hybrid” GA algorithms [60, 66, 67, 68].

It is important to immediately remark that, with the assumptions intrinsic to GA, wave phenomena (e.g. edge diffraction) can not be directly computed from a physical point of view. The term *classical* GA is applied to all the models that assume sound propagating through straight lines, basing on the Fermat principle for the order of reflections: the angle of incidence is equal to the angle of reflections. Instead, various current GA algorithms are also called “GA++”, meaning that they implement the wave phenomena through scattering coefficients and edge diffraction models [16]. So the main difference between the classic GA and the modern GA++ is that the first one considers the sound only travelling through specular reflections while the second enlarges the view of the problem including also diffraction issues.

### 2.3.1 Image Source Method

The Image Source Method (ISM) for sound propagation modelling was implemented for the first time in the 1970s. The ISM is based on the principle

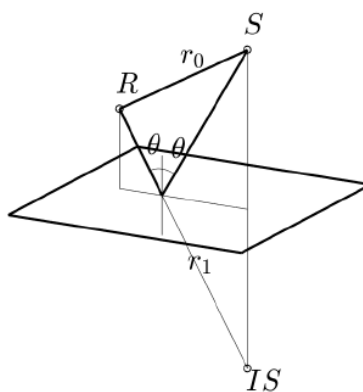


Figure 2.13: Basic principle of ISM.  $S$  is the sound source,  $R$  is the receiver,  $\theta$  is the incidence angle,  $r_0$  is the path of the direct sound,  $IS$  is the image source,  $r_1$  is the path built from  $IS$  to  $R$ . Credit picture: Svensson, P. (2018) [16].

according to which it is possible to geometrically trace a specular reflection by mirroring the sound source with respect to the plane of the surface hit by the sound wave. In other words, the source location is mirrored through the boundary - the one hit by the incident sound - of the enclosed space of interest. The distance between the receiver and the mirrored source, the so called “image source” ( $IS$  in Fig. 2.13), is used to determine the receiver arrival time. By storing the energy, angle, and time of arrival of each image path an echogram can be created and used as an impulse response [69, 70, 71].

In detail, in Fig. 2.13 it is possible to see the sound source ( $S$ ), the receiver ( $R$ ), the incidence angle ( $\theta$ ), the path of the direct sound ( $r_0$ ), the image source ( $IS$ ), the path built from  $IS$  to  $R$  ( $r_1$ ). In case of an enclosure constituted by  $N$  planar walls, each wall is associated with an image source of the original sound source. Then, each of these image sources is mirrored through all the walls of the room leading to a number of new images sources of second order equal to  $N(N-1)$ . By replicating this process an increasing number of images is generated, which grows with the increase of the distance from the original source. The number of images of order  $i$  is:

$$N(N-1)^{i-1} \quad \text{for} \quad i \geq 1. \quad (2.86)$$

Therefore, the total number of image sources,  $N_{IS}$ , of order up to  $i_d$  in an enclosure with  $N$  walls is obtained by the following expression:

$$N_{IS}(i_d, N) = N \frac{(N-1)^{i_d} - 1}{N-2} \quad (2.87)$$

which is a number of  $O(N^{i_d})$  order. It is quite straightforward to notice that the number of sources exponentially grows with increasing order [9].

Actually, defined the locations of sound source and receiver in the enclosure, the echogram is reconstructed only with *valid* image paths. Only those paths which have been generated by mirroring at the inside of a wall are *visible* from the receiver. This is connected with a sort of directivity owned by each image source: it only “illuminates” a solid angle, determined by the dimensions of the walls. A well consolidated method to calculate visible surfaces to each image source is the beam tracing [72]. The detection of all the obstructed source images is made with a tree-like structure in which levels are the orders of reflection and the nodes are the valid image sources within the beam. Therefore, it occurs - and in non-trivial geometries it often happens - that lots of image sources are *invisible* from a certain receiving location. Hence, the actual number of valid image sources is of order  $O(N_v^{i_d})$  where  $N_v$  is the number of visible surfaces to an image source.

The image source method process is very efficient at calculating the specular reflection paths. In fact, it is particularly accurate to exactly identify

the pathways and is considerably influenced by the location of sound source and receiver in relation to the room. For this reason, ISM proves to be specifically suited to calculate early reflections in trivial enclosures [73]. Instead, increasing the order of reflections or considering a more articulated geometry contribute to make the ISM drastically less efficient due to exponential growth of computational cost. In fact, with increasing size and complexity of the geometry the calculation of the beam tree requires a considerable amount of time.

### 2.3.2 Stochastic ray-tracing

The stochastic ray-tracing (SRT) method represents one of the earliest attempts at computer modelling for acoustic simulations [65]. It describes the stochastic process of particle radiation (energy emitted from a source by a finite number of rays in various directions) and detection at the receiver (the intensity of the ray is calculated if the ray passes through it). Paths are calculated throughout the domain considering the reflections from the boundaries. The rays lose energy at each reflection according to the absorbing material properties of the surface [73].

In room acoustics, the assumption at the basis of the stochastic ray tracing is the diffuse field condition. Indeed, it is only an ideal condition but with certain hypotheses the approximation is quite accepted by the acoustic community [1]. As pointed out in the previous chapters, it is certainly correct to describe the behaviour of the sound field in enclosures through a wave-based theoretical description. Nevertheless, it is generally not convenient solving common problems in the practice of room acoustics, such as the design of a concert hall or the enhancement of a given critical issue. This lack of efficiency is mainly due to the extremely high number of modes that need to be calculated with the aim of covering a wider frequency range. In fact, it is well known that the total number  $N_f$  of eigenfrequencies corresponding to the modes of the room (the eigenfunctions) between 0 and a certain frequency  $f$  increases with the geometrical volume  $V$  of the room and with third power of the frequency  $f^3$  [9, 74]:

$$N_f = \frac{4\pi}{3} V \left( \frac{f}{c} \right)^3 \quad (2.88)$$

where  $N_f$  is the total number of modes up to the frequency  $f$ ,  $V$  is the volume of the room, in  $\text{m}^3$ ,  $f$  is the frequency investigated, in Hz,  $c$  is the speed of sound in the air at  $20^\circ \text{C}$ ,  $R.H. = 20\%$ , assumed as 343 m/s. As a consequence, the density of modes  $dN_f/df$  increases with the second power

of the frequency  $f^2$ :

$$\frac{dN_f}{df} = 4\pi V \frac{f^2}{c^3} \quad (2.89)$$

as can be visualized in Fig. 2.14 [75].

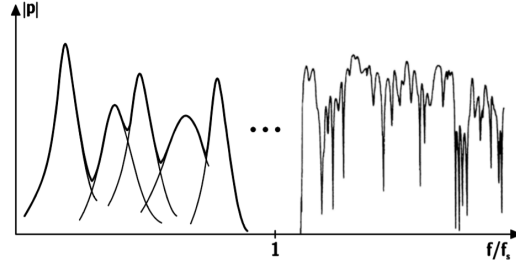


Figure 2.14: Magnitude of a stationary room transfer function [75, 12]. On the y-axis  $|p|$  is the sound pressure absolute value, on the x-axis  $f/f_s$  is the ratio of the frequency over the Schroeder frequency.

As the environments are typically excited by broadband and transient signals, as noise, music, and speech, the total sound field is a complex overlap of modes. The so-called *stationary room transfer function* may be expressed as [1, 75]:

$$p(\mathbf{x}, \mathbf{y}) \propto i\omega \sum_{\nu} \frac{p_{\nu}(\mathbf{x})p_{\nu}(\mathbf{y})}{\mathbf{K}_{\nu}(\omega^2 - \omega_{\nu}^2 - 2i\delta_{\nu}\omega_{\nu})} \quad (2.90)$$

where

- $\mathbf{x}$  is the vector of the position of the receiver,
- $\mathbf{y}$  is the vector of the position of the sound source,
- $\nu$  represents the combination of the positive integers  $l, m, n$  that define modes type,
- $\mathbf{K}_{\nu}$  are constants that depend on the modes' amplitude,
- $\omega_{\nu}$  are the angular frequencies,
- $\delta_{\nu}$  are the damping constants of the room, with the assumption that  $\delta_{\nu} \ll \omega_{\nu}$ .

Since the overlap of sound pressures drastically increases at higher frequencies, Schroeder and Kuttruff defined the so-called *Schroeder frequency* as the frequency that separates the region that can be considered modal from the region that can be considered stochastic [9, 12]. According to the definition,

on average three modes overlap should be within their average bandwidth as follows:

$$\Delta f_n = 3 \frac{c^3}{4\pi V f^2} \quad (2.91)$$

to define the Schroeder frequency. At this point considering that:

$$\begin{aligned} - \Delta f_n &= \frac{\delta_\nu}{\pi}, \\ - T &= \frac{3 \ln 10}{\delta} \approx \frac{6.91}{\delta} \end{aligned}$$

it is possible to obtain the Schroeder frequency:

$$f_s = \sqrt{\frac{c^3}{4V\delta_\nu}} \approx \frac{5500}{\sqrt{V\delta_\nu}} \approx 2000 \sqrt{\frac{T}{V}} \quad (2.92)$$

where  $T$  is the reverberation time, in seconds. The stochastic nature of the sound pressure over the Schroeder frequency has always led to employ stochastic ray-tracing method in large scale rooms at high frequencies with great success. The SRT turns to be independent on the sound source and receiver location in the room and thus, it is more suited to compute the reverberant tail rather than the first order of reflections [73].

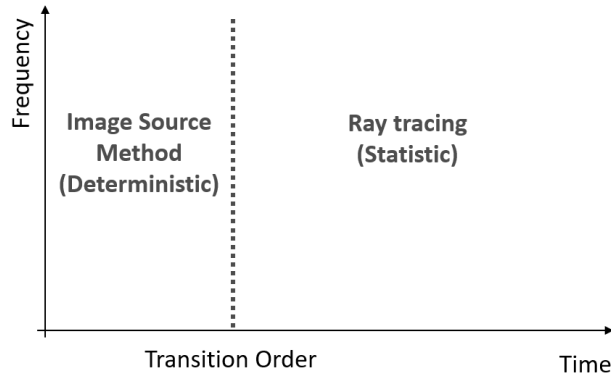


Figure 2.15: Typical principle of a GA hybrid model. The ISM is used for early reflections and SRT for late reflections. Credit picture: Rindel, J. H. (2000) [73]

As ISM and SRT compute better, respectively, the first orders of reflections and the late reflections, what is usually employed by the most popular commercial software is a hybrid method combining the advantages of these two approaches. Since these methods work in time domain, a consequent hybrid method combining the image source method and the stochastic ray tracing requires a transition order referred to the orders of reflections and thus, to the time domain, as shown in Fig. 2.15.

### 2.3.3 The inclusion of diffraction in GA++ techniques

In wave propagation theory, the diffraction is a typical phenomenon occurring any time a wave encounters an obstacle or a small opening. The description of this phenomenon is provided by the Huygens–Fresnel principle: each point of the wavefront - when hitting the obstacle or the small opening - becomes a source of a spherical wave itself. The interference among all these secondary spherical waves form the subsequent global wavefront. In room acoustics, diffraction may happen for distinct reasons: edge diffraction (Fig. 2.16(a)), material discontinuities (Fig. 2.16(b)), roughness of the surface (Fig. 2.16(c)). The first kind of diffraction occurs when the sound wave

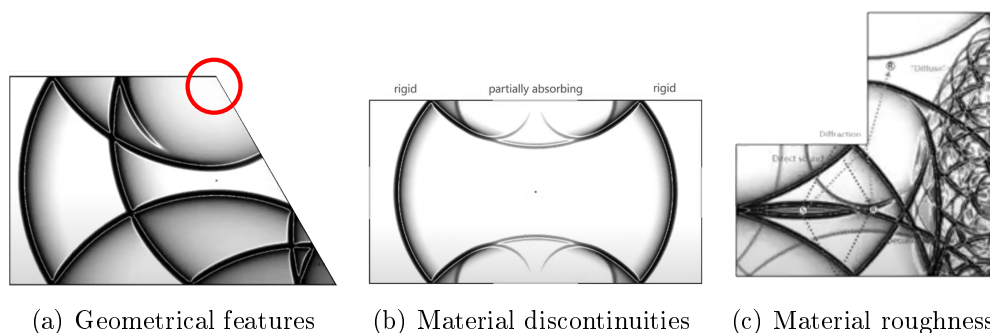


Figure 2.16: Example of different kinds of diffraction: geometrical features, material discontinuities, roughness.

hits any corner or edge whose angle  $\theta$  is not equal to a precise portion of  $\pi$ , i.e.  $\theta \neq \frac{\pi}{n}$  with  $n$  as integer number ( $n = 1, 2, \dots$ ) [76]. For instance, Figure 2.16(a) shows a simple 2D geometry - which can be a plan of a longitudinal section of any room - and only one edge properly causes diffraction: the  $120^\circ$  angle on top right of Figure 2.16(a). The second cause of diffraction is probably less intuitive because it is due to material discontinuities (see Fig. 2.16(b)). Even in absence of edges or corners, diffraction can occur, caused by two different material properties of the same surface. The third type of diffraction is affected by the roughness of the surfaces, as long as the depth of the elements are comparable with the wavelength of the incident sound (see Fig. 2.16(c)).

It is worth to point out the difference between two quantities often retained interchangeable: the scattering and the diffusion coefficient. They are defined by two parts of the same standard ISO 17497:

- ISO 17497-1:2004 defines a random-incidence scattering coefficient as caused by surface roughness (quantitative approach) [77];

- ISO 17497-2:2010 defines the diffusion coefficient in terms of the uniformity of the reflected polar distribution from a surface (qualitative approach)[78].

The scattering coefficient,  $s$ , has the following expression [77]:

$$s = \frac{\alpha_{spec} - \alpha_s}{1 - \alpha_s} \quad (2.93)$$

where  $\alpha_{spec}$  is the random-incidence specular absorption coefficient and  $\alpha_s$  is the random-incidence absorption coefficient. In other words, it quantifies the quantity of the reflected sound energy which is not reflected in the specular direction, as shown in Figure 2.17.

The diffusion coefficient,  $d$ , has the following expression [78]:

$$d_\theta = \frac{\left(\sum_{i=1}^n 10^{L_i/10}\right)^2 + \sum_{i=1}^n \left(10^{L_i/10}\right)^2}{(n-1) \sum_{i=1}^n \left(10^{L_i/10}\right)^2} \quad (2.94)$$

where  $\theta$  refers to the direction of the sound source,  $L_i$  is the sound pressure level at the  $i$ -th microphone,  $n$  is the number of the microphones. The main difference between the two coefficients is that the absorption coefficients  $s$  returns just quantitative information about the sound energy reflected in non-specular directions (see Fig. 2.17), while the diffusion coefficient  $d$ , measuring the uniformity of the reflected sound energy, is able to return also qualitative information about the same amount of energy.

Commonly, the simulation algorithms are focused on the computation of the scattering coefficient rather than the diffusion coefficient [79]. Differently from the wave-based methods, in which all the wave phenomena are naturally computed, ray-based methods do not take directly into account the full wave nature of the sound. Therefore, they need to compensate this lack with further consideration, typically involving the assignment of the scattering coefficient to the surfaces of the virtual model [60, 80, 81, 82, 66]. As already mentioned, the estimation of a part of the energy scattered from the surfaces makes the difference between what is usually called classical GA and the recent definition of GA++ [16].

The scattering coefficient may be expressed as:

$$s = 1 - (1 - s_d)(1 - s_s) \quad (2.95)$$

combining the surface roughness scattering coefficient,  $s_s$ , with the scattering coefficient due to edge diffraction,  $s_d$  [82]. This way, the resulting direction

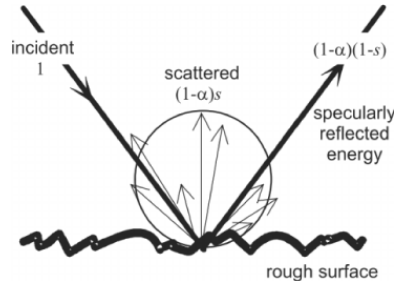


Figure 2.17: Scattering coefficient [82].

of the reflected sound energy is a weighted combination of the specular reflection,  $(1 - s)$ , and the scattered portion,  $s$ , as can be seen in Figure 2.17. The surface scattering coefficient  $s_s$  is due to the surface roughness, as defined in ISO 17497-1 [77] and it typically increases in a logarithmic way with frequency. Concerning the term  $s_d$ , it is related to the edge diffraction [83]. Considering a single finite reflector, as the one shown in Figure 2.18(a), the scattering coefficient due to edge diffraction may be calculated as:

$$s_d = 1 - K_w K_l \quad (2.96)$$

where  $K_w$  and  $K_l$  are attenuation factors respectively related to the width,  $w$ , and the length,  $l$  of the reflector.

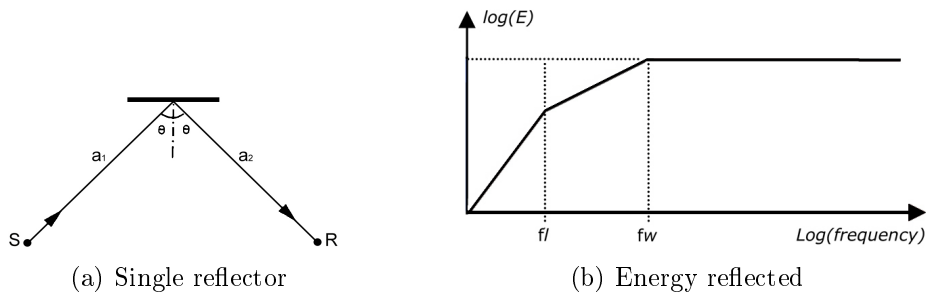


Figure 2.18: Specular reflection and energy reflected from a single finite sized reflector long  $l$  and wide  $w$  [83]. At high frequencies ( $f > f_w$ ) the surface specularly reflects energy while at low frequencies ( $f < f_w$ ) energy is scattered. Credits picture: Christensen, C. L. and Rindel, J. H. (2005) [80].

The quantity  $(1 - K_w K_l)$  returns information on how much the panel response is far from a perfectly specular reflection (infinite surface), since  $K_w$  and  $K_l$  quantify the specularly reflected portion of energy. They are

defined as:

$$K_w = \begin{cases} 1, & \text{for } f > f_w \\ \frac{f}{f_w}, & \text{for } f \leq f_w \end{cases} \quad K_l = \begin{cases} 1, & \text{for } f > f_l \\ \frac{f}{f_l}, & \text{for } f \leq f_l \end{cases} \quad (2.97)$$

where  $f_l$  and  $f_w$  are two thresholds in the frequency domain (see Fig. 2.18(b)), defined as:

$$f_l = \frac{c \cdot a^*}{2 \cdot l^2} \quad (\text{Hz}) \quad f_w = \frac{c \cdot a^*}{2(w \cdot \cos \theta)^2} \quad (\text{Hz}) \quad (2.98)$$

where

- $f_l$  is the threshold frequency provided by the biggest dimension  $l$ , in Hz,
- $c$  is the speed of sound in the air at 20° C, in m/s,
- $a^* = \frac{2a_1 \cdot a_2}{a_1 + a_2}$  is the characteristic distance in meters (with  $a_1 \ll a_2$ ), a sort of average between source-panel and panel-receiver paths (see figure 2.18(a)),
- $l$  is the length of the panel, in m,
- $f_w$  is the threshold frequency provided by the shortest dimension  $w$ , in Hz,
- $w$  is the width of the panel, in m,
- $\theta$  is the angle of incidence.

Above the upper limiting frequency  $f_w$  the response is flat, meaning that the finite reflector's behaviour is the same of an infinite surface (specular reflection). Between  $f_l$  and  $f_w$  the response decreases by 3 dB per octave, and below  $f_l$  drops with 6 dB per octave. The assumption of  $a_1 \ll a_2$  implies that all these considerations are valid in the far field from the edge where the diffraction occurs. This hypothesis is the result of the Fresnel-Kirchhoff diffraction simplification, that is also called *far field approximation*. It represents one of the ways GA++ approaches are able to handle the complex diffraction phenomena.

In general, the inclusion of scattering coefficient values in geometrical acoustics is a widely debated topic. The freedom of choice in scattering coefficient values makes the experience of the user still fundamental in the simulation process.

# Chapter 3

## Method

### 3.1 Combined FDTD/GA simulations

As outlined in the previous chapter, there is a complementarity between the basic principles, the advantages, the natural limits and the frequency range of reliability of wave-based and ray-based simulation approaches. On one hand, with a wave-based approach the difficulties to simulate the modes in a wide frequency range are compounded by the challenge in computing them in non-trivial geometries. All these issues have been constraining the application of these models to small volumes, trivial geometries and low frequencies analysis up to recent years. On the other hand, GA models approximate sound waves to straight lines, using stochastic assumptions, that are as valid as the volume of the hall is higher and with increasing frequency. Therefore, a combined system able to exploit the different codes in their application fields (see Figure 3.1) is up to now one of the most widely accepted solutions [84, 85]. In fact, what seems to be the most suitable

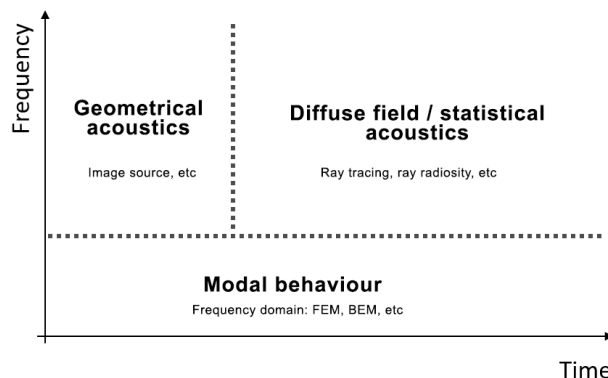


Figure 3.1: Conventional approaches to room acoustic simulations.

approach for broadband analysis is the use of hybrid methods combining wave-based models up to a certain frequency and then GA algorithms for the stochastic behaviours [6]. This way, a combined broadband impulse response would be simulated exploiting the benefits of both the approaches in terms of accuracy of results, reliability, time cost and efficiency [28, 86]. Efforts in this direction have been made since the 90s [87, 88] and more recently important experimentations have been furtherly developed [2, 89, 90].

As already mentioned, among the wave-based models, the FDTD proves to be the most suited to [6]:

- model large environments,
- compute signals evolving in time domain,
- model the frequency dependent complex boundary conditions,
- be computed in parallel tasks through processing units.

In addition, the latest advances in parallel computing task through next generation GPU devices [55, 91] and the outline of more efficient FDTD schemes [92, 19] are able to significantly expand the traditional constrained application field (small rooms and low frequencies). With regard to this major breakthrough in the macro-group of FDTD models, a hybrid FDTD/GA model was chosen for the present study.

This chapter is intended to present the hybrid simulation framework employed and the procedure to test its feasibility in large scale rooms up to high frequencies. Figure 3.2 aims to remark that in this case the term hybrid is referred to a transition threshold in the frequency domain, while the same term seen at the end of section 2.3 was referred to the transition between ISM and SRT in the time domain (see Fig. 2.15). The hybrid FDTD/GA

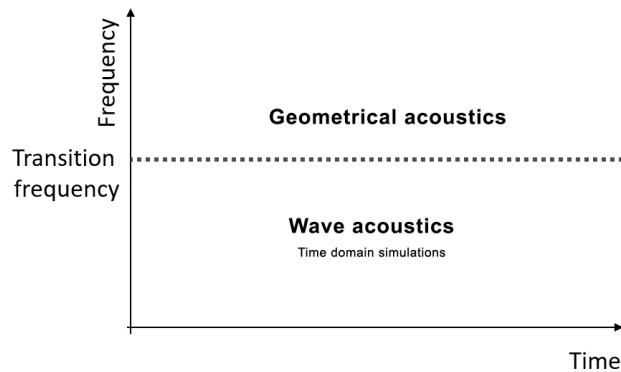


Figure 3.2: Hybrid FDTD/GA model employed.

scheme employed in the present study combines through a crossover filter [17, 19]:

- a finite-difference time-domain algorithm with finite volume optimization at the boundaries up to a certain transition frequency ( $f_{max}$ ),
- a classical GA stochastic ray-tracing (with no diffraction phenomena computed) over transition frequency ( $f_{max}$ ).

Since the GA part of the model is a classical ray-tracing (see 2.3.2) with no compensation for diffraction phenomena, in the author's opinion the attention should be more focused on the FDTD part, especially because wave acoustics is hardly ever used in composite large architectures. The main peculiarities of the FDTD model are:

1. the efficient choice of a suitable non-Cartesian scheme, even though described with the parameters of the Cartesian grid, ensuring computational power savings [91];
2. a powerful computational capacity thanks to which the high computation requirements, intrinsic to FDTD models, were partly overcome (clusters of CUDA-enabled Nvidia GPUs provided by the *Acoustics and Audio Group* of the University of Edinburgh, consisting of either GTX1080Ti, Tesla K80, or Titan X Maxwell GPUs);
3. an accurate method to derive frequency-dependent complex acoustic impedance used as boundary conditions (see also Appendix) [52, 92];
4. the physical implementation of the sound energy losses due to the air absorption, increasingly significant with higher frequencies and bigger volumes [93].

The difference between a Cartesian and a non-Cartesian scheme is briefly shown in Figure 3.3. The Cartesian grid, drawn with dashed lines, remains the same between the three options shown in Figure 3.3, with its corresponding grid spacing  $h$ . This visualization facilitates the comparison between the schemes, that can be Cartesian (Fig. 3.3(a)) or not (13-point lattice in Fig. 3.3(b) and 9-point lattice in Fig. 3.3(c)). It should be noticed that when a non-Cartesian scheme as the 13-point lattice is chosen, the actual distance between two neighbor points proves to be  $h' = h\sqrt{D}$ , with  $D = 3$ , instead of just the grid spacing  $h$ . The standard finite difference scheme expressed in Equation 2.63 has the maximum error, i.e. the maximum phase speed variation, along the coordinate line, and the minimum along the diagonals and thus, the 13-stencil CCP, with  $a = 0.25$ ,  $b = 0$ ,  $\lambda = 1$  turns to have

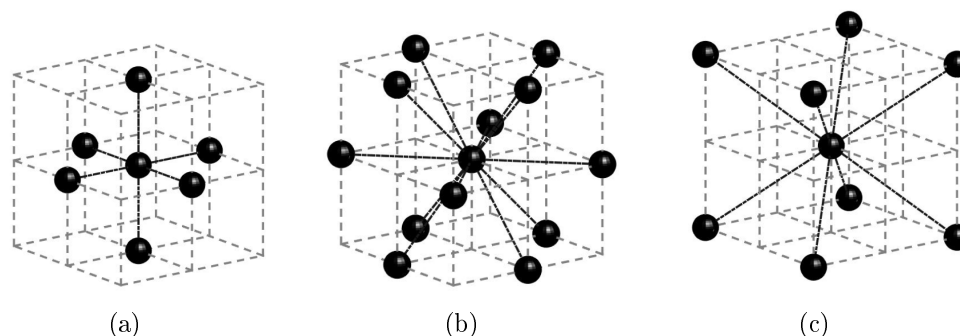


Figure 3.3: Three possible stencils: standard 7-point (a) and cubic close-packed (CCP) 13-point (b) and 9-point (c) lattices. Credits picture: Hamilton. B. (2016) [52].

favorable numerical dispersion properties [19]. As a consequence, in order to minimize the dispersion error, a cubic close-packed (CCP) 13-point stencil can be used rather than the standard 7-point stencil. For those reasons, the 13-stencil non-Cartesian cubic close-packed (CCP) scheme was selected in the present work (see Fig. 3.3(b)): it has been proven that it is an efficient solution to simulate the isotropic sound propagation of an omnidirectional pulsating sphere [19, 91].

Concerning the finite-volume time-domain (FVTD) approach at boundaries, it has been proven that it is a valid solution to the problem of complex boundary conditions over non-trivial geometries [17]. It is intended to reduce the well known issue due to staircase effects in regular-grid FDTD schemes, as it can be seen in Figure 3.4 [52]. As it can be easily understood, it is

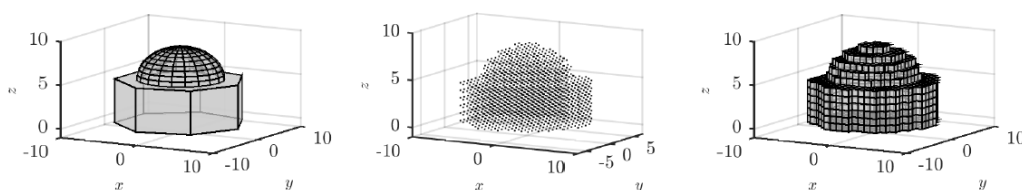


Figure 3.4: Example of non-trivial geometry (left), a Cartesian grid (center), and the consequent staircase effect (right). Credits picture: Hamilton. B. (2016) [52].

quite difficult to correctly estimate the surface areas of boundaries, leading to uncorrect estimation of decay times. The solution employed in this work involves a considerable reduction of effective surface area errors, which are caused by the actual difference between the target boundary surfaces and the *voxel* (from “volume” and “element”) boundary surfaces. A reduction from 50% to even 1% allows a more accurate estimation of decay times and

more consistent simulations even modifying the grid resolution. More details concerning the FVTD approach are provided in [94].

### 3.1.1 Air absorption

It is well known that the assumptions underlying the 3D wave equation imply a simplified model to describe sound propagation in the air [27, 62]. Nevertheless, the air absorption can significantly influence the acoustic behaviour in enclosed spaces, especially at high frequencies and in large rooms. The standard ISO 9613 states that viscous losses due to friction of atmosphere molecules produce a damping effects, resulting in an attenuation of the sound, more relevant at high frequencies [95]. Therefore, in order to get more reliable representation of the actual condition, the virtual sound fields should take into account this phenomenon [18, 96]. While in small rooms and at low frequencies, that are the usual application fields of wave-based methods, the absorption of the air may typically be neglected, in large enclosed spaces it should be accurately calculated to obtain reliable full bandwidth simulations.

The present work considers the viscothermal effects in air according to References [52, 93]. Energy losses caused by the viscosity of the air have been introduced into the three-dimensional wave equation, according to reasonable indoor typical conditions, in terms of relative humidity of the air, temperature and pressure (see Fig. 1 in Reference [93]). Relaxation processes of the two primary molecules that make up 99% of air, i.e. the two diatomic molecules of nitrogen ( $N_2$ ) and oxygen ( $O_2$ ), are taken into account. The outcome is a set of suitable ranges of absorption values, expressed in terms of a total absorption of the air provided by the expression (see Fig. 3.5):

$$\alpha_{tot} = \alpha'_{cl} + \alpha_{O_2} + \alpha_{N_2} \quad (\text{Nepers/m}) \quad (3.1)$$

where  $\alpha'_{cl}$  is the spatial absorption coefficient, whereas  $\alpha_{O_2}$  and  $\alpha_{N_2}$  model the relaxation process of nitrogen and oxygen during the return of the perturbed system to the equilibrium. The parameter  $\alpha'_{cl}$  is also known as the *modified classical absorption coefficient* [62] and expresses the attenuation over the distance. It is derived from:

$$\alpha'_{cl} = \frac{\alpha}{c} \quad (\text{Nepers/m}) \quad (3.2)$$

where  $\alpha$  is the temporal absorption coefficient, in Nepers/s. It should be noted that even though those values are called “absorption coefficients”, the actual units are Nepers/s for the temporal coefficient and Nepers/m for the spatial coefficient [93, 95].

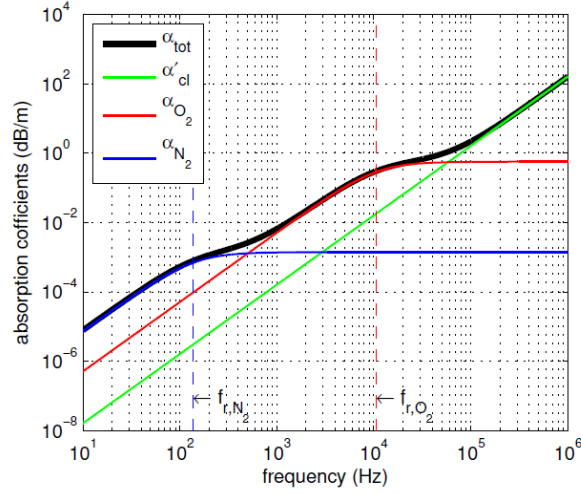


Figure 3.5: Absorption of the air at 20°C and 1 atm. The total absorption is the sum of the classical  $\alpha'_{cl}$  the relaxation of oxygen  $O_2$  and nitrogen  $N_2$ . Credit image: B. Hamilton 2014 [93].

### 3.1.2 Computational cost

The FDTD method has inherently high computational costs, especially when applied to large domains and high frequencies. Indeed, there are several factors that influence the computational cost. The interest of the author is to provide simplified correlations between the memory requirements and the main simulation parameters to be set to run a simulation. The goal is to provide enough information to be aware of which factors, and in which way, affect the calculation time.

Basically, the computational cost is proportional to two quantities: the spatial density and the spatiotemporal density. In an ideal scenario with an infinite accurate model, in a Cartesian grid we can define these two quantities as:

$$\rho_{SD} = \frac{1}{h^D} \quad (3.3)$$

and

$$\rho_{STD} = \frac{1}{kh^D} \quad (3.4)$$

where  $h$  is the grid spacing,  $k$  is the time step and  $D$  is the dimension of the domain. The spatial density,  $\rho_{SD}$ , is the number of spatial samples per unit volume of space, whereas the spatiotemporal density,  $\rho_{STD}$ , is the number of spatiotemporal samples per unit volume of space and time [19].

As can be seen from Equations 3.3 and 3.4, the computational cost is drastically affected by the sampling of the space and time domains. In case

of the Helmholtz problem in a 3D domain, as the one the present thesis is focused on, the spatial density is proportional to  $\frac{1}{h^3}$  and the spatiotemporal density to  $\frac{1}{h^4}$  (since  $k = \lambda h/c$ ).

When compared with this ideal scenario, in finite difference schemes there are more critical issues: the numerical stability and the accuracy in terms of dispersion error. It is actually difficult to achieve a compromise between the stability requirement, the desired time cost, and the minimization of the dispersion error, that returns higher accuracy.

Therefore, in the FDTD scheme employed the equation of the spatial density (Eq. 3.3) and the equation of the spatiotemporal density (Eq. 3.4) become:

$$\rho_{SD} = \sigma^D \frac{1}{h^D} \quad (3.5)$$

and

$$\rho_{STD} = \sigma^{D+1} \frac{1}{kh^D} \quad (3.6)$$

where  $\sigma$  is the oversampling factor. This new quantity increases with the accuracy of the process and thus, with the drop of the numerical dispersion.

In general, it turns out that the compromise between computational cost, accuracy, dispersion error and efficiency is in the choice of the maximum Courant number allowed  $\lambda = \lambda_{max}$  for a given scheme [19]. The advantageous factor in FDTD computational requirement is that the formulation of the scheme is easily parallelizeable over the spatial domain and the update equation can be applied uniformly across the domain [53]. Moreover, significant improvements have been achieved in the last years by using graphics processing units (GPUs) and parallel programming [55]. It is important to remind that the actual time cost depends on several further factors, such as the number of GPUs available and the quantity of other jobs running at the same time, that are beyond the objective of the present thesis.

## 3.2 Approach to the simulation setup

Keeping in mind the FDTD features described in Section 2.2.3, the main parameters to be optimized and set for each simulation run are here listed, along with the relative consideration behind each choice. A qualitative flowchart of this approach is provided in Figure 3.6.

**The transition frequency ( $f_{max}$ )** It is the threshold between the FDTD and GA approach (see Fig. 3.2). Indeed, the author tried to set  $f_{max}$  as high as possible (always with acceptable and reasonable time costs) because

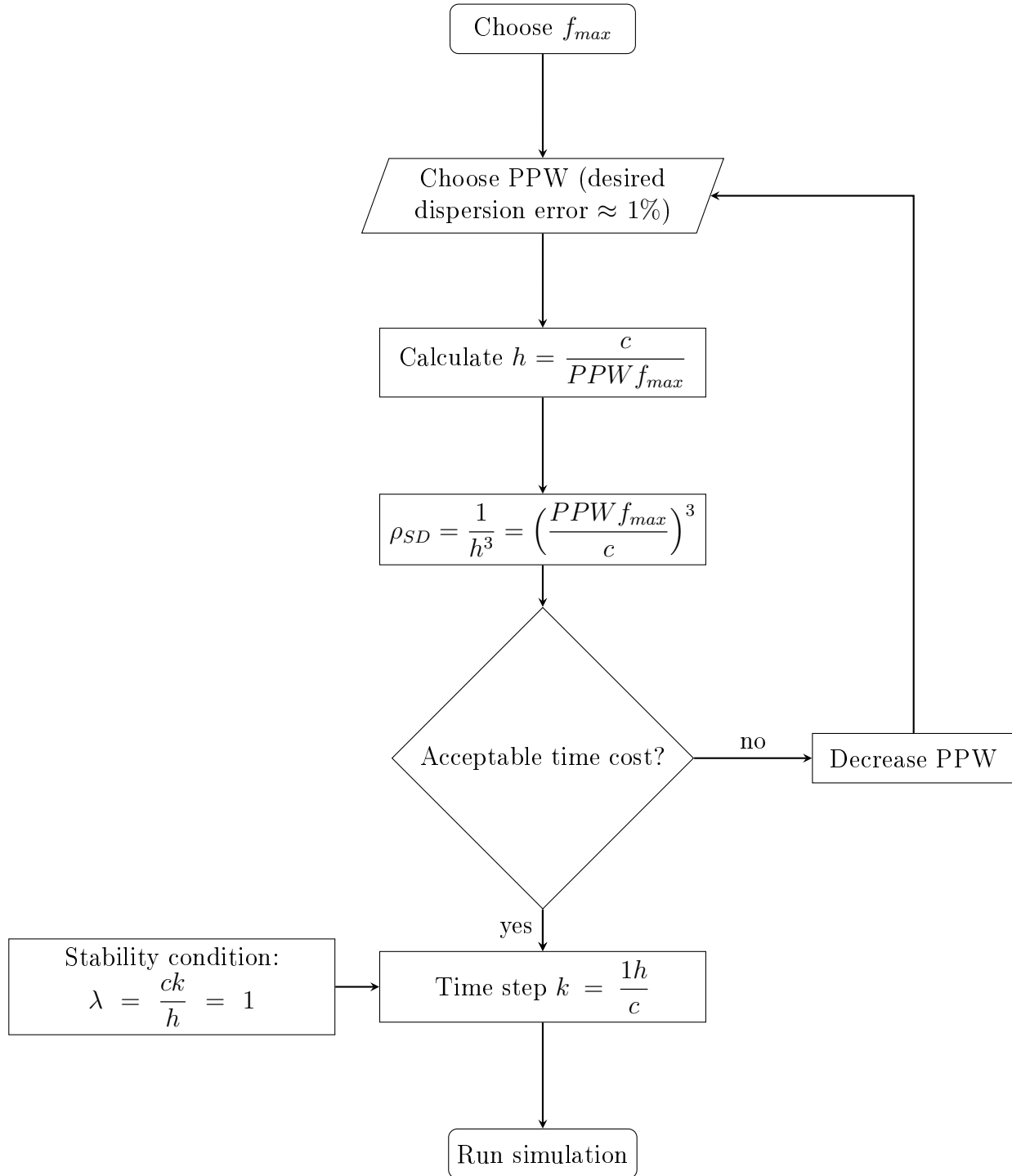


Figure 3.6: Qualitative and simplified flowchart for the FDTD simulation initial setting. The actual time cost depends on several further factors, such as the number of GPUs available and the quantity of other jobs running at the same time, that are beyond the objective of the present thesis.

the purpose is to test a wave-based method simulation in a frequency range wider than common applications. Nevertheless, it should be recalled that the computational cost increases with the third power of the cut-off frequency ( $\rho_{SD} \propto f_{max}^3$ ). As a rule of thumb, at the beginning of the simulation settings  $f_{max}$  is chosen enough high to fill around the 80% of GPU memory in order to keep a certain tolerance (around 20%) for the frequency-dependent boundary nodes [52].

**The number of points per wavelength (PPW)** This value is equal to the double of the oversampling factor:  $PPW = 2\sigma$  where  $\sigma > 1$  and thus  $PPW > 2$ . As FDTD needs oversampling in order to reduce as much as possible the dispersion error, in the method employed in this study the values of PPW belongs to the range 6 – 8 [52].

**The grid spacing ( $h$ )** It is referred to the Cartesian grid independently whether the stencil adopted is referred to a Cartesian grid or not. Otherwise, mentioning the proper grid spacing of the specific scheme adopted (for instance  $h' = h\sqrt{D}$  in 13-point CCP scheme) would not allow to maintain the scheme comparable with other finite difference schemes. The computational cost increases with the inverse third power of the grid spacing ( $\rho_{SD} \propto h^{-3}$ ).

**The Courant number ( $\lambda = ck/h$ )** It is of fundamental importance to guarantee the stability of the system. It is here always referred to the Cartesian spatial grid  $h$  for reasons of comparability with other schemes. It has been shown as in the simplest 3D scheme in a Cartesian grid  $\lambda$  should assume values lower than  $1/\sqrt{3}$ , but in 13-point scheme ( $h' = h\sqrt{3}$ ) the requirement becomes  $\lambda \leq 1$ . It has been proven that the choice  $\lambda = \lambda_{max}$ , is generally an optimized setting that keeps the dispersion error around 1% and  $h$  values close to the minimum imposed by stability needs [19].

**The time step ( $k$ )** It is finally derived after the decision of all the other parameters. The time step is, therefore, calculated with the formula  $k = \lambda h/c = h/c$ . Consequently, the sample rate  $F_s$  can be calculated as  $F_s = 1/k$  (Hz).

### 3.3 Simulation studies on specific aspects

The present thesis investigates the feasibility of the hybrid FDTD/GA model described in previous section when applied to broadband analysis of

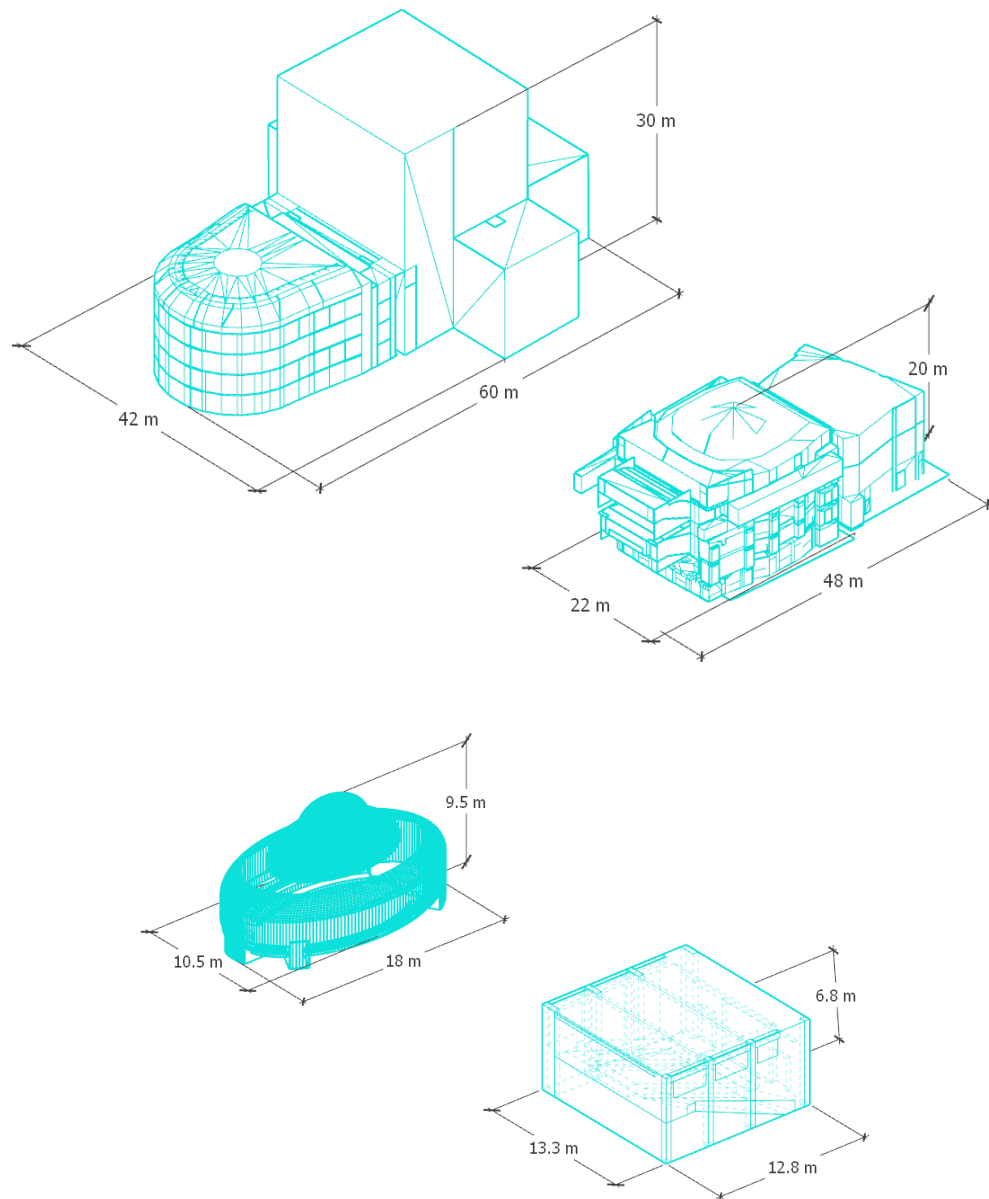


Figure 3.7: Case studies selected for the present work: a historical Italian opera house (top left), a modern theatre (top right), an elliptical concert hall (bottom left), an university lecture hall (bottom right).

large non-trivial performance spaces. The model afore presented have been applied to four distinct case studies: a historical opera house, a modern opera house, an elliptical concert hall, and a university lecture hall. To

have a general idea of the size and the geometry of the environments, main dimensions are provided in Figure 3.7. The reasons behind the choices are introduced hereafter and then deeply explained in the following chapters.

### Two large opera houses

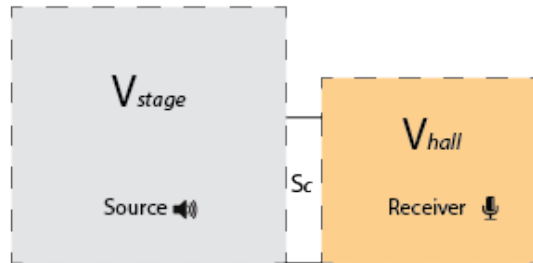
In the sample of the selected case studies, the first two are large opera houses located in Bologna (Italy). The first one is the *Teatro Comunale* (TCB) and it has the traditional opera house shape, the second one is the *Duse theatre* (DUS) and it has the modern opera house shape [97]. The main reason behind the choice of these theatres is that among all the typologies of performance spaces, the opera house certainly is one of the most articulated from an architectural point of view. A consequence of the peculiarities of these performance spaces is the difficulty in simulating the extremely different acoustic conditions depending on the location of the sound source and the location of the listener. The chance to compute with high degree of accuracy all these peculiar acoustic conditions in the various audience areas represents a challenge in room acoustic simulation sector. In addition, the large total volume associated is even more challenging for a wave-based model, as the one chosen for the present work. Moreover, the fact that the volumetric proportions are completely different in the two opera houses under study allows the analysis of particular traits of different categories of performance spaces.

In opera houses, from the analysis of the overall volumes generally it can be assumed, at first approximation, the presence of two main coupled volumes (see Fig. 3.8): the stage tower and the main hall. Actually, it should be evaluated the presence of other volumes that are acoustically connected with the main hall: the orchestra pit, the theatre boxes and the gallery. This represents the typical volumetric scheme for opera houses [97, 98, 99].

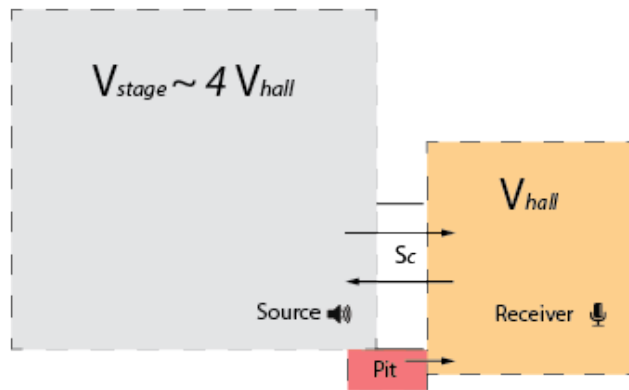
At the top of Figure 3.8 the simplest example of coupled volumes is shown, according to Müller and Cremer's theory [100].  $V_{stage}$  is the volume containing the sound source,  $V_{hall}$  is the volume containing the receiver, and  $S_c$  is the coupling area. The difference between the energy density in  $V_{stage}$  in case of coupled volumes,  $E_{stage}$ , and the common energy density considering the two volumes as a unique one,  $E$ , is represented by the *coupling factor*  $k_c$ :

$$k_c = \frac{S_c}{A'_{hall}} = \frac{S_c}{A_{hall} + S_c}. \quad (3.7)$$

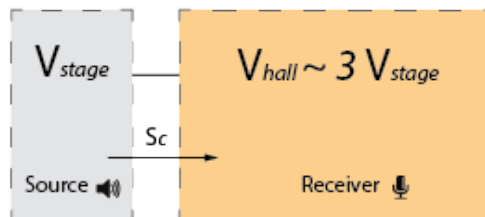
where  $A_{hall}$  is the equivalent absorption area of  $V_{hall}$ , in  $\text{m}^2$ . This factor is always lower than the unity and it depends not only on the geometrical



(a) Coupled volumes (Müller and Cremer's theory) [100].



(b) Case of TCB.



(c) Case of DUS.

Figure 3.8: Analysis of the volumes of the first two case studies: the opera house (TCB) and the modern theatre (DUS). View of the vertical section of TCB and DUS as an adaptation to the particular cases from the volumetric scheme (a) of the coupled volumes theory [100]. Different proportion between  $V_{stage}$  and  $V_{hall}$  are highlighted. See the text for the explanations of the arrows.

characteristics of the coupling area  $S_c$  but also on the absorption coefficients in  $V_{hall}$ . Two limit conditions are:

- $A_{hall} \ll S_c \Rightarrow k_c \approx 1$ , when the surfaces in  $V_{hall}$  are highly reflective and the two volumes acoustically behave as a single volume,
- $A_{hall} \gg S_c \Rightarrow k_c \approx 0$ , when the surfaces in  $V_{hall}$  are highly sound absorbing and the coupling effects between the volumes are not negligible.

The coupling factor  $k_c$  can be also expressed as:

$$k_c = \frac{S}{A'_{hall}} = \frac{E_{hall}}{E_{stage}} \quad (3.8)$$

meaning that when  $k_c \approx 1$  there is not a significant decrease in loudness in  $V_{hall}$  compared with  $V_{stage}$ .

A further parameter, the *damping constant*  $\delta$ , describes the rate of decay of sound pressure. According to this descriptor there are two cases:

- $\delta_{stage} > \delta_{hall}$  is the case of a multi-rate decay because  $V_{stage}$  has a shorter decay and  $V_{hall}$  has longer decay;
- $\delta_{stage} < \delta_{hall}$  is the case of a single rate decay because the longer reverberation in  $V_{stage}$  is more relevant than the shorter decay of  $V_{hall}$  [100].

When the equivalent absorption in  $V_{hall}$  is quite low, the two volumes can be handled as a single volume. When the equivalent absorption in  $V_{hall}$  is higher - as in case of opera houses - complex coupling effects, as the multi-slope decay for instance, should be taken into account.

Figure 3.8 shows the proportion between the volume of the stage and the volume of the main hall of the two opera houses considered, in comparison with the simple scheme provided by Müller and Cremer's theory [100]. In TCB, where  $S = 120 \text{ m}^2$  and  $A_{hall} = 220 \text{ m}^2$ ,  $k_s \simeq 0.35$  meaning that there are evident coupling phenomena. The two arrows in Figure 3.8(b) indicate the sound propagation main directions [101, 99]. In DUS, where  $S = 110 \text{ m}^2$  and  $A_{hall} = 500 \text{ m}^2$ ,  $k_s \simeq 0.18$  meaning that there are weaker coupling effects. The single arrow in Figure 3.8(c) indicates the preferential direction of sound propagation (from the stage tower to the main hall) [102].

In detail, the motivation of the choice of TCB are here summarized.

- With a huge volume of  $25000 \text{ m}^3$ , it represents one of the biggest challenge for the wave-based part of the model selected and thus, it certainly may be used to push the boundary of  $f_{max}$  value between FDTD and GA (indeed depending also on the time cost desired).

- Belonging to the architectural category of the opera houses, it gives the opportunity to simulate acoustic coupling effects (main hall, orchestra pit, boxes, stage house, gallery) [97, 103, 104];
- The presence of the orchestra pit allows a series of considerations about the peculiarity of sound fields created by sound sources placed in it [105]. For instance, placing the sound source in the orchestra pit various source-receiver pairs lack of direct sound, meaning that the main energy contributions at the receiver are caused by reflected and diffracted sound energy, physically modeled by the FDTD part of the algorithm.
- The presence of four tiers of boxes entails the exploration on the particular behaviour of these audience areas [106, 107] and on the way they affect the acoustic condition at the receivers.

In detail, the motivation of the choice of DUS are here summarized.

- The presence of the balconies, instead of the boxes of the previous case study, permits some peculiar analyses about the acoustic condition at those listeners position below the balcony overhangs [108].
- Even though its volume of 10000 m<sup>3</sup> is not as huge as the volume of the opera house aforementioned, this modern opera house still belongs to the category of large scale rooms - usually simulated with the standard GA procedure - so that it turns to be suitable to test the performance of the wave-based part of the model selected.
- A further reason behind the choice of this modern theatre is the presence of a sound reflectors array in the stage house. According to the author, a system of wooden panels installed over the stage represent an ideal case for studying edge diffraction with a FDTD model [83, 109, 110].

Elements concerning the first two case studies, especially for what concerns the acoustic surveys and the 3D modelling phase, are partially taken from two papers by the same author [111, 112].

### **An elliptical concert hall**

The third architecture selected as test sample in this study is an elliptical concert hall, St Cecilia's hall (STC). Even though it is a performance space as the other two halls selected, it is different and peculiar for various reasons. Focusing arising from concave surfaces, as the one shown in Figure 3.9, has

always been a well known phenomenon in room acoustics [113, 114]. The focusing can cause high concentrations of sound pressure levels, or flutter echoes.

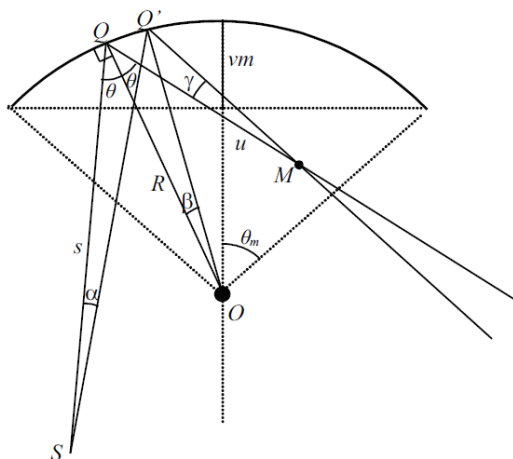


Figure 3.9: Focusing effects caused by curved surfaces. Credit image: M. Vercammen 2010 [114].

The motivations of the choice of STC are here summarized.

- The fundamental reason behind the choice of St Cecilia's hall is its elliptical shape. Indeed, the fact that all the walls of the performance space consist of curved surfaces creates some well known acoustic phenomena as sound concentration and flutter echoes [115, 116, 117].
- These phenomena are even more emphasized by the presence of a central double dome in the case under study [118].
- The volume of this concert hall is quite moderate compared to the other two case studies, meaning that the threshold frequency between FDTD and GA can be higher, allowing the user to perform a full wave-based simulation at least at the frequency more concerned by music (up to 6000 Hz).

### An university lecture hall

The fourth room selected is a historical university lecture hall (ULH).

- Differently to the other performance spaces, this hall is an ordinary room with moderate volume. This allows to use even higher values of  $f_{max}$  (up to 8000 Hz).

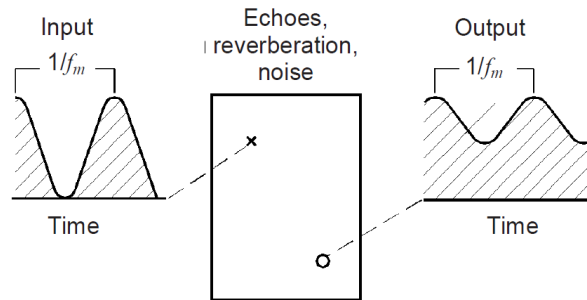


Figure 3.10: Deterioration of the speech signal caused by the acoustic features of the room: echoes, reverberation, noise [119].

- The second main difference concerns the intended use, namely the teaching purpose, more related to speech communication rather than to music. Consequently the specific room criteria concerned are focused on speech intelligibility indicators. Moreover, the time-domain nature of FDTD model is expected to be suited to simulate temporal fluctuations of speech modulations (see Fig. 3.10).
- The availability of experimental data about a sample of next generation microperforated panels, gives the chance to simulate a ceiling-mounted acoustic treatment directly using the complex acoustic impedances as boundary conditions in the simulations.

Part of the work concerning the lecture hall is taken from a work recently published by the author [120].

### 3.4 Practical procedure

In the present section the method adopted in this work is described and explained. From a chronological point of view the tasks carried out are listed, referring to all the environments selected. A schematic flowchart describing the method adopted is reported in Figure 3.11.

1. **The preliminary study** A preliminary study on each building had been developed. The aim was not only to historically frame the building but also to find out information that can be important from an acoustic point of view. The way a performance place was used in the past can explain some acoustic characteristics or suggest some further investigation. For instance, the location of the musicians within St Cecilia's hall in 16<sup>th</sup> century may arise some questions on the preferred perception of

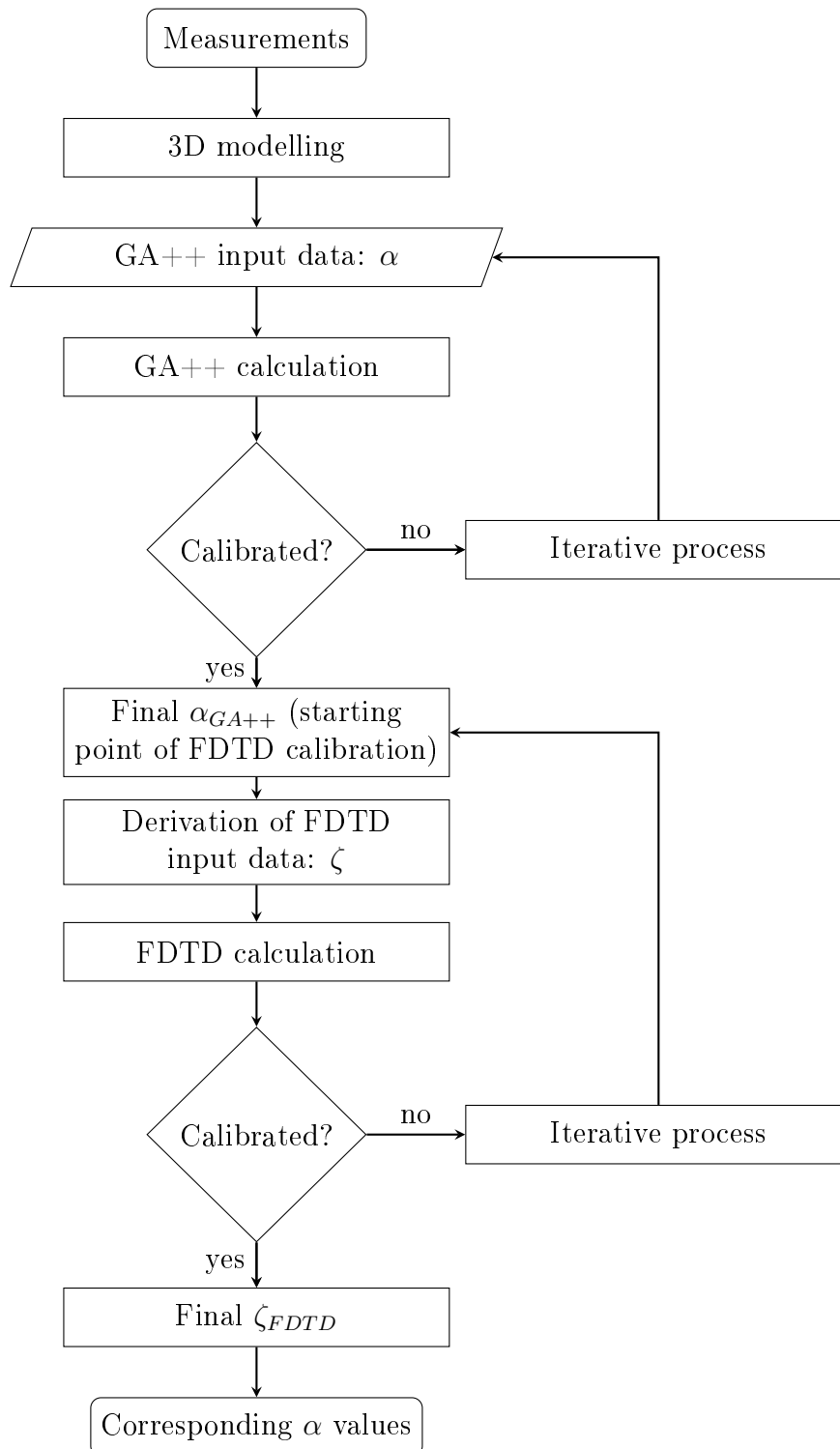


Figure 3.11: Flowchart of the double calibration process (FDTD/GA and GA++) carried out in each of the 3D virtual models.

the acoustics of the hall. Moreover, information concerning the exact materials employed in the construction of each architecture helps in the acoustic analysis of the place.

2. **Measurements** The fundamental phase in the workflow is represented by the acoustic measurements performed according to the relative standards. The campaigns of acoustic surveys returned the acquirement of the impulse responses and the objective room criteria, i.e. the main descriptors of the acoustic condition in the room. The measurements results, both in terms of impulse responses and collection of room criteria, are the reference point during the whole successive process and support the analysis and the final considerations. It is worth to notice that the method of each campaign of acoustic measurements is considerably affected by the intended use of the hall and the relative acoustic effect to be investigated.
3. **3D modeling** The 3D modeling phase of the virtual rooms is generally carried out according to the state-of-the-art guidelines of ray-based techniques [63, 121], except for specific variations described in the following chapters. All the models of this work were built with SketchUp following the GA++ standard approximations rules [122, 123]. It is important to remark that even though a wave-based model as FDTD could support even more detailed model, the choice to use as first approximation the same guidelines recommended for ray-based computations guarantees the comparison with corresponding GA++ models. During the modeling process, the choice was to reduce the actual numbers of distinct materials present in the real places to a relative small number of layers. This contributes to minimize the uncertainty connected with the input data, as the material properties to be assigned to the surfaces [124, 64].
4. **GA++ calibration** Each model was previously calibrated by means of the commercial hybrid GA++ software Odeon Room Acoustics [66, 67], which combines the image source method for the first orders of reflections and the stochastic ray tracing for the successive orders of reflections. The initial values of sound absorption coefficients and scattering coefficients applied to the surfaces were taken from available databases [81, 80, 121, 125], previous research [126], and in some cases from measurements performed in the laboratories of the University of Bologna. Then, the values were adjusted in an iterative way to achieve the calibration, as the common practice states [127]. The final set of absorption coefficients and scattering coefficient for each layer in each model

is provided in the second part of the Appendix A while the GA++ simulations setup is described in detail in Section 3.5.

5. **From GA++ to FDTD** This step represents a crucial point in the work from a decisional point of view, because it may be seen like a linking point between the GA++ procedure and the FDTD/GA procedure. The choices of the author concern two peculiar aspects:

- the 3D modeling level of detail,
- the initial values to set for the material properties.

With regard to the virtual models, as already mentioned, even though the wave-based part of the model chosen is able to naturally compute the diffraction on the edges, details and smaller objects were not modeled for comparison reasons. With regard to the initial material properties for the FDTD part of the FDTD/GA calibration, the choice was to start with the final energy parameters outcoming from the GA++ calibration (see Fig. 3.11) and to derive the corresponding complex acoustic impedances, notwithstanding the non univocity of the solution [35, 36, 92]. Both these choices have been made with the aim of maintaining comparable all the steps of the two different procedures and to carry out analyses on the results basing on the same starting points.

6. **FDTD/GA calibration** The FDTD/GA calibration was achieved with an iterative process that involved the variations of the starting energy parameters, as shown in Figure 3.11. It should be noticed that the variations of the material properties were mostly made on those input data assigned to particular materials, such as the seats or the wooden parts of a building, where a certain compensation of the lack of wave computation is taken into account in the energy parameters used in GA++ software [121, 125]. The main discrepancies in those materials properties depending on the approaches evaluated are provided in section 5.2. The tolerance ranges chosen for the calibration achievement are generally the JNDs provided by standards [128, 119], except for certain cases implying the reverberation time values [64] or the challenging effort of calibrating in octave bands for each audience area.
7. **Room criteria** The room criteria involved in this study are mostly the ISO 3382-1 criteria [128] for performance spaces and the IEC 60268-16 [119] for the lecture hall:

- reverberation time ( $T_{30}$ ),
- early decay time (EDT),
- sound clarity ( $C_{80}$ ),
- centre time ( $T_S$ ),
- speech transmission index (STI).

For the first four criteria, the results of the acoustic measurements in each hall are provided in octave bands from 125 Hz to 4000 Hz. With calibration purposes, the match between measured and simulated values was checked for the mean values of those criteria at mid frequencies (500 Hz - 1000 Hz). Moreover, the comparison between simulated and measured values as functions of frequency is provided for EDT, because it is more connected to the subjective perception, and  $T_S$  because it expresses the variation of the IR's energetic barycentre depending on the source-receiver pair considered.

Once all the models have been calibrated, there was the chance to perform various analyses and to outline some remarks. The attention was mostly focused on the following aspects.

- The first brief remark regards the 3D modeling approach in ray-based and in wave-based methods. Even if the same 3D virtual models were employed in the two distinct calibration procedures, an early experiment was conducted on the seats of ULH. Through a 2D visual comparison of sound propagation throughout a longitudinal section of the lecture hall, it is possible to qualitative assess the effects of a high scattering coefficient assigned to a box surface (GA++) and the direct handling of the edges of the seats rows (FDTD).
- The second considerations concerns one of the most debated critical point of any calibration works: the different input data employed as boundary conditions. While Appendix A provides all the input data for GA++ and FDTD calibrations in each environment assessed, Section 7.2 reports a further analysis on specific group of materials. The interesting thing regards the percentage of difference between the input data sets employed in ray-based and in wave-based algorithms at the end of the corresponding calibrations.
- The third group of remarks is about the multi-decay analysis carried out on the energy decay curves of measured and simulated IRs. The different acoustic coupling effects depending on the receiver location

in complex geometries (as in TCB, for instance) allows an exploration of the ability of the simulation method to render even the peculiar acoustic traits of each listeners areas.

- Last remarks involves the analysis of the frequency response in challenging acoustic condition, i.e. where no direct sight-line is granted between the sound source and the receiver. Most of the discrepancies between ray-based and wave-based are at low frequencies (125 Hz - 250 Hz), as expected from the nature of each simulation approach.

### 3.5 GA++ simulations setup

In the whole workflow illustrated in Figure 3.11 and described in Section 3.4, the numerical simulations performed with GA++ techniques on the same environments is of fundamental importance for at least two reasons. First of all, as already explained, the energy parameters obtained at the end of GA++ calibrations helped to determine the first starting set of acoustic impedances for FDTD calibrations. This choice turned to be relevant for the final comparison among the boundary conditions of the two distinct simulation approaches. Secondly, when both ray-based and wave-based calibrations had been carried out, the IRs simulated with ray-based methods lend themselves to be an ideal term of comparison with IRs simulated with wave-based methods and with IRs acquired through measurements as well. Therefore, GA++ results plays a key role during the discussions of the present thesis. For all these reasons, the present section is intended to describe in detail the simulations setup and procedure of this parallel - actually chronologically previous - calibration of the models. With this purpose, it is important to remind that the author - which took part to a published benchmark for ray-based room acoustical simulation [129] - performed all the stages of the process according to the state-of-the-art at the time of writing [25].

Firstly, the hybrid ray-based commercial software employed is Odeon Room Acoustics version 12.15. The 3D virtual models were built with the proper geometry reduction required in room acoustics [122]. The general approach to the 3D modeling has been already mentioned in Section 3.4 and it will be resumed in the specific description of each model (Chapters 4, 5, 6). Again, the most important aspect is that the same 3D virtual models were employed both in ray-based and wave-based calibrations. All the models were created using the commercial software SketchUp 2019 and then converted into ODEON rooms through the specific SU2Odeon plugin [130]. A direct use of SketchUp models in ODEON allows to avoid the several issues

due to the import of cad files in the dxf format [123].

The GA ++ calculation setting is summarized in Table 3.1 for each hall assessed. The transition order (TO), i.e. the threshold between the image source method and the stochastic ray-tracing (see Fig. 2.15) was set as 0 for large and articulated geometries with a large number of surfaces (TCB, DUS) and set as 2 or 3 for smaller and more ordinary environments (STC, ULH), as recommended by the specific guidelines [67, 73]. In fact, the former environments under study are large enough to allow a TO value equal to 0, leading to a whole stochastic ray-tracing approach, while the latter environments need at least two reflections orders handled with image source method to grant a higher accuracy in the early reflections computation. The number of *early rays* is partially a consequence of the TO choices. Therefore, in TCB and DUS the number of early rays was automatically set equal to 0, while in STC and ULH the number of early rays was chosen according to the value recommended by ODEON, i.e., respectively 55,000 (likely because of the high number of surfaces) and 4000. Concerning the number of *late rays*, it was set at least equal to the suggested value corresponding to “Precision” to obtain high level of accuracy, leading to values of 100,000 late rays for complex geometries as TCB, DUS, and STC. The maximum reflection order was chosen equal to 2000 for all the spaces assessed, except for STC in which peculiar phenomena due to the curved surfaces require more reflection orders. The temperature and the relative humidity were set equal to 20 C° and 50 % in all the GA++ simulations of the present work.

Table 3.1: GA++ simulation setup in TCB, DUS, STC, ULH. The transition order (TO), the number of early rays, the number of late rays , the length of the impulse response, and the maximum reflection order [131, 73, 67].

Hall	TO	Early rays	Late rays	IR length (ms)	Max. Refl. order
TCB	0	0	100,000	3500	2000
DUS	0	0	100,000	2500	2000
STC	2	55,00	100,000	2000	10,000
ULH	3	4000	60,000	2500	2000

All the virtual models were calibrated through a first assignment of suitable sound absorption and scattering coefficients to the various materials layers taken from consolidated scientific literature [25] and then a slight adjustment - within reliable ranges - along the calibration iterative process [127]. In particular cases, as for instance the carpet in TCB opera house, it was possible to obtain a sample of the carpet, which has been measured with

---

the impedance tube method (ISO 10534) in the laboratories of the University of Bologna [111]. As it often happens in GA++ calibrations, absorption and scattering coefficient tend to compensate the lack of modeling details and the geometries approximation [132]. Therefore, it often occurs that plaster materials, especially when relative to the stage house of TCB and DUS, have absorption and scattering coefficients higher than “regular” plasters values that can be found in materials datasets. Peculiar absorbing characteristics of some materials, as the stage grid in the fly tower of TCB and DUS, were taken from specific studies conducted on this particular kind of element [126].



# Chapter 4

## Systems of coupled rooms

The acoustics of historical opera houses is a widely investigated topic in scientific literature [133, 134, 98, 97, 99]. As already pointed out in the previous chapter, the geometrical and architectural features of this typology of performance spaces is so peculiar that several acoustic phenomena can be observed. In order to have an idea of the typical composite system of volumes within opera houses a cutaway is provided in Figure 4.1. Traditionally assessed with GA++ models due to their size and their non-trivial geometries, in the present chapter the opera houses are investigated through the hybrid FDTD/GA model previously described. With the purpose of exploring the wave-based simulation results in these performance spaces, the cut-off frequency  $f_{max}$  was chosen as high as possible considering the desired time cost. The opera houses presented are two out of four opera houses previously simulated and assessed by the author [135].

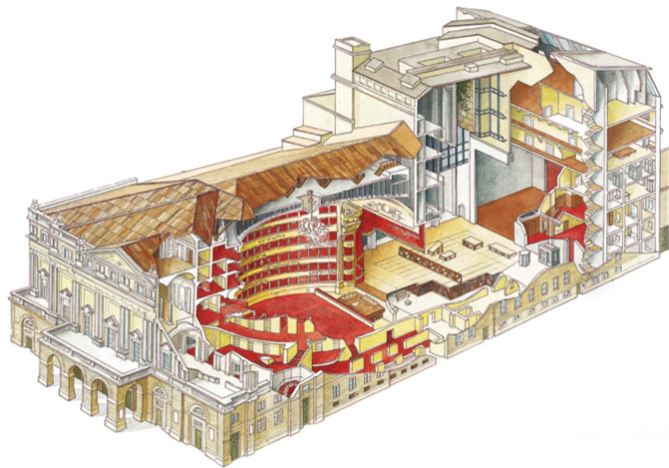


Figure 4.1: Typical cutaway of the composite system of volumes involved in opera houses.

## 4.1 A traditional historical opera house

In the present section the acoustics of a traditional opera house is explored. In a previous study, the same hall was used to simulate a virtual orchestra placed in the orchestra pit and thus, part of the work is taken from the reference [111], especially for the description of the building and the measurements setup.



Figure 4.2: *Sala Bibiena* of the *Teatro Comunale* in Bologna.

The *Teatro Comunale* (TCB) in Bologna, Italy was designed by the Italian architect Antonio Galli-Bibiena, a member of the popular Italian family of artists and architects in the 17<sup>th</sup> and 18<sup>th</sup> centuries. On 14 May 1763 the TCB was inaugurated: it was contemporary to the early period of the Italian Melodrama. At that time the pre-Sabinian theatre proved to be quite innovative due to specific design choices by the architect, as the bell shape of the main hall. Moreover, the use of construction materials was pretty uncommon compared to the usual opera house buildings. In fact, instead of the wide amount of wood typically present in opera houses, stone and gypsum were employed as main material in the hall (see Fig. 4.2). Over the time, TCB was restored more than once. In 1935 a fire that destroyed most of the stage house, that successively was rebuilt wider than the previous one and with a higher ceiling. The last renovation was in August 2016 when all the seats of the stalls were replaced, while the original materials of the walls, ceilings and floors were not affected. The shape, the materials, and the huge size of the

stage house compared to the main hall provide a quite reverberant field. It was so different from the “dry” acoustics generally required in opera houses that at the end of the 19<sup>th</sup> century TCB became one of the best places for performing Wagner’s operas outside Germany.

The opera house hosts up to 1000 people, with a total volume of around 25,400 m<sup>3</sup>, approximately divided into:

- 5,400 m<sup>3</sup> of the main hall, i.e. the part of the theatre including all the listeners areas of the stalls, the boxes, and the gallery,
- 20,000 m<sup>3</sup> of stage house (or stage tower), i.e. the part of the theatre which contains the proscenium arch, the stage, the wings, the sceneries, the grid.

The main geometrical features of TCB are provided in Table 4.1.

Table 4.1: Geometrical features of the *Teatro Comunale* in Bologna (TCB). The reference ID, the century of construction, the shape, the volume of the main hall ( $V_{hall}$ ), the volume of the stage house ( $V_{stage}$ ), the seating capacity (N), the number of tiers (not counting the upper gallery), the presence of the orchestra pit are provided [97, 99, 136, 137].

ID	Century	Shape	$V_{hall}$ (m <sup>3</sup> )	$V_{stage}$ (m <sup>3</sup> )	N	$V_{hall}/N$ (m <sup>3</sup> /seat)	Tiers	Pit (y/n)
-	-	-	-	-	-	-	-	-
TCB	XVIII	Bell	5,400	20,000	1000	5.4	4	y

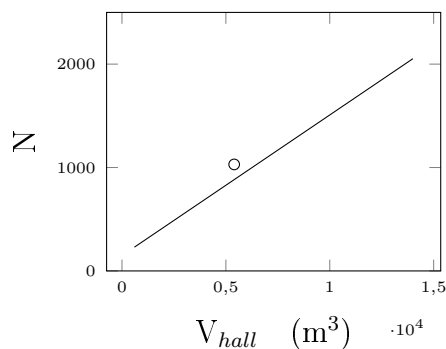


Figure 4.3: Relation between the seating capacity, N, and the volume of the main hall,  $V_{hall}$ . The plot of seating capacity as function of volume is taken from previous studies on opera houses [97].

In TCB the relation between the seating capacity and the volume of the main hall in line with previous studies on Italian opera houses (see Fig. 4.3)

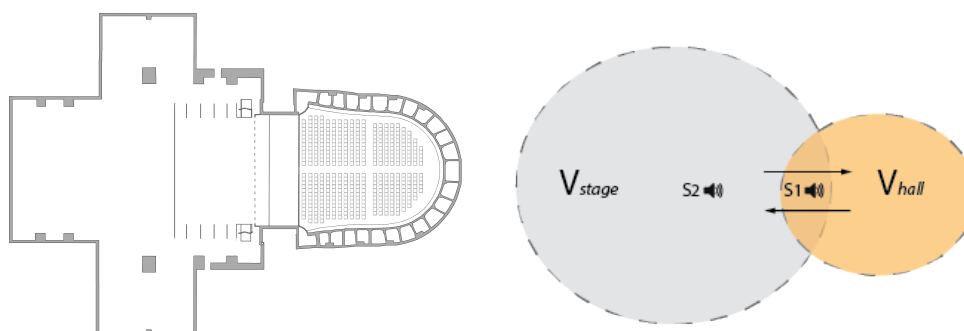


Figure 4.4: Scheme of the volumetric proportion in the traditional opera house (TCB). View from the top of the strategic location of the sound sources used in the acoustic measurements of the halls. The arrows indicate the main direction of the sound energy (see more details in Chapter 3) [100].

[97, 111]. In the same work the Italian opera houses was ranked in different groups, adjusting the theories developed in concert halls [136]. According to these studies, since TCB is characterised by a huge stage house and a relevant disproportion between  $V_{stage}$  and  $V_{hall}$  (see Fig. 4.4), it belongs to the A group [97, 135]. This category of opera houses is characterised by large stage towers and an overall reverberant sound field.

#### 4.1.1 Acoustic measurements

Between August and September 2016, several acoustic measurements campaigns were made in TCB. During each one of them, impulse responses (IRs) have been acquired with the exponential sine sweep (ESS) technique (2.5 seconds of signal). A custom software was employed for the necessary deconvolution process to acquire the IRs [138]. During measurements the opera house was in unoccupied state according to the standard ISO 3382-1 [128]. The stage house was equipped with the usual opera scenery and sound absorbing objects, as drapes and curtains, while the orchestra pit was lacking chairs and music stands.

The locations of sound sources and receivers were chosen following the Ferrara Charter procedure [98], in line with the aim of collecting information about the acoustic conditions in the most used positions by the singers and the musicians, and about the coupled volumes phenomena (see Fig. 4.4). Therefore, four locations were chosen for the sound source (see Fig. 4.5):

1. on the stage under the proscenium arch (S1),
2. at the centre of the stage (S2),

3. in the orchestra pit, in the uncovered part (S3),
4. in the orchestra pit, in the covered part (S4).

Among the sound source positions on the stage, S1 is placed basically in correspondence with the coupling area between the volume of the stage and the volume of the main hall, whereas S2 is located in the former volume.

The sound source placed in these specific locations was an omnidirectional high-SPL dodecahedron [139], driven with enough gain to guarantee a good signal-to-noise ratio [140]. The dodecahedron sound source may be considered as an omni-directional sound source within a certain frequency range [141].

Receivers were organised following a mesh of points in one-half of the audience, exploiting the symmetry of the hall (see Fig. 4.5) [98]. In order to collect information about the acoustic conditions in the different parts of the opera house, the receivers were spread throughout the three listeners area (see Fig. 4.7) [106]:

- the stalls, at the ground floor in the main hall,
- the theatre boxes (1<sup>st</sup>, 2<sup>nd</sup>, 3<sup>rd</sup> and 4<sup>th</sup> tier),
- the gallery, at the highest level of the building.

Each receiver's position is reported in Fig. 4.5 while the distinction of the three audience areas is shown in figure 4.7.

Table 4.2: Measurements results in TCB. Reverberation time ( $T_{30,M}$ ), early decay time ( $EDT_M$ ), sound clarity referred to 80 ms ( $C_{80,3}$ ), centre time ( $T_{S,3}$ ) measured values are provided [128], along with the Schroeder frequency ( $f_c$ ) and the number of sound source and receivers points. Values signed with "M" indicates the average over 500-1000 Hz, with "3" the average over 500-1000-2000 Hz. The type refers to the rankings provided in [136] and readapted to Italian Historical Opera Houses in [97].

ID	Type	$T_{30,M}$ (s)	$EDT_M$ (s)	$C_{80,3}$ (dB)	$T_{S,3}$ (ms)	$f_c$ (Hz)	Sources/Receivers
TCB	A	1.57	1.58	0.1	119	16	2/26

In order to estimate the influence of sound absorbing materials on the whole sound field behaviour, the acoustic measurements were performed with and without the drapes in the stage house (see Fig. 4.6(a)). It is well known that their presence significantly influences the acoustic of an opera house [126, 142, 143]. Moreover, exploiting the refurbishment of the stalls occurring

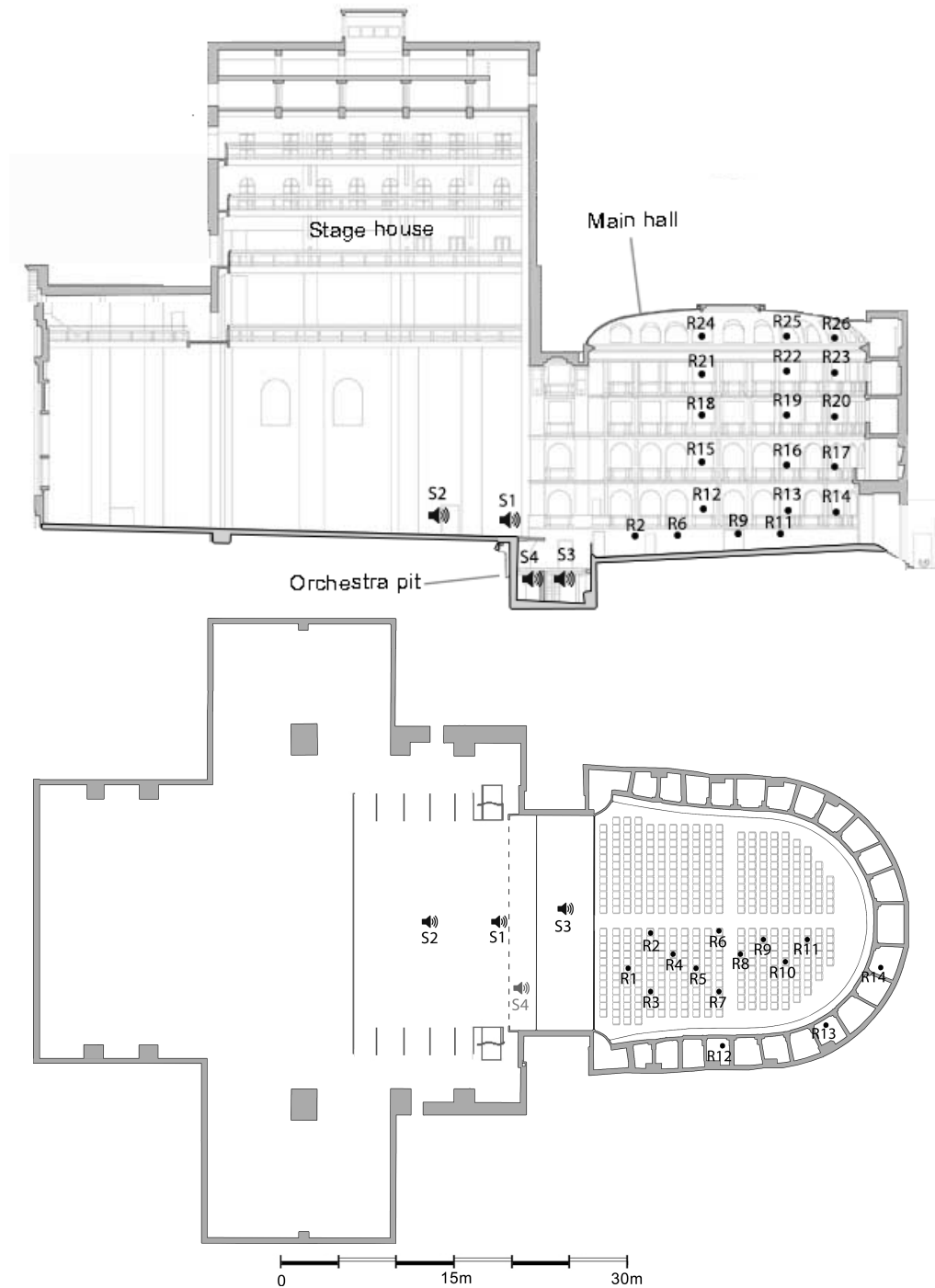


Figure 4.5: Positions of sound sources (S) and receivers (R) selected in the acoustic measurements campaign in TCB. The receivers in the 1<sup>st</sup> tier of boxes are then repeated at the same corresponding positions in all the rest of the tiers and in the gallery.

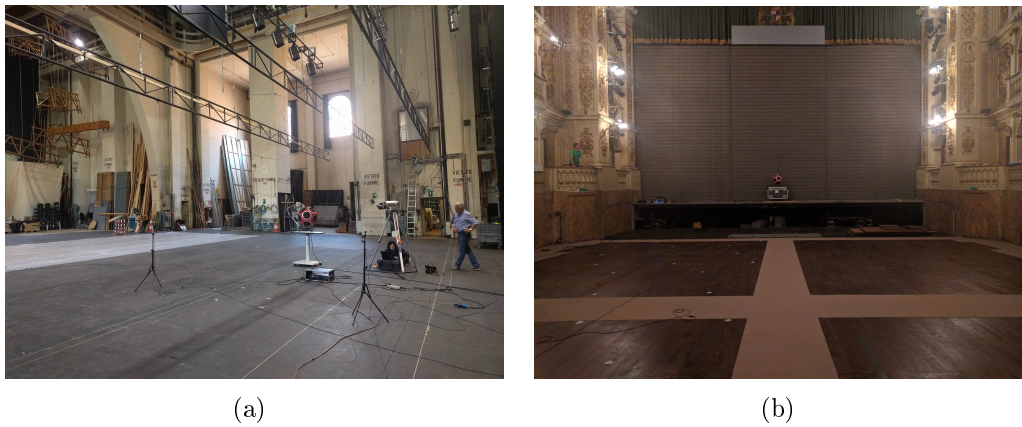


Figure 4.6: Views of TCB during different measurements configurations: (a) without the curtains in the stage house, (b) without the chairs in the stalls (fire-curtains closed).

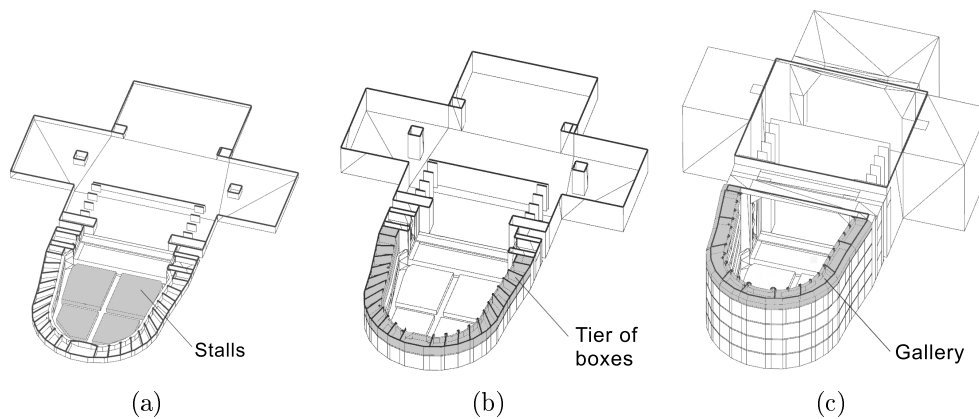


Figure 4.7: Distinct audience areas in TCB: (a) stalls, (b) boxes, (c) gallery.

in the same year of the measurements, it was possible to carry out the acoustic measurements with and without the chairs in the main hall (Fig. 4.6(b)). Results confirm the significant influence of the equivalent absorption area of the chairs on measured room criteria [144]. The main objective room criteria collected from measured IRs are presented:

- in Table 4.2 in terms of mean values averaged over the mid frequencies;
- in Figure 4.8 in terms of  $C_{80,3}$ ,  $EDT_M$ , and  $V_{hall}$  values compared to previous studies on opera houses,
- in Figure 4.9 in terms of  $T_{30}$ ,  $EDT$ ,  $C_{80}$ ,  $T_S$  in octave bands along with the standard deviations.

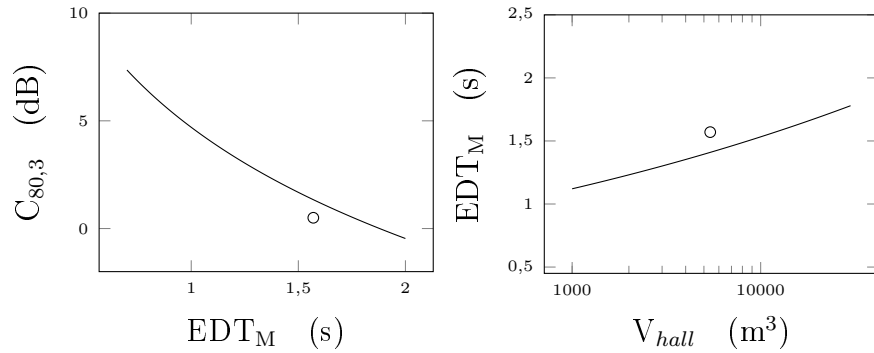


Figure 4.8: Relation between  $C_{80,3}$ ,  $EDT_M$ , and  $V_{hall}$  in TCB. The curves are referred to the A group according to previous studies on opera houses [97].

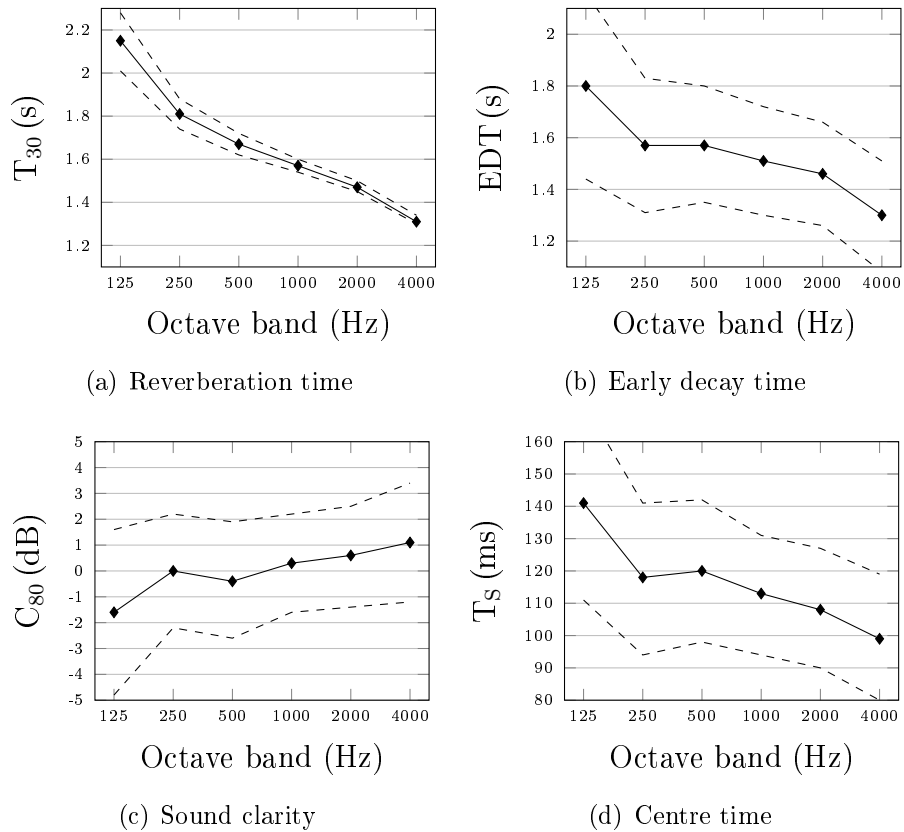


Figure 4.9: Measured  $T_{30}$ , EDT,  $C_{80}$ ,  $T_S$  values in TCB in octave bands with relative standard deviations (dashed lines). Mean values are averaged over all the source-receivers pairs shown in Figure 4.5.

### 4.1.2 FDTD calibration

As mentioned in the previous chapter, the methodological approach to the simulation was kept as similar as possible to the traditional GA++ procedure. This is intended to allow a systematic comparison with classical practice in large scale room acoustic simulation. The following part outlines the choices influencing the simulation process according to the method explained in Chapter 3.

#### 3D modeling

Concerning the 3D modeling step, it should be reminded that a calibration of the 3D virtual model had been already achieved in a previous work by means of GA++ techniques, as described in [111]. Again, as in a FDTD model diffraction phenomena would be naturally computed without the need of using scattering coefficients (see Fig. 4.10), in general a 3D virtual model specifically built for a wave-based simulation could allow the presence of more elements and geometrical details [122]. For instance, this consideration may be applied to the most simplified group of elements in a performance space: the seats [117]. Nevertheless, since the intention of simulating a huge theatre with wave-based models is accompanied by the need of a reference point taken from the classical calibration process, the choice was to use the same level of approximation used in GA++ models also for FDTD model. Therefore, the state-of-the-art 3D modeling in large scale room acoustics simulation rules have been followed [123, 122, 127]:

- great attention was paid to avoid any overlapping surface, otherwise there would be misleading material properties associated to the overlapped faces;
- curved surfaces were discretized in planar surfaces according to the common rule of thumb that requires the approximation occurring every 10 degree angle of the whole curvature considered,
- no detail smaller than 0.34 meters (wavelength corresponding to 1000 Hz) was modeled to optimize the computational cost and reducing the unnecessary level of detail.

The 3D model obtained at the end of the modeling phase includes 2150 surfaces with a total surface area of about 12,500 m<sup>2</sup> and a total volume of about 26,000 m<sup>3</sup> (see Fig. 4.11). The virtual model was organised in different layers corresponding to macro-groups of the actual materials in TCB. In the real opera house the numbers of different materials are certainly higher than

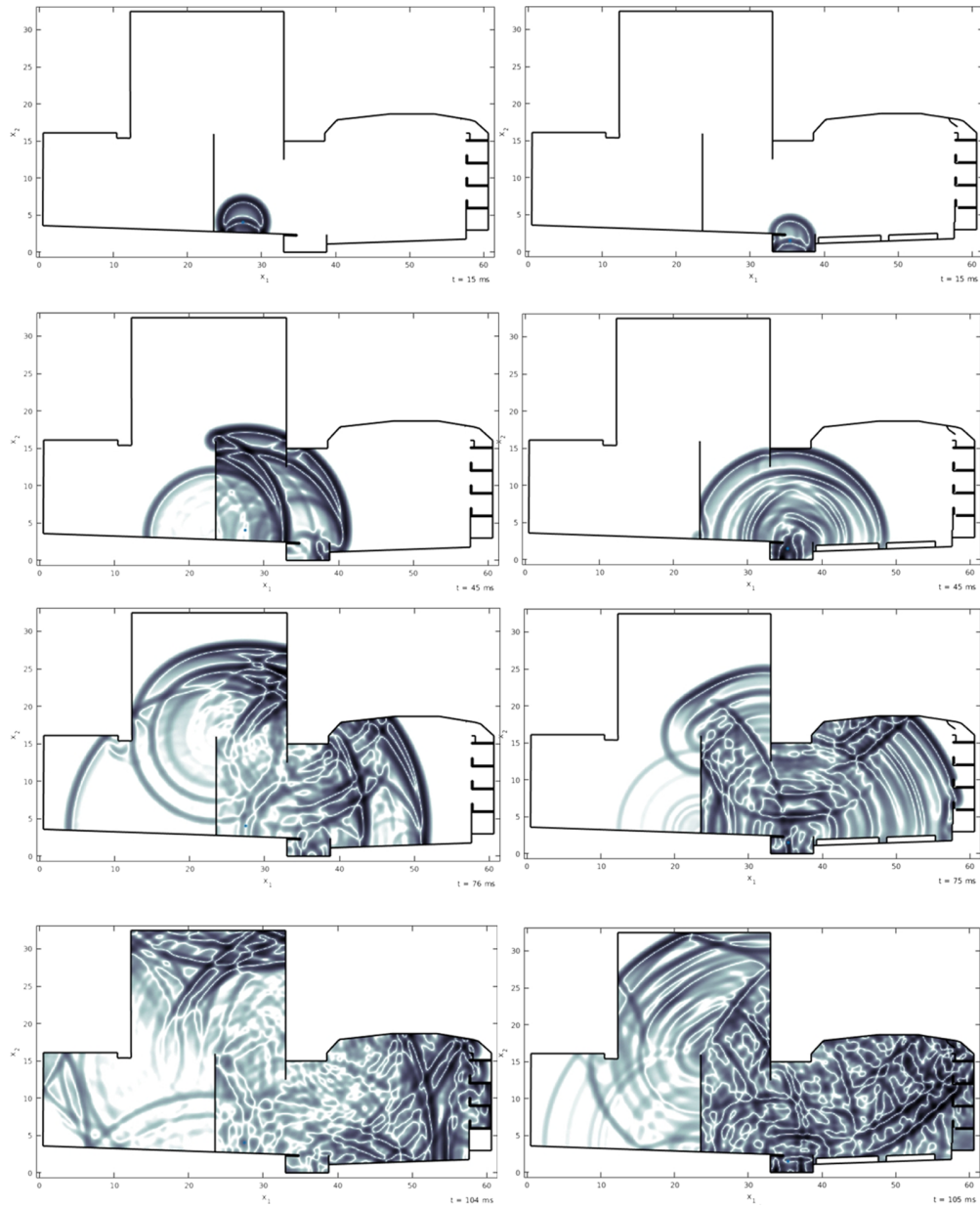


Figure 4.10: Visualization of sound propagation in TCB considering the sound source positions in the centre of the stage (left) and in the orchestra pit (right).

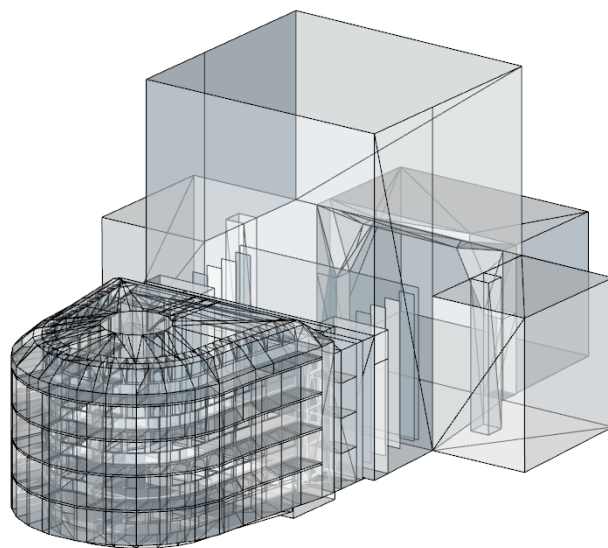


Figure 4.11: View of *Teatro Comunale*'s CAD model as shown in the modelling software [145].

the numbers of the layers. The subdivision in a relative small number of layers during the modeling process helped to better organise the workflow and to reduce the uncertainty connected with the material properties to be assigned to the surfaces [64].

### Simulation setup

In TCB it was possible to run simulations with the wave-based part of the method up to the frequency of 4 kHz. Therefore, a full wave-based simulated impulse response is available for most of the octave bands usually analysed in performance spaces (from 125 Hz to 2 kHz). A qualitative visualization of the wave simulation run within TCB is provided in Figure 4.10, considering the sound source in S2 and S3 positions. As it can be seen, when the sound source is located in the orchestra pit the diffraction from the edges of the pit affects the sound field since the beginning of the propagation.

The value  $f_{max} = 4$  kHz should be assessed as a significant achievement, considering the huge volume of the hall and the extremely articulated geometry. For upper frequencies a classical ray tracing at high-density (1 billion rays) was employed. The impulse response length was set equal to 3.5 s to be sure to include even the higher values of reverberation time at lower frequencies. The computational task has been parallelized using CUDA and four Nvidia Titan X (Maxwell) GPUs, in collaboration with the University of

Edinburgh. The time cost was approximately 1 hour per second of simulated impulse response.

Table 4.3: Simulation setup of FDTD simulation in TCB. The maximum frequency simulated with FDTD ( $f_{max}$ ), the points per wavelength (PPW), the oversampling factor ( $\sigma$ ), the grid spacing ( $h$ ), the time step ( $k$ ), the Courant number ( $\lambda$ ), the time cost (in hours of runtime  $h$  per second of computed impulse response  $s_{output}$ ), and the dispersion error (in percentage) are provided.

$f_{max}$ (Hz)	PPW	$\sigma$	$h$ (mm)	$F_s = 1/k$ (Hz)	$\lambda$	Time cost (h/ $s_{output}$ )	Dispersion error%
4000	6.75	3.375	12.3	27500	$\simeq 1$	1	1%-2%

A value of 6.75 PPW was chosen, returning a value of 3.4 as oversampling factor ( $\sigma$ ). The corresponding numerical dispersion errors are limited between the range of 1% - 2%. As a consequence, the grid spacing  $h = 12.6$  mm and  $k = 3.65 \cdot 10^{-5}$  s. To summarize the simulation setup in the FDTD region the maximum frequency ( $f_{max}$ ), the points per wavelength (PPW), the oversampling factor ( $\sigma$ ), the grid spacing ( $h$ ), the time step ( $k$ ), the Courant number ( $\lambda$ ), the time cost (in hours per second of computed impulse response), and the dispersion error (in percentage) are provided in table 4.3.

At this point, the choice of the acoustic indicators selected as the targets of the calibration is closely related to the intended use of the performance space under study [132]. The significant indexes suited to describe the acoustics of opera houses typically are [128, 146]:

- the reverberation time  $T_{30}$ , in seconds, typical trait of the hall (quite uniform throughout the space),
- the early decay time EDT, in seconds, closely related to the subjective perception of reverberance,
- the sound clarity  $C_{80}$ , in decibel, where the threshold at 80 ms between early and late reflections is for the sound clarity of music,
- the centre time  $T_S$ , in milliseconds, the centre of gravity of the IR's energy.

The choice was to calibrated the model using two out of four sound source positions used in the measurements campaign, the first one on the stage (S2, central position) and the second one in the orchestra pit (S3, uncovered area). Table 4.4 summarizes the calibration results in terms of main room criteria

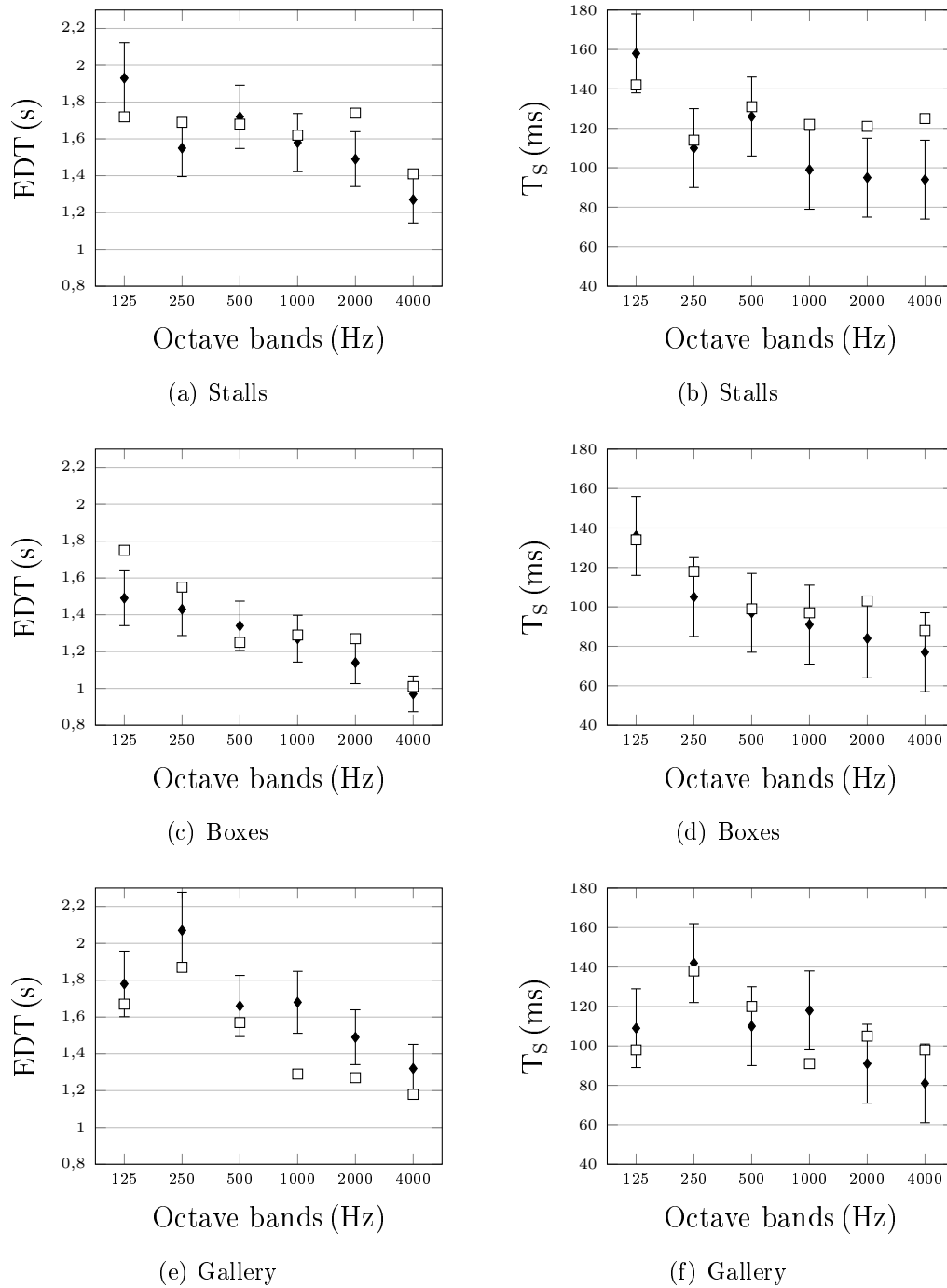


Figure 4.12: TCB calibration: measured (black) and simulated (white) EDT and  $T_S$  values in octave bands. Mean values are referred to the sound source placed in the centre of the stage (see Fig. 4.5) and to the distinct audience areas: stalls, boxes, gallery (see Fig. 4.7). The error bars are referred to the tolerance range chosen for the calibration process.

( $T_{30,M}$ ,  $EDT_M$ ,  $C_{80,M}$ ,  $T_{S,M}$ ) at mid frequencies (500 – 1000 Hz). In line with the standard procedure, the calibration of the 3D model was achieved when the differences between simulated and measured values were within the Just Noticeable Differences (JND) defined by the standard [128], except for  $T_{30,M}$  and  $EDT_M$  for which twice the JND was considered as the reference point during the calibration process, according to recent remarks concerning the uncertainty behind those room criteria [64]. Therefore at mid frequencies the tolerance ranges were the following:

- 10% in  $T_{30,M}$  and  $EDT_M$  evaluation,
- 1 dB in  $C_{80,M}$  evaluation,
- 10 ms in  $T_{S,M}$  evaluation.

With regard to this calibration choice, at the end of the iterative process the 83% of the simulated mean values at mid frequencies are within the tolerance range chosen (see Table 4.4).

To visualize the behaviour of those room criteria as functions of the frequency, Figure 4.12 reports the results of the achieved calibration in terms of EDT and  $T_S$ , measured and simulated, in octave bands. The choice of such room criteria is due to the deviation of resulting values throughout the space [132]. A calibration performed with spatially varied room criteria is expected to be more accurate rather than a calibration performed on quite uniform indicators, as the reverberation time. EDT criterion was chosen because it is extremely important in opera houses. In fact, it is connected to the subjective perception of the reverberation time [128].  $T_S$  criterion was chosen because it returns the effective centre of gravity of the IR's energy and thus, do not arbitrarily divides the reflections in early and late, as it happens using  $C_{80}$  criterion. The values displayed in the graphs are referred to the sound source in S2 position, the centre of the stage, (see Fig. 4.5) and the resulting values are shown averaged over the three receivers areas (stalls, boxes and gallery), as a function of the frequency. Since calibrating in each audience area and considering the trend of the criteria in octave bands is considerably challenging, the author chose to double the tolerance of the centre time to twice the JND (20 ms instead of 10 ms). This choice is also supported by the highly reverberant field within TCB [147]. At the end of this calibration step, 80% of the values were between the tolerance range assessed in this work.

With regard to material properties assigned to the surfaces, the initial values of absorption coefficients - from which the complex acoustic impedances are derived and given as input data in FDTD model - correspond to the final values obtained with the achievement of the previous GA++ calibration.

Table 4.4: Measured and simulated room criteria in TCB. Results at medium frequencies (500-1000 Hz) for center stage source positions, averaged over receivers in stalls, boxes and gallery. The difference between mean measured and simulated values are reported between brackets. See text for the tolerance range adopted for each metrics.

Room criteria	Measured	Simulated (Diff.)	Receivers
$T_{30,M}$ (s)	1.53	1.62(-5.5%)	stalls
	1.53	1.56(-1.8%)	boxes
	1.66	1.51 (+9.6%)	gallery
$EDT_M$ (s)	1.56	1.59(-1.7%)	stalls
	1.38	1.33(+4.0%)	boxes
	1.69	1.38 (+18%)	gallery
$C_{80,M}$ (dB)	-0.2	-0.2(-)	stalls
	1.2	0.3(+0.9)	boxes
	-0.8	0.2 (-1.0)	gallery
$T_{S,M}$ (ms)	122	118(+4)	stalls
	106	108(-2)	boxes
	130	103 (+27)	gallery

The outgoing values of absorption coefficients obtained at the end of the FDTD simulation are shown in Table 4.5. The normalised LRC coefficients for the boundary complex impedances are provided in the first part of the Appendix. The difference found with the corresponding values used in the GA++ model are provided in the second part of the Appendix.

Concerning the peculiar materials in TCB, it is important to point out some considerations:

- a sample of the carpet was taken and measured in laboratory (ISO 354) allowing to obtain an accurate absorption value for the corresponding layer;
- the absorption coefficients referred to the plaster in the main hall are higher than regular plasters to compensate the lack of details resulting from the modelling approximation,
- absorbing characteristics of the whole stage house, which is a composite system including trusses, service facilities, catwalks and lighting fixtures, were taken partly from literature [126] and partly from the results of previous GA++ calibration [111],

Table 4.5: Materials involved in TCB simulations. The energy-based parameters  $\alpha$  represent the starting point in the backward process to obtain the acoustic impedances  $\zeta$  for the FDTD simulation. The macro-layers used in the present work divide the materials according to the type of the surface and the role within the opera house, e.g. the plaster related to “stage house” is not handled as the plaster in the “boxes”. References are provided for most of the absorption coefficients. Normalised LRC (inductance, resistance, capacitance) coefficients employed as input data in FDTD simulations to approximate boundary admittances are provided in the first part of the Appendix.

	Energy-based parameters $\alpha$						Ref.
	125 Hz	250 Hz	500 Hz	1 kHz	2 kHz	4 kHz	
Carpet	0.04	0.05	0.06	0.08	0.16	0.20	Measured [148]
Velvet drapes	0.11	0.16	0.50	0.65	0.73	0.73	[142]
Wood	0.20	0.15	0.10	0.10	0.10	0.10	[143]
Plaster (boxes)	0.08	0.12	0.14	0.15	0.15	0.15	Estimated
Marble	0.02	0.02	0.03	0.04	0.04	0.04	[121]
Stage house	0.25	0.25	0.25	0.25	0.20	0.20	Estimated
Stage grid	0.35	0.45	0.50	0.65	0.65	0.65	[126]
Seats	0.35	0.45	0.55	0.60	0.60	0.60	[144]

- the measurements carried out with and without the drapes on the stage facilitated the evaluation of the properties of these absorbing materials [142].

Once the calibration process is achieved, the calibrated model is expected to return reliable acoustic features compared to the actual opera house. Therefore, as it often happens in room acoustics, the calibrated model is employed to study and analyse those peculiar acoustic traits of the hall assessed. In case of opera houses, as already explained in detail, the acoustic consequences of the presence of coupled volumes is thoroughly investigated in detail.

### 4.1.3 Acoustic coupling

The assessment of the acoustical effects due to coupled volumes is closely related to the study of the energy decay curves. The energy decay curve (EDC) is typically computed with the backward integration of the squared impulse response, which was proposed and first applied by Schroeder [149]:

$$\text{EDC}(t) = \int_t^\infty h^2(\tau) d\tau = \int_0^\infty h^2(\tau) d\tau - \int_0^t h^2(\tau) d\tau \quad (4.1)$$

where  $h^2(\tau)$  is the squared room impulse response as a function of time.

The calculation of many room criteria is based on the assumption that within the evaluation range, a straight line can approximate the slope of the decay curve. The decay curve measured in a room is often slightly non-linear. In an opera house, typically the initial part of the decay is steeper than the rest of the decay, contributing to EDT/ $T_{30}$  ratio lower than 1 [137]. It is, therefore, interesting to investigate how far the shape of the energy decay is from the linear decay. Several metrics have been developed to detect the non linearity of the energy decay time [150, 151, 152] and the presence of the multi-slope decays [104].

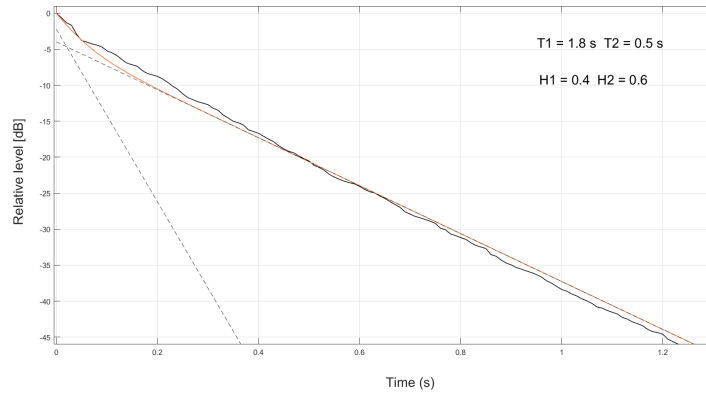
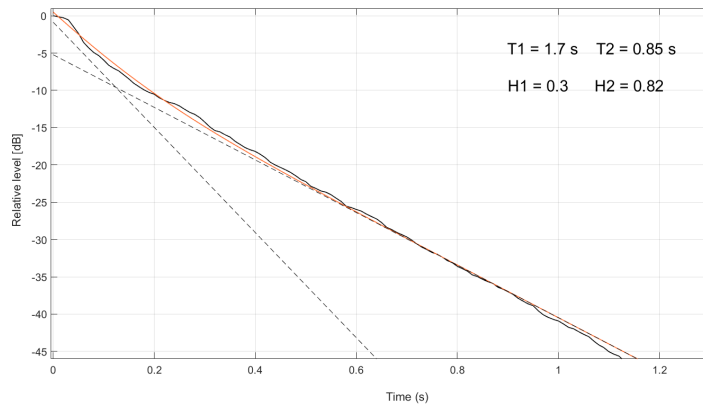
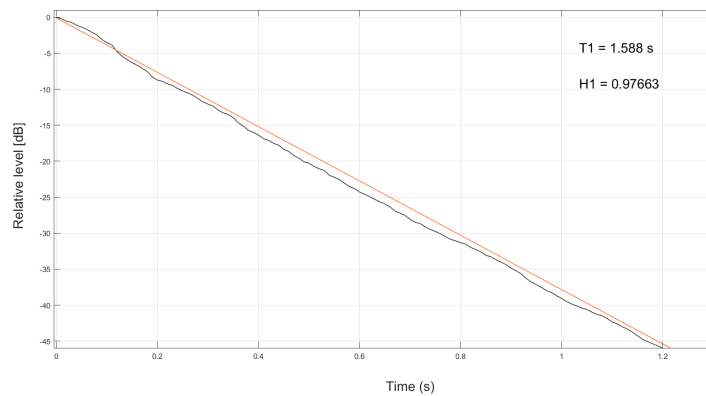
**The degree of curvature** The ISO 3382-2 [150] standard proposes the degree of curvature as an indicator of the non-linearity of the decay curve. The curvature parameter,  $C$ , is based on two evaluation ranges that can be used to obtain the reverberation time: 20 dB (from -5 dB to -25 dB) and 30 dB (from -5 dB to -35 dB). It is defined as the percentage deviation from a perfectly straight line:

$$C = 100 \left( \frac{T_{30}}{T_{20}} - 1 \right) \quad (4.2)$$

Typical values of  $C$  are in the range between 0 % and 5 %.  $C$  values that prove to be higher indicate a decay curve which is far from being a straight line.

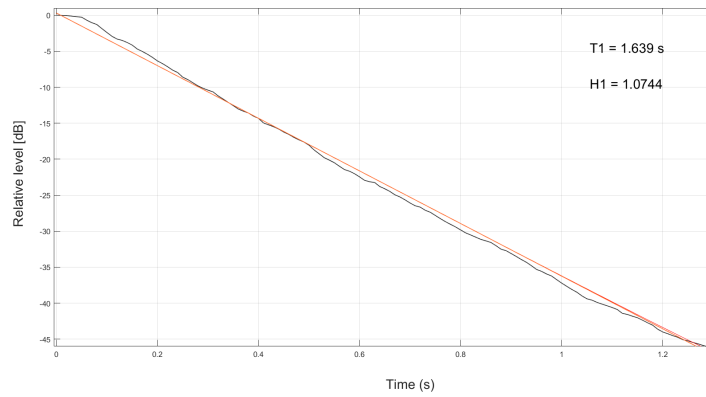
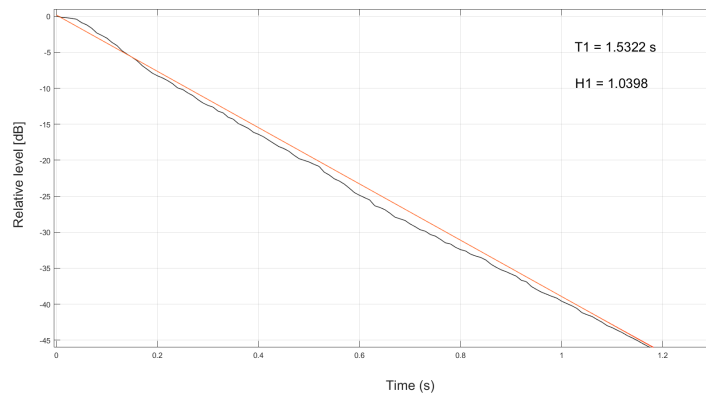
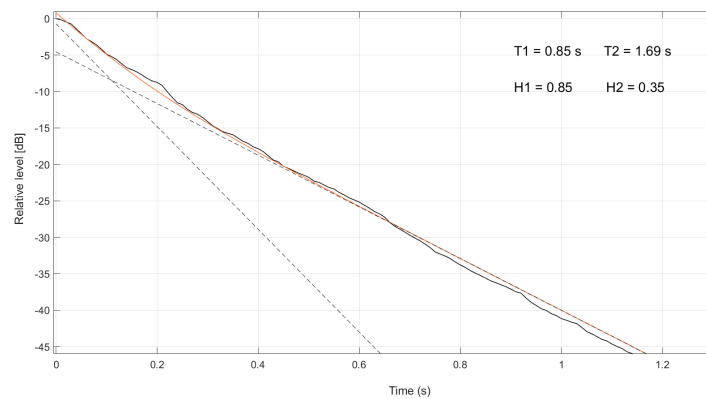
**Multi-slope sound decay analysis** In opera houses and concert halls, the double sloped behaviour is expected from the multi-decay analysis [137, 112]. In this peculiar typology of performance spaces the decays of impulse responses are generally characterised by “cliff-type” characteristics, being the EDT values smaller than the  $T_{30}$  ones, according to the consolidated literature [137]. The main reasons behind this particular sound decay are the strong early reflections provided by the proscenium arch, the vault over the main hall and, for the listeners in the stalls area, from the smooth concave side walls. When the sound source is on the stage, in the stalls the direct sound is enhanced by those early reflections. Since the gaussian properties of the energy decay curve between -5 and -35 dB make the  $T_{30}$  a constant of the hall, the EDT, which depends on the first deterministic part (10 dB) of the decay curve, is more variable.

Multi-decay analysis [104] of simulated impulse responses (IRs) allowed to detect and understand these effects, which vary depending on the listener position, in the present case the stalls, the boxes and the gallery [103, 111]. Concerning this analysis performed on the simulated IRs, the following ex-

(a) S2 (centre stage) - R6 (11<sup>th</sup> row in the stalls)(b) S2 (centre stage) - R22 (4<sup>th</sup> tier of boxes)

(c) S2 (centre stage) - R24 (gallery)

Figure 4.13: Multi-decay analysis of simulated IRs in TCB at 1000 Hz [104]. The position of the sound source is in the centre of the stage (S2 in Fig. 4.5) and each receiver's position belongs to a specific audience area (see Fig. 4.7). See text for the explanation of the quantities.

(a) S3 (orchestra pit) - R10 (16<sup>th</sup> row in the stalls)(b) S3 (orchestra pit) - R16 (2<sup>nd</sup> tier of boxes)

(c) S3 (orchestra pit) - R24 (gallery)

Figure 4.14: Multi-decay analysis of simulated IRs in TCB at 1000 Hz [104]. The position of the sound source is in the uncovered part of the orchestra pit (S3 in Fig. 4.5) and each receiver's position belongs to a specific audience area (see Fig. 4.7). See the text for the explanation of the quantities.

pression should be taken as reference:

$$H_s(\mathbf{H}, \mathbf{T}, t_k) = H_0(t_K - t_k) + \sum_{S=1}^2 H_s e^{-13.8t_k/T_s} \quad (4.3)$$

where

- $H_s$  is the Schroeder curve,
- $\mathbf{T} = T_1, T_2$  and  $\mathbf{H} = H_1, H_2$  are the decay parameters [104],
- $K$  is a large number of data points,
- $H_0$  is the background noise (not shown in Fig. 4.13).

Using the “integrated tone-burst method” proposed in the 1960s by Schroeder [153] the first 5 dB of the sound decay - usually omitted in this kind of analysis [104] - can also be taken into account [154].

Figure 4.13 and 4.14 provide the multi-decay Bayesian analysis applied to the simulated IRs corresponding, respectively, to the sound source in the centre stage position (S2) and in the uncovered part of the orchestra pit (S3) in each of the audience area of Fig. 4.7. When the sound source location is on the stage, the sound energy decay at the receivers has mainly two contributions corresponding to the sound field of the main hall and the stage house. The multi-decay effects are more visible in the boxes rather than the remaining sound source-audience area combinations. In fact, the first part of the decay curve is affected by the reflections due to the nearest walls - which in generally are quite absorbing in each box - while the second part by the diffuse sound field of the cavea. The consequent effect of a considerably lower EDT compared to the  $T_{30}$  is in line with the typical perception of acoustic dry condition in the boxes. It should be noticed that this effect is less visible when listeners are in the stalls. Moreover, in the gallery, where there is the highest perceived reverberance in TCB, the effect becomes null (straight line decay).

Figure 4.14 provides the multi-decay Bayesian analysis applied to the simulated IRs corresponding to the sound source in the uncovered part of the orchestra pit (S3) and receiver in each of the audience area of Fig. 4.7. It is possible to observe that the source-receiver pairs corresponding to the sound source in the pit and the receiver in the gallery, return the most evident double decay effect. In fact, the upper gallery may be seen as the farthest acoustic volume from the orchestra pit among the audience areas. Therefore, the multi-decay analysis detects the different arrival time of the energy coming from the orchestra pit and the energy coming from the main

hall. Conversely, in the stalls and in the boxes the two sound energy amounts arrive at the receiver closer in time (straight lines).

The same analysis has been carried out in several further source-receiver pairs but for sake of brevity, only the most significant ones have been reported in the present section. The most evident results provided visually in Figures 4.13 and 4.14 are also shown in Table 4.6, along with the EDT/ $T_{30}$  values, the curvature parameter  $C$  and the  $T_{30}/T_{15}$  ratio. It is possible to notice that in those two particular source-receiver pairs the EDT/ $T_{30}$  ratio is around 0.9 and the  $C$  parameter is around 5 %, being consistent with the other analyses results.

Table 4.6: Different metrics describing coupled volumes in two specific source-receiver pairs: S2 (centre stage) - R22(boxes) and S3 (orchestra pit) - R24 (galley). The EDT/ $T_{30}$  ratio [137], the multi-decay Bayesian results [104, 155, 156], the curvature parameter  $C$  [150], and the  $T_{30}/T_{15}$  ratio are provided citebradley2005,bradley2010.

Source-receiver	Metrics	Simulated	Ref.
S2-R22	EDT/ $T_{30}$	0.92	[137]
	$T_1, T_2, H_1, H_2$	1.70, 0.85, 0.3, 0.82,	[104, 155, 156]
	$C$	4.7%	[150]
	$T_{30}/T_{15}$	1.02	[151, 152]
S3-R24	EDT/ $T_{30}$	0.94	[137]
	$T_1, T_2, H_1, H_2$	1.69, 0.85, 0.85, 0.35	[104, 155, 156]
	$C$	5%	[150]
	$T_{30}/T_{15}$	1.02	[151, 152]

## 4.2 A modern opera house

In the present section, a modern opera house is evaluated. Part of the work is taken from a previous study by the author that was undertaken for the design of an overhead array of reflectors for the stage house [112]. Compared to the hall analysed in the previous section, the presence of large balconies instead of the theatre boxes is one of the difference that contribute to ranke this theatre as “modern”, at least from a geometrical point of view. Moreover, the presence of the balconies allows to explore the particular acoustic conditions at listeners areas located below the overhangs that were largely investigated by scholars [108]. In this case study the attention is also focused on the effects at the listener caused by a sound reflectors array placed in stage tower.



Figure 4.15: *Duse theatre* (DUS) in Bologna.

The architecture under study is the *Duse theatre* (DUS), in Bologna. The building assumed the current aspect in 1940-42 (see Fig. 4.15). Actually, the hall is a refurbishment of an earlier theatre dating back to the 17<sup>th</sup> century. In the 1820s the main hall was expanded to its current size hosting up to two thousand people, distributed in three tiers of boxes. In 1940-42 the boxes were replaced by balconies and the chairs have progressively been refurbished using velvet instead of the original wood. At the same time the occupancy of the theatre was halved for safety reasons. According to the rankings provided in [136] and readapted to Italian Historical Opera Houses in [97], DUS is categorized as a “modern” theatre, due to its shape and acoustic features.

Since the stage tower has never been expanded from the original construction due to structural constraints, its current size in plan and its height are both small compared with modern stage towers and with the main hall (see Fig. 3.8). The main geometrical characteristics of the opera house at the present time are provided in Table 4.7. In comparison with TCB, this modern theatre have completely different proportions:

- 7,400 m<sup>3</sup> of main hall, i.e. the part of the theatre including all the listeners areas of the stalls and the balconies,
- 2,500 m<sup>3</sup> of stage house, still including the proscenium arch, the stage, wings, the sceneries, the grid.

The ratio between the seating capacity and the volume of the main hall is provided in Figure 4.16.

Table 4.7: Geometrical features of the *Duse theatre* in Bologna (DUS). The reference ID, the century of construction, the shape, the volume of the main hall ( $V_{hall}$ ), the volume of the stage house ( $V_{stage}$ ), the seating capacity (N), the number of balconies, the presence of the orchestra pit are provided [97, 136, 99, 137].

ID	Century	Shape	$V_{hall}$ ( $m^3$ )	$V_{stage}$ ( $m^3$ )	N	$V_{hall}/N$ ( $m^3/seat$ )	Balconies	Pit (y/n)
-	-	-			-		-	(y/n)
DUS	XX	Modern	7400	2500	1000	7.4	3	n

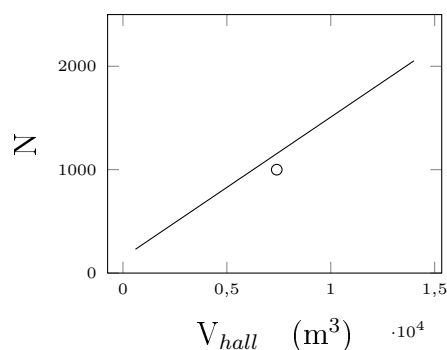


Figure 4.16: Relation between the seating capacity and the volume of the main hall. The plot of seating capacity as function of volume is taken from previous studies on opera houses [97].

The choice fell on DUS as interesting case study also because of the design and the installation of a set sound reflecting panels in the stage area. When symphonic music is played in an opera house the orchestra usually is located on the stage and the high amount of sound absorption of side drapes leads to a “dead” acoustic effect, undermining the sound strength at the listeners. Consequently the orchestral sound reaches the audience with low energy and fewer early reflections. Furthermore, it may be unbalanced in frequency due to sound absorption at mid-high frequencies in the stage tower [126]. Inadequate values of reverberation time and an unbalanced orchestral timbre – too loud strings, with respect to low woodwinds and brass – are some of the resulting effects reported in literature [109].

For these reasons in recent years an overhead array of wooden reflectors has been designed and built specifically for the stage of this theatre (see Fig. 4.17) [112, 83, 110]. The new system is intended to enhance the orchestral sound [157, 158] and to improve the mutual listening between the musicians and the conductor [159]. It should be noticed that at the same time most of the sound absorbing elements on the stage, i.e. curtains and drapes, are

removed when the wooden panels are installed on the stage. Moreover, the introduction of a system of stage risers and a backdrop are mounted along with the reflectors array, as shown in figure 4.17.

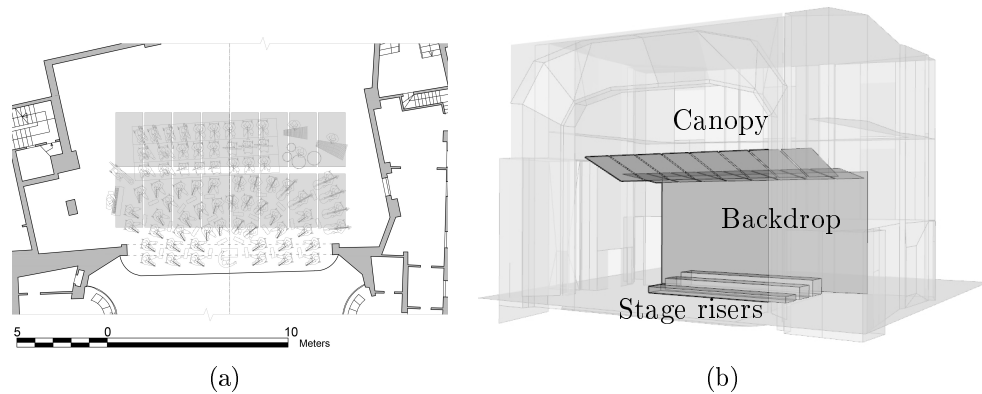


Figure 4.17: Configuration of the stage with the array of sound reflectors, the backdrop and the stage risers.

### 4.2.1 Acoustic measurements

Two campaigns of acoustic measurements were performed in DUS in unoccupied state, complying with ISO 3382-1 [128].

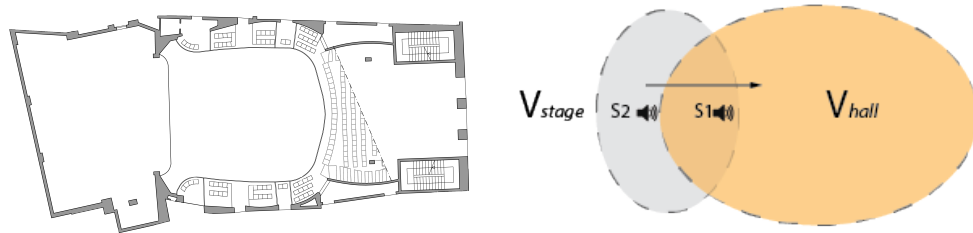


Figure 4.18: Scheme of the main coupling volumes in the modern opera house (DUS). View from the top of the strategic location of the sound sources used in the acoustic measurements of the halls.

1. The first campaign of measurements was performed with the configuration of the stage organised as during an opera, i.e. with the side drapes of the stage (*legs*) and the short curtains (*borders*) hung above the stage. These measurements were carried out before the design of the overhead reflecting panels.

2. The second campaign of measurements was done after the design and the installation of the sound reflectors array, i.e. with the configuration of the stage organised as during a symphonic concert. As already mentioned, the installation of the reflecting system is intended to be complemented by the removal of most of the absorbing curtains from the stage and the introduction of stage risers for musicians.

Since the study of DUS is aimed to evaluate the effects at the listeners of the edge diffraction caused by the reflectors, from here onwards the analysis of the measurements results, the calibration of the model and all the other steps are referred to the second configuration. It should be noted that the removal of part of the sound absorbing elements on the stage and the installation of the sound reflecting arrays affects the coupling effects between  $V_{stage}$  and  $V_{hall}$  (see Fig. 4.18). In the configuration here analysed the two volumes act more as one, as it has been previously demonstrated by the author [112].

Measurements were carried out using the following equipment:

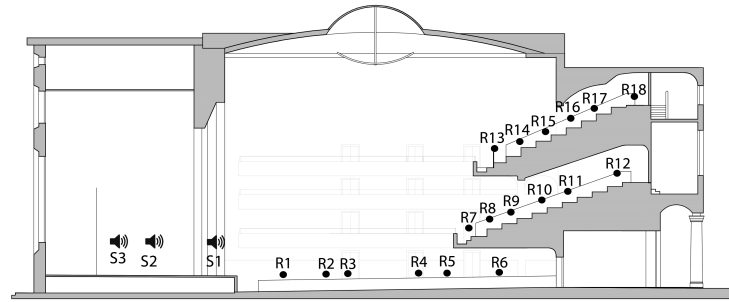
- high-SPL dodecahedron as omnidirectional sound source [139];
- four Bruel & Kjaer 4190 half inch microphones as monoaural receivers;
- RME Fireface 800 at 24 bit / 48 kHz;
- laptop and custom software providing exponential sine sweep (ESS) 128K length as signal emitted.

Table 4.8: Measurements results in DUS. Reverberation time ( $T_{30,M}$ ), early decay time ( $EDT_M$ ), sound clarity referred to 80 ms ( $C_{80,3}$ ), centre time ( $T_{S,3}$ ) measured values are provided [128], along with the Schroeder frequency ( $f_c$ ) and the number of sound source and receivers points. Values signed with “M” indicates the average over 500-1000 Hz, with “3” the average over 500-1000-2000 Hz. The type refers to the rankings provided in [136] and readapted to Italian historical opera houses in [97].

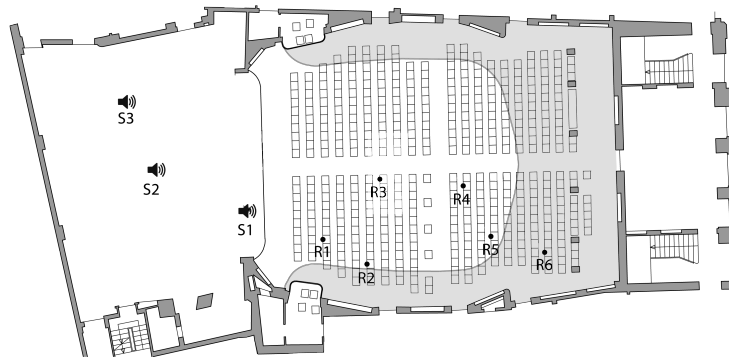
ID	Type	$T_{30,M}$ (s)	$EDT_M$ (s)	$C_{80,3}$ (dB)	$T_{S,3}$ (ms)	$f_c$ (Hz)	Sources/Receivers
TCB	“modern”	1.57	1.40	2.3	90	25	2/18

Three different locations on the stage were chosen as sound source positions in order to take into account both the asymmetry of the stage and the distinct location of the three main orchestra sections:

- S1 in the position corresponding to first violins section (below the proscenium arch),



(a) Longitudinal section



(b) Stalls

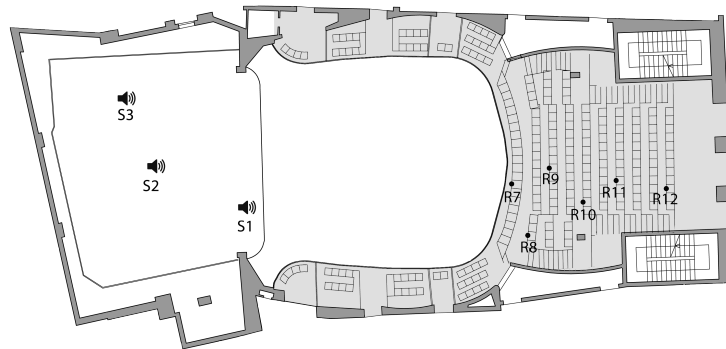
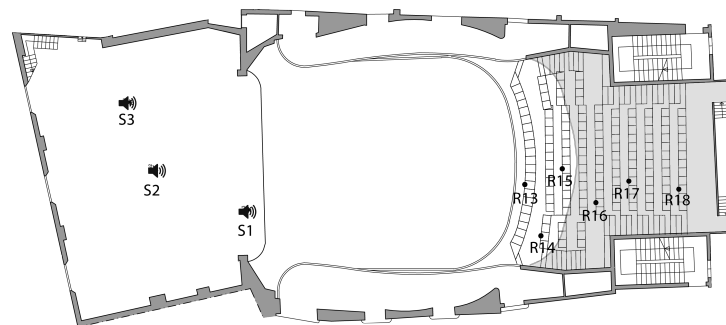
(c) 1<sup>st</sup> balcony(d) 1<sup>st</sup> balcony

Figure 4.19: Positions of sound sources (S) and receivers (R) selected in the acoustic measurements campaign in DUS. Gray areas correspond to audience regions below the overhangs of the upper balconies.

- S2 in the position corresponding to woodwinds (centre of the stage),
- S3 in the position corresponding to percussion (back of the stage).

Eighteen receivers positions were chosen in the audience area, spread throughout the stalls and the two galleries. Most of the receivers positions are below the overhangs of the balconies (gray areas in Fig. 4.19). Figure 4.19 shows the positions of sound sources and receivers selected for the acoustic survey of the opera house.

The main objective room criteria collected from measured IRs are presented:

- in Table 4.8 in terms of mean values averaged over the mid frequencies;
- in Figure 4.20 in terms of  $C_{80,3}$ ,  $EDT_M$ , and  $V_{hall}$  values compared to previous studies on opera houses,
- in Figure 4.21 in terms of  $T_{30}$ , EDT,  $C_{80}$ ,  $T_S$  in octave bands along with the standard deviations.

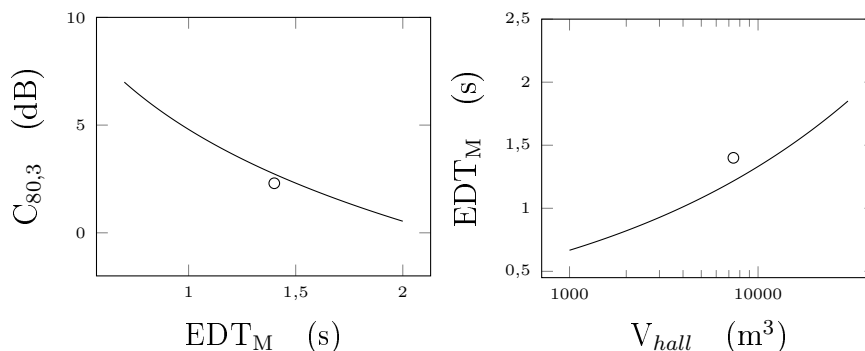


Figure 4.20: Relation between  $C_{80,3}$ ,  $EDT_M$ , and  $V_{hall}$  in DUS. The curves are referred to the “modern” group according to previous studies on opera houses [97].

As already shown in TCB case, the stage tower of opera houses is a system composed of several elements, including trusses, ropes, and sceneries. The absorption characteristics of the side drapes on the stage [142] can significantly vary depending on their actual position. Therefore, in order to quantify the equivalent absorption area of the most absorbing objects in the stage tower, measurements were also performed without drapes and curtains, placing receivers on the stage [160].

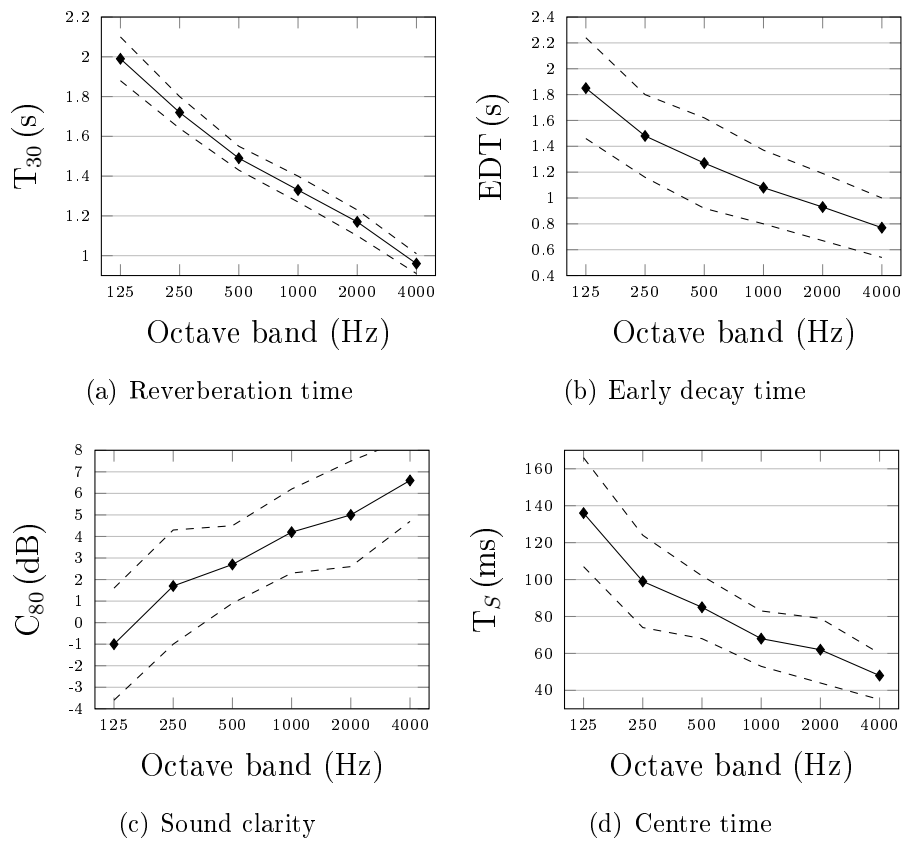


Figure 4.21: Measured  $T_{30}$ , EDT,  $C_{80}$ ,  $T_s$  values in DUS in octave bands with relative standard deviations (dashed lines). Mean values are averaged over all the source-receivers pairs, shown in Figure 4.19.

### 4.2.2 FDTD calibration

Concerning the calibration of the 3D model, as a rule of thumb the same method applied in TCB opera house and described in the previous chapter is employed also in DUS opera house. The difference is that in the present case the construction of two virtual models had been necessary during the work described in [112], but only the model with the sound reflectors will be discussed in this section. The results of the calibration process are reported in Figure 4.24 in terms of comparison between measured and simulated main criteria in octave bands.

#### 3D modeling

A first 3D model was made in the configuration without the sound reflectors on the stage and with the common amount of sound absorbing materials in the stage house. After the GA++ calibration of this first model, a second model was built according to the optimized, designed and then actually installed array of suspended panels. The second model involves a reduction of

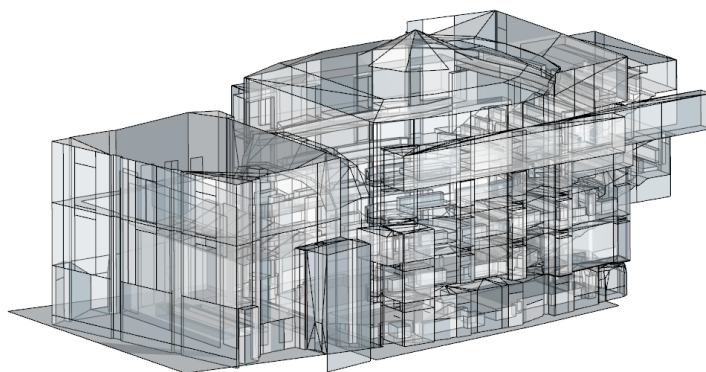


Figure 4.22: View of *Duse Theatre*'s CAD model as shown in the modeling software [145].

velvet drapes on the stage along with the presence of the overhead reflectors. Both the models - corresponding to the distinct configurations previously analysed in DUS opera house - have been calibrated with the FDTD model as well.

For the sake of brevity, thorough description and analysis of wave-based process are here described only for the second model, exploiting the presence of the sound reflectors to explore the simulation performance in computing the diffraction from the edges (see Fig. 4.23). Nevertheless, the availability of both the set of data allows further investigation able to compare the situation before and after the installation of the panels on the stage.

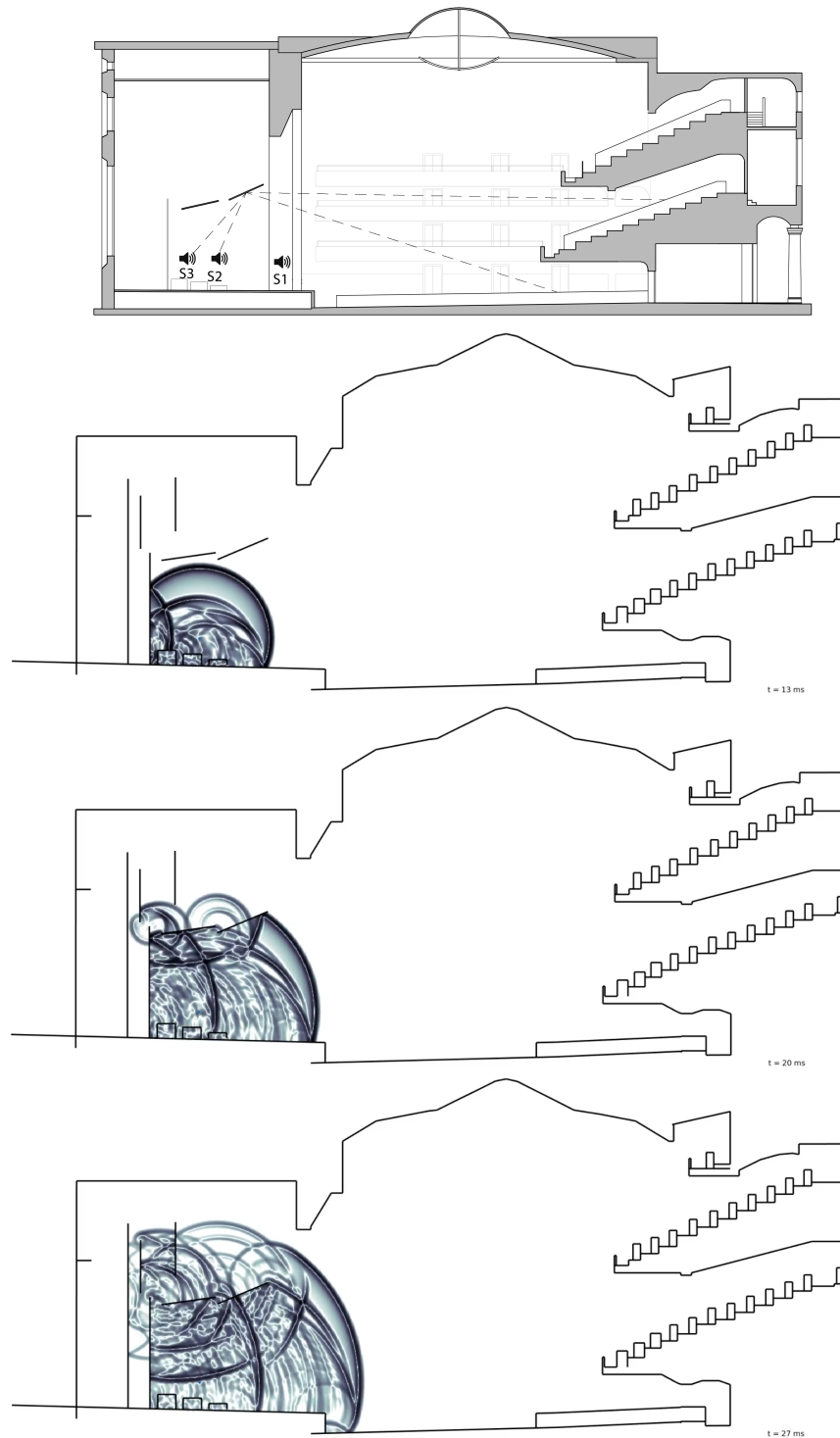


Figure 4.23: Longitudinal section view in DUS opera house. Qualitative representation of the ray-traced coverage by sound reflectors (top) and demonstration of diffraction at different time instances using a 2D FDTD simulation along y-z slice of model (last three images).

The geometrical 3D virtual model of the hall was built with SketchUp software following the same recommendations applied in TCB opera house [161, 63]. Therefore, much effort was employed to avoid as many overlapping surfaces as possible, to discretize the curved surfaces, and to properly approximate the details of small objects. The final model consists of 3800 flat surfaces for a total surface area of about 7650 m<sup>2</sup> and a total volume of 9900 m<sup>3</sup> (see Fig. 4.22).

### Simulation setup

Concerning the simulation setup employed in DUS, it was possible to use the same variables used in TCB (see Table 4.3). Consequently, the simulations were performed with  $f_{max}$  equal to 4 kHz. The only slight difference, but not properly measurable, is the computational time in terms of runtime hours per second of output, i.e. second of the simulated impulse response. This is probably due to a smaller volume (9900 m<sup>3</sup> vs 25000 m<sup>3</sup>). However, it is important to remark that the computational time is never affected by a single factor. Furthermore, computational time is also affected by the fraction of grid points that are boundary nodes (points next to surfaces) and thus require additional operations for general impedance boundary conditions [19]. This is one of difficulties while handling non-trivial geometries as the articulated system of a 3D virtual opera house. In the simulation setup the impulse response length was set equal to 3 s to be sure to include even the higher values of reverberation time at lower frequencies.

At this point, the choice of the acoustic indicators selected as the targets of the calibration is the same employed in the TCB calibration. Therefore the indexes considered as suited to describe the acoustics of DUS are  $T_{30}$ , EDT,  $C_{80}$ ,  $T_S$  [132, 128, 146]. The choice was to calibrated the model using two out of three sound source positions used in the measurements campaign, the first one on violins position (S1 below the proscenium arch) and the second one in the woodwinds position (S2 in the centre stage). Table 4.9 summarizes the calibration results in terms of main room criteria ( $T_{30,M}$ ,  $EDT_M$ ,  $C_{80,M}$ ,  $T_{S,M}$ ) at mid frequencies (500 – 1000 Hz). In line with the state-of-the-art procedure, the calibration of the 3D model was achieved when the differences between simulated and measured values were within the Just Noticeable Differences (JND) defined by the standard [128], except for  $T_{30,M}$  and  $EDT_M$  for which twice the JND was considered as the reference point during the calibration process, according to recent remarks concerning the uncertainty behind those room criteria [64]. Therefore at mid frequencies the tolerance ranges were the following:

- 10% in  $T_{30,M}$  and  $EDT_M$  evaluation,

- 1 dB in  $C_{80,M}$  evaluation,
- 10 ms in  $T_{S,M}$  evaluation.

With regard to this calibration choice, at the end of the iterative process the 83% of the simulated mean values at mid frequencies are within the tolerance range chosen (see Table 4.9).

To visualize the behaviour of those room criteria as functions of the frequency, Figure 4.21 reports the results of the achieved calibration in terms of EDT and  $T_S$ , measured and simulated, in octave bands. The choice of such room criteria is due to the deviation of resulting values throughout the space, as already explained in case of TCB [132]. The values displayed in the graphs are referred to the sound source in S2 position, the centre of the stage, (see Fig. 4.19) and the resulting values are shown averaged over the three receivers areas (stalls, 1<sup>st</sup> and 2<sup>nd</sup> balcony), as a function of the frequency. Since calibrating in each audience area and in octave bands is considerably challenging, the author chose to double the tolerance of the centre time to twice the JND (20 ms instead of 10 ms). At the end of this calibration step, 89% of the values were between the tolerance range assessed in this work.

Table 4.9: Measured and simulated room criteria in DUS. Results at medium frequencies (500-1000 Hz) for center stage source position (S2), averaged over receivers in stalls, 1<sup>st</sup> and 2<sup>nd</sup> balcony. The difference between mean measured and simulated values are reported between brackets. See text for the tolerance range adopted for each metrics.

Room criteria	Measured	Simulated (Diff.)	Receivers
$T_{30,M}$ (s)	1.59	1.54 (+3.1%)	stalls
	1.53	1.44 (+5.9%)	1 <sup>st</sup> balcony
	1.59	1.51 (+5.0%)	2 <sup>nd</sup> balcony
EDT <sub>M</sub> (s)	1.54	1.58 (-2.6%)	stalls
	1.21	1.06 (+12.1%)	1 <sup>st</sup> balcony
	1.42	1.29 (+9.2%)	2 <sup>nd</sup> balcony
$C_{80,M}$ (dB)	2.1	2.2 (-0.1)	stalls
	3.4	4.4 (-1.0)	1 <sup>st</sup> balcony
	2.5	3.5 (-1.0)	2 <sup>nd</sup> balcony
$T_{S,M}$ (ms)	93	91 (+2)	stalls
	79	66 (+13)	1 <sup>st</sup> balcony
	90	80 (+10)	2 <sup>nd</sup> balcony

With regard to material properties, the management of the layers used in the 3D model was done with the aim to reduce the uncertainty by employ-

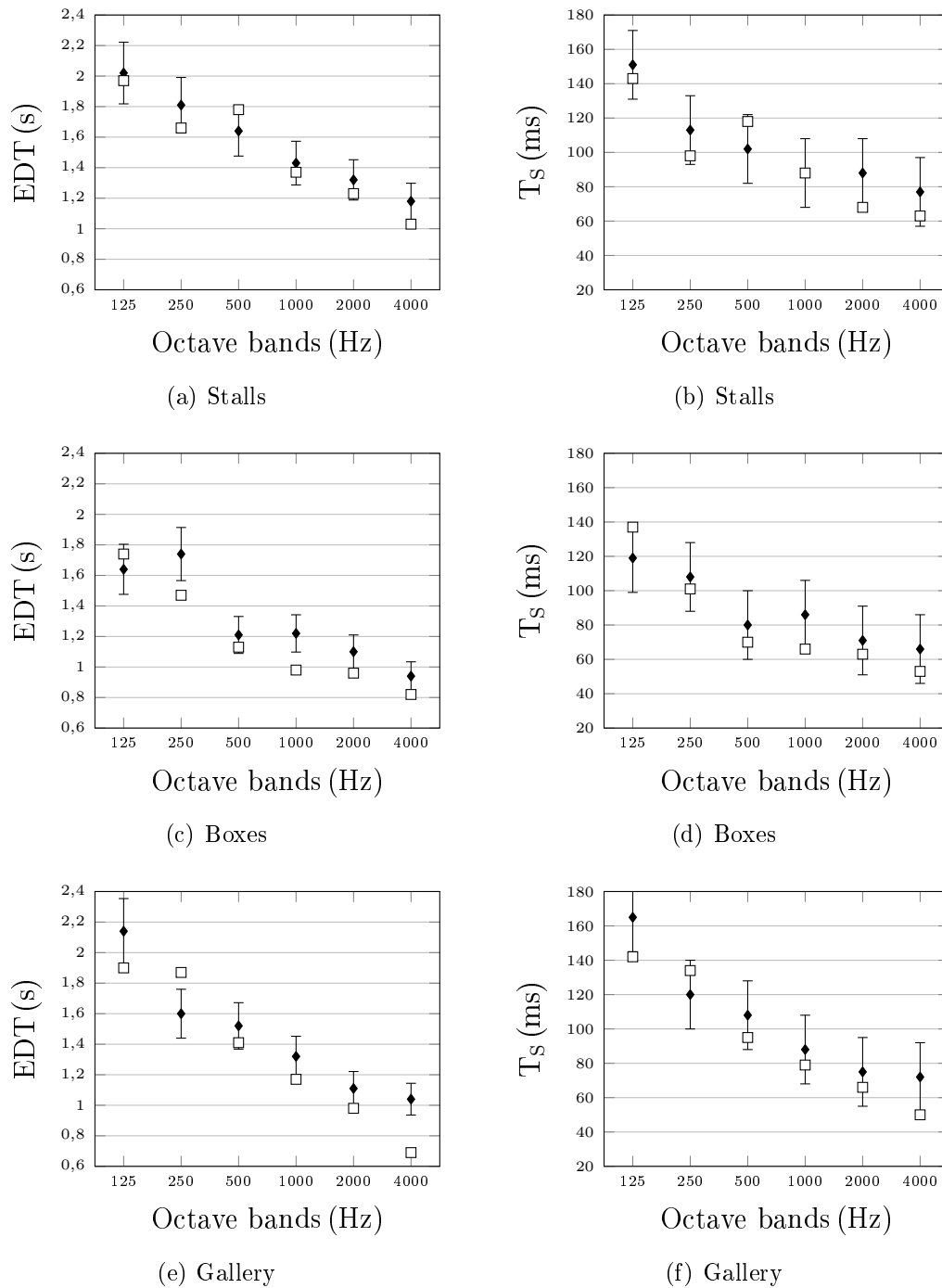


Figure 4.24: DUS calibration: measured (black) and simulated (white) EDT and  $T_S$  values in octave bands. Mean values are referred to the sound source placed in the centre of the stage (see Fig. 4.19) and to the distinct audience areas: stalls, 1<sup>st</sup> gallery, 2<sup>nd</sup> gallery. The error bars are referred to the tolerance range chosen for the calibration process.

ing less layers than the actual materials present in the theatre [64]. Hence, similar materials were joined together in the macro-groups provided in Table 4.10. The same Table provides the outcoming values of absorption coefficients - from which the complex acoustic impedances are derived and given as input data in FDTD model - obtained at the end of the FDTD simulation. The normalised LRC coefficients for the boundary complex impedances are provided in the first part of the Appendix. The difference found with the corresponding values used in the GA++ model are provided in the second part of the Appendix.

Table 4.10: Materials involved in TCB simulations. The energy-based parameters  $\alpha$  represent the starting point in the backward process to obtain the acoustic impedances  $\zeta$  for the FDTD simulation. The macro-layers used in the present work divide the materials according to the type of the surface and the role within the opera house, e.g. the plaster related to “stage house” is not handled as the plaster in the main hall. References are provided for most of the absorption coefficients. Normalised LRC (inductance, resistance, capacitance) coefficients employed as input data in FDTD simulations to approximate boundary admittances are provided in Appendix.

	Energy-based parameters $\alpha$						Ref.
	125 Hz	250 Hz	500 Hz	1 kHz	2 kHz	4 kHz	
Marble	0.01	0.01	0.02	0.02	0.03	0.03	[121]
Plaster (hall)	0.01	0.03	0.03	0.04	0.06	0.06	[121]
Stage house	0.12	0.15	0.15	0.18	0.18	0.18	Estimated
Stage grid	0.15	0.15	0.25	0.40	0.50	0.50	[126]
Wood	0.18	0.18	0.12	0.07	0.07	0.07	[162]
Velvet drapes	0.20	0.35	0.35	0.45	0.50	0.50	[125]
Seats (stalls)	0.35	0.32	0.40	0.50	0.60	0.65	[144]
Seats (balconies)	0.45	0.35	0.35	0.40	0.42	0.42	[144]
Carpet	0.04	0.07	0.15	0.20	0.25	0.30	[125]
Sound reflectors	0.08	0.05	0.03	0.03	0.02	0.02	[25]

Once calibrated the 3D model of DUS opera house, also in this case the resulting virtual environment allows specific further analysis. Given the availability of the double configuration of the model (with and without the sound reflectors on the stage), it was possible to assess the consequence of the overhead array of panels on the acoustic coupling effects through the analysis of simulated impulse responses. In order to present the results, briefly the method followed to design and built the array of reflectors is hereafter introduced.

### 4.2.3 Sound reflectors

Reflectors are some devices specifically designed to enhance the early sound, which plays a fundamental role in affecting sound perception. In DUS case, a panel array of overhead reflectors was designed and installed to make the acoustic condition of an opera house suited to the symphonic music. It has been proved that a system of more components separated from each other by gaps is more effective in enhancing the way we perceive sound rather than an entire continuous surface. In fact, with no open area above the zone the sound comes from, strong directional reflections may cause the comb filtering effect due to specular reflections with the same frequency content but delayed in time [83]. An array solution allows to avoid these undesired effects thanks to the gaps among the panels. Since the amount of open area and thus the relative density of panels, are properties able to optimize reflectors performance, we have to investigate about their precise characteristics.

During the design process of the suspended panels system, it was useful to investigate the possible variables to change both during the evaluation of the single surface and dealing with the total array [112]. Single panel features to be settled are:

- size: maybe the most important trait to define because the two main dimensions of the element determine the wavelength range concerned by the specular reflection and the wavelength range concerned by diffraction;
- shape: flat or bowed reflectors lead to different diffusive effects and thus distinct losses of reflected energy compared with the specular reflection coming from an ideal flat infinite surface;
- tilt: its purpose is to guide in a better way the useful sound to the audience area;
- material: it is important that absorption coefficient are quite low in every octave band, especially at high frequencies;
- thickness: it is a feature linked with the resonance frequency of the panel and thus with its vibration mode;
- weight per square meter: it is recommended to select a light panel (usually around  $5 \text{ kg/m}^2$  [100]).

Moreover, putting more elements together in a panels array, the attention should be focused on:

- the relative density  $\mu_{panels} = \frac{S_{panels}}{S_{tot}}$  where  $S_{panels}$  is the area of all the reflectors and  $S_{tot}$  is the total area covered by the array;
- the number of panels  $N_{panels}$ ;
- the height of installation;
- the position in plan.

With reference to the edge diffraction theory described in Sec. 2.3.3, the attenuation due to diffraction has the following expression:

$$\Delta L_{diff} = 10 \log K = 10 \log K_1 \cdot K_2 \quad (\text{dB}) \quad (4.4)$$

where

- $K$  is a quantity less than 1 that reduces the energy reflected from an ideal infinite surface, which is taken as reference point (similarly to the case of a single panel);
- $K_1$  and  $K_2$  respectively correspond to  $x$  direction and  $y$  direction sections of reflectors system.

In view of the difference between high and low frequencies, Rindel proposed this approximation:

$$K = \mu_{panels}^2 \quad \text{for } f \leq f_g \quad (4.5)$$

where  $f_g$  is the limiting frequency [83]. The expression 4.5 explains the two distinct kinds of phenomena depending on the frequency assessed:

- above  $f_g$ , the contribution of the single reflector is relevant because at high frequencies there are strong local variations whether the sound hits the surface or not;
- below  $f_g$ , instead, the role played by the single component becomes less relevant because at low frequencies what is important is just the relative density of the whole array system.

To summarize the resulting choices of the design process:

- the dimensions of each panel were chosen as 3 x 1.5 m, allowing a wide-frequency diffraction effect [157, 163],
- given the size of the single panel, two rows of 8 panels were proposed in order to cover the orchestra area maintaining a coverage of about 80%, purposely leaving half of the first violins not covered (see fig. 4.17),

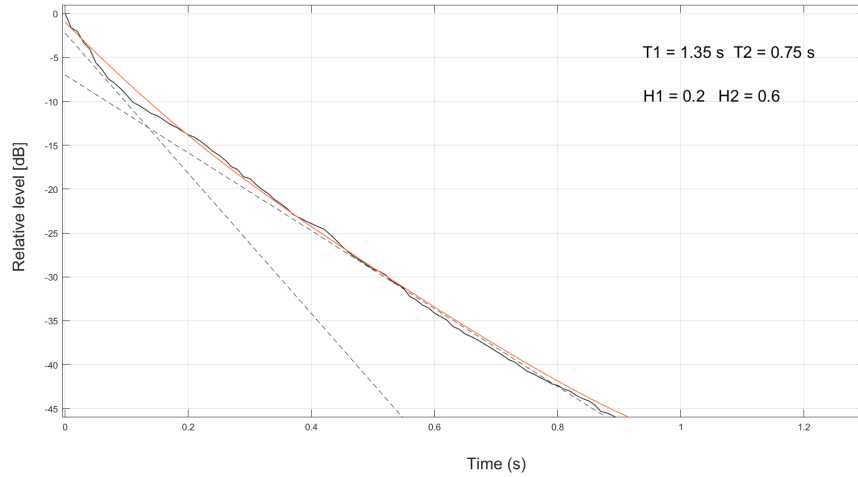
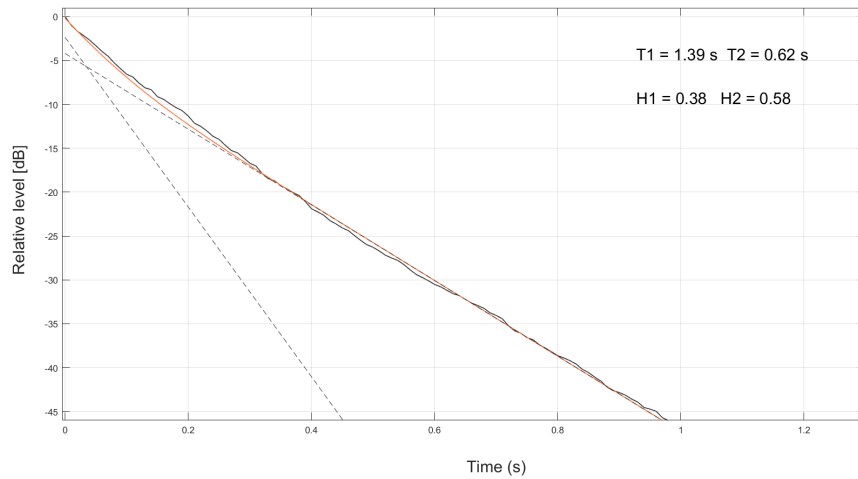
(a) Without reflectors: S2 (centre stage) - R10 (1<sup>st</sup> gallery)(b) With reflectors: S2 (centre stage) - R10 (1<sup>st</sup> gallery)

Figure 4.25: Multi-decay analysis of simulated IRs in DUS at 1000 Hz [104]. Comparison between the same source-receiver pair in configuration without (top) and with reflectors (bottom). The position of the sound source is in the centre of the stage (S2 in Fig. 4.19) and the receiver's position is in the first balcony. See text for the explanation of the quantities.

- the overall height of the system was set equal to 7 meters above the stage floor to optimize the support among musicians and a proper blend of the orchestral sections [112].

According to these geometrical choices, it is possible to state that the

design of the sound reflectors in DUS was made in accordance with the best results from Rindel experiments [83]. Given the dimensions of the chosen panels and the hall size, the Fresnel-Kirchoff approximation is suitable for the medium–high frequencies for all the seats of the case study’s audience area [83]. The outcoming effects of sound reflectors have already been shown from a qualitative point of view in Figure 4.23.

From a quantitative point of view a multi-decay Bayesian analysis on the simulated impulse responses was helpful to detect some effects caused by the reflectors. Figure 4.25 offers a comparison between the same source-receiver pair in the two configurations available, with and without the reflectors on the stage. The sound source position is in the centre of the stage (S2) and the receiver is in the first balcony (R10), below the overhang of the second balcony (see Fig. 4.19). At the top of the figure there is an evident double-slope decay as the result of a Bayesian analysis. It corresponds to the configuration with all the absorbing elements on the stage and without the suspended panels. This kind double-slope decay is typical of an acoustic condition suited to opera performance, i.e. a perceived reverberance (EDT) lower than the actual reverberation time ( $T_{30}$ ) [112, 102]. Moreover, a  $EDT/T_{30}$  ratio lower than 1 is also a trait of listener position below the overhang balconies. At the bottom of the same figure there is the result of the same Bayesian analysis on the corresponding simulated impulse response when the reflectors are on the stage and part of the velvet drapes are removed. It is possible to notice a significant reduction of the double-slope effect and that the intersection of the two slopes corresponds to around - 5 dB. Theoretically a Bayesian analysis of this kind [104] should be performed removing the first 5 dB of the decay curve. In order to better visualize the phenomenon and the differences, results are reported from 0 dB. Given that the intersection corresponds to -5 dB, it means that basically the main effects of sound reflectors in the first gallery is a reduction of the double-slope decay and an increase of EDT values.

The same analysis has been carried out in several further source-receiver pairs but for sake of brevity only the most significant ones have been reported in Figure 4.25. For the explanation of the outcoming indicators, T and H, see section 4.1.3. Indeed, the most evident consequences caused by the sound reflectors on the stage occur in the audience areas of the stalls and the first balcony, as it can be seen in Figure 4.23. This is mainly due to the tilt and the location of the overhead panels system [112]. In the second balcony, where the perceived reverberance is quite high even in the configuration without the sound reflectors [164], the reverberant field is expected to enhance mostly because of the removal of the sound absorbing drapes on the stage.

The peculiarity of seats below the overhang balconies have been investi-

---

gated by Barron [108]. Their particularly dry acoustic condition make them suited to the opera and less suited for symphonic music. The multi-decay Bayesian analysis conducted on the simulated impulse response allow to see how the system of panels on the stage could increase the EDT values, as preferred requirement for symphonic music.



# Chapter 5

## Elliptic performance space

The third case study assessed in the present thesis is an elliptical-domed concert hall, St Cecilia's Hall, in Edinburgh. This particular room represents a great opportunity to investigate the performances of the FDTD platform to model the complex effects caused by curved architectures and echo flutter phenomena [117]. Among the acoustic consequences of elliptic shapes, there is the sound focusing in certain areas of the room. Moreover, the moderate volume of the hall allows a full wave-based approach up to the highest frequencies of interest, compared to the lower cut-off frequencies allowed in the opera houses previously analysed. Part of the present chapter was presented in 2019 at the International Symposium on Room Acoustics [165].

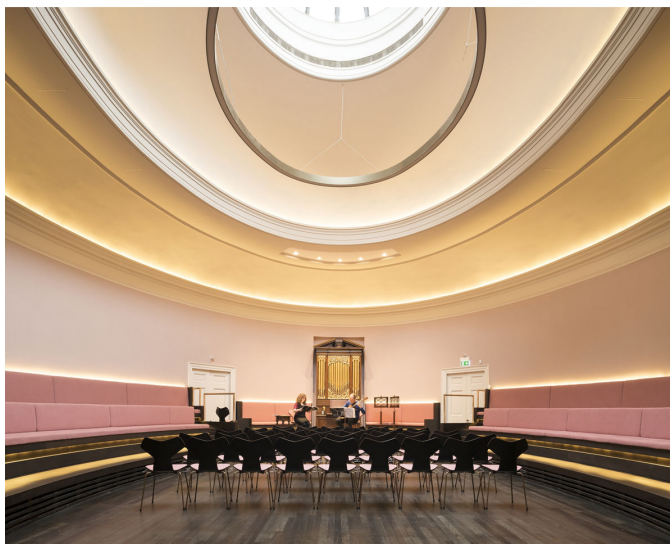


Figure 5.1: View of St Cecilia's hall, Edinburgh (UK).

## 5.1 An elliptic multipurpose hall

St Cecilia’s Hall (STC), located within the Music Museum in Edinburgh (UK), is one of the oldest purpose-built concert halls in Scotland. This Georgian venue was originally built by the Edinburgh Musical Society in 1762 [166]. All the building in which the hall is was designed by the young architect Robert Mylne (1733-1811) for the Edinburgh Musical Society, a group of musicians who met regularly to rehearse. The Society also organised weekly formal concerts engaging professional directors, singers, and instrumentalists from home and abroad. By the 1750s the Society had become sufficiently ambitious and wanted to build a prestigious concert room of its own, and this building is the result [166]. The current concert hall is actually a reconstruction. When the University of Edinburgh took ownership of the building, in 1959, this room was rectangular and had Victorian windows on the East Wall. Eighteenth-century sources, however, show that the room was originally elliptic in shape, and without windows, natural light coming solely through the oval dome, which also supplied ventilation [166]. Successively, the room was refurbished returning to its original shape and use.

Table 5.1: Geometrical features of St Cecilia’s Hall (STC) in Edinburgh. The reference ID, the century of construction, the shape, the total volume of the hall (V), the seating capacity (N), the presence of the orchestra pit are provided [97, 136, 99, 137].

ID	Century	Shape	V (m <sup>3</sup> )	N	V/N (m <sup>3</sup> /seat)	Pit (y/n)
STC	XVIII	Elliptic	950	200	4.8	n

The hall is currently used for different purposes: it hosts concerts, conferences, events, and theatre performances. With a volume of around 950 m<sup>3</sup>, this event venue has a seating capacity of approximately 200 people. This number is referred to the sum of the fixed seats ( $\sim 120$ ) at the lateral curved walls and the movable seats ( $\sim 80$ ) at the centre of the oval room (see Fig. 5.1). The main characteristics of this hall is the combination of an ellipsoidal shape with a double dome as ceiling that makes the geometry quite entirely curved. This peculiar shape affects the sound field behaviour, contributing to non-diffuse acoustical characteristics. Similarly to the data reported for the previous case studies, Table 5.1 provides the main features of STC. It should be noticed that the column referred to the “Type”, corresponding to the rankings provided in [136], is not available because of the moderate size of the hall. In order to compare the characteristics of STC with the performance spaces previously analysed, the relation between the seating capacity,

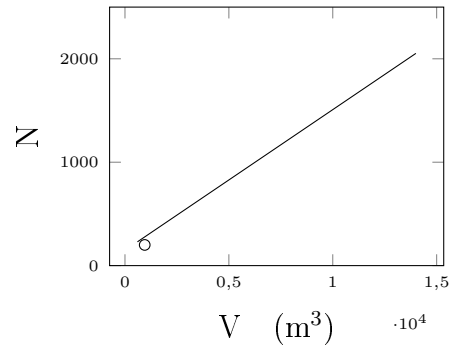


Figure 5.2: Relation between the seating capacity,  $N$ , and the volume of the hall,  $V$ . The plot of seating capacity as function of volume is taken from previous studies on opera houses [97] and it is here reported for a comparison with cases previously analysed.

$N$ , and the volume,  $V$ , is still provided with the same regression line of the other cases (see Fig. 5.2).

### 5.1.1 Acoustic measurements

In April 2019 St Cecilia's hall was surveyed with a campaign of acoustic measurements. According to ISO 3382-1 the measurements was done in unoccupied state, except for the operators. Having the chance to remove all the movable seats in the central area, the choice was to investigate the sound field characteristics without the seats. It should be noticed that this configuration represents the usual state during theatre performances. The configuration of the hall during the measurements is shown in Figure 5.3.



Figure 5.3: Configuration without seats during the acoustic measurements in STC.

Compared to the articulated geometries of the previous case studies, STC,

at least in a plan view, may be represented with a schematic single volume in which both the sound sources and the receivers are (see Fig. 5.4).

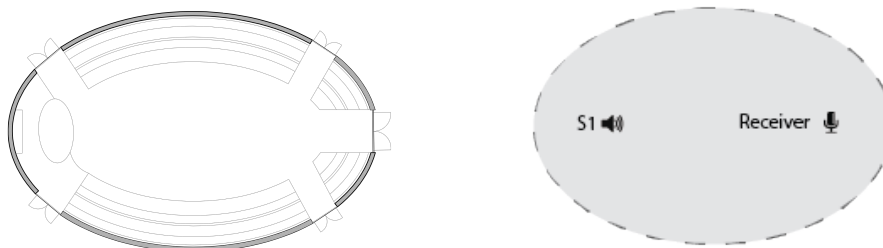


Figure 5.4: Scheme of the single acoustic volume in STC (view from the top).

The measurements were performed with a Matlab code developed by the research team of the University of Edinburgh. An omnidirectional dodecahedron and a monoaural microphone were used to acquire the impulse response.

The presence of a wooden riser, a sort of tiny “stage”, was exploited to select the first sound source position. It corresponds to the position of a lecturer during a conference or otherwise of a musician during a concert. Therefore this first position (S1) was chosen to represent an actual sound source among the possibilities of the multipurpose STC hall. Instead, the second location in the middle of the hall (S2) for the sound source was selected mostly to detect wave phenomena such as flutter echoes. Moreover, in the theatre performance configuration (without the central seats), the second sound source location is intended to represent a standing theatre player. To summarize, the two positions chosen for the sound source are:

- on the wooden tiny stage (S1)
- in the middle of the hall, moved at one side (S2).

The receivers were spread throughout the hall, both in the central area below the double dome and among the lateral seats. The layout of sound sources and receivers is shown in Figure 5.5. Probably, the best position for the sound source to detect the strong flutter echo, subjectively perceivable, that occurs between the long curved walls, would have been among the lateral seats rows. Nevertheless, that position among the fixed seats would barely be used as a musician position. However, some of the receivers (R4, R5) were actually placed in location where flutter echoes were perceivable to investigate whether the simulation model would have been able to render the same effect. The main results of IRs acquisition are provided:

- in Table 5.2 in terms of mean values averaged over the mid frequencies;

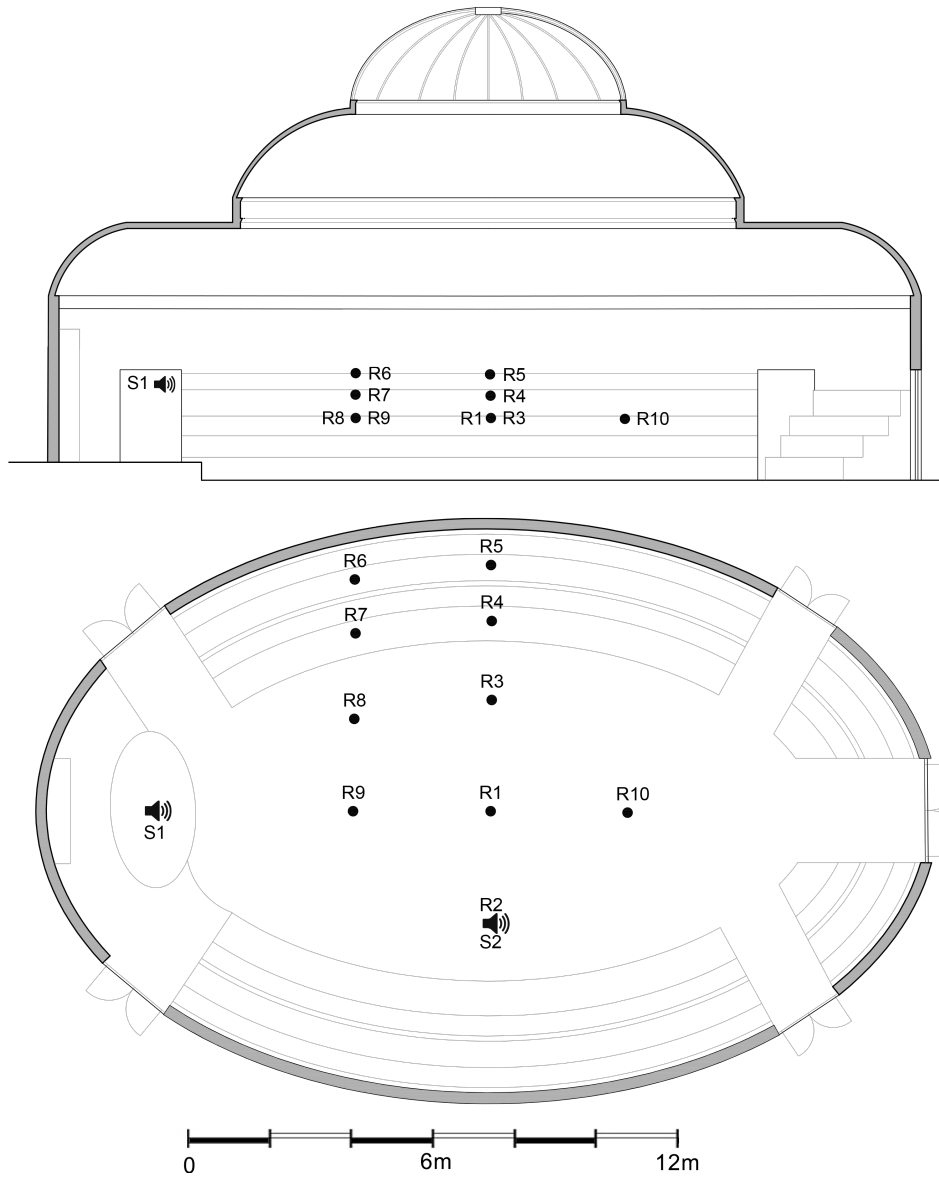


Figure 5.5: Positions of sound sources (S) and receivers (R) selected in the acoustic measurements campaign in STC.

Table 5.2: Measurements results in STC. Reverberation time ( $T_{30,M}$ ), early decay time ( $EDT_M$ ), sound clarity referred to 80 ms ( $C_{80,3}$ ), centre time ( $T_{S,3}$ ) measured values are provided [128], along with the Schroeder frequency ( $f_c$ ) and the number of sound source and receivers points. Values signed with “M” indicates the average over 500-1000 Hz, with “3” the average over 500-1000-2000 Hz. The column referred to the ‘Type’, corresponding to the rankings provided in [136], is not available to the moderate size of the hall.

ID	Type	$T_{30,M}$ (s)	$EDT_M$ (s)	$C_{80,3}$ (dB)	$T_{S,3}$ (ms)	$f_c$ (Hz)	Sources/Receivers
STC	–	1.33	1.28	1.5	86	75	2/10

- in Figure 5.9 in terms of  $T_{30}$ , EDT,  $C_{80}$ ,  $T_S$  in octave bands along with the standard deviations.

With reference to the measured reverberation time mean values provided at the top left corner on Figure 5.9, some remarks can be made. Among the octave bands considered, the lowest  $T_{30}$  value turns to be at 125 Hz. This is not a common acoustic feature in concert halls or in multipurpose halls. By a first observation on the materials constituting STC, this peculiarity is probably connected with the great amount of wooden elements in the hall (the floor, the tiny stage, part of the seats). Moreover, the upper part of the double dome is made up of thin linings and glass. Generally, wooden elements and thin glass panels have quite low sound absorbing properties at mid-high frequencies but they give a significant contribution to the overall equivalent absorption area at low frequencies.

A further consideration on measured  $T_{30}$  values is related to the standard deviation values. Comparing Figure 5.9 with the equivalent data provided for TCB and DUS (Figs. 4.9 and 4.21) it is possible to see that, on average, the standard deviation of reverberation time values is higher in STC. Indeed, this can be justified by the moderate number of receivers employed during the acoustic measurements in STC (10 instead of 26 or 18). Nevertheless, given the gaussian properties of the energy decay between - 5 dB and - 35 dB,  $T_{30}$  values are usually quite even throughout the space. For this reason,  $T_{30}$  is considered as a trait of the hall according to the consolidated literature. In STC case, the sound focusing effects caused by the curved lateral walls may be the responsible for higher spatial variation of reverberation time values.

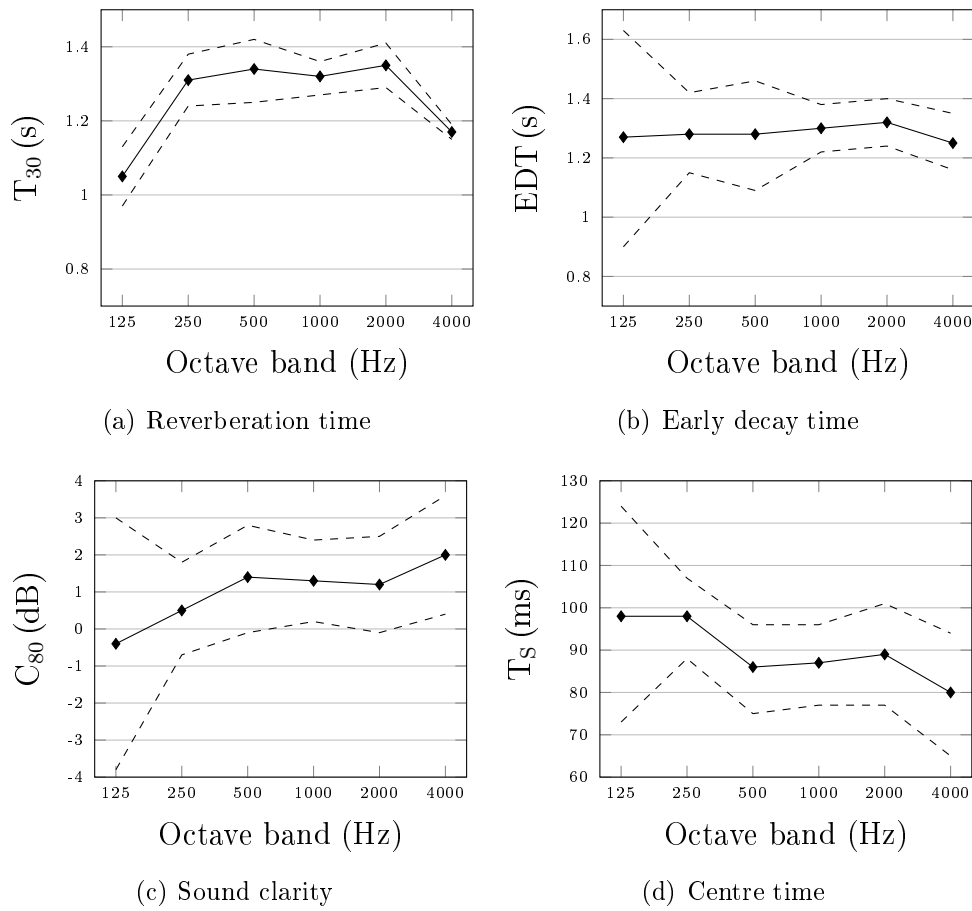


Figure 5.6: Measured  $T_{30}$ , EDT,  $C_{80}$ ,  $T_s$  values in STC in octave bands with relative standard deviations (dashed lines). Mean values are averaged over all the source-receivers pairs, shown in figure 5.5.

## 5.1.2 FDTD calibration

### 3D modeling

Compared to the previous case studies, the 3D modeling phase of the virtual room has been handled in a slightly different way. While so far the common rule of thumb - taken from GA++ state-of-the-art - to omit the modeling of all the details below 0.34 meters was followed, in this case the overall shape of the hall has been modeled with higher fidelity. Indeed, this choice is closely related to the particular shape of the hall. In fact, GA++ guidelines would suggest a certain degree of discretization of curved surfaces into planar surfaces. Nevertheless, the author chose to increase the fidelity of the model compared to the real shape, since FDTD simulations do not necessarily require a low level of discretization. Therefore, for the discretization of the 3D virtual models a high level of accuracy was chosen in order to make more reliable the peculiar trait of the hall. The result is a model made up of 18000 surfaces, as it is shown in Figure 5.7.

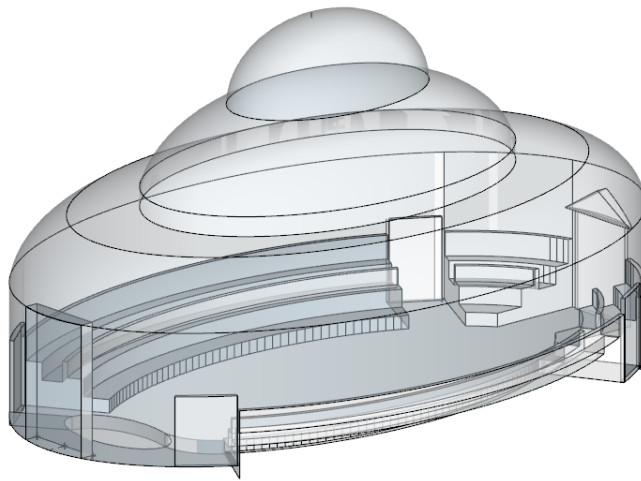


Figure 5.7: View of the 3D virtual model of St Cecilia's hall [145].

In addition, an intuitive visualization of the wave simulation run within STC to detect focusing effects and flutter echoes is provided in Fig. 5.8, considering the sound source in S1 position.

### Simulation setup

The moderate size of this multipurpose hall allowed to run simulations pushing the boundary of the wave-based part of the model up to 6 kHz.

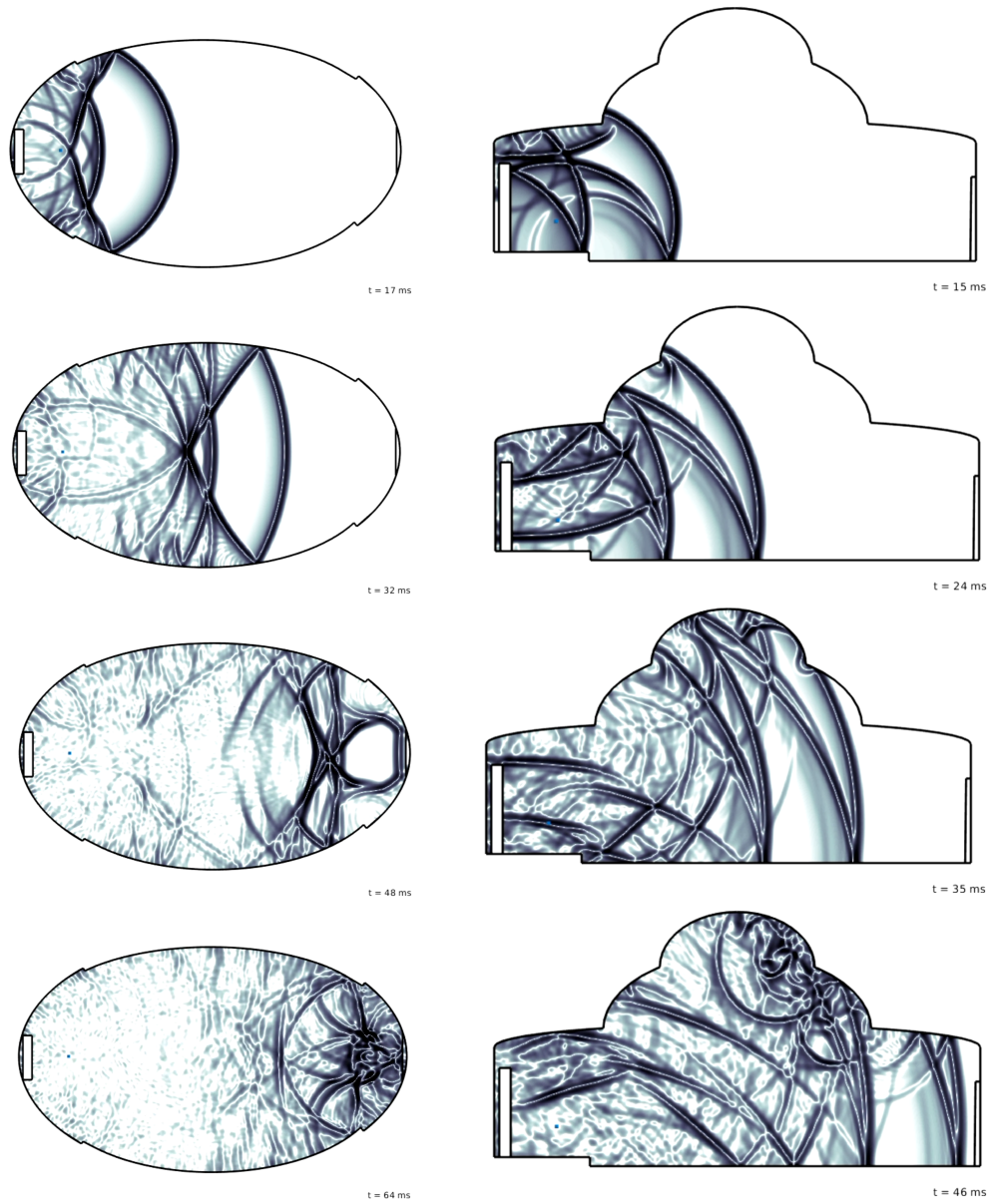


Figure 5.8: Plan and longitudinal section view of STC. Qualitative representation of the sound propagation in an elliptical-shaped concert hall (STC).

Therefore, a full wave-based simulated impulse response is available in all the octave bands of interest, from the octave band centered in 125 Hz to the octave band centered in 4 kHz included. The value  $f_{max} = 6$  kHz is a significant achievement, considering the usual constraints of wave-based approach due to its considerable computational cost. This time, the computational task has been parallelized using three GTX1080Ti GPUs, in collaboration with the University of Edinburgh. At higher frequencies the high-density ray-tracing algorithm was employed using about 1 billion of rays.

Table 5.3: Simulation setup of FDTD simulation in STC. The maximum frequency simulated with FDTD ( $f_{max}$ ), the points per wavelength (PPW), the oversampling factor ( $\sigma$ ), the grid spacing ( $h$ ), the time step ( $k$ ), the Courant number ( $\lambda$ ), the time cost (in hours of runtime  $h$  per second of computed impulse response  $s_{output}$ , and the dispersion error (in percentage) are provided.

$f_{max}$ (Hz)	PPW	$\sigma$	$h$ (mm)	$F_s = 1/k$ (Hz)	$\lambda$	Time cost (h/ $s_{output}$ )	Dispersion error%
6000	8	4	7.2	48000	$\simeq 1$	1 h 10 m	1%-2%

The calibration process was performed considering the sound source in the position that is most likely used during any performance in this multi-purpose hall, i.e. S1 of Figure 5.5. The acoustic indicators selected as the targets of the calibration are the same employed in TCB and DUS calibration. Therefore the indexes considered as suited to describe the acoustics of STC are  $T_{30}$ , EDT,  $C_{80}$ , and  $T_S$  [132, 128, 146]. Table 5.4 summarizes the calibration results in terms of main room criteria ( $T_{30,M}$ ,  $EDT_M$ ,  $C_{80,M}$ ,  $T_{S,M}$ ) at mid frequencies (500 – 1000 Hz). In line with the state-of-the-art procedure, the calibration of the 3D model was achieved when the differences between simulated and measured values were within the Just Noticeable Differences (JND) defined by the standard [128]. Even though in TCB and DUS twice the JND was considered for  $T_{30,M}$  and  $EDT_M$ , in STC the single JND of 5% was employed during the calibration. In fact, there are no significant subdivisions of audience areas - STC hall is a single acoustic volume - and thus the calibration is more straightforward. Therefore at mid frequencies the tolerance ranges are the same stated by ISO 3382-1 standard [128]:

- 5% in  $T_{30,M}$  and  $EDT_M$  evaluation,
- 1 dB in  $C_{80,M}$  evaluation,
- 10 ms in  $T_{S,M}$  evaluation.

With regard to this calibration choice, at the end of the iterative process 100% of the simulated mean values at mid frequencies are within the tolerance range chosen (see Table 5.4).

Table 5.4: Measured and simulated room criteria in STC. Results at medium frequencies (500-1000 Hz) for center stage source positions, averaged over the receivers. The difference between mean measured and simulated values are reported between brackets. See text for the tolerance range adopted for each metrics.

Room criteria	Measured	Simulated (Diff.)
$T_{30,M}$ (s)	1.30	1.29 (+0.7%)
$EDT_M$ (s)	1.31	1.26 (+3.8%)
$C_{80,M}$ (dB)	1.3	1.5 (-0.2)
$T_{S,M}$ (ms)	86	85 (+1)

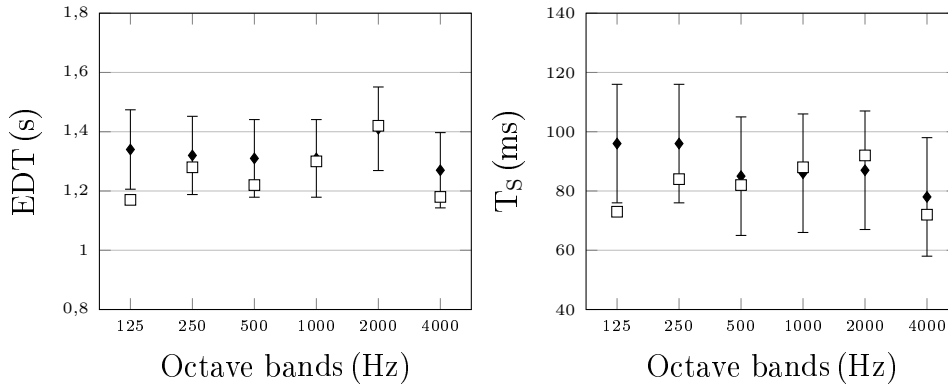


Figure 5.9: STC calibration: measured (black) and simulated (white) EDT and  $T_S$  values in octave bands. Mean values are referred to the sound source placed in S1 position (see Fig. 5.5). The error bars are referred to the tolerance range chosen for the calibration process.

Furthermore, Figure 5.9 provides the calibration results in terms of comparison between measured and simulated EDT and  $T_S$  values to visualize the behaviour of those room criteria as functions of the frequency. The diagrams report the results of the achieved calibration in terms of EDT and  $T_S$ , measured and simulated, in octave bands. The choice of such room criteria is due to the deviation of resulting values throughout the space, as already explained in case of TCB and DUS [132]. The values displayed in the graphs are referred to the sound source in S1 position, the centre of the tiny stage. The resulting values in octave bands are shown averaged over all the positions of the receivers. Also in this case, since calibrating in all the octave

bands concerned is still challenging, the author chose to double the tolerance of both the JND: from 5% to 10% in case of EDT, from 10 ms to 20 ms in case of  $T_S$ . At the end of this calibration step, 83% of the values are between the tolerance range assessed in this work.

With regard to material properties, as already seen in TCB and DUS the number of the layers was kept as low as possible to reduce the uncertainty connected with the assignment of material properties [64]. Table 5.5 provides the outcoming values of absorption coefficients - from which the complex acoustic impedances are derived and given as input data in FDTD model - obtained at the end of the FDTD simulation. The normalised LRC coefficients for the boundary complex impedances are provided in the first part of the Appendix. The difference found with the corresponding values used in the GA++ model are provided in the second part of the Appendix.

Table 5.5: Materials involved in STC simulations. The energy-based parameters  $\alpha$  represent the starting point in the backward process to obtain the acoustic impedances  $\zeta$  for the FDTD simulation. The macro-layers used in the present work divide the materials according to the type of the surface and the role within the hall: wooden furniture has acoustic features that are different from wooden floor. References are provided for most of the absorption coefficients. Normalised LRC (inductance, resistance, capacitance) coefficients employed as input data in FDTD simulations to approximate boundary admittances are provided in Appendix A.

	Energy-based parameters $\alpha$						Ref.
	125 Hz	250 Hz	500 Hz	1 kHz	2 kHz	4 kHz	
Ceiling	0.09	0.09	0.09	0.10	0.10	0.10	[121]
Plasterboard (walls)	0.18	0.15	0.14	0.13	0.12	0.12	Estimated
Wood	0.15	0.15	0.12	0.10	0.06	0.06	Estimated
Furniture	0.28	0.25	0.20	0.16	0.12	0.12	[125]
Seats	0.28	0.30	0.45	0.60	0.58	0.58	[144]

### 5.1.3 Flutter echoes

Flutter echoes are multiple echoes that occur in rapid succession. They are produced by sound travelling between two parallel walls, in a sort of “infinity mirrors” system. They are caused by the sound bouncing back and forth in a series of reflections between two walls [9].

Even though the two long sidewalls in STC are not properly parallel because of their curved shape, flutter echoes are clearly detectable in the room. Probably affected by the hard and reflective surfaces of the longer

plastered sidewalls, the acoustic of STC is definitely characterised by perceivable flutter echoes. In fact, negative complaints by common users of the multipurpose hall concern some undesired acoustic effects that are closely related to what is defined as “flutter echo”. During the campaign of measurements, when no movable seats were present in the middle of the hall, the effect was significantly perceivable by the author and the other operators involved. Especially in receivers’ position such as R4 or R5 (see Fig. 5.5) the flutter echo was definitely present from a subjective point of view. Therefore, during the measurements part of the positions selected for source-receiver pairs were specifically chosen in order to detect that undesired effect.

Now the question is: can an accurate wave-based simulation process return this phenomenon? Therefore, once having calibrated the 3D model according to consolidated room criteria, the simulated impulse response corresponding to the sound source in R2 location - and thus in the central empty area of the hall in asymmetrical position - and the receiver in one of the most affected positions by the flutter echo, R4, was analysed. The objective is to investigate the accuracy of a FDTD model - calibrated on the basis of specific considerations - when other acoustic consequences are evaluated.

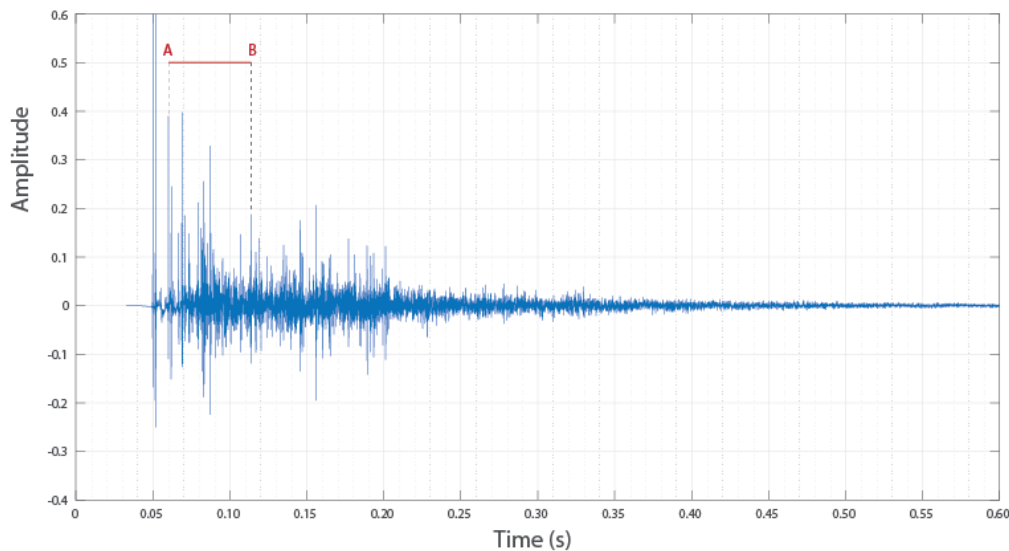


Figure 5.10: Normalised simulated impulse response corresponding to the sound source in position S2 and the receiver in position R4 (see Fig. 5.5).

In Figure 5.10 the normalised simulated impulse response corresponding to the sound source in position S2 and the receiver in position R4 is shown. The time delay between two specific reflections are highlighted with a red line. With reference to R4 receiver in Figure 5.5:

- point A indicates the arrival of the backward reflection from the nearest sidewall, approximately 10 ms ( $\sim 1.7 \text{ m} \times 2 = 3.4 \text{ m}$ ) after the direct sound,
- point B indicates the arrival of the reflection coming from the opposite sidewall, approximately 54 ms ( $\sim 9 \text{ m} \times 2 = 18 \text{ m}$ ) after the reflection indicated with point A.

It should be noticed that point B is one of the strongest late reflections arriving to the receiver. This fact may confirm that the FDTD model is able to detect, even only analysing the simulated impulse response corresponding to a precise source-receiver combination, the clearly audible effect of flutter echoes. Certainly, listening to the impulse response or a convolution with an anechoic signal is expected to return an auralization with a perception comparable to the actual within the hall.

#### 5.1.4 Focusing effects

As already mentioned in Chapter 3, focusing effects occurring in elliptical shapes can cause high concentrations of sound pressure levels, or echoes. This is caused by geometrical reasons, as it can be visualized in Figure 3.9.

In the 18<sup>th</sup> and 19<sup>th</sup> centuries much of the attention of the scholars was focused on the acoustic and optical effects due to curved surfaces. In particular, there was a certain school of thought according to which in a concert hall or in a theatre an elliptical plan should be preferable [167, 168]. Authors of the relative ancient publications recommend the elliptical shape to enhance the sound pressure level at the farthest rows of listeners. Moreover, there also was another way of thinking supporting the half circular plan in order to maintain the audience at the same distance from the scene on the stage [169]. Nevertheless, also the possible negative effects of such curved surfaces were well-known. In fact in a treatise on acoustics, Langhans stated that elliptical shape returns unwanted echo effects, especially in quite large halls, where the sound at the receiver is heard as two separate signals [170].

Recently, scholars focused their attention on the actual focusing effects of concave shapes within theatres and concert halls. There are several possible consequences to curved surfaces in acoustics: high sound pressure levels, sound coloration, and echoes. It is important to notice that shapes that are spherical or elliptic, i.e. curved in two directions, caused much stronger focusing effects rather than cylindrical surfaces, i.e. curved in only one direction [114].

In the case under study, the wave-based method adopted is expected to return a raise of sound pressure level in focusing points [114]. It has been

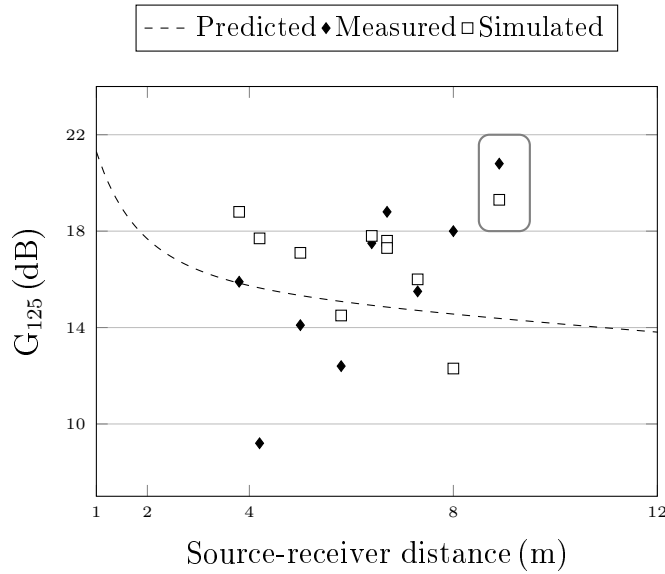


Figure 5.11: Analytical predictive model (dashed line), measured (black) and simulated (white)  $G$  values at 125 Hz as a function of the source-receiver distance.

proven that a wave-based approach is suited for determining sound focusing, since wave interference are naturally computed even in the near field [116]. Therefore, acoustic focusing effects can be detected through the analysis of the sound strength,  $G$ , which is the normalised sound pressure level at the receiver [128] derived from the simulated impulse responses of the calibrated STC model. In Figure 5.5 and Figure 5.8 it can be visualized that the sound source in S1 position and the receiver in R10 position are approximately in the geometrical focus points of the elliptical shape. Hence, the sound pressure level distribution throughout the space is evaluated considering the sound source in S1 position: Figure 5.11 shows the analytical predicted behaviour, the measured values at the receivers (R1, R2, ..., R10) and the corresponding simulated values. As analytical prediction, the author chose to display the spatial decay of the sound strength at 125 Hz according to Barron and Lee's *revised theory* [171]:

$$G_{125} = 10 \log_{10} \left( \frac{100}{r^2} + 31200 \frac{T_{125}}{V} e^{-0.04x/T_{125}} \right) \quad (\text{dB}) \quad (5.1)$$

where  $G_{125}$  is the normalised sound pressure level at 125 Hz in dB,  $r$  is the sound source-receiver distance in m,  $T_{125}$  is the reverberation time at 125 Hz in s, and  $V$  is the volume in  $\text{m}^3$ . Indeed, even though the predictive theory here used was not derived for small performance spaces, it is a useful reference point to easily detect the discrepancies from the standard spatial

sound energy decay. The results of Equation 5.1 in case of STC, with  $T_{125} = 1.05$  s and  $V = 950$  m<sup>3</sup>, are provided through the dashed line in Figure 5.11. It is interesting to notice how the measured and simulated values corresponding to R10 position (highlighted at top right of the Figure) are higher both compared to the expected behaviour according to the predicted trend and to the rest of receiving points. Since R10 is the farthest receiver from S1, the  $G_{125}$  should be lower because of the spatial loss of sound intensity. It is reliable to retain that R10 actually is affected by acoustic focusing effects. The measurements results seem to be a confirm of this remark and FDTD simulations proved to be suited to detect the phenomenon.

# Chapter 6

## Space for verbal communication

The present chapter deals with a full-spectrum simulation of a historical university lecture hall of the University of Bologna (Italy). Compared to the previous case studies, the intended use of the room is significantly different. In this case, the room criteria describing the speech intelligibility play a fundamental role during the analysis. Therefore, the sound clarity at 50 milliseconds and the Speech Transmission Index (STI) will be assessed along with the reverberation time, the early decay time, the centre time. Part of this chapter is taken from a paper concerning the simulated acoustic treatment with sustainable materials within the hall [120].

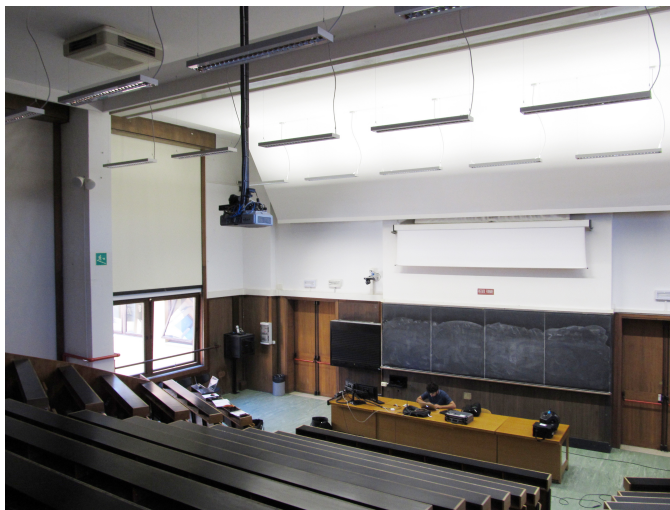


Figure 6.1: Interior view of the university lecture hall (ULH) of the University of Bologna.

## 6.1 An university lecture hall

The case study assessed in this section is a large university lecture hall (ULH) of the School of Arts, Humanities, and Cultural Heritage in Bologna. The hall is located in the city centre, within one of the oldest buildings of the University of Bologna. Hence, ULH may be considered as a historical lecture hall with an amphitheatre geometry in the audience area (see Fig. 6.1). Most of the walls are plastered and reflective whereas the rear wall and a sidewall are made up of wood with an air cavity behind. The seats and the benches are made of wood. The total volume is of about 900 m<sup>3</sup> and the maximum seating capacity is of 200 students. Main data about ULH geometric features are provided in Table 6.1.

Table 6.1: Geometrical features of the university lecture hall (ULH) in Bologna. The reference ID, the century of construction, the shape of the audience area, the total volume of the hall (V), the seating capacity (N), are provided.

ID	Century (last renovation)	Shape	V (m <sup>3</sup> )	N	V/N (m <sup>3</sup> /seat)
ULH	XX	Amphitheatre	900	200	4.5

### 6.1.1 Acoustic measurements

In 2017, a campaign of acoustic measurements was carried out within the university lecture hall [172, 173], allowing to collect the main room criteria [128] and intelligibility indexes [119]. The objective was to qualify ULH according to ISO 3382 [128] and IEC 60268-16 [119] standards.

Acoustic measurements were performed with the presence of only two operators in the room, in furnished condition. ESS technique with a signal 512 K in length and sampled at 48 kHz was used for the purpose. The equipment consisted in:

- a laptop for launching the ESS signal;
- a signal converter (Motu UltraLite AVB);
- an amplifier to increase the signal power (Crown 2500 W);
- a dodecahedron with custom loudspeakers used as an omnidirectional source;

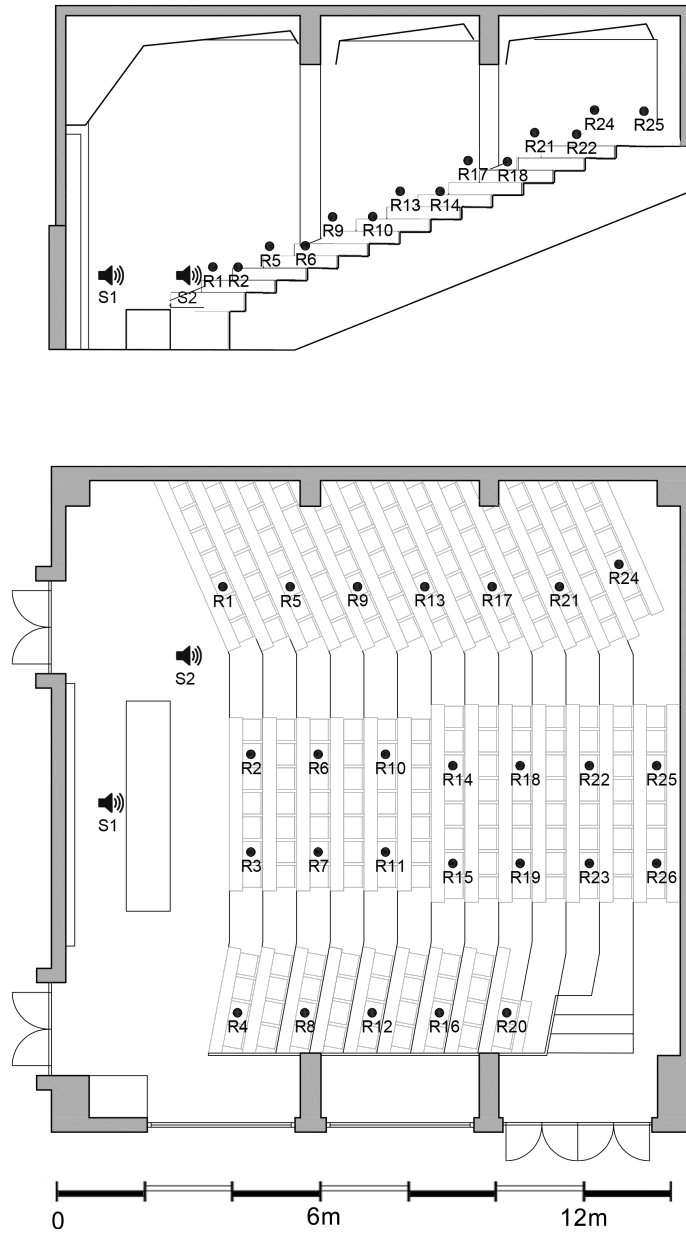


Figure 6.2: View of longitudinal section and plan of ULH. Sound sources and microphone receivers used in the measurements campaign are reported.

- one monoaural half inch free-field microphones (NTI audio MA220) as receiver.

The dodecahedron sound source was calibrated in the reverberation room according to ISO 3741 [174]. The first position of the sound source (S1) corresponds to the teacher in his/her common seated position, while the second position of the sound source (S2) corresponds to the standing teacher closer to the students area. Similarly to the guidelines to perform measurements in opera houses [97, 98], the recommended configuration in lecture halls involves a symmetrical and an asymmetrical position for the sound source, as stated by the recently updated Italian standard on the acoustic quality in classrooms [172, 175, 176]. This practice is aimed to thoroughly characterize the speech intelligibility at the listeners during measurements, since it is considerably affected by the signal-to-noise ratio and thus from the location of the speaker. In Figure 6.2 the configuration of positions for the sound sources and the receivers is shown. The main results of IRs acquirement are provided:

- in Table 6.2 in terms of mean values of  $T_{30}$ , EDT,  $C_{50}$ ,  $T_S$ , and STI averaged over the sound-receiver pairs and over the mid frequencies (500 - 1000 Hz or 500 - 1000 - 2000 Hz, except for STI);
- in Figure 6.6 in terms of  $T_{30}$ , EDT,  $C_{50}$ ,  $T_S$  in octave bands averaged over the receivers considering the sound source in S1 position along with the standard deviations.

Table 6.2: Measurements results in ULH. Reverberation time ( $T_{30,M}$ ), early decay time ( $EDT_M$ ), speech clarity referred to 50 ms ( $C_{50,3}$ ), centre time ( $T_{S,3}$ ), STI measured values are provided [128, 119], along with the Schroeder frequency( $f_c$ ) and the number of sound source and receivers points. Values signed with “M” indicates the average over 500-1000 Hz, with “3” the average over 500-1000-2000 Hz.

ID	$T_{30,M}$ (s)	$EDT_M$ (s)	$C_{50,3}$ (dB)	$T_{S,3}$ (ms)	STI -	$f_c$ (Hz)	Sources/Receivers -
ULH	1.71	1.69	-1.8	118	0.47	67	2/26

Since the speech intelligibility is largely affected by the reverberation time and the signal-to-noise ratio at the receiver, the acoustic measurements of the background noise were carried out in the hall. Being far enough from the external traffic noise, the main factor causing the background noise in ULH is the HVAC system. The measurements were performed by means of a class 1 sound meter level. The background noise was detected in about two

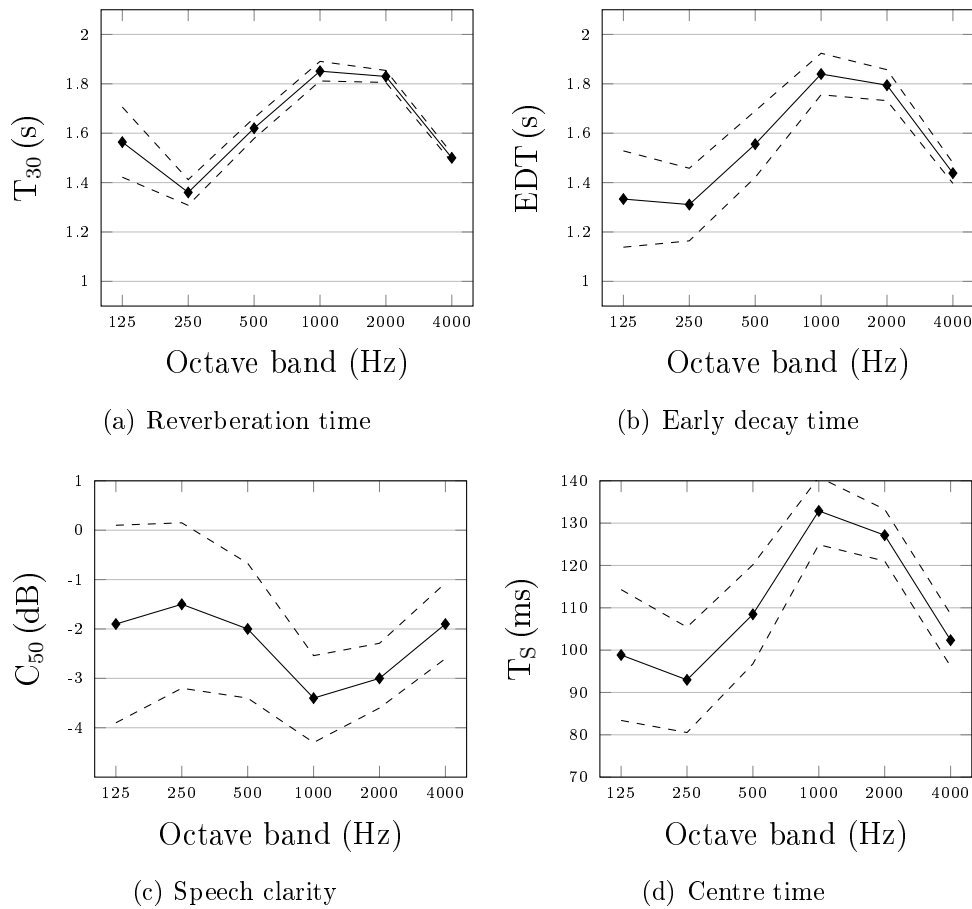


Figure 6.3: Measured  $T_{30}$ , EDT,  $C_{50}$ ,  $T_s$  values in STC in octave bands with relative standard deviations (dashed lines). Mean values referred to sound source S1 and averaged over all the receivers, shown in Figure 6.2.

hours with the air condition system turned on at medium power. The noise level due to systems is necessary to define STI in numerical simulation and in prediction models. Equivalent sound pressure levels of background noise can be considered as quite even throughout the hall and then the values were averaged on all the receivers' points.

## 6.1.2 FDTD calibration

### 3D modeling

The 3D virtual model of ULH was built with Sketchup [145] following the same guidelines used in the first two case studies for most of its parts [121, 127]. The only element handled in differently from the GA++ standard recommendations is the group of seats. In ULH the geometry of the wooden benches was specifically modified to be computed with FDTD models. This choice is closely related to the fundamental role of the edge diffraction in the acoustic features of lecture halls. Hence, arrays of “staircase” boxes representing the edges of each row of seats have been introduced in the model instead of simplified boxes with planar upper parts (see Fig. 6.4).

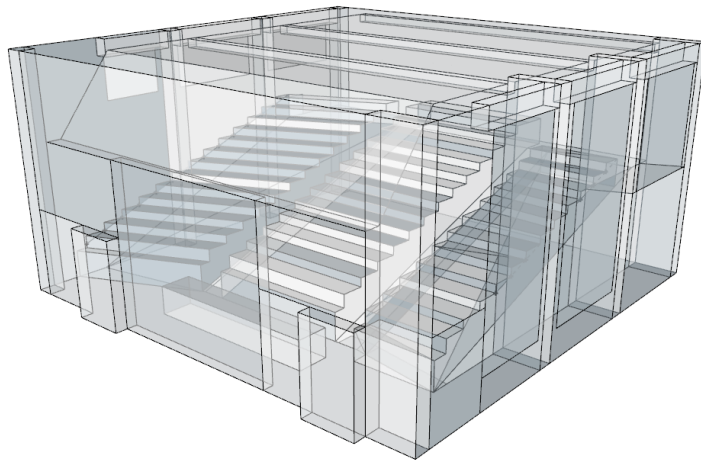


Figure 6.4: View of the 3D virtual model of the university lecture hall (ULH) [145].

The result is a model made up of 1100 surfaces, as it is shown in Figure 6.4. The usual division in macro-layers depending on the materials was carried out, using a small group of different materials to reduce the uncertainties underlying the assignment of material properties to each surface.

### Simulation setup

Among all the case studies assessed in the present thesis, ULH is the room for which the highest value of cut-off frequency between FDTD algorithm and classical ray tracing was used. In fact, thanks to the availability of high computational power and the moderate size of the room, it was possible to run simulations with the wave-based part of the model up to the frequency of 8 kHz. Therefore, a full wave-based simulated impulse response is avail-

Table 6.3: Simulation setup of FDTD simulation in ULH. The maximum frequency simulated with FDTD ( $f_{max}$ ), the points per wavelength (PPW), the oversampling factor ( $\sigma$ ), the grid spacing ( $h$ ), the time step ( $k$ ), the Courant number ( $\lambda$ ), the time cost (in hours of runtime  $h$  per second of computed impulse response  $s_{output}$ ), and the dispersion error (in percentage) are provided.

$f_{max}$ (Hz)	PPW	$\sigma$	$h$ (mm)	$F_s = 1/k$ (Hz)	$\lambda$	Time cost (h/ $s_{output}$ )	Dispersion error%
8000	6.75	3.375	6.3	54000	$\simeq 1$	1	1%-2%

able for most the octave bands involved in the computation of the speech transmission index (from 125 Hz to 4 kHz included) [119]. The only octave band that remains partially computed with the wave-based part of the model is that one centered at 8 kHz, still taken into account in STI calculation.

The rough length of the impulse response at the beginning of the calculation was set equal to 2.5 s, to guarantee enough seconds even at low frequencies where reverberation time are higher. Hence, the global time cost was almost 2 hours per sound source, corresponding to about 1 hour per second of simulated impulse response the author decided to spend. The computational task has been parallelized using three Titan GPUs, in collaboration with the University of Edinburgh. An intuitive visualization of the wave simulation run within ULH is provided in Fig. 6.5, considering the sound source in S2 and S3 positions.

The value of 6.75 points per wavelength was chosen, returning a value of around 3.4 as oversampling factor ( $\sigma$ ). The corresponding numerical dispersion errors are limited between the range of 1% - 2%. As a consequence, the grid spacing  $h = 6.3$  mm and  $k = 1.85 \cdot 10^{-5}$ . To summarize the simulation setup in the FDTD region (up to the cut-off frequency), the maximum frequency ( $f_{max}$ ), the points per wavelength (PPW), the oversampling factor ( $\sigma$ ), the grid spacing ( $h$ ), the time step ( $k$ ), the Courant number ( $\lambda$ ), the time cost (in hours per second of computed impulse response), and the dispersion error (in percentage) are provided in Table 6.3.

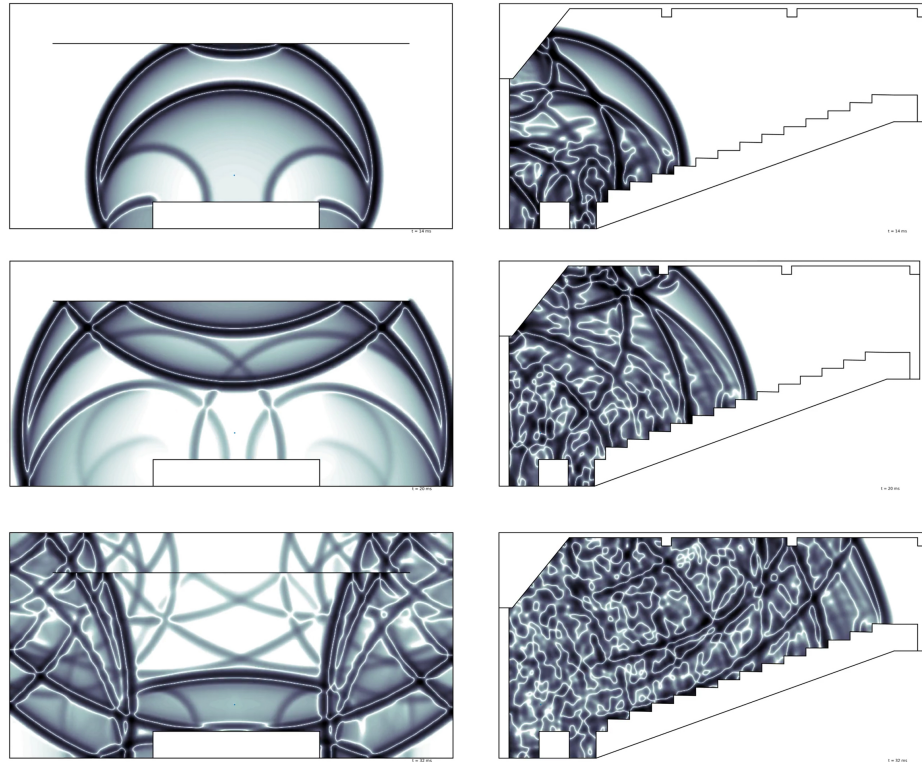


Figure 6.5: Qualitative visualization of sound wave propagation in ULH. Cross (left) and longitudinal (right) sections of the room. The sound source is located in the teacher's position (S1 in Fig. 6.2).

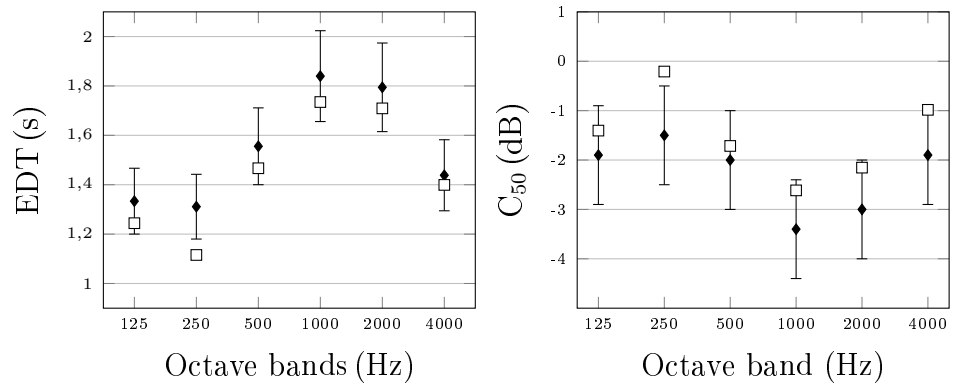


Figure 6.6: ULH calibration: measured (black) and simulated (white) EDT and  $C_{50}$  values in octave bands. Mean values are referred to the sound source placed in S1 position (see Fig. 6.2). The error bars are referred to the tolerance range chosen for the calibration process.

Table 6.4: Measured and simulated room criteria in ULH. Results at medium frequencies (500-1000 Hz) for center stage source positions, averaged over the receivers. The difference between mean measured and simulated values are reported between brackets. See text for the tolerance range adopted for each metrics.

Room criteria	Measured	Simulated (Diff.)
$T_{30,M}$ (s)	1.70	1.60(+5.9%)
$EDT_M$ (s)	1.74	1.63(+6.3%)
$C_{50,M}$ (dB)	-2.7	-2.2(-0.5)
$T_{S,M}$ (ms)	121	113(+7)
STI	0.47	0.51(+0.04)

Table 6.5: Materials involved in ULH simulations. The energy-based parameters  $\alpha$  represent the starting point in the backward process to obtain the acoustic impedances  $\zeta$  for the FDTD simulation. The macro-layers used in the present work divide the materials in: hard/reflective surfaces (Plaster-floor), elements absorbing slightly at low frequencies (Wood, Windows) and the most sound absorbing area (Seats). References are provided for most of the absorption coefficients. Normalised LRC (inductance, resistance, capacitance) coefficients employed as input data in FDTD simulations to approximate boundary admittances are provided in Appendix A.

	Energy-based parameters $\alpha$						Ref.
	125 Hz	250 Hz	500 Hz	1 kHz	2 kHz	4 kHz	
Plaster	0.01	0.02	0.03	0.03	0.04	0.06	[121]
Wood	0.15	0.18	0.04	0.04	0.04	0.04	[25]
Windows	0.10	0.10	0.08	0.04	0.04	0.04	[125]
Seats	0.40	0.37	0.26	0.19	0.17	0.16	Estimated

The calibration process was performed considering the sound source in the position that is most likely used by the teacher during the lectures, i.e. S1 of Figure 6.2. The acoustic indicators selected as the targets of the calibration are the indexes considered as suited to describe the acoustics of ULH:  $T_{30}$ ,  $EDT$ ,  $C_{50}$ ,  $T_S$ , and  $STI$  [132, 128, 146]. Table 6.4 summarizes the calibration results in terms of main room criteria ( $T_{30,M}$ ,  $EDT_M$ ,  $C_{50,M}$ ,  $T_{S,M}$ ) at mid frequencies (500 – 1000 Hz) and  $STI$ . The tolerance ranges in ULH have been selected as follows [128]:

- 10% in  $T_{30}$  and  $EDT$  evaluation,
- 1 dB in  $C_{50}$  evaluation,
- 10 ms in  $T_S$  evaluation,

- 0.03 in STI evaluation.

With regard to this calibration choice, at the end of the iterative process 83% of the simulated mean values at mid frequencies are within the tolerance range chosen (see Table 6.4).

With regard to material properties and absorption area distribution, it should be noticed that, generally, the seats are the most sound absorbing objects in a lecture hall in unoccupied state [177, 178, 179, 180]. The remaining layers of the model (walls, floor, ceiling) are made up of quite hard and reflective surfaces and thus, they show low values in the whole frequency range. It should be also highlighted that the random incidence absorption coefficients at low frequencies of wooden parts are due to the air cavity behind (see dataset in Table 6.5).

### 6.1.3 Micro-perforated acoustic treatment

From measurements results it can be noticed that the acoustic features of the lecture hall are not suited to speech signals. In fact, on average the speech clarity values are lower than 0 meaning that the sound energy contribution of the late reflections is higher than the contribution of the early reflection, which would enhance the direct sound and the intelligibility. For this reason, the design of a ceiling-mounted acoustic treatment has been designed and simulated in ULH. In lecture halls, porous and fibrous absorbers [181, 182, 183] have until now been the most used materials in noise control application because of their high performance-to-cost ratio in the frequency band of interest. However, the interest in more durable and sustainable sound absorbing materials is growing [184, 185, 186]. In the last decades, new requirements have become important, such as durability, recyclability, hygienic problems, environmental sustainability and optical transparency, no longer suitable for porous and fibrous materials. In order to satisfy these requirements, specific classes of sound absorbing materials have been proposed: among them, the micro-perforated panels (MPPs) [187, 188, 189, 190, 191]. During the 70s, the first MPP acoustic model proposed by Maa [187] defined the absorbers as a combination of a thin panel with sub-millimetric holes, an air cavity and a rigid wall. The air cavity is required to perform the Helmholtz-type resonance. In the last decades, the applications, the improvements and the theoretical developments of such materials have been extensively studied and MPP multiple layers have been introduced to provide wide-band absorption, creating more efficient sound absorbing systems [192, 193, 194].

MPPs can be made of various materials, including plywood, glass and

sheet metal. Therefore, they are extremely attractive from an ecological point of view, especially for architectural applications [195]. Moreover, MPP absorbers are theoretically expected to return the same acoustic behaviour regardless of their constitutive material. Therefore, concerning sustainability aspects they can be made of any green material, reducing the environmental footprint of the whole process. Since in the last years the acoustical comfort of teachers and students is one of the most debated topics [196, 180, 197], the possibility to choose a sustainable and high-performance material could meet the need of improving the acoustics in existing lecture halls.

For all these reasons, a wide employment of double-layer MPPs have been chosen to enhance the verbal communication in ULH case study, replacing the common sound absorbing treatments [198, 199, 200]. Reducing the reverberant field in a specific frequency range (500 - 1000 Hz) contributes to decrease the vocal effort of the speaker and the distraction of the students [201, 202, 203].

The acoustic simulation of a wide application in a 3D virtual enclosure is a useful tool in a preliminary step in the assessment of their performance [177, 178, 179]. With this purpose, the acoustic condition of ULH has been

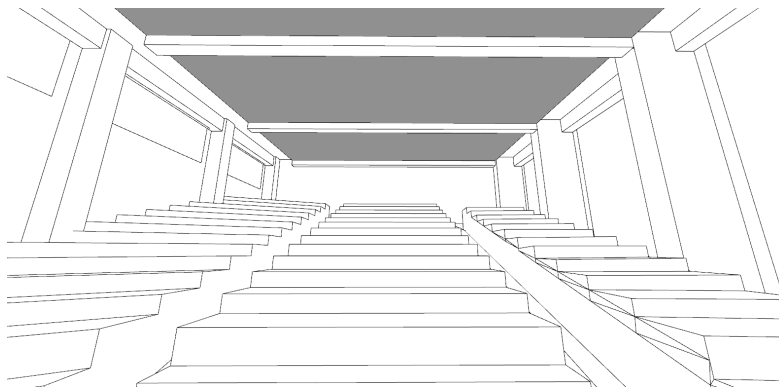


Figure 6.7: Interior view of the acoustic treatment virtually introduced into ULH model. The ceiling mounted MPPs are highlighted in red.

simulated with a ceiling mounted system of double-layer MPPs (see Fig. 6.7). Such kind of large rooms shows the highest values of reverberation time at 500 and 1000 Hz (see Fig. 4 in [172]), the same frequency range interested by the main contribution of the human voice [119]. As too high values of reverberation time deteriorates the speech intelligibility, a material whose sound absorbing properties are mostly centered in such frequency range may return useful outcomes in acoustic treatments of existing university halls. Otherwise, an acoustic treatment with porous or fiber materials would provide the most significant absorbing contribution at higher frequencies [204],

sometimes entailing too dry conditions at 2000 Hz and 4000 Hz.

Table 6.6: Specific normalised impedances  $\zeta$  corresponding to the double layer MPP. Octave band data have been fitted basing on the outcomes of the compensation model described in [120].

125 Hz	250 Hz	500 Hz	1 kHz	2 kHz	4 kHz
$1.3 - 16.4i$	$1.3 - 6.8i$	$1.8 - 0.9i$	$2.2 + 2.0i$	$1.6 + 8.4i$	$4.4 + ai$

$a \rightarrow \infty$ : the function diverges to infinity or minus infinity.

While in the practice used so far the LRC circuit parameters are derived to fit the acoustic impedances from absorption coefficients, in this case it has been possible to avoid some of the uncertainties due to these steps in the workflow, at least for what concerns the MPP layer. The complex acoustic impedances of double layer MPP were available thanks to the experimental measurements carried out in laboratories (see Table 6.6). Working with wave-based simulation methods instead of the energy-based geometrical acoustics allowed the direct use of complex acoustic impedances as input boundary conditions [205, 206]. Therefore, with the reference to Table 6.6, the data corresponding to a configuration of double layer MPP was employed as input data in FDTD simulations.

Table 6.7: Trend in frequency of  $T_{30}$  mean values corresponding to the results of the measurements (“Meas”), the equivalent values derived from the calibrated FDTD model (“w/o MPP”) and the variations due to the introduction of MPPs (“w MPP”).

$T_{30}$ (s)	125 Hz	250 Hz	500 Hz	1000 Hz	2000 Hz	4000 Hz
w/o MPP (Meas.)	1.48	1.36	1.60	1.84	1.83	1.51
w/o MPP (FDTD)	1.44	1.25	1.54	1.73	1.70	1.45
w MPP (FDTD)	1.32	0.92	0.88	1.22	1.52	1.44

Simulations results show that the introduction of double layer MPPs at the ceiling of the lecture hall contributes to enhance the acoustic behaviour of the sound field at 500 - 1000 Hz, improving the condition for speech communication. The improvements are evaluated in terms of  $T_{30}$  values variations averaging all the source-receiver pairs considered (see locations of sources and receivers in Fig. 6.2). The simulation results show a significantly decrease of

reverberation time values at the mid frequencies assessed, as shown in Table 6.7.

Moreover, in order to evaluate the enhancement of the acoustic condition with the virtual installation of micro-perforated panels in terms of intelligibility criteria, a further analysis has been carried out involving the modulation transfer indexes defined in [119]. It is well known that the speech is assumed as amplitude-modulated signal, and the acoustic environment influences the talker-receiver path. The Speech Transmission Index (STI) quantifies the degree of degradation of the signal identified by the impulse response of the room. The metrics of such degradation is the preservation of envelopes whose frequency spans from 0.63 Hz to 12.5 Hz. The modulation transfer function is defined [119]:

$$m_k(f_m, \mathbf{x}, \mathbf{y}) = \frac{\left| \int_0^\infty h_k(t, \mathbf{x}, \mathbf{y}) e^{-j2\pi f_m t} dt \right|}{\int_0^\infty h_k(t, \mathbf{x}, \mathbf{y}) dt} \quad (6.1)$$

where  $h(t, \mathbf{x}, \mathbf{y})$  is the impulse response with sound source in  $\mathbf{y}$  and receiver in  $\mathbf{x}$ , filtered in the  $k$ -th octave band (from 125 to 8000 Hz), and  $f_m$  is the modulation frequency (from 0.63 Hz to 12.5 Hz). It could be assumed – and the technical standard confirms – that in almost all the environments the  $m(f_m)$  values decrease when the modulation frequency  $f_m$  increases. Higher the modulation function value at a certain modulation frequency, less-degraded is the information carried by this  $f_m$  carrier. In other words, the speech intelligibility of an environment increases when its modulation function increases. From the modulation transfer matrix made up 98 components (14 modulation frequency for each one of the 7 octave bands considered) it is possible to calculate the STI values, after calculation steps as [119]:

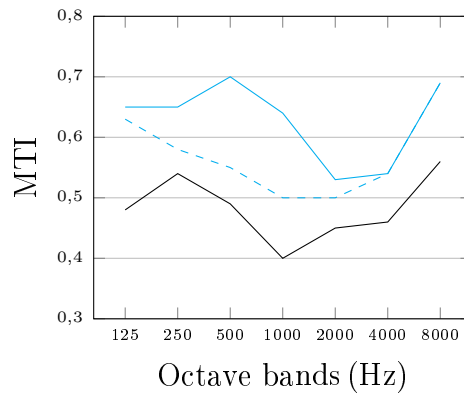
$$\text{STI} = \sum_{k=1}^7 \alpha_k \cdot \text{MTI}_k - \sum_{k=1}^6 \beta_k \cdot \sqrt{\text{MTI}_k \cdot \text{MTI}_{k+1}} \quad (6.2)$$

where  $\alpha_k$  is the weighting factor for octave band  $k$ ,  $\text{MTI}_k$  is the modulation transfer index for octave band  $k$ ,  $\beta_k$  is the redundancy factor between octave band  $k$  and octave band  $k + 1$ . Since MTI values represent the behaviour of speech intelligibility for each octave band - being the last step before the final calculation of STI [119] - it has been chosen to report MTI values for three receivers.

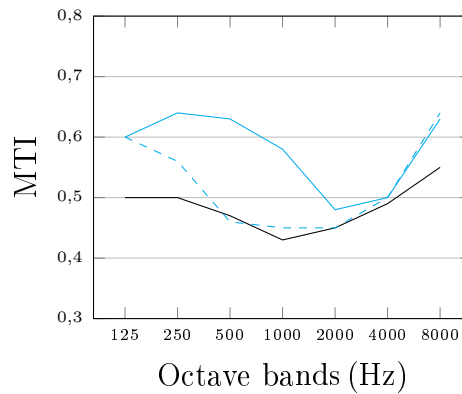
Figure 6.8 shows the trends of the modulation transfer indexes:

- measured IRs in the measured configuration, i.e. without any acoustic treatment (see section 6.1.1),

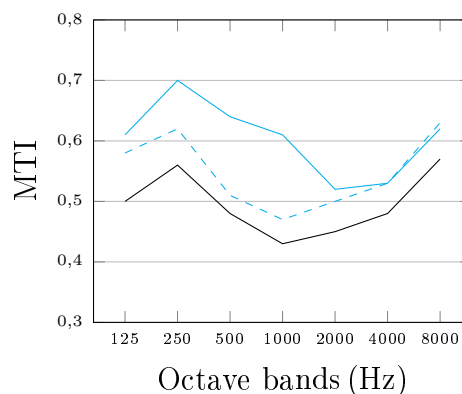
— Meas. (w/o MPP) - - - FDTD (w/o MPP) — FDTD (w MPP)



(a) Third row (R6)



(b) Seventh row (R15)



(c) Eleventh row (R22)

Figure 6.8: Modulation transfer index MTI in octave bands acquired from measured and simulated IRs referred to the configuration without the treatment (w/o MPP) and with the treatment (w MPP) of ULH [119]. The results are shown referring to the sound source placed in the teacher's position (S1 in Fig. 6.2) and the receivers placed in the third row (R6), seventh row (R15), and eleventh row (R22).

- simulated IRs from the calibrated FDTD model (see section 5.1.2),
- simulated IRs from the configuration with the acoustic treatment.

The omnidirectional sound source is considered located in teacher's position (S1 in Fig. 6.2) and three monaural receivers in the audience (R6, R15, R22).

In the simulated configuration with the ceiling-mounted MPP results provided through numerical simulations show that the modulation transfer index is significantly enhanced (see Fig. 6.5). As expected, the influence of the treatment is focused on 500 - 1000 - 2000 Hz octave bands, contributing to decrease the reverberance in this frequency range and thus, to enhance the speech intelligibility. When the ceiling is treated with MPP, the reflections in the range of 500 Hz, 1000 Hz and 2000 Hz are time delayed by the reactive part of the materials. It should be assumed - but this point needs further study - that the sum of the effects, replayed by a distributed holes, generated a diffuse reflection. This is well-modeled by FDTD simulation considering both active and reactive parts of the impedance.



# Chapter 7

## Discussions

The present chapter is intended to outline the most evident considerations on the outcomes obtained through the methodological approach described in Chapter 3 and reported in Chapters 4, 5, 6. It should be reminded that every case study had been also handled with GA++ algorithms, with the procedure described in Section 3.5, for different reasons:

- in a previous work in TCB model all the musicians sections of a virtual orchestra were reproduced within the pit of the opera house [111],
- in DUS the array of sound reflectors was designed, optimized and validated through the acoustic simulations of the double configuration available on the stage [112],
- in case of STC and ULH the models were calibrated in parallel with GA++ and the full-spectrum FDTD approach [120, 165].

The availability of medium and large scale models calibrated with the hybrid FDTD/GA method allows several kinds of analyses in comparison with the same models handled with standard GA++ procedure [20]. Basing on existing systematic similar studies [28, 68, 207], the results of the challenges achieved with wave-based techniques are compared with the outcomes of the traditional way to simulate large-scale room environments. At this point, considering that Appendices A and B provides all the necessary data for reproducing the same simulations with both the methods, a preliminary benchmark among the methods may be undertaken focusing on peculiar aspects of the simulated impulse responses [208, 21].

In the whole remarking process, the necessary premise is that it still remains quite difficult to accurately estimate the precision of any simulation method since each simulation technique is based on specific assumptions

[20, 129]. With the purpose of increasing and enhancing the quality of the tools for this estimation, the need to collect data through a group of benchmark case studies in computational acoustics even entailed long-term projects [209]. This chapter is intended to enrich existing works with further comparisons, remarks and assessments on the results coming from thorough acoustic calibrations.

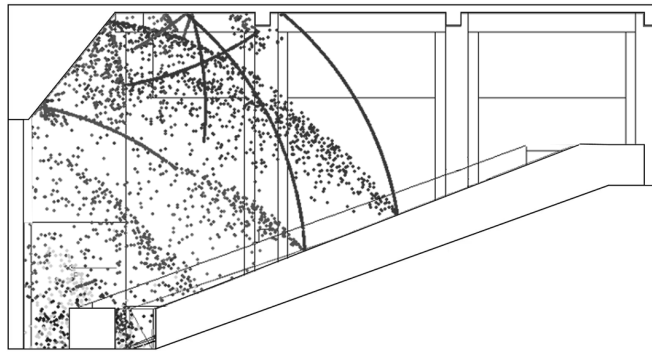
A considerable amount of analyses were carried out by the author for each case study. The most significant results obtained are here presented, along with the considerations and the remarks concerning the choices made during simulation process. Those remarks and the main outcomes from the post-processing analysis is reported hereafter. It should be highlighted that the evaluations of the results are primarily conducted on the basis of measurements results and theoretically expected acoustic phenomena peculiar of each case study.

## 7.1 3D modeling

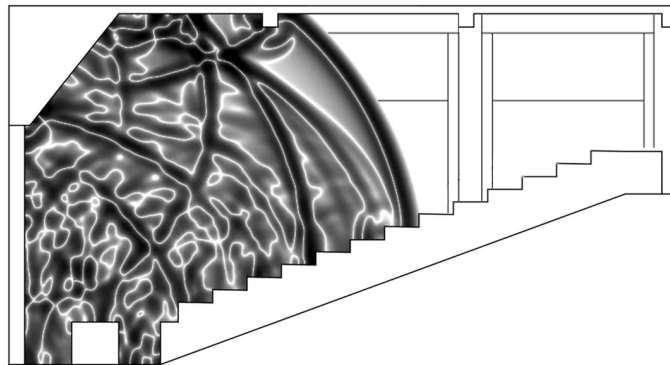
First of all, a comparison between the 3D modeling approximation in wave-based and ray-based approaches is carried out. As it has already been shown, different choices were made from time to time concerning the proper approximation of details or discretization of curved elements [122]. As a general rule of thumb decided by the author, in the present work the same 3D virtual geometries were employed in both FDTD/GA and GA++ calibration processes. This choice is justified by two main factors: the need to have the same starting point for the two distinct approaches and the need to reduce the computational time in the wave-based model due to boundary nodes. Following these two motivations all the models have basically been built according to the state-of-art of GA procedures [25, 123]. According to specific studies on 3D modeling approximation in room acoustics simulation, the recommendations for 3D modeling phase - listed hereafter- are directly derived from the factors affecting the acoustical features of a hall [122].

- Since the volume of the room plays a fundamental role in affecting the acoustic properties of the hall, it is important that the overall geometry of the model - rather than the details - is preserved.
- Given that the equivalent absorption area  $A$  is the product of the surface area  $S$  and the absorption coefficient  $\alpha$ , reducing the complexity of the model implies reducing the surface of some elements. Hence, it is often necessary to take into account a compensation by means of adjustments of absorption coefficient.

- The tilt of the surfaces is a feature that should be preserved because it brings the directional information of the reflections. The higher the distance between the reflection point on a surface and the receiver, the higher the importance of the orientation of the faces. Even small differences in the tilt of a face can involve significant differences in the resulting paths.
- The selection of details that should not be modeled is closely related to the fact that the effects of small details are neglectable in the acoustic simulation when the wavelength of the sound is greater than the dimensions of the details.



(a) GA++ (planar seats surface + scattering coefficient)



(b) FDTD (modeled edges of the seats)

Figure 7.1: Qualitative visualization of sound wave propagation within the lecture hall by means of GA++ (top) and FDTD (bottom) simulations throughout the longitudinal section. The sound source is located in the teacher's position (S1 in Fig. 6.2).

Only in ULH case study the geometry was specifically modified to be computed with FDTD models (see Fig. 7.1). This choice is due to the

role of the edge diffraction in classrooms and lecture halls, given the strong relevance of seats area on the overall acoustics. Considering the common features of those kinds of environments, it should be reminded that most of the linings involved in lecture halls are made up of hard and reflective materials, involving plastered rigid walls, floors and ceilings. The consequence is that the elements that absorb and scatter the sound energy more than all the rest of materials involved are generally the seats. This is also confirmed by studies undertaken by the author concerning the acoustic characterization of the block of the seats in terms of consequent scattered sound energy [120, 172]. Therefore, the seats in ULH - that are wooden benches in this case - have been modeled as boxes with upper planar surfaces in Odeon (as recommended in the software's user manual) and boxes with an upper "staircase" representing the edges of each row of seats in the FDTD/GA method. A qualitative visualization of sound wave propagation within the lecture hall by means of GA++ and FDTD simulations throughout the longitudinal section of the hall is provided in Figure 7.1, considering the sound source located in the teacher's position (S1 in Fig. 6.2). The frame from Odeon GIF shows the results of a specific tool of the software [66, 81] that returns the sound propagation from an omnidirectional sound source by means of small billiard balls [80, 82]. This tool is usually used to track phenomena like flutter echoes or focusing from cruved surfaces, besides for checking the watertightness of the model. The amount of scattered billiard balls depends on the scattering coefficient assigned to the surfaces concerned. In case of seats, a scattering coefficient is typically set equal to  $0.6 \pm 0.1$  (see also Appendix A). It is important to also remark that the visualization is provided considering the scattering but not the absorption coefficient, meaning that the sound propagation does not follow the actual decay. Instead, the frame from the FDTD animation shows exactly the sound propagation throughout the space taking into account the boundary conditions and naturally computing the diffraction caused by the edges of the seats.

This qualitative assessment entails two early considerations.

- On one hand, modeling both the seats area with boxes with upper planar surface could have returned an unlikely sound wave propagation in case of FDTD code. On the other hand, modeling both the seats area with the "staircase" effects due to the seats rows could have returned more uncertainties (connected to the choice of the scattering coefficient and the edge diffraction computation) in GA++ results.
- Given that the same absorption values have been assigned to the seats in the two algorithms employed (directly in case of GA++ simulations and passing through acoustic admittances in FDTD simulations), it

is possible to deduce that in ordinary room as the lecture hall under study, the 3D modeling choices and the scattering coefficient in Odeon Room Acoustics are the factors that most affect the simulations results in ordinary rooms.

Indeed, further simulations with different modeling choices would allow a deeper insight on this peculiar issue.

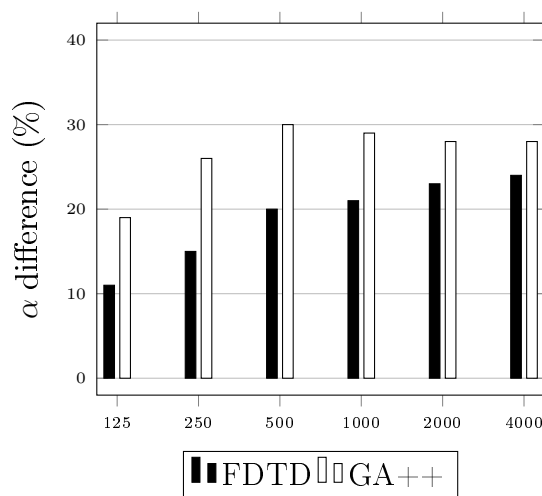
## 7.2 Input data

The second type on remark concerns a thorough investigation of the input data resulting from the calibrated configuration with the two techniques. The uncertainty behind the material properties is a well-known issue in room acoustic simulation field and it probably represents the most crucial aspect in numerical simulation [25, 124].

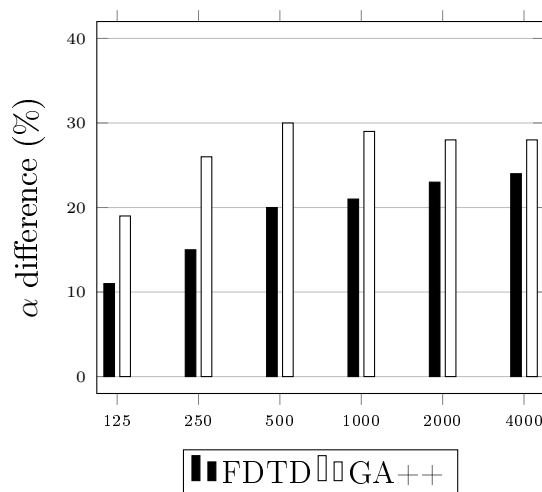
Even though the absorption coefficients are such relevant input data in a virtual sound field simulation, as they strongly affect the acoustic conditions of a real environment, defining the exact value for any material still remains a debated topic among scholars [115, 210]. Among the several sources of uncertainties, a considerable one is related to the method used to measure the random incidence absorption coefficient, reported in the international standard ISO 354 [211]. A recent draft of the ISO 354 attempts to standardize and to redefine the procedure used for measuring the absorption coefficient to limit the degree of arbitrariness in each step of the measurement [210, 212].

Moreover, the different nature of the boundary conditions required by GA++ and FDTD models increases the uncertainty. With this purpose in Appendix A, Tables A.5 and A.6 show the sets of  $\alpha$  values obtained at the end of calibration processes. There are evident differences between the values employed in GA++ and those ones used to derive impedances in FDTD models. That phenomenon is mostly visible at low frequencies and in particular categories of materials. To better visualize the discrepancies, a histogram in octave bands is here provided (see Fig. 7.2). In detail, the figure shows the percentage of differences of  $\alpha$  values between:

- theatre boxes (in TCB), that still represent an open question because it is difficult to assign suited material properties to the articulated system of small coupled volumes, which behave as resonators and return sound energy in the main hall delayed in time;
- seats (mean values among TCB and DUS opera houses), that are the layer most interested by edge diffraction phenomena and thus by the



(a) Boxes (TCB)



(b) Seats (mean values in TCB and DUS)

Figure 7.2: Variations of input data for the two simulation methods in the peculiar cases of theatre boxes and the seats. Black histograms are referred to absorption coefficients derived from the acoustic impedances employed in FDTD algorithm (Table A.5), where white histograms are referred to absorption coefficients directly used as input data in GA++ algorithm (Table A.6).

main theoretical and computational difference between wave-based and ray-based methods.

It should be noted that, for the reasons upon mentioned, these two macro-layers are quite particular compared to the rest of groups of materials. In those cases, a decrease up to 40 % proves to be necessary from  $\alpha$  values

resulting from Odeon to  $\alpha$  values converted in impedances to calibrate the FDTD models. The discrepancy seems to be caused by peculiar wave phenomena as the resonance. In fact, while the scattering coefficients is useful to manage the roughness of the surfaces and the presence of edges and details of the objects, time shift of reflected energy due to particular cases is handled with much effort by GA++ algorithms. For instance, the acoustic behaviour of theatre boxes may be considered similar to an array of resonator cavities, giving back sound energy in the main hall after a certain time delay [106]. At the same way, the material labeled as *wood* (see Tables A.5 and A.6) in TCB is mostly made up of the hollow wooden structure on joists. Therefore, the typical absorption behaviour at low frequencies due to resonance effect is necessarily converted in a higher absorption coefficient in those octave bands.

A further group of objects with different input data for the two simulations approaches is related to the seats. This fact may be due to the well known dip-seat effect, occurring in concert halls and theatres when a high number of seat rows is present. All those discrepancies, highlighted in italics in Table A.6 and stressed in Figure 7.2, confirm how much the experience of the user is important while handling with the available dataset of absorption coefficients for deriving acoustic impedances for wave-based simulations.

A further cause of uncertainty is due to the intrinsic difference between wave-based and ray-based models: the computation of wave phenomena. As it has been widely shown, while GA techniques compensate the lack of diffraction computation through the scattering coefficients (and higher absorption coefficients), FDTD methods naturally handle all the wave phenomena with a physical wave model, overcoming the inherent uncertainty in choosing the scattering value. The need to apply a further material property - besides the absorption coefficient - as input information in GA++ calculation increases the inherent uncertainty of the whole process. This fact is compounded by a limited presence of scattering datasets in current literature, compared to the wide availability of absorption coefficients [79].

### 7.3 Multi-decay analysis

As already explored in Sections 4.1.3 and 4.2.3 in Chapter 4, the energy decay curves return a lot of information about the acoustic characteristics of the environment. In fact, it is no coincidence that most of the common room criteria are derived from the envelope of the sound energy decay [128]. For the same reason, energy decay curves are often used to compare IRs derived from different simulation algorithms and the corresponding IRs acquired through acoustic measurements [35]. It has been proven that coupled

volume geometries significantly affect the decay-curve shape. This is mainly caused by spatial depending factors, deriving from nondiffuse transfer of energy between the subvolumes and the strong influence of the source-receiver relative position [89]. In opera houses the decays generally show the so-called “cliff-type” characteristics, being EDT values smaller than  $T_{30}$  values [137]. Multi-decay analysis performed on the impulse responses (IRs) generally allow to detect and understand these effects caused by coupled volumes [104].

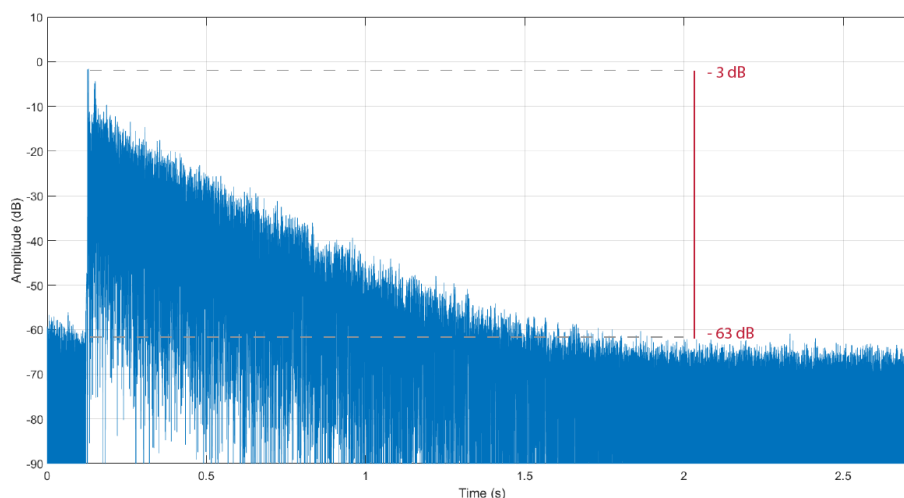


Figure 7.3: Example of energy decay range in an acquired IR in TCB. With reference to Fig. 4.5, the sound source is located in the centre of the stage (S2) and the receiver in a lateral box of the third tier (R19).

First of all, it should be highlighted that all the measurements campaign carried out in the present work were performed with enough gain to obtain a significant signal-to-noise ratio, and thus enough headroom to accurately derive room criteria [139]. An example is provided in Figure 7.3 where a considerable decay range ( $\sim 60$  dB) of a measured IR is shown. The IR assessed corresponds to the following source-receiver pair in TCB: the sound source is located in the centre of the stage (S2) and the receiver in a lateral box of the third tier (R19) (see Fig. 4.5). In TCB, DUS, STC sound pressure levels at the listeners positions were comparable to those caused by an orchestra and a singer, in order to properly excite the wooden parts of the theatre [111, 112]. Furthermore, in ULH a considerable decay range is also fundamental to guarantee the evaluation of the speech transmission index - in particular the so called  $STI_{\infty}$  [196] - with neglectable background noise compared to the received sound pressure level at the receiver [119, 178, 202, 213].

As already illustrated in Chapter 4, in case of particularly articulated geometries - as the two Italian opera houses TCB and DUS - the presence of

multi-slope sound energy decays is firstly investigated through the analysis of IRs obtained with acoustic measurements. In other words, the acoustic behaviour of the coupled volumes - the orchestra pit, the stage house, the theatre boxes, the main hall - are investigated through precise locations of sources and receivers. Hence, placing the sound sources and the microphone receivers in many points of different parts of the opera houses led to a wide amount of IRs with different multi-slope characteristics. In the present section multi-decay analyses are employed not only to better understand the distinct acoustic conditions depending on the location of the listeners but also to test the performance of FDTD models to render those complex acoustic phenomena [104].

The first consideration concern the comparison between TCB and DUS acoustic characteristics. Figure 7.4 provides Bayesian analyses' results of FDTD simulated IRs at 1000 Hz corresponding to three different source-receiver pairs in each hall. In this kind of analysis, the sound source is always located in the centre stage position (S2 points in Figures 4.5 and 4.19) and each receiver belongs to a distinct audience area (stalls, boxes and gallery in TCB, stalls, I balcony and II balcony in DUS). In TCB the multi-decay effects are more visible in the boxes (Fig. 7.4(c)) rather than the remaining source-receiver combinations. In fact, the first part of the decay curve is expected to be affected by the absorbing walls of each theatre box, while the second part by the more diffuse sound field of the main hall [106]. The consequent effect of a considerably lower EDT compared to the  $T_{30}$  is in line with the typical perception of acoustic dry condition in the boxes [137]. It should be noticed that this effect is less visible when listeners are in the stalls due to the presence of reflective sidewalls all around the seats [101]. In detail, coupling effects are present in most of the listeners positions, i.e. in the stalls and in the boxes, with more evidence in the latter ones (Figs. 7.4(a), 7.4(c)). In the gallery, where there is the highest perceived reverberance in TCB, the effect becomes null being EDT more similar to  $T_{30}$  (linear decay in Fig. 7.4(e)). Conversely, in DUS a slight presence of double-slope decay is detected in the whole audience area, with more accentuated evidence in balconies overhangs, confirming the theories by [108].

The second remark concern the comparison with measured IRs and simulated IRs through GA++ techniques. In this analysis, energy decay curves are exploited as a term of analysis and comparison between two impulse responses computed from different simulations approaches [207, 35]. In order to make a comparison between the hybrid FDTD/GA method and Odeon, Figure 7.5 provides the energy decay curves of a measured IR along with the corresponding energy decay curves of simulated IRs in octave bands. The choice fell on a particular source-receiver pair in TCB: S3 (sound source in

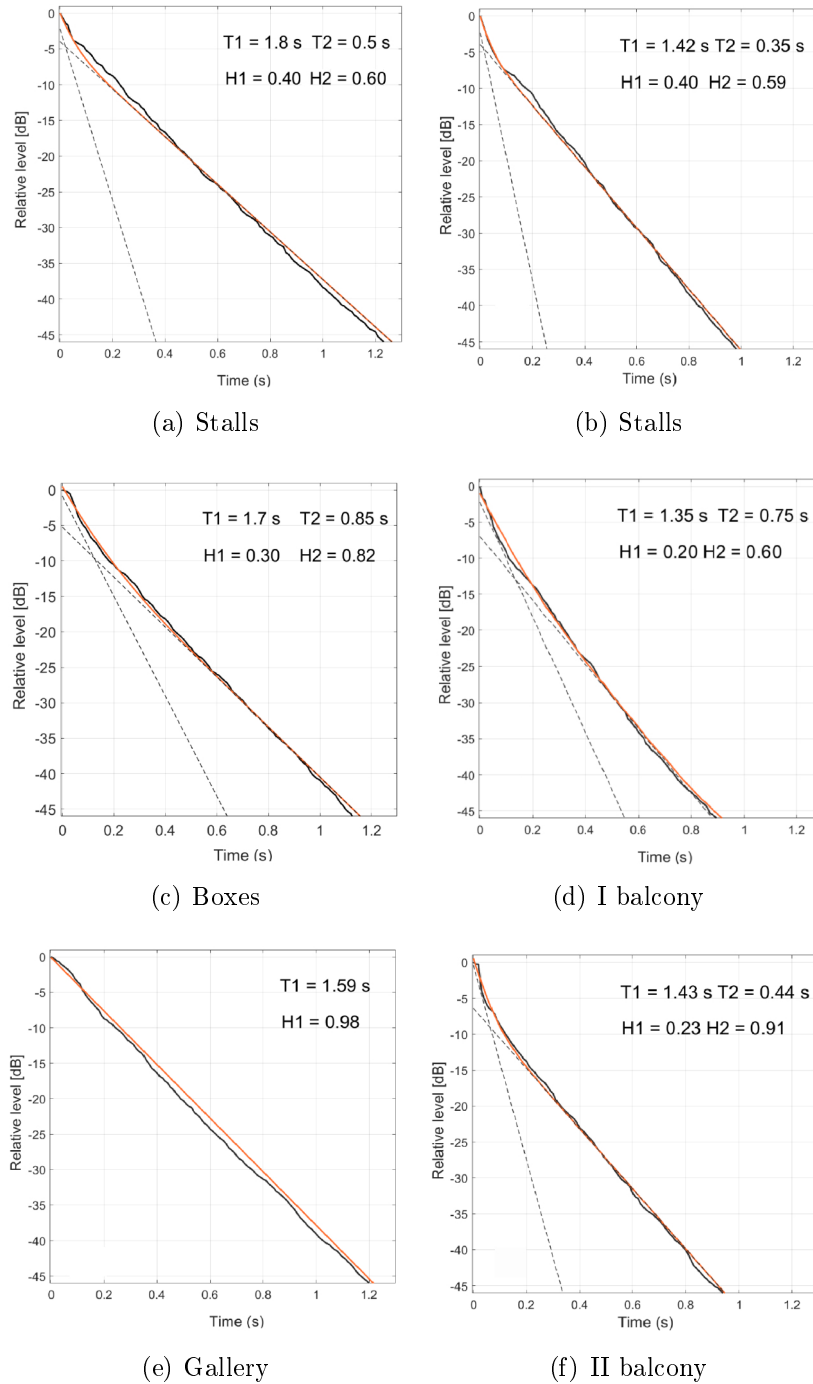


Figure 7.4: Multi-decay analysis of simulated IRs in TCB and DUS at 1000 Hz [104]. The position of the sound source is in the centre of the stage (S2 in Figures 4.5 and 4.19) and each receiver's position belongs to a specific audience area. See Section 4.1.3 for the explanation of the quantities.

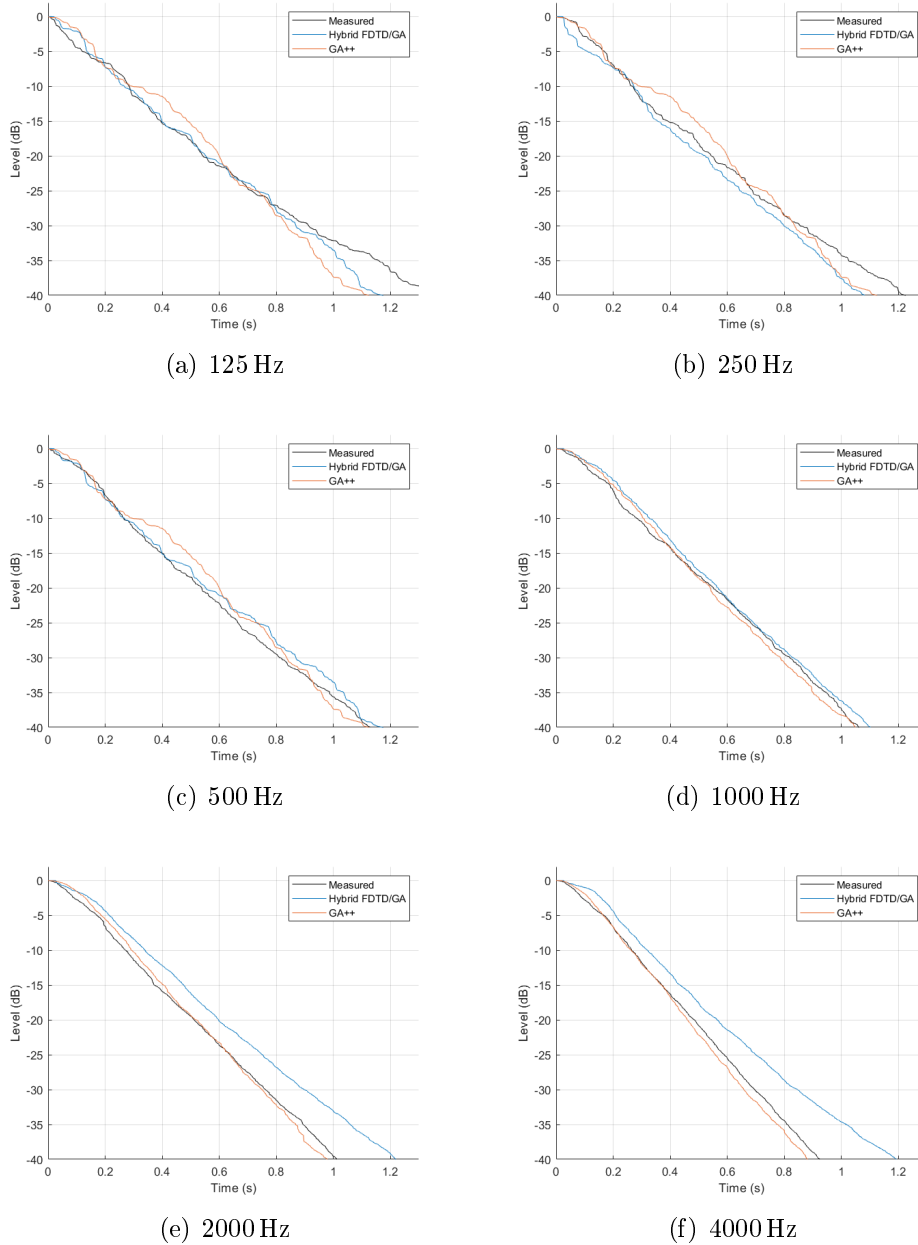


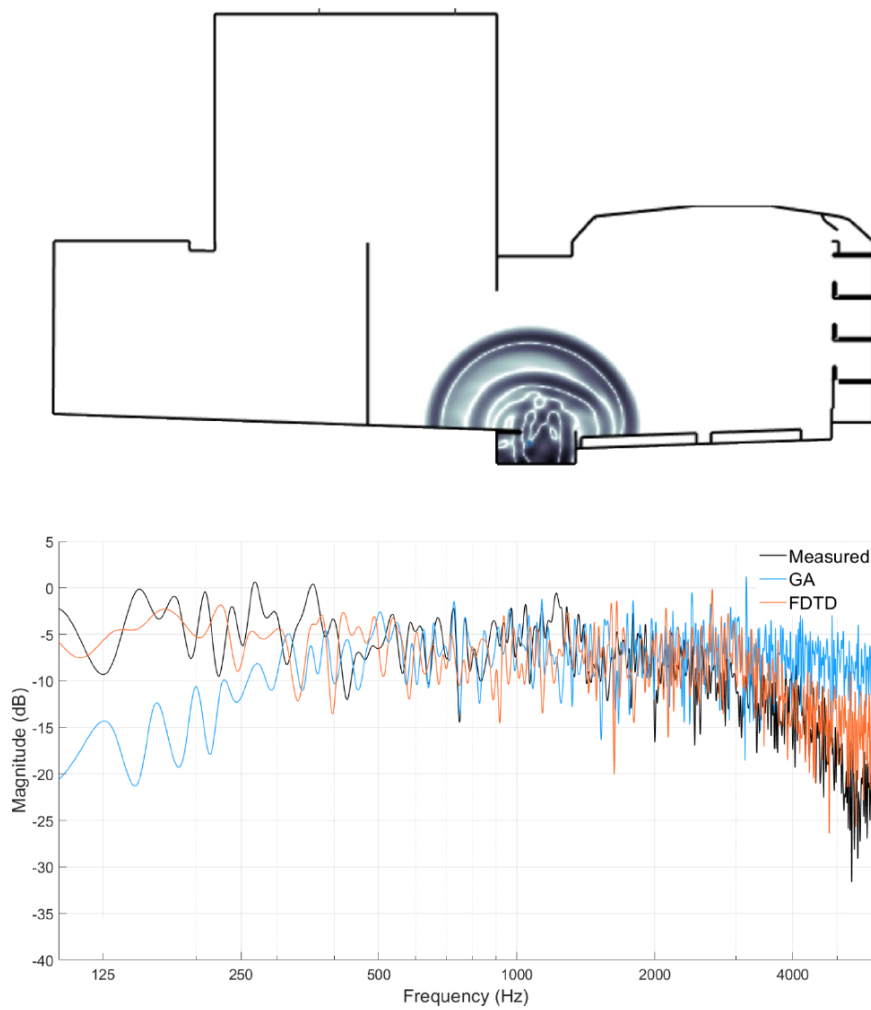
Figure 7.5: Energy decay curve (EDCs) in TCB: sound source in the orchestra pit and receiver in the third row of the stalls (no direct sight line). Comparison between the measured and the simulated IRs with hybrid FDTD/GA and with GA++ methods. Energy decay curve extrapolated using ITA Toolbox for Matlab developed by RWTH Aachen University [214].

the orchestra pit) and R3 (third row of the stalls) where no direct sight line occurs and most of the energy is expected to be diffracted from the edges of the pit. It should be recalled that the GA++ IR was produced using a transition order equal to 0, meaning that no image sources was computed but only stochastic ray tracing (100,000 rays employed) was used (see Table 3.1).

## 7.4 Frequency response

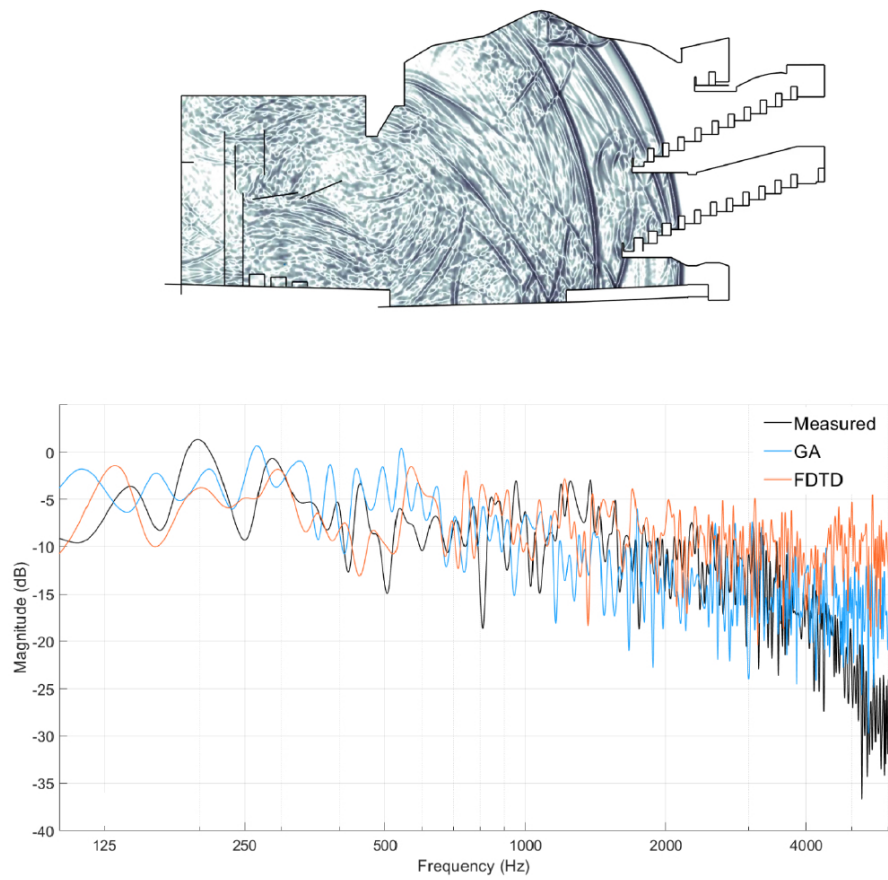
With the goal to furtherly investigate the performance of FDTD simulations, peculiar acoustic aspects deriving from the simulated impulse responses are evaluated [208]. A useful analysis - that can be also employed to compare the IRs obtained with wave-based and ray-based methods - may be the spectral analysis [35, 86, 215]. This important tool allows the exploration of the normalized magnitude of frequency responses for peculiar source-receiver pairs. In fact, the spectral analysis of measured and simulated impulse responses could be useful to assess the ability of the FDTD simulation framework to return reliable results in complex scenarios and to detect the octave bands more concerned by potential discrepancies [86]. In particular, the attention is mainly focused on the low frequency behaviour, which are the octave bands more concerned by the difference of the two methods analysed.

For instance, Figure 7.6 shows measured and simulated frequency responses corresponding to the same source-receiver pair assessed in aforementioned multi-decay analysis (see Fig. 7.5): S3-R3 in TCB opera house, i.e. the sound source located in the orchestra pit and the listener in the third row of the stalls (see Figure 4.5). This source-receiver pair represents a challenge for any simulation approach because there is no direct sightline between the sound source and the receiver [216]. Most of the energy contribution at the receiver is expected to come from reflections and the scattered sound energy from the edges and the rail of the orchestra pit [26]. Measured (black) and simulated (orange) frequency responses are shown along with the corresponding scenarios simulated through GA++ techniques (blue). All the frequency responses involved have been normalized by their maximum values to make the amplitude comparable in this kind of analysis. Then, the upper term of the envelope of each frequency response has been drawn using MATLAB 2019b for ease of comparison. At the bottom of Figure 7.6 is possible to notice significant differences in the energy contributions of the simulated IRs at low frequencies (below 250 Hz). This is probably connected with the intrinsic nature of the two simulation approaches assessed. Unsurprisingly, up



(a) Orchestra pit (S) - Stalls (R)

Figure 7.6: Spectral content of IRs corresponding to a peculiar acoustic scenario in TCB: sound source in the orchestra pit and listener in the third row of the stalls. Comparison between measured, FDTD/GA simulated and GA++ simulated frequency response.



(a) Stage (S) - II balcony (R)

Figure 7.7: Spectral content of IRs corresponding to a peculiar acoustic scenario in DUS: sound source on the stage and receiver in the first rows of the II balcony. Comparison between measured, FDTD/GA simulated and GA++ simulated frequency response.

to a certain frequency the wave phenomena - which are probably crucial in a source-receiver pair with no direct sight-line - are not negligible and thus, the inherent approximation behind geometrical acoustics principles is more evident. Instead, the behaviour of the frequency response of the IR simulated with FDTD/GA method at the same low frequencies matches better with the measured impulse response due to the absence of approximation of wave phenomena [63].

Figure 7.7 provides the results for the following configuration in DUS: S2-R14, i.e. the sound source located in the center of the stage and the listener in the first rows of the second balcony (see Figure 4.19). Being DUS a performance space with weaker coupling effects, the acoustic condition in the different audience areas is expected to be rendered generally with more accuracy by acoustic simulation algorithms [89]. In fact, it is possible to observe the great similarity between the spectral information of the measured IRs and the simulated IRs with FDTD and GA++ methods. Even though the listeners placed near to the rail of the balcony receives a certain amount of scattered energy, probably the direct sightline between the sound source and the receiver grants a better accuracy in rendering the spectral information for both the simulation techniques adopted.

Therefore, the FDTD simulation method was here used as research tool through specific analysis on the simulated impulse responses in calibrated models. Multi-slope analysis and frequency response demonstrated that the wave-based simulation code employed is able to handle large scale volumes with high level of accuracy and to render particular acoustic effects such as those ones caused by acoustic coupling effects in distinct audience areas.



# Chapter 8

## Conclusions

### 8.1 Summary

The ability of numerical methods to predict the acoustic features of enclosures has entailed many scholars to deepen the topic for a long time. Indeed, the possibility to design and predict - or even only render and analyze - the sound field behaviour in any environment is an attractive subject for multi-sectorial disciplines and for several purposes. The whole work of the present thesis has been conceived as a thorough exploration of the feasibility of a cutting-edge hybrid simulation method to model broadband acoustic simulations in non-trivial geometries with specific acoustic conditions. A representative sample of halls was selected by the author and then employed to prove the capability of the selected FDTD/GA simulation framework to tackle large volumes up to high frequencies with reliable results, exploiting the opportunity given by the computational power available at the time of writing.

At the beginning of the manuscript, a comprehensive overview of the main fundamental topics helps to provide a proper starting point for framing the field of action of the whole study. A general description of the numerical methods usually employed in room acoustics is reported, outlining the advantages and the disadvantages of each approach. Spanning from wave-based simulation methods (FEM, BEM, FDM) to ray-based simulation methods (IMS, SRT), the most significant challenges and limitations are pointed out to obtain a proper awareness about the inherent approximations behind the assumptions at the basis of each group of methods. Special attention is paid to the way the different methods are able to handle wave phenomena, such as the edge diffraction and the scattering of the surfaces, and the typology of input data required. In fact, these are two among the factors that

cause the most considerable discrepancies between the two macro-categories of simulation approaches. For instance, it should be kept in mind that wave-based methods naturally handle all the wave phenomena with a physical wave model, while classical ray-based algorithms typically imply an inherent approximation and thus, a further degree of uncertainty. Moreover, the boundary conditions required in the former group of methods involve the use of complex acoustic impedances/admittances, whereas the boundary conditions required by the latter group of methods involve energy parameters as the absorption coefficients.

The simulation framework developed by the *Acoustics and Audio Group* of the University of Edinburgh (UK) is presented and described along with detailed guidelines for the best combination of simulation setup parameters for the desired purposes, especially focussing on the FDTD part of the code. Some simplified flowcharts are outlined to explain the optimization process developed to obtain accurate results with reasonable time costs. The hybrid model was conceived as a combination of FDTD at low-mid frequencies (with FVTD at the boundaries) and, by means of a crossover filter, a classical GA algorithm at high frequencies with the possibility to choose - among all the setup variables - the threshold frequency ( $f_{max}$ ) between the two approaches from time to time. The main concerns about using FDTD methods in large environments have been caused by the high computational cost so far. Moreover, the implementation of frequency-dependent wall impedances in non-trivial geometries maintaining the stability of the system has been quite challenging up to recent years. Both those challenges - that represented significant obstacles up to this moment - have been considerably overcome in the last years. The present work provides the method and the results of the application of the hybrid model under study to different challenging scenarios. The boundary of the whole challenge was pushed especially concerning the huge size of some non-trivial environments and the full-spectrum wave-based simulation in environments with moderate volume. The study exploits the current technological opportunities in FDTD applications assessing the accuracy of the results, the computational costs, the necessary input data, and the ability to detect specific acoustic effects.

The hybrid FDTD/GA was tested in four different case studies: a traditional opera house, a modern opera house, an elliptical concert hall, and a large university lecture hall. All these environments show different features in terms of shape, size, materials, and purpose. The choice of the halls has been thoroughly explained in Chapter 3 and then described in detail in Chapters 4, 5, 6, 7. The results of the measurements campaigns carried out in each environment were considered as an important reference point to calibrate the 3D virtual models with a rigorous approach. Specific room

and intelligibility criteria have been selected to describe the different acoustic features in the cases under study, according to the standards and existing scientific literature. FDTD simulations were used as a useful research tool through several analyses on the simulated impulse responses in calibrated models. The multi-slope analysis reported for the two opera houses demonstrated that the wave-based simulation code is able not only to simulate large-scale volumes with a high level of accuracy but also to detect particular acoustic effects such as those ones caused by acoustic coupling volumes. In the elliptical concert hall, the simulations proved to be able to exactly return the acoustic phenomena caused by the curved sidewalls and clearly perceivable in the architecture: the flutter echoes and the focusing effects in specific receiving points. Within the university lecture hall, the time-domain simulation approach has been employed to render the complex behaviour of the time-dependent modulations of the speech signal and the time-delayed acoustic response of the acoustic treatment made up of micro-perforated panels. The model returned thorough results in reasonable time costs, due to particularly efficient calculation schemes and to the availability of considerable computational power. Specific acoustic effects have been observed, consistently with the measurements results, the subjective perception at the listeners' locations, and theoretical expectations.

The chapter on the main remarks outlines some of the key points of the whole work, such as the 3D modeling phase, the assignment of the input data, the multi-decay analysis, and the frequency response in peculiar source-receiver pairs. Moreover, similarities and differences with the GA++ approach usually employed in large-scale room acoustics simulations are discussed. Among those topics, the open issues of the degree of approximation needed during the 3D modeling phase and the proper threshold size for geometrical details in FDTD simulations are developed. Further considerations have been made analyzing the frequency responses of the measured and simulated impulse responses employing the two distinct simulation approaches. The challenging acoustic scenario of source-receiver pairs with no direct sight-line was chosen. For instance, the peculiar case of a sound source within an orchestra pit and a listener in the first rows of the stalls seats in a coupled volume hall was assessed, where a considerable contribution of the scattered energy due to the edge diffraction is expected. The most evident differences between the simulation methods occurring at low frequencies have been reported and discussed. Concerning the other crucial topic of the boundary conditions, a comparison is made among the input data required to calibrate the FDTD and GA++ models based on the same measurements results. Not surprisingly, there are significant discrepancies especially in the frequency range and in those materials concerned by the stronger approximation of

geometrical acoustics. With this purpose, in the Appendix A and in the freely available repository described in the Appendix B of the present thesis, the input data of the simulations involved in the whole work are reported, providing a collection of data useful for a preliminary benchmark procedure.

## 8.2 Outlook and future work

At the end of the present dissertation, several topics are still debated and need further investigations. Indeed, an important area of investigation still remains the uncertainty connected to the material input data. The degree of uncertainty behind the inherent non-unique conversion of random incidence absorption coefficient to complex acoustic impedances is quite challenging to be quantified. Future works may develop the opposite workflow, employing theoretically consolidated models for complex acoustic impedances in wave-based models and then converting the values in energy based parameters in ray-based models. That will be probably helpful in compensating the lack of large datasets of acoustic impedances in literature. Still on the topic of boundary conditions and input data, at the time of writing it remains difficult to implement extended reaction in impedance model employed in FDTD simulations. Therefore, a short-term possible outlook is the application of locally reactive model of boundary conditions depending on the incidence angle for a more reliable representation of the actual material properties.

The second important issue deals with the computational cost inherent to the calculation process, that still remains a challenging point, as expected in wave-based simulation models. While up to now the computational cost of the simulation appears to be generally too high to fully exploit the wave-based model in composite large environments, it would be desirable to be able to simulate with reduced time costs from now on, employing recent and future advances in parallel computing tasks. That important breakthrough could allow people involved in the acoustic design, such as architects, engineers, and acousticians, to enhance the effectiveness of their work and to obtain more reliable data for a better final comfort of the users.

With this purpose, the present thesis is intended to create a useful combination of practical guidelines, technical suggestions and theoretical considerations for a standardized and optimized approach to room acoustics simulations. The final objective of the thesis is to define a neutral benchmark between the state-of-art of large-scale rooms simulation and the new boundaries allowed by recent research successes in wave-base methods by testing one of the models belonging to this latter category. The work outlines theoretical and practical remarks on the effectiveness of the hybrid simulation

method adopted, enhancing the existing scientific literature with further data and case studies for an increasingly thorough benchmark of computational acoustics techniques.



# Appendix A

## Boundary conditions

### A.1 LRC coefficients

In the present work, the frequency-dependent boundary admittances employed in the FDTD part of the FDTD/GA simulation framework are approximated with electrical-acoustical analogies. In detail, the following formula expresses the relationship between the normalized LRC (inductance, resistance, capacitance) and the acoustic admittance ( $\gamma$ ) [17, 52]:

$$\gamma(\mathbf{x}) = \sum_{m=1}^M \frac{s}{L^{(m)}(\mathbf{x})s^2 + R^{(m)}(\mathbf{x})s + \frac{1}{C^{(m)}(\mathbf{x})}} \quad (\text{A.1})$$

where

- $\gamma$  is the complex specific admittance,
- $M$  is the number of different branches involved in the circuit,
- $s$  is the usual transform variable,
- $L$  is the real-valued non-negative inductance of the circuit,
- $R$  is the real-valued non-negative resistance of the circuit,
- $C$  is the real-valued non-negative capacitance of the circuit.

It is important to notice that for  $M = 1$  the circuit represents the combination of a mass, spring and resistance, as it occurs in the simpler models of wall admittances [4]. In the present Appendix, Tables A.1, A.2, A.3, A.4 provide the necessary data ( $L$ ,  $R$ ,  $1/C$ ) for calculating the frequency-dependent acoustic admittances of each material involved.

Table A.1: Normalised LRC (inductance, resistance, capacitance) coefficients employed as input data in FDTD simulations to approximate frequency dependent boundary admittances in TCB.

<b>Carpet</b>			<b>Velvet drapes</b>		
L	R	1/C	L	R	1/C
0	$3.80 \times 10^2$	0	0	$3.95 \times 10^1$	0
1.01	$5.62 \times 10^2$	$6.24 \times 10^5$	$1.32 \times 10^{-1}$	$7.35 \times 10^1$	$8.17 \times 10^4$
$2.98 \times 10^{-1}$	$3.31 \times 10^2$	$7.36 \times 10^5$	$2.14 \times 10^{-2}$	$2.38 \times 10^1$	$5.28 \times 10^4$
$1.16 \times 10^{-1}$	$2.58 \times 10^2$	$1.15 \times 10^6$	$3.78 \times 10^{-3}$	8.39	$3.73 \times 10^4$
$4.63 \times 10^{-2}$	$2.06 \times 10^2$	$1.83 \times 10^6$	$3.34 \times 10^{-3}$	$1.49 \times 10^1$	$1.32 \times 10^5$
$6.76 \times 10^{-3}$	$6.01 \times 10^1$	$1.07 \times 10^6$	$1.47 \times 10^{-3}$	$1.31 \times 10^1$	$2.32 \times 10^5$
$2.54 \times 10^{-3}$	$4.52 \times 10^1$	$1.61 \times 10^6$	$4.16 \times 10^{-4}$	7.39	$2.63 \times 10^5$
<b>Wood</b>			<b>Plaster (boxes)</b>		
L	R	1/C	L	R	1/C
0	$1.43 \times 10^2$	0	0	$1.82 \times 10^2$	0
$9.43 \times 10^{-2}$	$5.23 \times 10^1$	$5.81 \times 10^4$	$5.56 \times 10^{-1}$	$3.09 \times 10^2$	$3.43 \times 10^5$
$8.05 \times 10^{-2}$	$8.95 \times 10^1$	$1.99 \times 10^5$	$9.83 \times 10^{-2}$	$1.09 \times 10^2$	$2.43 \times 10^5$
$1.10 \times 10^{-1}$	$2.44 \times 10^2$	$1.08 \times 10^6$	$3.95 \times 10^{-2}$	$8.78 \times 10^1$	$3.90 \times 10^5$
$4.28 \times 10^{-2}$	$1.90 \times 10^2$	$1.69 \times 10^6$	$1.78 \times 10^{-2}$	$7.90 \times 10^1$	$7.02 \times 10^5$
$2.14 \times 10^{-2}$	$1.90 \times 10^2$	$3.38 \times 10^6$	$9.06 \times 10^{-3}$	$8.05 \times 10^1$	$1.43 \times 10^6$
$1.07 \times 10^{-2}$	$1.90 \times 10^2$	$6.76 \times 10^6$	$4.53 \times 10^{-3}$	$8.05 \times 10^1$	$2.86 \times 10^6$
<b>Marble</b>			<b>Stage house</b>		
L	R	1/C	L	R	1/C
0	$7.78 \times 10^2$	0	0	$6.51 \times 10^1$	0
1.86	$1.03 \times 10^3$	$1.15 \times 10^6$	$9.63 \times 10^{-2}$	$5.35 \times 10^1$	$5.94 \times 10^4$
1.16	$1.29 \times 10^3$	$2.87 \times 10^6$	$4.81 \times 10^{-2}$	$5.35 \times 10^1$	$1.19 \times 10^5$
$2.29 \times 10^{-1}$	$5.09 \times 10^2$	$2.26 \times 10^6$	$2.41 \times 10^{-2}$	$5.35 \times 10^1$	$2.38 \times 10^5$
$7.06 \times 10^{-2}$	$3.14 \times 10^2$	$2.79 \times 10^6$	$1.12 \times 10^{-2}$	$4.98 \times 10^1$	$4.43 \times 10^5$
$4.03 \times 10^{-2}$	$3.58 \times 10^2$	$6.37 \times 10^6$	$1.11 \times 10^{-2}$	$9.82 \times 10^1$	$1.75 \times 10^6$
$1.33 \times 10^{-2}$	$2.36 \times 10^2$	$8.39 \times 10^6$	$4.87 \times 10^{-3}$	$8.66 \times 10^1$	$3.08 \times 10^6$
<b>Stage grid</b>			<b>Seats</b>		
L	R	1/C	L	R	1/C
0	$3.23 \times 10^1$	0	0	$3.23 \times 10^1$	0
$9.23 \times 10^{-2}$	$5.13 \times 10^1$	$5.69 \times 10^4$	$9.23 \times 10^{-2}$	$5.13 \times 10^1$	$5.69 \times 10^4$
$2.02 \times 10^{-2}$	$2.24 \times 10^1$	$4.98 \times 10^4$	$2.14 \times 10^{-2}$	$2.37 \times 10^1$	$5.27 \times 10^4$
$9.33 \times 10^{-3}$	$2.07 \times 10^1$	$9.20 \times 10^4$	$6.49 \times 10^{-3}$	$1.44 \times 10^1$	$6.41 \times 10^4$
$2.10 \times 10^{-3}$	9.32	$8.28 \times 10^4$	$2.65 \times 10^{-3}$	$1.18 \times 10^1$	$1.05 \times 10^5$
$1.14 \times 10^{-3}$	$1.01 \times 10^1$	$1.80 \times 10^5$	$1.37 \times 10^{-3}$	$1.22 \times 10^1$	$2.17 \times 10^5$
$5.70 \times 10^{-4}$	$1.01 \times 10^1$	$3.60 \times 10^5$	$6.86 \times 10^{-4}$	$1.22 \times 10^1$	$4.33 \times 10^5$

Table A.2: Normalised LRC (inductance, resistance, capacitance) coefficients employed as input data in FDTD simulations to approximate frequency dependent boundary admittances in DUS.

<b>Marble</b>			<b>Plaster (hall)</b>		
L	R	1/C	L	R	1/C
0	$1.57 \times 10^3$	0	0	$1.57 \times 10^3$	0
3.77	$2.09 \times 10^3$	$2.33 \times 10^6$	$1.85 \times 10^1$	$1.03 \times 10^4$	$1.14 \times 10^7$
3.11	$3.45 \times 10^3$	$7.67 \times 10^6$	$3.17 \times 10^{-1}$	$3.52 \times 10^2$	$7.82 \times 10^5$
$2.74 \times 10^{-1}$	$6.08 \times 10^2$	$2.70 \times 10^6$	$1.99 \times 10^{-1}$	$4.42 \times 10^2$	$1.96 \times 10^6$
$1.78 \times 10^{-1}$	$7.90 \times 10^2$	$7.02 \times 10^6$	$6.88 \times 10^{-2}$	$3.05 \times 10^2$	$2.71 \times 10^6$
$4.24 \times 10^{-2}$	$3.77 \times 10^2$	$6.70 \times 10^6$	$1.88 \times 10^{-2}$	$1.67 \times 10^2$	$2.97 \times 10^6$
$2.29 \times 10^{-2}$	$4.07 \times 10^2$	$1.45 \times 10^7$	$1.01 \times 10^{-2}$	$1.79 \times 10^2$	$6.36 \times 10^6$
<b>Stage house</b>			<b>Stage grid</b>		
L	R	1/C	L	R	1/C
0	$1.17 \times 10^2$	0	0	$9.10 \times 10^1$	0
$3.14 \times 10^{-1}$	$1.75 \times 10^2$	$1.94 \times 10^5$	$2.18 \times 10^{-1}$	$1.21 \times 10^2$	$1.34 \times 10^5$
$8.33 \times 10^{-2}$	$9.25 \times 10^1$	$2.05 \times 10^5$	$1.60 \times 10^{-1}$	$1.77 \times 10^2$	$3.94 \times 10^5$
$4.81 \times 10^{-2}$	$1.07 \times 10^2$	$4.74 \times 10^5$	$2.29 \times 10^{-2}$	$5.08 \times 10^1$	$2.26 \times 10^5$
$1.53 \times 10^{-2}$	$6.79 \times 10^1$	$6.04 \times 10^5$	$4.65 \times 10^{-3}$	$2.06 \times 10^1$	$1.83 \times 10^5$
$8.05 \times 10^{-3}$	$7.15 \times 10^1$	$1.27 \times 10^6$	$1.53 \times 10^{-3}$	$1.36 \times 10^1$	$2.41 \times 10^5$
$4.03 \times 10^{-3}$	$7.15 \times 10^1$	$2.54 \times 10^6$	$8.09 \times 10^{-4}$	$1.44 \times 10^1$	$5.11 \times 10^5$
<b>Wood</b>			<b>Velvet drapes</b>		
L	R	1/C	L	R	1/C
0	$2.10 \times 10^2$	0	0	$6.51 \times 10^1$	0
$1.07 \times 10^{-1}$	$5.94 \times 10^1$	$6.60 \times 10^4$	$1.56 \times 10^{-1}$	$8.66 \times 10^1$	$9.62 \times 10^4$
$4.92 \times 10^{-2}$	$5.47 \times 10^1$	$1.21 \times 10^5$	$1.28 \times 10^{-1}$	$1.42 \times 10^2$	$3.15 \times 10^5$
$5.04 \times 10^{-2}$	$1.12 \times 10^2$	$4.97 \times 10^5$	$1.34 \times 10^{-2}$	$2.98 \times 10^1$	$1.32 \times 10^5$
$9.08 \times 10^{-2}$	$4.04 \times 10^2$	$3.59 \times 10^6$	$3.22 \times 10^{-3}$	$1.43 \times 10^1$	$1.27 \times 10^5$
$3.15 \times 10^{-2}$	$2.80 \times 10^2$	$4.97 \times 10^6$	$1.43 \times 10^{-3}$	$1.27 \times 10^1$	$2.25 \times 10^5$
$1.57 \times 10^{-2}$	$2.80 \times 10^2$	$9.94 \times 10^6$	$5.41 \times 10^{-4}$	9.61	$3.41 \times 10^5$
<b>Seats (Stalls)</b>			<b>Seats (balconies)</b>		
L	R	1/C	L	R	1/C
0	$3.64 \times 10^1$	0	0	$3.23 \times 10^1$	0
$6.69 \times 10^{-2}$	$3.72 \times 10^1$	$4.13 \times 10^4$	$3.85 \times 10^{-2}$	$2.14 \times 10^1$	$2.37 \times 10^4$
$5.33 \times 10^{-2}$	$5.92 \times 10^1$	$1.32 \times 10^5$	$4.61 \times 10^{-2}$	$5.13 \times 10^1$	$1.14 \times 10^5$
$1.33 \times 10^{-2}$	$2.95 \times 10^1$	$1.31 \times 10^5$	$2.09 \times 10^{-2}$	$4.65 \times 10^1$	$2.07 \times 10^5$
$4.01 \times 10^{-3}$	$1.78 \times 10^1$	$1.58 \times 10^5$	$6.68 \times 10^{-3}$	$2.97 \times 10^1$	$2.64 \times 10^5$
$1.30 \times 10^{-3}$	$1.15 \times 10^1$	$2.05 \times 10^5$	$3.00 \times 10^{-3}$	$2.67 \times 10^1$	$4.74 \times 10^5$
$5.38 \times 10^{-4}$	9.56	$3.40 \times 10^5$	$1.53 \times 10^{-3}$	$2.73 \times 10^1$	$9.69 \times 10^5$

Table A.3: Normalised LRC (inductance, resistance, capacitance) coefficients employed as input data in FDTD simulations to approximate frequency dependent boundary admittances in STC.

<b>Ceiling</b>			<b>Plasterboard (walls)</b>		
L	R	1/C	L	R	1/C
0	$1.60 \times 10^2$	0	0	$1.43 \times 10^2$	0
$3.84 \times 10^{-1}$	$2.13 \times 10^2$	$2.37 \times 10^5$	$1.13 \times 10^{-1}$	$6.29 \times 10^1$	$6.99 \times 10^4$
$1.92 \times 10^{-1}$	$2.13 \times 10^2$	$4.74 \times 10^5$	$8.35 \times 10^{-2}$	$9.28 \times 10^1$	$2.06 \times 10^5$
$1.01 \times 10^{-1}$	$2.24 \times 10^2$	$9.94 \times 10^5$	$4.49 \times 10^{-2}$	$9.97 \times 10^1$	$4.43 \times 10^5$
$3.72 \times 10^{-2}$	$1.65 \times 10^2$	$1.47 \times 10^6$	$2.56 \times 10^{-2}$	$1.36 \times 10^2$	$2.41 \times 10^6$
$1.93 \times 10^{-2}$	$1.72 \times 10^2$	$3.05 \times 10^6$	$1.53 \times 10^{-2}$	$1.36 \times 10^2$	$2.41 \times 10^6$
$9.65 \times 10^{-3}$	$1.72 \times 10^2$	$6.10 \times 10^6$	$6.98 \times 10^{-3}$	$1.24 \times 10^2$	$4.41 \times 10^6$
<b>Furniture</b>			<b>Wood</b>		
L	R	1/C	L	R	1/C
0	$1.43 \times 10^2$	0	0	$7.78 \times 10^2$	0
$5.91 \times 10^{-2}$	$3.28 \times 10^1$	$3.64 \times 10^4$	$1.26 \times 10^{-1}$	$6.988 \times 10^1$	$7.75 \times 10^4$
$3.53 \times 10^{-2}$	$3.92 \times 10^1$	$8.72 \times 10^4$	$6.09 \times 10^{-2}$	$6.76 \times 10^1$	$1.50 \times 10^5$
$2.57 \times 10^{-2}$	$5.72 \times 10^1$	$2.54 \times 10^5$	$3.79 \times 10^{-2}$	$8.42 \times 10^1$	$3.74 \times 10^5$
$1.80 \times 10^{-2}$	$8.01 \times 10^1$	$7.12 \times 10^5$	$2.26 \times 10^{-2}$	$1.00 \times 10^2$	$8.93 \times 10^5$
$1.69 \times 10^{-2}$	$1.50 \times 10^2$	$2.67 \times 10^6$	$2.65 \times 10^{-2}$	$2.36 \times 10^2$	$4.19 \times 10^6$
$6.98 \times 10^{-3}$	$1.24 \times 10^2$	$4.41 \times 10^6$	$9.55 \times 10^{-3}$	$1.70 \times 10^2$	$6.03 \times 10^6$
<b>Seats</b>					
L	R	1/C			
0	$4.23 \times 10^1$	0			
$1.07 \times 10^{-1}$	$5.95 \times 10^1$	$6.61 \times 10^4$			
$5.69 \times 10^{-2}$	$6.32 \times 10^1$	$1.40 \times 10^5$			
$9.61 \times 10^{-3}$	$2.13 \times 10^1$	$9.48 \times 10^5$			
$2.33 \times 10^{-2}$	$1.04 \times 10^1$	$9.20 \times 10^4$			
$1.39 \times 10^{-3}$	$1.24 \times 10^1$	$2.20 \times 10^5$			
$6.78 \times 10^{-4}$	$1.22 \times 10^1$	$4.34 \times 10^6$			

Table A.4: Normalised LRC (inductance, resistance, capacitance) coefficients employed as input data in FDTD simulations to approximate frequency dependent boundary admittances in ULH.

<b>Plaster</b>			<b>Wood</b>		
L	R	1/C	L	R	1/C
0	$1.57 \times 10^3$	0	0	$3.80 \times 10^2$	0
6.22	$3.45 \times 10^3$	$3.83 \times 10^6$	$1.30 \times 10^{-1}$	$7.24 \times 10^1$	$8.04 \times 10^4$
$6.20 \times 10^{-1}$	$6.88 \times 10^2$	$1.53 \times 10^6$	$4.19 \times 10^{-2}$	$4.65 \times 10^1$	$1.03 \times 10^5$
$1.83 \times 10^{-1}$	$4.07 \times 10^2$	$1.81 \times 10^6$	$9.45 \times 10^{-2}$	$2.10 \times 10^2$	$9.33 \times 10^5$
$6.12 \times 10^{-2}$	$2.72 \times 10^2$	$2.42 \times 10^6$	$1.95 \times 10^{-1}$	$8.65 \times 10^2$	$7.69 \times 10^6$
$3.23 \times 10^{-2}$	$2.87 \times 10^2$	$5.10 \times 10^6$	$5.68 \times 10^{-2}$	$5.05 \times 10^2$	$8.98 \times 10^6$
$1.62 \times 10^{-2}$	$2.87 \times 10^2$	$1.02 \times 10^7$	$2.84 \times 10^{-4}$	$5.05 \times 10^2$	$8.98 \times 10^6$
<b>Windows</b>			<b>Seats</b>		
L	R	1/C	L	R	1/C
0	$3.80 \times 10^2$	0	0	$8.45 \times 10^1$	0
$2.11 \times 10^{-1}$	$1.17 \times 10^2$	$1.30 \times 10^5$	$3.74 \times 10^{-2}$	$2.08 \times 10^1$	$2.31 \times 10^4$
$1.00 \times 10^{-1}$	$1.11 \times 10^2$	$2.48 \times 10^5$	$2.06 \times 10^{-2}$	$2.28 \times 10^1$	$5.07 \times 10^4$
$6.76 \times 10^{-2}$	$1.50 \times 10^2$	$6.67 \times 10^5$	$2.12 \times 10^{-2}$	$4.71 \times 10^1$	$2.09 \times 10^5$
$1.95 \times 10^{-1}$	$8.65 \times 10^2$	$7.69 \times 10^6$	$1.97 \times 10^{-2}$	$8.75 \times 10^1$	$7.78 \times 10^5$
$5.68 \times 10^{-2}$	$5.05 \times 10^2$	$8.98 \times 10^6$	$1.13 \times 10^{-2}$	$1.01 \times 10^2$	$1.79 \times 10^6$
$2.84 \times 10^{-2}$	$5.05 \times 10^2$	$1.80 \times 10^7$	$6.50 \times 10^{-3}$	$1.16 \times 10^2$	$4.11 \times 10^6$

## A.2 Energy parameters

The present section provides the main material properties involved in the calibration of the environments in terms of energy based parameters. For each case study, the input data corresponding to the achievement of calibration process are provided. It should be remembered that the material properties are reported in terms of absorption coefficients in order to compare the input data of the hybrid FDTD/GA model employed with the standard GA++ procedure. On one hand, Table A.5 provides the corresponding absorption coefficients derived from the acoustic admittances used in FDTD calibration. On the other hand, Table A.6 provides the absorption coefficients employed in GA++ simulations. It should be noticed that in Table A.6  $\alpha$  values that differ from the corresponding  $\alpha$  values derived from the acoustic admittances used in FDTD calibration are highlighted in italics, along with the percentage of difference between brackets. For more details, see FDTD and GA++ calibration procedures, respectively, in Sections 3.4 and 3.5.

The choice of the author on which layers had to be adjusted is justified by the characteristics of the objects belonging to that layer. Therefore, main discrepancies between input data of the two simulation approaches are referred to surfaces corresponding to:

- wooden elements, especially when backed by an air cavity as it occurs in wooden floors or in opera houses linings (since wooden layers behave as a membrane sound absorber);
- plaster of the theatre boxes (in TCB), because no furniture inside each theatre box was modeled and due to the fact that these spaces act as acoustic resonators;
- seats, because they are elements in which the removal of details is most significant and the material properties tend to compensate the lack of geometries especially in GA++ procedure.

It is interesting to notice that in STC and ULH there are no discrepancies between the  $\alpha$  values derived from the acoustic admittances used in FDTD calibration and the  $\alpha$  values employed in GA++ simulations (see last rows of Tables A.5 and A.6). This is probably due to the fact that in spaces more ordinary than opera houses it is generally plausible to divide the materials at most in four or five layers depending on the main acoustic properties of the objects involved. Consequently, with less variables as control parameters, achieving the acoustic calibration proves to be in a certain way simplified, leading to a smoother overall workflow.

Table A.5: Corresponding absorption coefficients derived from the acoustic admittances used in FDTD calibration. See text for details.

Material	125 Hz	250 Hz	500 Hz	1000 Hz	2000 Hz	4000 Hz
<b>TCB</b>						
Carpet	0.04	0.05	0.06	0.08	0.16	0.20
Velvet drapes	0.30	0.45	0.65	0.56	0.59	0.71
Wood	0.20	0.15	0.10	0.10	0.10	0.10
Plaster (boxes)	0.08	0.12	0.14	0.15	0.15	0.15
Marble	0.02	0.02	0.03	0.03	0.04	0.04
Stage house	0.25	0.25	0.25	0.25	0.20	0.20
Stage grid	0.35	0.45	0.50	0.65	0.65	0.65
Seats	0.35	0.45	0.55	0.60	0.60	0.60
<b>DUS</b>						
Marble	0.01	0.01	0.02	0.02	0.03	0.03
Plaster (hall)	0.01	0.03	0.03	0.04	0.06	0.06
Stage house <sup>c</sup>	0.12	0.15	0.15	0.18	0.18	0.18
Stage grid	0.15	0.15	0.25	0.40	0.50	0.50
Wood	0.18	0.18	0.12	0.07	0.07	0.07
Velvet drapes	0.20	0.35	0.35	0.45	0.50	0.50
Seats (stalls)	0.35	0.35	0.40	0.50	0.60	0.65
Seats (balconies)	0.48	0.50	0.50	0.60	0.52	0.62
<b>STC</b>						
Ceiling	0.09	0.09	0.09	0.10	0.10	0.10
Plasterboard (walls)	0.18	0.15	0.14	0.13	0.12	0.12
Furniture	0.28	0.25	0.20	0.16	0.12	0.12
Wood	0.15	0.15	0.12	0.10	0.06	0.06
Seats	0.28	0.30	0.45	0.60	0.58	0.58
<b>ULH</b>						
Plaster	0.01	0.02	0.03	0.03	0.04	0.06
Wood	0.15	0.18	0.04	0.04	0.04	0.04
Windows	0.10	0.10	0.08	0.04	0.04	0.04
Seats	0.40	0.37	0.26	0.19	0.17	0.16

Table A.6: Absorption ( $\alpha$ ) and scattering ( $s$ ) coefficients employed in GA++ simulations:  $\alpha$  values that differ from the corresponding  $\alpha$  values derived from the acoustic admittances used in FDTD calibration are highlighted in italics, along with the percentage of difference between brackets. See text for details.

Material	$\alpha$						$s$
	125 Hz	250 Hz	500 Hz	1000 Hz	2000 Hz	4000 Hz	
<b>TCB</b>							
Carpet	0.04	0.05	0.06	0.08	0.16	0.20	0.05
Velvet drapes	0.30	0.45	0.65	0.56	0.59	0.71	0.05
Wood	<i>0.30 (+33%)</i>	<i>0.28 (+46%)</i>	<i>0.20 (+50%)</i>	<i>0.16 (+38%)</i>	<i>0.14 (+29%)</i>	<i>0.10 (0%)</i>	0.02
Plaster (boxes)	<i>0.16 (+50%)</i>	<i>0.25 (+52%)</i>	<i>0.29 (+52%)</i>	<i>0.29 (+48%)</i>	<i>0.30 (+50%)</i>	<i>0.30 (+50%)</i>	0.30
Marble	0.02	0.02	0.03	0.03	0.04	0.04	0.05
Stage house	0.25	0.25	0.25	0.25	0.20	0.20	0.50
Stage grid	0.35	0.45	0.50	0.65	0.65	0.65	0.50
Seats	0.35	0.45	0.55	0.60	0.60	0.60	0.70
<b>DUS</b>							
Marble	0.01	0.01	0.02	0.02	0.03	0.03	0.05
Plaster (hall)	0.01	0.03	0.03	0.04	0.06	0.06	0.30
Stage house <sup>a</sup>	0.12	0.15	0.15	0.18	0.18	0.18	0.30
Stage grid	0.15	0.15	0.25	0.40	0.50	0.50	0.25
Wood	0.18	0.18	0.12	0.07	0.07	0.07	0.40
Velvet drapes	0.20	0.35	0.35	0.45	0.50	0.50	0.15
Seats (stalls)	<i>0.48 (+27%)</i>	<i>0.50 (+30%)</i>	<i>0.50 (+20%)</i>	<i>0.58 (+14%)</i>	<i>0.58 (-3%)</i>	<i>0.60 (-8%)</i>	0.60
Seats (balconies)	<i>0.52 (+8%)</i>	<i>0.60 (+17%)</i>	<i>0.78 (+36%)</i>	<i>0.88 (+32%)</i>	<i>0.70 (+26%)</i>	<i>0.65 (+5%)</i>	0.60
<b>STC</b>							
Ceiling	0.09	0.09	0.09	0.10	0.10	0.10	0.05
Plasterboard (walls)	0.18	0.15	0.14	0.13	0.12	0.12	0.02
Furniture	0.28	0.25	0.20	0.16	0.12	0.12	0.10
Wood	0.15	0.15	0.12	0.10	0.06	0.06	0.15
Seats	0.28	0.30	0.45	0.60	0.58	0.58	0.50
<b>ULH</b>							
Plaster	0.01	0.02	0.03	0.03	0.04	0.06	0.05
Wood	0.15	0.18	0.04	0.04	0.04	0.04	0.05
Windows	0.10	0.10	0.08	0.04	0.04	0.04	0.05
Seats	0.40	0.37	0.26	0.19	0.17	0.16	0.50

# Appendix B

## Repository

### B.1 Aim and description

At the end of the present thesis, this appendix is intended to allow any other researcher to have the access to the main data of the work. With this purpose, the freely available repository “*Materials for calibrating four complex virtual environments through acoustic simulations*” - updated in September 2021 - can be found at the following link: [doi.org/10.17632/y7xnv6xg5s](https://doi.org/10.17632/y7xnv6xg5s).

This repository provides the necessary materials to perform the acoustic simulation of the four peculiar spaces assessed: the historical opera house (TCB); the modern opera house (DUS), the elliptical concert hall (STC), and the university lecture hall (ULH). Each subfolder contains all the materials involved in the calibration of the models:

- the 3D virtual models of the halls (SketchUp 2019);
- the main results of the acoustic measurements performed *in situ* (room criteria according to ISO 3382, IEC 60268);
- the boundary conditions - already provided in the Appendix A of the present thesis - in terms of normalized LRC coefficients employed as input data in FDTD simulations to approximate frequency-dependent boundary admittances;
- the corresponding energy parameters derived from the acoustic admittances used in FDTD calibration compared with the energy parameters employed in GA++ simulations (absorption and scattering coefficients), here provided in the Appendix A;
- the simulated impulse responses obtained through the hybrid FDTD/GA code.

The repository files are intended to support the whole work reported in the present Ph.D. thesis and to allow other researchers in the room acoustics simulation field to reproduce the calibration of the four spaces. The broader objective is to contribute to enlarging the scientific and practical knowledge of 3D modeling rules and input data employment in the acoustic simulations application field with further useful datasets.

# Symbols

$x, y, z$	spatial coordinates in $\mathbb{R}^3$	m
$\mathbf{x}$	spatial vector in $\mathbb{R}^3$ , $\mathbf{x} = (x, y, z)$	m
$c$	speed of sound	m/s
$t$	time	s
$T$	temperature	$^{\circ}\text{C}$
$p$	sound pressure	Pa
$p_0$	atmospheric pressure	Pa
$\rho$	instantaneous density	$\text{kg}/\text{m}^3$
$\rho_0$	atmospheric density	$\text{kg}/\text{m}^3$
$\mu_0$	viscosity of the air	Pa s
$u$	particle velocity potential	$\text{m}^2/\text{s}$
$\mathbf{v}$	particle velocity vector, $\mathbf{v} = (v_x, v_y, v_z)$	m/s
$\nabla$	3D gradient operator, $\nabla = (\partial_x, \partial_y, \partial_z)^{\text{T}}$	
$\Delta$	3D Laplacian operator, $\Delta = \nabla \cdot \nabla = (\partial_x^2 + \partial_y^2 + \partial_z^2)$	
$\lambda$	Courant number, $\lambda = ck/h$	–
$f_s$	sampling frequency	Hz
$k$	time step	s
$h$	grid spacing	m
$\sigma$	oversampling factor	–
$\omega$	angular frequency	rad/s
$\beta$	wavenumber	rad/m
$A$	equivalent absorption area	$\text{m}^2$ (Sabine)
$S_c$	coupling area	$\text{m}^2$
$k_c$	coupling factor	–
$\alpha$	absorption coefficient	–
$R$	reflection factor	–
$Z_a$	acoustic impedance	$\text{kg}/(\text{m}^4\text{s})$
$Z_s$	specific acoustic impedance	rayl
$Z_c$	characteristic acoustic impedance	rayl
$\zeta$	normalized acoustic impedance	–
$\gamma$	specific acoustic admittance	–



# Abbreviations

D	Dimension of the domain
3D	Three-Dimensional
LTI	Linear Time-Invariant
PDE	Partial Differential Equation
FEM	Finite Element Method
BEM	Boundary Element Method
FFT	Fast Fourier Transform
RTF	Room Transfer Function
CAD	Computer-Aided Design
EDT	Early Decay Time
ISM	Image Source Method
SRT	Stochastic Ray Tracing
EDC	Energy Decay Curve
PPW	points per wavelength
FDTD	Finite-difference time-domain
FVTD	Finite-volume time-domain
GA	Classical geometrical acoustic
GA++	Geometrical acoustic with diffraction handled
TCB	<i>Teatro Comunale</i> in Bologna (Chapter 4)
DUS	<i>Duse theatre</i> in Bologna (Chapter 4)
STC	St Cecilia's hall in Edinburgh (Chapter 5)
ULH	University lecture hall in Bologna (Chapter 6)
LOD	Level of detail



# Bibliography

- [1] M. Vorländer, “Room acoustics–fundamentals and computer simulation,” in *Springer Handbook of Systematic Musicology*, pp. 197–215, Springer, 2018.
- [2] P. Svensson and U. R. Kristiansen, “Computational modelling and simulation of acoutic spaces,” in *Audio Engineering Society Conference: 22nd International Conference: Virtual, Synthetic, and Entertainment Audio*, Audio Engineering Society, 2002.
- [3] S. Siltanen, T. Lokki, S. Kiminki, and L. Savioja, “The room acoustic rendering equation,” *The Journal of the Acoustical Society of America*, vol. 122, no. 3, pp. 1624–1635, 2007.
- [4] D. Botteldooren, “Finite-difference time-domain simulation of low-frequency room acoustic problems,” *The Journal of the Acoustical Society of America*, vol. 98, no. 6, pp. 3302–3308, 1995.
- [5] K. Kowalczyk and M. Van Walstijn, “Room acoustics simulation using 3-d compact explicit ftd schemes,” *IEEE Transactions on Audio, Speech, and Language Processing*, vol. 19, no. 1, pp. 34–46, 2010.
- [6] L. Savioja, “Real-time 3d finite-difference time-domain simulation of low and mid frequency room acoustics,” in *Proc. 13th Conf. on Digital Audio Effects (DAFx)*, vol. 1, p. 75, 2010.
- [7] A. Krokstad, S. Strom, and S. Sørstal, “Calculating the acoustical room response by the use of a ray tracing technique,” *Journal of Sound and Vibration*, vol. 8, no. 1, pp. 118–125, 1968.
- [8] I. Bork, “Report on the 3rd round robin on room acoustical computer simulation–part i: Measurements,” *Acta Acustica united with Acustica*, vol. 91, no. 4, pp. 740–752, 2005.
- [9] H. Kuttruff, *Room acoustics*. Crc Press, 2016.

- 
- [10] L. E. Kinsler, A. R. Frey, A. B. Coppens, and J. V. Sanders, *Fundamentals of acoustics*. 1999.
- [11] M. Schroeder, “Die statistischen parameter der frequenzkurven von großen räumen,” *Acta Acustica united with Acustica*, vol. 4, no. 5, pp. 594–600, 1954.
- [12] M. R. Schroeder and K. Kuttruff, “On frequency response curves in rooms. comparison of experimental, theoretical, and monte carlo results for the average frequency spacing between maxima,” *The Journal of the Acoustical Society of America*, vol. 34, no. 1, pp. 76–80, 1962.
- [13] A. Wareing and M. Hodgson, “Beam-tracing model for predicting sound fields in rooms with multilayer bounding surfaces,” *The Journal of the Acoustical Society of America*, vol. 118, no. 4, pp. 2321–2331, 2005.
- [14] G. Marbjerg, J. Brunskog, C.-H. Jeong, and E. Nilsson, “Development and validation of a combined phased acoustical radiosity and image source model for predicting sound fields in rooms,” *The Journal of the Acoustical Society of America*, vol. 138, no. 3, pp. 1457–1468, 2015.
- [15] C.-H. Jeong, J.-G. Ih, and J. H. Rindel, “An approximate treatment of reflection coefficient in the phased beam tracing method for the simulation of enclosed sound fields at medium frequencies,” *Applied Acoustics*, vol. 69, no. 7, pp. 601–613, 2008.
- [16] U. P. Svensson, “Geometrical acoustics++(preliminary version),”
- [17] S. Bilbao, B. Hamilton, J. Botts, and L. Savioja, “Finite volume time domain room acoustics simulation under general impedance boundary conditions,” *IEEE/ACM Transactions on Audio, Speech, and Language Processing*, vol. 24, no. 1, pp. 161–173, 2015.
- [18] C. J. Webb and S. Bilbao, “Computing room acoustics with cuda-3d fdtd schemes with boundary losses and viscosity,” in *2011 IEEE International Conference on Acoustics, Speech and Signal Processing (ICASSP)*, pp. 317–320, IEEE, 2011.
- [19] B. Hamilton, “Finite difference and finite volume methods for wave-based modelling of room acoustics. ph.d. dissertation. university of edinburgh, uk.” 2016.
- [20] S. Siltanen, T. Lokki, and L. Savioja, “Rays or waves? understanding the strengths and weaknesses of computational room acoustics modeling techniques,” in *Proc. Int. Symposium on Room Acoustics*, 2010.

- 
- [21] M. Hornikx, “Acoustic modelling for indoor and outdoor spaces,” 2015.
- [22] J. Picaut, L. Simon, and J.-D. Polack, “A mathematical model of diffuse sound field based on a diffusion equation,” *ACTA Acustica united with Acustica*, vol. 83, no. 4, pp. 614–621, 1997.
- [23] V. Valeau, J. Picaut, and M. Hodgson, “On the use of a diffusion equation for room-acoustic prediction,” *The Journal of the Acoustical Society of America*, vol. 119, no. 3, pp. 1504–1513, 2006.
- [24] Y. Jing and N. Xiang, “On boundary conditions for the diffusion equation in room-acoustic prediction: Theory, simulations, and experiments,” *The Journal of the Acoustical Society of America*, vol. 123, no. 1, pp. 145–153, 2008.
- [25] M. Vorländer, *Auralization*. Springer, 2020.
- [26] M. Barron, *Auditorium acoustics and architectural design*. Routledge, 2009.
- [27] P. M. Morse and K. U. Ingard, *Theoretical acoustics*. Princeton university press, 1986.
- [28] M. Aretz, *Combined wave and ray based room acoustic simulations of small rooms*, vol. 12. Logos Verlag Berlin GmbH, 2012.
- [29] S.-I. Thomasson, *Theory and experiments on the sound absorption as function of the area*. Department of Acoustics, Royal Institute of Technology, 1982.
- [30] J. H. Rindel, “Modelling the angle-dependent pressure reflection factor,” *Applied Acoustics*, vol. 38, no. 2-4, pp. 223–234, 1993.
- [31] J. L. Davy, D. J. Larner, R. R. Wareing, and J. R. Pearse, “The average specific forced radiation wave impedance of a finite rectangular panel,” *The Journal of the Acoustical Society of America*, vol. 136, no. 2, pp. 525–536, 2014.
- [32] C.-H. Jeong and J. Brunskog, “The equivalent incidence angle for porous absorbers backed by a hard surface,” *The Journal of the Acoustical Society of America*, vol. 134, no. 6, pp. 4590–4598, 2013.
- [33] M. Meissner, “Influence of wall absorption on low-frequency dependence of reverberation time in room of irregular shape,” *Applied Acoustics*, vol. 69, no. 7, pp. 583–590, 2008.

- 
- [34] S. D. Bilbao, *Numerical sound synthesis*. Wiley Online Library, 2009.
- [35] G. Marbjerg, J. Brunskog, and C.-H. Jeong, “The difficulties of simulating the acoustics of an empty rectangular room with an absorbing ceiling,” *Applied Acoustics*, vol. 141, pp. 35–45, 2018.
- [36] B. Mondet, J. Brunskog, C.-H. Jeong, and J. H. Rindel, “From absorption to impedance: Enhancing boundary conditions in room acoustic simulations,” *Applied Acoustics*, vol. 157, p. 106884, 2020.
- [37] R. D. Cook *et al.*, *Concepts and applications of finite element analysis*. John Wiley & Sons, 2007.
- [38] S. Kirkup, “The boundary element method in acoustics: A survey,” *Applied Sciences*, vol. 9, no. 8, p. 1642, 2019.
- [39] D. V. Hutton, *Fundamentals of finite element analysis*. McGraw-hill, 2004.
- [40] S. Marburg and B. Nolte, *Computational acoustics of noise propagation in fluids: finite and boundary element methods*, vol. 578. Springer, 2008.
- [41] O. Zienkiewicz, D. Kelly, and P. Bettess, “The coupling of the finite element method and boundary solution procedures,” *International journal for numerical methods in engineering*, vol. 11, no. 2, pp. 355–375, 1977.
- [42] K. Bathe, “Finite element procedures. 2. tot. new. rev. and enl. ed.; finite-elemente-methoden,” 2001.
- [43] S. Marburg, “Six boundary elements per wavelength: is that enough?,” *Journal of computational acoustics*, vol. 10, no. 01, pp. 25–51, 2002.
- [44] A. Pietrzyk and M. Kleiner, “The application of the finite-element method to the prediction of soundfields of small rooms at low frequencies,” in *Audio Engineering Society Convention 102*, Audio Engineering Society, 1997.
- [45] T. Łodygowski and W. Sumelka, “Limitations in application of finite element method in acoustic numerical simulation,” *Journal of theoretical and applied mechanics*, vol. 44, no. 4, pp. 849–865, 2006.
- [46] J. Strikwerda, “Finite difference schemes partial differential equations. wadsworth & brooks/cole,” 1989.

- 
- [47] R. Courant, K. Friedrichs, and H. Lewy, “Über die partiellen differenzgleichungen der mathematischen physik,” *Mathematische annalen*, vol. 100, no. 1, pp. 32–74, 1928.
- [48] R. Richtmyer, “Difference methods for initial-value problems, 238 pp,” 1957.
- [49] G. E. Forsythe and W. R. Wasow, “Finite difference methods,” *Partial Differential*, 1960.
- [50] K. Yee, “Numerical solution of initial boundary value problems involving maxwell’s equations in isotropic media,” *IEEE Transactions on antennas and propagation*, vol. 14, no. 3, pp. 302–307, 1966.
- [51] A. Taflove, “Application of the finite-difference time-domain method to sinusoidal steady-state electromagnetic-penetration problems,” *IEEE Transactions on electromagnetic compatibility*, no. 3, pp. 191–202, 1980.
- [52] B. Hamilton, C. Webb, N. Fletcher, and S. Bilbao, “Finite difference room acoustics simulation with general impedance boundaries and viscothermal losses in air: Parallel implementation on multiple gpus,” in *Proc. Int. Symp. Musical Room Acoust*, 2016.
- [53] J. Saarelma, J. Botts, B. Hamilton, and L. Savioja, “Audibility of dispersion error in room acoustic finite-difference time-domain simulation as a function of simulation distance,” *The Journal of the Acoustical Society of America*, vol. 139, no. 4, pp. 1822–1832, 2016.
- [54] G. Barton and G. Barton, *Elements of Green’s functions and propagation: potentials, diffusion, and waves*. Oxford University Press, 1989.
- [55] C. J. Webb, “Parallel computation techniques for virtual acoustics and physical modelling synthesis,” 2014.
- [56] A. Southern, D. Murphy, T. Lokki, and L. Savioja, “The perceptual effects of dispersion error on room acoustic model auralization,” in *Proc. Forum Acusticum*, pp. 1553–1558, 2011.
- [57] J. S. Juntunen and T. D. Tsiboukis, “Reduction of numerical dispersion in fdtd method through artificial anisotropy,” *IEEE Transactions on Microwave Theory and Techniques*, vol. 48, no. 4, pp. 582–588, 2000.
- [58] J.-D. Polack, “Modifying chambers to play billiards: the foundations of reverberation theory,” *Acta Acustica united with Acustica*, vol. 76, no. 6, pp. 256–272, 1992.

- [59] M. Born and E. Wolf, “Principles of optics, 7th (expanded) edition,” *United Kingdom: Press Syndicate of the University of Cambridge*, vol. 461, 1999.
- [60] B.-I. Dalenbäck, *A new model for room acoustic prediction and auralization*. Chalmers University of Technology, 1995.
- [61] J.-D. Polack, “Playing billiards in the concert hall: The mathematical foundations of geometrical room acoustics,” *Applied Acoustics*, vol. 38, no. 2-4, pp. 235–244, 1993.
- [62] A. D. Pierce, *Acoustics: an introduction to its physical principles and applications*. Springer, 2019.
- [63] L. Savioja and U. P. Svensson, “Overview of geometrical room acoustic modeling techniques,” *The Journal of the Acoustical Society of America*, vol. 138, no. 2, pp. 708–730, 2015.
- [64] M. Vorländer, “Computer simulations in room acoustics: Concepts and uncertainties,” *The Journal of the Acoustical Society of America*, vol. 133, no. 3, pp. 1203–1213, 2013.
- [65] A. Krokstad, S. Strom, and S. Sørsdal, “Calculating the acoustical room response by the use of a ray tracing technique,” *Journal of Sound and Vibration*, vol. 8, no. 1, pp. 118–125, 1968.
- [66] G. M. Naylor, “Odeon—another hybrid room acoustical model,” *Applied Acoustics*, vol. 38, no. 2-4, pp. 131–143, 1993.
- [67] C. L. Christensen, “Odeon room acoustics program version 3.1-user manual: Industrial, auditorium and combined editions,” 1998.
- [68] F. Brinkmann, L. Aspöck, D. Ackermann, S. Lepa, M. Vorländer, and S. Weinzierl, “A round robin on room acoustical simulation and auralization,” *The Journal of the Acoustical Society of America*, vol. 145, no. 4, pp. 2746–2760, 2019.
- [69] B. M. Gibbs and D. Jones, “A simple image method for calculating the distribution of sound pressure levels within an enclosure,” *Acta Acustica united with Acustica*, vol. 26, no. 1, pp. 24–32, 1972.
- [70] J. B. Allen and D. A. Berkley, “Image method for efficiently simulating small-room acoustics,” *The Journal of the Acoustical Society of America*, vol. 65, no. 4, pp. 943–950, 1979.

- [71] J. Borish, "Extension of the image model to arbitrary polyhedra," *The Journal of the Acoustical Society of America*, vol. 75, no. 6, pp. 1827–1836, 1984.
- [72] T. Funkhouser, I. Carlbom, G. Elko, G. Pingali, M. Sondhi, and J. West, "A beam tracing approach to acoustic modeling for interactive virtual environments," in *Proceedings of the 25th annual conference on Computer graphics and interactive techniques*, pp. 21–32, 1998.
- [73] J. H. Rindel, "The use of computer modeling in room acoustics," *Journal of vibroengineering*, vol. 3, no. 4, pp. 219–224, 2000.
- [74] V. O. Knudsen and C. M. Harris, *Le projet acoustique en architecture*. Dunod, 1957.
- [75] M. R. Schroeder, "The "schroeder frequency" revisited," *The Journal of the Acoustical Society of America*, vol. 99, no. 5, pp. 3240–3241, 1996.
- [76] J. B. Keller, "Geometrical theory of diffraction," *Josa*, vol. 52, no. 2, pp. 116–130, 1962.
- [77] *ISO 17497-1:2004 Acoustics — Sound-scattering properties of surfaces — Part 1: Measurement of the random-incidence scattering coefficient in a reverberation room*.
- [78] *ISO 17497-2:2010 Acoustics — Sound-scattering properties of surfaces — Part 2: Measurement of the directional diffusion coefficient in a free field*.
- [79] L. Shtrepi, "Investigation on the diffusive surface modeling detail in geometrical acoustics based simulations," *The Journal of the Acoustical Society of America*, vol. 145, no. 3, pp. EL215–EL221, 2019.
- [80] C. L. Christensen and J. H. Rindel, "A new scattering method that combines roughness and diffraction effects," in *Forum Acousticum, Budapest, Hungary*, pp. 344–352, 2005.
- [81] J. H. Rindel, G. B. Nielsen, and C. L. Christensen, "Diffraction around corners and over wide barriers in room acoustic simulations," in *Proceedings of the 16th International Congress on Sound Vibration*, 2009.
- [82] X. Zeng, C. L. Christensen, and J. H. Rindel, "Practical methods to define scattering coefficients in a room acoustics computer model," *Applied acoustics*, vol. 67, no. 8, pp. 771–786, 2006.

- [83] J. H. Rindel, "Design of new ceiling reflectors for improved ensemble in a concert hall," *Applied Acoustics*, vol. 34, no. 1, pp. 7–17, 1991.
- [84] L. Savioja, J. Backman, A. Järvinen, and T. Takala, "Waveguide mesh method for low-frequency simulation of room acoustics," in *Proceedings of the 15th International Conference on Acoustics (ICA-95), Trondheim, Norway*, pp. 637–640, 1995.
- [85] D. Murphy, M. Beeson, S. Shelley, A. Moore, and A. Southern, "Hybrid room impulse response synthesis in digital waveguide mesh based room acoustics simulation," in *Proceedings of the 11th International Conference on Digital Audio Effects (DAFx-08)*, pp. 129–136, Citeseer, 2008.
- [86] M. Aretz, R. Nöthen, M. Vorländer, and D. Schröder, "Combined broadband impulse responses using fem and hybrid ray-based methods," in *EAA Symposium on Auralization*, pp. 15–17, 2009.
- [87] M. Kleiner, B.-I. Dalenbäck, and P. Svensson, "Auralization-an overview," *Journal of the Audio Engineering Society*, vol. 41, no. 11, pp. 861–875, 1993.
- [88] E. Granier, M. Kleiner, B.-I. Dalenbäck, and P. Svensson, "Experimental auralization of car audio installations," *Journal of the Audio Engineering Society*, vol. 44, no. 10, pp. 835–849, 1996.
- [89] J. E. Summers, K. Takahashi, Y. Shimizu, and T. Yamakawa, "Assessing the accuracy of auralizations computed using a hybrid geometrical-acoustics and wave-acoustics method," *The Journal of the Acoustical Society of America*, vol. 115, no. 5, pp. 2514–2515, 2004.
- [90] W. Ahnert, M. Bansal, and S. Feistel, "First approach to combine particle model algorithms with modal analysis using fem," in *Audio Engineering Society Convention 118*, Audio Engineering Society, 2005.
- [91] B. Hamilton and C. J. Webb, "Room acoustics modelling using gpu-accelerated finite difference and finite volume methods on a face-centered cubic grid," *Proc. Digital Audio Effects (DAFx), Maynooth, Ireland*, pp. 336–343, 2013.
- [92] S. Bilbao, "Modeling of complex geometries and boundary conditions in finite difference/finite volume time domain room acoustics simulation," *IEEE Transactions on Audio, Speech, and Language Processing*, vol. 21, no. 7, pp. 1524–1533, 2013.

- [93] B. Hamilton, S. Bilbao, and C. J. Webb, “Improved finite difference schemes for a 3-d viscothermal wave equation on a gpu,” in *Proc. Forum Acusticum*, 2014.
- [94] B. Hamilton, “Pfftd software,” 2021. <https://github.com/bsxfun/pfftd>.
- [95] *ISO 9613-1:1993 Acoustics — Attenuation of sound during propagation outdoors*.
- [96] A. Southern, S. Siltanen, D. T. Murphy, and L. Savioja, “Room impulse response synthesis and validation using a hybrid acoustic model,” *IEEE transactions on audio, speech, and language processing*, vol. 21, no. 9, pp. 1940–1952, 2013.
- [97] N. Prodi, R. Pompoli, F. Martellotta, and S.-i. Sato, “Acoustics of italian historical opera houses,” *The Journal of the Acoustical Society of America*, vol. 138, no. 2, pp. 769–781, 2015.
- [98] R. Pompoli and N. Prodi, “Guidelines for acoustical measurements inside historical opera houses: procedures and validation,” *Journal of sound and vibration*, vol. 232, no. 1, pp. 281–301, 2000.
- [99] M. Garai, F. Morandi, D. D’Orazio, S. De Cesaris, and L. Loreti, “Acoustic measurements in eleven italian opera houses: Correlations between room criteria and considerations on the local evolution of a typology,” *Building and Environment*, vol. 94, pp. 900–912, 2015.
- [100] L. Cremer and H. A. Müller, *Die wissenschaftlichen grundlagen der raumakustik*. Hirzel Stuttgart, 1978.
- [101] M. Garai, F. Morandi, D. D’Orazio, S. De Cesaris, and L. Loreti, “Acoustic measurements in eleven italian opera houses: Correlations between room criteria and considerations on the local evolution of a typology,” *Building and Environment*, vol. 94, pp. 900–912, 2015.
- [102] D. D’Orazio, G. Fratoni, and M. Garai, “Overhead stage canopies in a coupled volume theatre: Effects on the sound energy distribution and on the secondary reverberation,” *The Journal of the Acoustical Society of America*, vol. 146, no. 4, pp. 2802–2802, 2019.
- [103] M. Garai, S. De Cesaris, F. Morandi, and D. D’Orazio, “Sound energy distribution in italian opera houses,” in *Proceedings of Meetings on Acoustics 22ICA*, vol. 28, p. 015019, Acoustical Society of America, 2016.

- 
- [104] N. Xiang, P. Goggans, T. Jasa, and P. Robinson, “Bayesian characterization of multiple-slope sound energy decays in coupled-volume systems,” *The Journal of the Acoustical Society of America*, vol. 129, no. 2, pp. 741–752, 2011.
- [105] D. D’Orazio, S. De Cesaris, F. Morandi, and M. Garai, “The aesthetics of the bayreuth festspielhaus explained by means of acoustic measurements and simulations,” *Journal of Cultural Heritage*, vol. 34, pp. 151–158, 2018.
- [106] S.-i. Sato, S. Wang, Y. Zhao, S. Wu, H. Sun, N. Prodi, C. Visentin, and R. Pompoli, “Effects of acoustic and visual stimuli on subjective preferences for different seating positions in an italian style theater,” *Acta Acustica united with Acustica*, vol. 98, no. 5, pp. 749–759, 2012.
- [107] F. Milizia, *Trattato completo, formale e materiale del teatro*. No. 64, Forni, 1794.
- [108] M. Barron, “Balcony overhangs in concert auditoria,” *The Journal of the Acoustical Society of America*, vol. 98, no. 5, pp. 2580–2589, 1995.
- [109] C. Jaffe, “Design considerations for a demountable concert enclosure (symphonic shell)(reprint),” *Journal of the Audio Engineering Society*, vol. 22, no. 3, pp. 163–170, 1974.
- [110] T. J. Cox and Y. Lam, “Evaluation of methods for predicting the scattering from simple rigid panels,” *Applied Acoustics*, vol. 40, no. 2, pp. 123–140, 1993.
- [111] A. R. M. G. D. D’Orazio, G. Fratoni, “A virtual orchestra to qualify the acoustics of historical opera houses,” *Building Acoustics*, p. 1351010X20912501, 2020.
- [112] D. D’Orazio, G. Fratoni, and M. Garai, “Enhancing the strength of symphonic orchestra in an opera house,” *Applied Acoustics*, vol. 170, p. 107532, 2020.
- [113] A. Kircher, *Musurgia universalis*. 1650.
- [114] M. Vercammen, “Sound reflections from concave spherical surfaces. part ii: Geometrical acoustics and engineering approach,” *Acta Acustica united with Acustica*, vol. 96, no. 1, pp. 92–101, 2010.

- [115] M. Vercammen, “Improving the accuracy of sound absorption measurement according to iso 354,” in *Proceedings of the International Symposium on Room Acoustics*, pp. 29–31, Melbourne Australia, 2010.
- [116] M. Vercammen, “Sound concentration caused by curved surfaces, phd thesis, eindhoven university of technology, bouwstenen 163,” 2012.
- [117] H. Lai and B. Hamilton, “Computer modeling of barrel-vaulted sanctuary exhibiting flutter echo with comparison to measurements,” in *Acoustics*, vol. 2, pp. 87–109, Multidisciplinary Digital Publishing Institute, 2020.
- [118] A. Magrini and P. Ricciardi, “The acoustic field under the dome in a central plan church: measurement and simulation,” *Proc 13th ICSV, Vienna, Austria*, pp. 2–6, 2006.
- [119] *EN 60268-16:2001 Sound system equipment*.
- [120] M. Cingolani, G. Fratoni, L. Barbaresi, D. D’Orazio, B. Hamilton, and M. Garai, “A trial acoustic improvement in a lecture hall with mpp sound absorbers and ftd acoustic simulations,” *Applied Sciences*, vol. 11, p. 2445, 2021.
- [121] M. Vorländer, *Auralization: fundamentals of acoustics, modelling, simulation, algorithms and acoustic virtual reality*. Springer Science & Business Media, 2007.
- [122] S. Siltanen, T. Lokki, L. Savioja, and C. Lynge Christensen, “Geometry reduction in room acoustics modeling,” *Acta Acustica united with Acustica*, vol. 94, no. 3, pp. 410–418, 2008.
- [123] C. L. Christensen, “Odeon import of cad files in the dxf format-problems and solutions,” *Odeon Technical note, www.odeon.dk*, 2007.
- [124] C.-H. Jeong, G. Marbjerg, and J. Brunskog, “Uncertainty of input data for room acoustic simulations,” in *Proc. of bi-annual Baltic-Nordic Acoustic Meeting*, 2016.
- [125] T. J. Cox and P. D’antonio, *Acoustic absorbers and diffusers: theory, design and application*. Crc Press, 2009.
- [126] Y. H. Kim, H. M. Lee, C. K. Seo, and J. Y. Jeon, “Investigating the absorption characteristics of open ceilings in multi-purpose halls using a 1: 25 scale model,” *Applied acoustics*, vol. 71, no. 5, pp. 473–478, 2010.

- [127] B. N. Postma and B. F. Katz, “Perceptive and objective evaluation of calibrated room acoustic simulation auralizations,” *The Journal of the Acoustical Society of America*, vol. 140, no. 6, pp. 4326–4337, 2016.
- [128] *ISO 3382-1:2009 Acoustics — Measurement of room acoustic parameters*.
- [129] F. Brinkmann, L. Aspöck, D. Ackermann, R. Opdam, M. Vorländer, and S. Weinzierl, “A benchmark for room acoustical simulation. concept and database,” *Applied Acoustics*, vol. 176, p. 107867, 2021.
- [130] “<https://odeon.dk/downloads/su2odeon/>,” last view: 2021.
- [131] J. H. Rindel, “An impedance model for estimating the complex pressure reflection factor,” in *Forum Acusticum*, vol. 2011, 2011.
- [132] A. Pilch, “Optimization-based method for the calibration of geometrical acoustic models,” *Applied Acoustics*, vol. 170, p. 107495, 2020.
- [133] D. D’Orazio, “Italian-style opera houses: A historical review,” *Applied Sciences*, vol. 10, no. 13, p. 4613, 2020.
- [134] D. D’Orazio and S. Nannini, “Towards italian opera houses: a review of acoustic design in pre-sabine scholars,” in *Acoustics*, vol. 1, pp. 252–280, Multidisciplinary Digital Publishing Institute, 2019.
- [135] A. R. B. H. D. D’Orazio, G. Fratoni, “Numerical simulations of italian opera houses using geometrical and wave-based acoustics methods,” in *Proceedings of the 23rd International Congress on Acoustics, Aachen, Germany*, pp. 9–13, 2019.
- [136] T. Hidaka and L. L. Beranek, “Objective and subjective evaluations of twenty-three opera houses in europe, japan, and the americas,” *The Journal of the Acoustical Society of America*, vol. 107, no. 1, pp. 368–383, 2000.
- [137] M. Barron, “Interpretation of early decay times in concert auditoria,” *Acta Acustica united with Acustica*, vol. 81, no. 4, pp. 320–331, 1995.
- [138] P. Guidorzi, L. Barbaresi, D. D’Orazio, and M. Garai, “Impulse responses measured with mls or swept-sine signals applied to architectural acoustics: an in-depth analysis of the two methods and some case studies of measurements inside theaters,” *Energy Procedia*, vol. 78, pp. 1611–1616, 2015.

- [139] D. D’Orazio, S. De Cesaris, P. Guidorzi, L. Barbaresi, M. Garai, and R. Magalotti, “Room acoustic measurements using a high spl dodecahedron,” in *Audio Engineering Society Convention 140*, Audio Engineering Society, 2016.
- [140] C. Hak, R. Wenmaekers, and L. Van Luxemburg, “Measuring room impulse responses: Impact of the decay range on derived room acoustic parameters,” *Acta Acustica united with Acustica*, vol. 98, no. 6, pp. 907–915, 2012.
- [141] C. Hak, R. H. Wenmaekers, J. P. Hak, and L. van Luxemburg, “The source directivity of a dodecahedron sound source determined by step-wise rotation,” in *Proceedings of Forum Acusticum, Aalborg*, pp. 1875–1879, 2011.
- [142] R. Pieren, B. Schäffer, S. Schoenwald, and K. Eggenschwiler, “Sound absorption of textile curtains—theoretical models and validations by experiments and simulations,” *Textile Research Journal*, vol. 88, no. 1, pp. 36–48, 2018.
- [143] M. G. D. D’Orazio, A. Rovigatti, “The proscenium of opera houses as a disappeared intangible heritage: a virtual reconstruction of the 1840s original design of the alighieri theatre in ravenna,” in *Acoustics*, vol. 1, pp. 694–710, Multidisciplinary Digital Publishing Institute, 2019.
- [144] L. L. Beranek, “Analysis of sabine and eyring equations and their application to concert hall audience and chair absorption,” *The Journal of the Acoustical Society of America*, vol. 120, no. 3, pp. 1399–1410, 2006.
- [145] *SketchUp, Trimble Connect, version Make, 2017.*
- [146] L. Alvarez-Morales and F. Martellotta, “A geometrical acoustic simulation of the effect of occupancy and source position in historical churches,” *Applied Acoustics*, vol. 91, pp. 47–58, 2015.
- [147] F. Martellotta, “The just noticeable difference of center time and clarity index in large reverberant spaces,” *The Journal of the Acoustical Society of America*, vol. 128, no. 2, pp. 654–663, 2010.
- [148] *ISO 10534-2:1998 Acoustics — Determination of sound absorption coefficient and impedance in impedance tubes.*

- [149] M. R. Schroeder, “New method of measuring reverberation time,” *The Journal of the Acoustical Society of America*, vol. 37, no. 6, pp. 1187–1188, 1965.
- [150] *ISO 3382-1:2008 Acoustics — Measurement of room acoustic parameters*.
- [151] D. T. Bradley and L. M. Wang, “The effects of simple coupled volume geometry on the objective and subjective results from nonexponential decay,” *The Journal of the Acoustical Society of America*, vol. 118, no. 3, pp. 1480–1490, 2005.
- [152] D. T. Bradley and L. M. Wang, “Optimum absorption and aperture parameters for realistic coupled volume spaces determined from computational analysis and subjective testing results,” *The Journal of the Acoustical Society of America*, vol. 127, no. 1, pp. 223–232, 2010.
- [153] M. Schroeder, “Response to “comments on ‘new method of measuring reverberation time’” [pw smith, jr., j. acoust. soc. am. 38, 359 (1)(1965)],” *The Journal of the Acoustical Society of America*, vol. 38, no. 2, pp. 359–361, 1965.
- [154] D.-I. J. Balint, “Analysis tools for multiexponential energy decay curves in room acoustics,” 2018.
- [155] N. Xiang and P. M. Goggans, “Evaluation of decay times in coupled spaces: Bayesian parameter estimation,” *The Journal of the Acoustical Society of America*, vol. 110, no. 3, pp. 1415–1424, 2001.
- [156] N. Xiang and P. M. Goggans, “Evaluation of decay times in coupled spaces: Bayesian decay model selection,” *The Journal of the Acoustical Society of America*, vol. 113, no. 5, pp. 2685–2697, 2003.
- [157] M. Holden, *Acoustics of multi-use performing arts centers*. CRC Press, 2015.
- [158] J. S. Bradley, “Some effects of orchestra shells,” *The Journal of the Acoustical Society of America*, vol. 100, no. 2, pp. 889–898, 1996.
- [159] J. J. Dammerud and M. Barron, “Attenuation of direct sound and the contributions of early reflections within symphony orchestras,” *The Journal of the Acoustical Society of America*, vol. 128, no. 4, pp. 1755–1765, 2010.

- [160] J. Y. Jeon, J. H. Kim, and J. K. Ryu, “The effects of stage absorption on reverberation times in opera house seating areas,” *The Journal of the Acoustical Society of America*, vol. 137, no. 3, pp. 1099–1107, 2015.
- [161] D. T. Bradley and L. M. Wang, “Comparison of measured and computer-modeled objective parameters for an existing coupled volume concert hall,” *Building Acoustics*, vol. 14, no. 2, pp. 79–90, 2007.
- [162] C. L. Christensen, G. Koutsouris, and J. H. Rindel, “Estimating absorption of materials to match room model against existing room using a genetic algorithm,” in *Forum Acusticum*, pp. 7–12, 2014.
- [163] T. Cox and P. D’Antonio, “Designing stage canopies for improved acoustics,” *PROCEEDINGS-INSTITUTE OF ACOUSTICS*, vol. 19, pp. 153–160, 1997.
- [164] M. Barron and S. Kissner, “A possible acoustic design approach for multi-purpose auditoria suitable for both speech and music,” *Applied Acoustics*, vol. 115, pp. 42–49, 2017.
- [165] B. Hamilton, M. Newton, G. Fratoni, and D. D’Orazio, “On the acoustics of st cecilia’s hall: Measurements and comparison of wave-based and geometrical acoustics modelling,” Universitätsbibliothek der RWTH Aachen, 2019.
- [166] “<http://www.stcecilias.ed.ac.uk/about/>, last view: December 2020.”
- [167] G.-P.-M. Dumont, *Parallele de plans des plus belles salles de spectacle de l’Italie et de la France*. 1766.
- [168] P. Patte, *Eassai sur l’architecture theatrale, 1782 (reprint Minkoff, Genève, 1974)*. 1782.
- [169] G. Saunders, *A treatise on theatres, London, 1790, reissued by Benjamin Blom, Inc., New York, 1968*. 1790.
- [170] K. F. Langhans, *Über Theater oder Bemerkungen über Katakustik in Beziehung auf Theater*. 1810.
- [171] M. Barron and L.-J. Lee, “Energy relations in concert auditoriums. i,” *The Journal of the Acoustical Society of America*, vol. 84, no. 2, pp. 618–628, 1988.

- [172] G. Fratoni, D. D’Orazio, D. De Salvio, and M. Garai, “Predicting speech intelligibility in university classrooms using geometrical acoustic simulations giulia fratoni1, dario d’orazio1, domenico de salvio1, massimo garai1 department of industrial engineering, university of bologna, bologna, italy,”
- [173] F. Martellotta, “Optimizing stepwise rotation of dodecahedron sound source to improve the accuracy of room acoustic measures,” *The Journal of the Acoustical Society of America*, vol. 134, no. 3, pp. 2037–2048, 2013.
- [174] *ISO 3741:2010 Acoustics — Determination of sound power levels and sound energy levels of noise sources using sound pressure — Precision methods for reverberation test rooms.*
- [175] *UNI 11532-2:2020 Internal acoustical characteristics of confined spaces - Design methods and evaluation techniques.*
- [176] A. Astolfi, V. Corrado, and A. Griginis, “Comparison between measured and calculated parameters for the acoustical characterization of small classrooms,” *Applied Acoustics*, vol. 69, no. 11, pp. 966–976, 2008.
- [177] R. Reich and J. Bradley, “Optimizing classroom acoustics using computer model studies,” *Canadian Acoustics*, vol. 26, no. 4, pp. 15–21, 1998.
- [178] S. R. Bistafa and J. S. Bradley, “Predicting reverberation times in a simulated classroom,” *The Journal of the Acoustical Society of America*, vol. 108, no. 4, pp. 1721–1731, 2000.
- [179] S. R. Bistafa and J. S. Bradley, “Predicting speech metrics in a simulated classroom with varied sound absorption,” *The Journal of the Acoustical Society of America*, vol. 109, no. 4, pp. 1474–1482, 2001.
- [180] G. E. Puglisi, F. Bolognesi, L. Shtrepi, A. Warzybok, B. Kollmeier, and A. Astolfi, “Optimal classroom acoustic design with sound absorption and diffusion for the enhancement of speech intelligibility,” *The Journal of the Acoustical Society of America*, vol. 141, no. 5, pp. 3456–3457, 2017.
- [181] D. L. Johnson, J. Koplik, and R. Dashen, “Theory of dynamic permeability and tortuosity in fluid-saturated porous media,” *Journal of fluid mechanics*, vol. 176, pp. 379–402, 1987.

- 
- [182] J.-F. Allard and Y. Champoux, “New empirical equations for sound propagation in rigid frame fibrous materials,” *The Journal of the Acoustical Society of America*, vol. 91, no. 6, pp. 3346–3353, 1992.
- [183] J. Cucharero, T. Hänninen, and T. Lokki, “Angle-dependent absorption of sound on porous materials,” in *Acoustics*, vol. 2, pp. 753–765, Multidisciplinary Digital Publishing Institute, 2020.
- [184] L. Pan and F. Martellotta, “A parametric study of the acoustic performance of resonant absorbers made of micro-perforated membranes and perforated panels,” *Applied Sciences*, vol. 10, no. 5, p. 1581, 2020.
- [185] F. Asdrubali and G. Pispola, “Properties of transparent sound-absorbing panels for use in noise barriers,” *The Journal of the Acoustical Society of America*, vol. 121, no. 1, pp. 214–221, 2007.
- [186] K. Sakagami and T. Okuzono, “Space sound absorbers with next-generation materials: additional sound absorption for post-pandemic challenges in indoor acoustic environments,” *UCL Open: Environment Preprint*, 2020.
- [187] D.-Y. Maa, “Theory and design of microperforated panel sound-absorbing constructions,” *Scientia Sinica*, vol. 18, no. 1, pp. 55–71, 1975.
- [188] D.-Y. Maa, “Microperforated-panel wideband absorbers,” *Noise control engineering journal*, vol. 29, no. 3, pp. 77–84, 1987.
- [189] D.-Y. Maa, “Potential of microperforated panel absorber,” *the Journal of the Acoustical Society of America*, vol. 104, no. 5, pp. 2861–2866, 1998.
- [190] R. Tayong and P. Leclaire, “Holes interaction effects under high and medium sound intensities for micro-perforated panels design,” in *10ème Congrès Français d’Acoustique*, pp. 5–p, 2010.
- [191] T. H. Melling, “The acoustic impedance of perforates at medium and high sound pressure levels,” *Journal of Sound and Vibration*, vol. 29, no. 1, pp. 1–65, 1973.
- [192] P. Cobo and F. Simón, “Multiple-layer microperforated panels as sound absorbers in buildings: a review,” *Buildings*, vol. 9, no. 2, p. 53, 2019.

- [193] D. Lee and Y. Kwon, “Estimation of the absorption performance of multiple layer perforated panel systems by transfer matrix method,” *Journal of sound and vibration*, vol. 278, no. 4-5, pp. 847–860, 2004.
- [194] K. Sakagami, M. Morimoto, and W. Koike, “A numerical study of double-leaf microperforated panel absorbers,” *Applied acoustics*, vol. 67, no. 7, pp. 609–619, 2006.
- [195] K. Hoshi, T. Hanyu, T. Okuzono, K. Sakagami, M. Yairi, S. Harada, S. Takahashi, and Y. Ueda, “Implementation experiment of a honeycomb-backed mpp sound absorber in a meeting room,” *Applied Acoustics*, vol. 157, p. 107000, 2020.
- [196] M. Hodgson, R. Rempel, and S. Kennedy, “Measurement and prediction of typical speech and background-noise levels in university classrooms during lectures,” *The Journal of the Acoustical Society of America*, vol. 105, no. 1, pp. 226–233, 1999.
- [197] C. Visentin, N. Prodi, F. Cappelletti, S. Torresin, and A. Gasparella, “Using listening effort assessment in the acoustical design of rooms for speech,” *Building and Environment*, vol. 136, pp. 38–53, 2018.
- [198] J. P. Arenas and K. Sakagami, “Sustainable acoustic materials,” 2020.
- [199] K. Sakagami, M. Morimoto, and M. Yairi, “A note on the effect of vibration of a microperforated panel on its sound absorption characteristics,” *Acoustical science and technology*, vol. 26, no. 2, pp. 204–207, 2005.
- [200] E. Arvidsson, E. Nilsson, D. B. Hagberg, and O. J. Karlsson, “The effect on room acoustical parameters using a combination of absorbers and diffusers—an experimental study in a classroom,” in *Acoustics*, vol. 2, pp. 505–523, Multidisciplinary Digital Publishing Institute, 2020.
- [201] Y.-J. Choi, “Evaluation of acoustical conditions for speech communication in active university classrooms,” *Applied Acoustics*, vol. 159, p. 107089, 2020.
- [202] D. D’Orazio, D. De Salvio, L. Anderlucci, and M. Garai, “Measuring the speech level and the student activity in lecture halls: Visual-vs blind-segmentation methods,” *Applied Acoustics*, vol. 169, p. 107448, 2020.

- [203] L. C. Brill, K. Smith, and L. M. Wang, “Building a sound future for students: Considering the acoustics of occupied active classrooms,” *Acoustics Today*, vol. 14, no. 3, pp. 14–22, 2018.
- [204] M. Garai and F. Pompoli, “A simple empirical model of polyester fibre materials for acoustical applications,” *Applied Acoustics*, vol. 66, no. 12, pp. 1383–1398, 2005.
- [205] T. Yoshida, T. Okuzono, and K. Sakagami, “Locally implicit time-domain finite element method for sound field analysis including permeable membrane sound absorbers,” *Acoustical Science and Technology*, vol. 41, no. 4, pp. 689–692, 2020.
- [206] C. Yang, L. Cheng, and J. Pan, “Absorption of oblique incidence sound by a finite micro-perforated panel absorber,” *The Journal of the Acoustical Society of America*, vol. 133, no. 1, pp. 201–209, 2013.
- [207] P. Luizard, M. Otani, J. Botts, L. Savioja, and B. F. Katz, “Comparison of sound field measurements and predictions in coupled volumes between numerical methods and scale model measurements,” in *Proceedings of Meetings on Acoustics ICA2013*, vol. 19, p. 015114, Acoustical Society of America, 2013.
- [208] M. Hornikx, C. Hak, and R. Wenmaekers, “Acoustic modelling of sports halls, two case studies,” *Journal of Building Performance Simulation*, vol. 8, no. 1, pp. 26–38, 2015.
- [209] M. Hornikx, M. Kaltenbacher, and S. Marburg, “A platform for benchmark cases in computational acoustics,” *Acta Acustica United With Acustica*, vol. 101, no. 4, pp. 811–820, 2015.
- [210] C. Scrosati, F. Martellotta, F. Pompoli, A. Schiavi, A. Prato, D. D’Orazio, M. Garai, N. Granzotto, A. Di Bella, F. Scamoni, *et al.*, “Towards more reliable measurements of sound absorption coefficient in reverberation rooms: An inter-laboratory test,” *Applied Acoustics*, vol. 165, p. 107298, 2020.
- [211] *ISO 354:2003 Acoustics — Measurement of sound absorption in a reverberation room.*
- [212] M. Vercammen, “On the revision of iso 354, measurement of the sound absorption in the reverberation room,” *ISO/WD*, vol. 354, 2018.

- [213] D. D’Orazio, D. De Salvio, L. Anderlucci, and M. Garai, “Signal-to-noise ratio in university lecture halls with low intelligibility,” Universitätsbibliothek der RWTH Aachen, 2019.
- [214] B. Masiero, R. Scharrer, and M. Vorländer, “Ita-toolbox—an open source matlab toolbox for acousticians pascal dietrich, martin guski, martin pollow, markus müller-trapet,”
- [215] T. Thydal, F. Pind, C.-H. Jeong, and A. P. Engsig-Karup, “Experimental validation and uncertainty quantification in wave-based computational room acoustics,” *Applied Acoustics*, vol. 178, p. 107939, 2021.
- [216] J. Meyer, *Acoustics and the performance of music: Manual for acousticians, audio engineers, musicians, architects and musical instrument makers*. Springer Science & Business Media, 2009.

# List of Figures

2.1	Sound propagation model. . . . .	21
2.2	Compression and rarefaction of the air caused by acoustic waves. . . . .	22
2.3	A fixed volume of the fluid showing the rate of mass flow. . . . .	23
2.4	Absorption coefficient depending on the specific acoustic impedance $\zeta$ and the angle of incidence $\theta$ . . . . .	30
2.5	Main differences between the currently used wave-based modeling methods. . . . .	33
2.6	2D visualization of interior and exterior problem referred to a closed boundary. . . . .	34
2.7	Finite difference simulation. . . . .	40
2.8	Visualization of the Cartesian grid. . . . .	42
2.9	Visualization of adjacent points in the Cartesian grid. . . . .	42
2.10	The stable and unstable regions in the z-plane. . . . .	44
2.11	Approximation of sound waves to rays. . . . .	46
2.12	Typical energy room impulse response. . . . .	47
2.13	Basic principle of ISM. . . . .	48
2.14	Magnitude of a stationary room transfer function. . . . .	51
2.15	Typical principle of a GA hybrid model. . . . .	52
2.16	Example of different kinds of diffraction. . . . .	53
2.17	Scattering coefficient. . . . .	55
2.18	Single reflector and energy reflected. . . . .	55
3.1	Conventional approaches to room acoustic simulations. . . . .	57
3.2	Hybrid FDTD/GA model employed. . . . .	58
3.3	Three possible stencils. . . . .	60
3.4	example of a staircase effect. . . . .	60
3.5	Absorption of the air at 20°C and 1 atm. . . . .	62
3.6	Qualitative and simplified flowchart for the FDTD simulation initial setting. . . . .	64
3.7	Case studies selected for the work. . . . .	66
3.8	Analysis of the volumes in TCB and DUS. . . . .	68

3.9	Focusing effects caused by curved surfaces. . . . .	71
3.10	Deterioration of the speech signal. . . . .	72
3.11	Flowchart of the double calibration. . . . .	73
4.1	Typical cutaway of the composite system of volumes within opera houses. . . . .	81
4.2	<i>Sala Bibiena</i> of the <i>Teatro Comunale</i> in Bologna. . . . .	82
4.3	Relation between the seating capacity, $N$ , and the volume of the main hall, $V_{hall}$ . . . . .	83
4.4	Scheme of the volumetric proportion in TCB. . . . .	84
4.5	Positions of sound sources (S) and receivers (R) in TCB. . . . .	86
4.6	Views of TCB during different measurements configurations. . . . .	87
4.7	Distinct audience areas in TCB. . . . .	87
4.8	Relation between $C_{80,3}$ , $EDT_M$ , and $V_{hall}$ in TCB. . . . .	88
4.9	Measured $T_{30}$ , EDT, $C_{80}$ , $T_S$ values in TCB in octave bands. . . . .	88
4.10	Visualization of sound propagation in TCB. . . . .	90
4.11	View of <i>Teatro Comunale</i> 's CAD model. . . . .	91
4.12	TCB calibration: measured and simulated EDT and $T_S$ values in octave bands. . . . .	93
4.13	Multi-decay analysis of simulated IRs in TCB at 1000 Hz. . . . .	98
4.14	Multi-decay analysis of simulated IRs in TCB at 1000 Hz. . . . .	99
4.15	<i>Duse theatre</i> (DUS) in Bologna. . . . .	102
4.16	Relation between the seating capacity, $N$ , and the volume of the main hall, $V_{hall}$ . . . . .	103
4.17	Configuration of the stage with the sound reflectors array. . . . .	104
4.18	Scheme of the main coupling volumes in DUS. . . . .	104
4.19	Positions of sound sources (S) and receivers (R) selected in the acoustic measurements campaign in DUS. . . . .	106
4.20	Relation between $C_{80,3}$ , $EDT_M$ , and $V_{hall}$ in DUS. . . . .	107
4.21	Measured $T_{30}$ , EDT, $C_{80}$ , $T_s$ values in DUS in octave bands. . . . .	108
4.22	View of <i>Duse Theatre</i> 's CAD model as shown in the modeling software. . . . .	109
4.23	Qualitative representation of sound reflectors effects in DUS. . . . .	110
4.24	DUS calibration: measured and simulated EDT and $T_S$ values in octave bands. . . . .	113
4.25	Multi-decay analysis of simulated IRs in DUS at 1000 Hz. . . . .	117
5.1	View of St Cecilia's hall, Edinburgh (UK). . . . .	121
5.2	Relation between the seating capacity, $N$ , and the volume of the hall, $V$ , in St Cecilia's hall. . . . .	123

---

5.3	Configuration without seats during the acoustic measurements in STC. . . . .	123
5.4	Scheme of the single acoustic volume in STC (view from the top). . . . .	124
5.5	Positions of sound sources (S) and receivers (R) selected in the acoustic measurements campaign in STC. . . . .	125
5.6	Measured $T_{30}$ , EDT, $C_{80}$ , $T_S$ values in STC in octave bands. . . . .	127
5.7	View of the 3D virtual model of St Cecilia's hall. . . . .	128
5.8	Plan and longitudinal section view of STC. . . . .	129
5.9	STC calibration: measured and simulated EDT and $T_S$ values in octave bands. . . . .	131
5.10	Normalised simulated impulse response in STC. . . . .	133
5.11	Analytical predictive model, measured and simulated G values at 125 Hz. . . . .	135
6.1	Interior view of the university lecture hall (ULH). . . . .	137
6.2	View of longitudinal section and plan of ULH. . . . .	139
6.3	Measured $T_{30}$ , EDT, $C_{50}$ , $T_S$ values in ULH in octave bands. . . . .	141
6.4	View of the 3D virtual model of the university lecture hall (ULH). . . . .	142
6.5	Qualitative visualization of sound wave propagation in ULH. . . . .	144
6.6	ULH calibration: measured and simulated EDT and $C_{50}$ values in octave bands. . . . .	144
6.7	Interior view of the acoustic treatment virtually introduced into ULH model. . . . .	147
6.8	Modulation transfer index MTI in octave bands. . . . .	150
7.1	Qualitative visualization of sound wave propagation in ULH. . . . .	155
7.2	Variations of input data for the two simulation methods. . . . .	158
7.3	Example of energy decay range in an acquired IR in TCB. . . . .	160
7.4	Multi-decay analysis of simulated IRs in TCB and DUS at 1000 Hz. . . . .	162
7.5	Energy decay curves (EDCs) in TCB. . . . .	163
7.6	Spectral content of IRs corresponding to a peculiar acoustic scenario in TCB. . . . .	165
7.7	Spectral content of IRs corresponding to a peculiar acoustic scenario in DUS. . . . .	166



# List of Tables

3.1	GA++ simulation setup. . . . .	78
4.1	Geometrical features of the <i>Teatro Comunale</i> in Bologna (TCB). . . . .	83
4.2	Measurements results in TCB. . . . .	85
4.3	Simulation setup of FDTD simulation in TCB. . . . .	92
4.4	Measured and simulated room criteria in TCB. . . . .	95
4.5	Materials involved in TCB simulations. . . . .	96
4.6	Different metrics describing coupled volumes. . . . .	101
4.7	Geometrical features of the <i>Duse theatre</i> in Bologna (DUS). . . . .	103
4.8	Measurements results in DUS. . . . .	105
4.9	Measured and simulated room criteria in DUS. . . . .	112
4.10	Materials involved in DUS simulations. . . . .	114
5.1	Geometrical features of St Cecilia's Hall (STC) in Edinburgh. . . . .	122
5.2	Measurements results in STC. . . . .	126
5.3	Simulation setup of FDTD simulation in STC. . . . .	130
5.4	Measured and simulated room criteria in STC. . . . .	131
5.5	Materials involved in STC simulations. . . . .	132
6.1	Geometrical features of the university lecture hall (ULH) in Bologna. . . . .	138
6.2	Measurements results in ULH. . . . .	140
6.3	Simulation setup of FDTD simulation in ULH. . . . .	143
6.4	Measured and simulated room criteria in ULH. . . . .	145
6.5	Materials involved in ULH simulations. . . . .	145
6.6	Specific normalised impedances $\zeta$ corresponding to the double layer MPP. . . . .	148
6.7	Trend in frequency of $T_{30}$ in ULH. . . . .	148
A.1	Normalised LRC (inductance, resistance, capacitance) coeffi- cients in TCB. . . . .	176

A.2	Normalised LRC (inductance, resistance, capacitance) coefficients in DUS. . . . .	177
A.3	Normalised LRC (inductance, resistance, capacitance) coefficients in STC. . . . .	178
A.4	Normalised LRC (inductance, resistance, capacitance) coefficients in ULH. . . . .	179
A.5	Corresponding absorption coefficients derived from acoustic admittances. . . . .	181
A.6	Absorption ( $\alpha$ ) and scattering (s) coefficients employed in GA++ simulations . . . . .	182